Digests

The 32ⁿᵈ Magnetic Recording Conference

TMRC 2021

Virtual Conference
Hosted by

Carnegie Mellon University

Pittsburgh, PA

August 16 – 19, 2021

DSSC
The Data Storage Systems Center

IEEE MAGNETICS

TMRC 2021 | Chairman's Welcome

Conference Chair

Moris Dovek
Headway / TDK

Program Co-Chairs

Ian McFadyen
Western Digital

Dmytro Apalkov
Samsung

Kevin R Heim
Seagate Technology

Alan Kalitsov
Western Digital

**Contributed Paper
Co-Chairs**

Tazumi Nagasawa
Toshiba Corporation

Thomas Boone
Spin Memory

Local Co-Chairs

Jian-Gang (Jimmy) Zhu
Carnegie Mellon University

James A. Bain
Carnegie Mellon University

Publication Co-Chairs

Simon Greaves
Tohoku University

Yuepeng Zhang
Argonne National Laboratory

Publicity Co-Chairs

Siddhesh Sakhalkar
Western Digital

Eric Evarts
IBM

Treasurer

Pavol Krivosik
Seagate Technology

Local Admin

Chloë Mattingly
Carnegie Mellon University

Welcome to The 32nd Magnetic Recording Conference. TMRC 2021 is organized under the auspices of the IEEE Magnetics Society; and it is exclusively devoted to magnetics-based data storage and memory technologies. TMRC is regarded as the premier conference for professionals in these fields.

Despite the tremendous progress so far towards ending the worldwide COVID-19 pandemic, the committee decided to hold this year's program in virtual format to allow more global participation in the conference. While the peer-to-peer interactions that made TMRC so unique in the past will be missed for one more year, our virtual platform and conference program promise to make this year's event a memorable one.

As has been the practice in recent years, one-half of the conference is devoted to the physics and applications of MRAM and related magnetic phenomena such as spin-orbit torque (SOT-MRAM), voltage-controlled (VC-MRAM) and other novel magnetic phenomena with potential impact on storage and memory applications. This year's focus is on "novel materials, devices and advanced technologies for magnetic data storage and memory applications"

The invited talks, each 30 min in length, cover six sessions on HDD and MRAM during the first three days of the conference. They encompass 38 invited speakers, all of whom are recognized experts in their fields. They will inform us about recent developments in Heat-Assisted Magnetic Recording (HAMR), Microwave-Assisted Magnetic Recording (MAMR), Read Heads, MRAM and related magnetic phenomena. The invited presentation sessions will be supplemented on the last day of the conference by two sessions consisting of 18 contributed talks of 20 minutes each. What used to be the poster sessions at prior in-person events, have been replaced with contributed talks. We are also happy to continue the recently established practice of allowing all presentations to be published, after proper peer review and acceptance, in the IEEE Transactions on Magnetics.

In closing, I would like to give my sincere thanks to the entire organizing committee. This is an all-volunteer team of dedicated professionals from academia and industry that has worked for almost a full year to make this event possible. We are grateful to CMU DSSC for providing logistics support to the conference, despite our inability to enjoy the event on their beautiful campus this year.

Last, but not least, I would like to take this opportunity to recognize the generosity of our corporate sponsors, for answering our call for help. Their contributions make it possible for us to offer this conference at very affordable rates.

On behalf of the entire organizing committee it is my pleasure to welcome you to TMRC 2021!

Moris M. Dovek
Conference Chair, TMRC 2021

TMRC 2021 | Corporate sponsors

Western Digital.

SEAGATE

TOSHIBA

TDK

BROADCOM®

TMRC 2021 Program Overview

All times are US Eastern Daylight Time (US-NY)

	Morning	Evening	
Monday August 16th			
Invited talks		Session A HAMR 6:00 pm to 8:45 pm	Session B MRAM I 6:00 pm to 9:45 pm
Tuesday August 17th			
Invited talks	Session C MRAM II 8:00am to 11:45am	Keynote Aaron Ogus, Microsoft 6:00pm to 7:00 pm	Session D HAMR, MAMR, Reader 7:00 pm to 9:45 pm
Wednesday August 18th			
Invited talks	Session E MRAM III 8:00 am to 11:45 am		Session F MAMR 6:00 pm to 9:15 pm
Thursday August 19th			
Contributed talks		Session G HDD, Tape 6:00 pm to 9:15 pm	Session H MRAM IV 6:00 pm to 9:15 pm

Time zone table

Live talks take place during periods indicated in green

US-CA	US-MN	US-NY	UTC	UK	CET	India	China Singapore	Japan Korea
5am	7am	8am	noon	1pm	2pm	5:30pm	8pm	9pm
6am	8am	9am	1pm	2pm	3pm	6:30pm	9pm	10pm
7am	9am	10am	2pm	3pm	4pm	7:30pm	10pm	11pm
8am	10am	11am	3pm	4pm	5pm	8:30pm	11pm	midnight
9am	11am	noon	4pm	5pm	6pm	9:30pm	midnight	1am
10am	noon	1pm	5pm	6pm	7pm	10:30pm	1am	2am
11am	1pm	2pm	6pm	7pm	8pm	11:30pm	2am	3am
noon	2pm	3pm	7pm	8pm	9pm	12:30am	3am	4am
1pm	3pm	4pm	8pm	9pm	10pm	1:30am	4am	5am
2pm	4pm	5pm	9pm	10pm	11pm	2:30am	5am	6am
3pm	5pm	6pm	10pm	11pm	midnight	3:30am	6am	7am
4pm	6pm	7pm	11pm	midnight	1am	4:30am	7am	8am
5pm	7pm	8pm	midnight	1am	2am	5:30am	8am	9am
6pm	8pm	9pm	1am	2am	3am	6:30am	9am	10am
7pm	9pm	10pm	2am	3am	4am	7:30am	10am	11am

Keynote Speech

Tuesday, August 17, 2021

6:00-7:00pm EDT

Storing zettabytes per year:
the never ending growth of cloud data storage

Aaron Ogus
Azure Core Storage

Biography

   Aaron is a Distinguished Engineer working in the Microsoft Azure Core Team. He works (with many others) on optimizing the co-design of Hardware and Software for Azure Storage, Compute and Networking. Aaron has been working on Azure Storage since its inception in 2008 and has helped Microsoft optimize storage design and deployment, and has worked with industry partners to optimize components, servers and switch designs for the cloud. Aaron has helped influence the evolution of Network Switches, SSDs, HDDs and Archival Systems for Cloud deployment.

   Aaron started at Microsoft in 1991, and before Azure worked on a few notable projects, including Windows 95, DirectX, XBOX and Forza Motorsport.

   Aaron has a regional SCCA racing championship in Formula Mazda, which was instrumental in helping make Forza the highest grossing racing franchise on XBOX.

   Aaron also plays a little poker from time to time. He finished second in a World Poker Tour Tournament at a Televised Final Table.

TMRC 2021 Invited Presentations

Monday August 16th, 6:00 pm to 8:45 pm (EDT)

Session A: HAMR			
Session chair: Randall Victora (University of Minnesota)			

Presentation	Mon PM	Title	Speaker
A1	6:00-6:30 PM	Opto-thermal simulation of metallic smear's impact on HAMR technology	Robert Smith Western Digital
A2	6:30-7:00 PM	Simulation of a thermally efficient HAMR ridge waveguide NFT on an AlN heat sink	Wenyi Zhang Carnegie Mellon University
A3	7:00-7:30 PM	Quasi-equilibrium Stoner-Wohlfarth versus strongly out-of-equilibrium dynamics in HAMR	Alain Truong Headway Technologies
	7:30-7:45 PM	Break	
A4	7:45-8:15 PM	Interplay of thermal and magnetic fields in HAMR	Niranjan Natekar Western Digital
A5	8:15-8:45 PM	Direct measurement of magnetic timing jitter in writers	Peter Czoschke Seagate Technology

Monday August 16th, 6:00 pm to 9:45 pm (EDT)

Session B: MRAM I			
Session chair: Jordan Katine (Western Digital)			

Presentation	Mon PM	Title	Speaker
B1	6:00-6:30 PM	Demonstration of narrow switching distributions in STT-MRAM arrays for LLC applications at 1x nm node	Guohan Hu IBM
B2	6:30-7:00 PM	3-dimensional integration of epitaxial magnetic tunnel junctions with new materials for future MRAM	Shinji Yuasa AIST
B3	7:00-7:30 PM	Revisiting Fe/MgO/Fe(001): giant tunnel magnetoresistance up to ~420% at room temperature	Hiroaki Sukegawa NIMS
	7:30-7:45 PM	Break	
B4	7:45-8:15 PM	Recent progresses in STT-MRAMs, SOT-MRAMs for low power AI/IoT Processors	Tetsuo Endoh Tohoku University
B5	8:15-8:45 PM	Voltage control spintronics memory (VoCSM)-based low energy consumption non-volatile logic-gates for binary neural networks	Hiroaki Yoda Spin-Orbitronics Technologies
B6	8:45-9:15 PM	Ferromagnet-induced spin-orbit torques	Kyung-Jin Lee KAIST
B7	9:15-9:45 PM	Spin-orbit torque switching based on topological spin textures and magnons	Hyunsoo Yang National University of Singapore

TMRC 2021 Invited Presentations

Tuesday August 17th, 8:00 am to 11:45 am (EDT)

Session C: MRAM II		
Session chair: Alan Kalitsov (Western Digital)		

Presentation	Tue AM	Title	Speaker
C1	8:00-8:30 AM	Chiral spin textures and chiral spin-orbit torques for spintronic memories	Stuart Parkin Max Planck Institute for Microstructure Physics
C2	8:30-9:00 AM	Interplay of voltage control of magnetic anisotropy, spin transfer torque, and heating on spin-orbit torque switching of magnetic tunnel junctions	Viola Krizakova ETH Zurich
C3	9:00-9:30 AM	PMA mechanisms at Fe/MgO interfaces: On its voltage control and temperature dependence	Fatima Ibrahim SPINTEC
	9:30-9:45 AM	Break	
C4	9:45-10:15 AM	Spin orbit torques from ferromagnetic layers with out-of-plane spin polarization	Andrew Kent New York University
C5	10:15-10:45 AM	Large perpendicular magnetic anisotropy and voltage controlled magnetic anisotropy effects at CoFe/MgO interface	Bhagwati Prasad Western Digital
C6	10:45-11:15 AM	Cryogenic MRAMs for superconducting computers	Minh-Hai Nguyen Western Digital
C7	11:15-11:45 AM	Using dopants and alloying to optimize spin Hall materials for MRAM devices	Derek Stewart Western Digital

Tuesday August 17th, 7:00 pm to 9:45 pm (EDT)

Session D: HAMR / MAMR / Read		
Session chair: Niranjan Natekar (Western Digital)		

Presentation	Tue PM	Title	Speaker
D1	7:00-7:30 PM	DC write head current driven energy assisted magnetic recording	Asif Bashir Western Digital
D2	7:30-8:00 PM	Rotated read head design for high-density heat-assisted shingled magnetic recording	Randall Victora University of Minnesota
	8:00-8:15 PM	Break	
D3	8:15-8:45 PM	Micromagnetic studies of spin torque oscillator reader phase noise and SNR	Olle Heinonen Argonne National Laboratory
D4	8:45-9:15 PM	TDMR performance gain with machine learning data detection channel	Yuwei Qin Carnegie Mellon University
D5	9:15-9:45 PM	Asynchronous partial-response equalization to time-varying target for multitrack detection of asynchronous tracks	Elnaz Banan Sadeghian Stevens Institute of Technology

TMRC 2021 Invited Presentations

Wednesday August 18th, 8:00 am to 11:45 am (EDT)

Session E: MRAM III			
Session chair: Dmytro Apalkov (Samsung)			

Presentation	Wed PM	Title	Speaker
E1	8:00-8:30 AM	Mitigating the write stochasticity in STT MRAMs: suppressing back hopping and making the wall motion reproducible	Thibaut Devolder Université Paris-Saclay, CNRS
E2	8:30-9:00 AM	Demonstration of nanosecond operation in stochastic magnetic tunnel junctions	Chris Safranski IBM
E3	9:00-9:30 AM	Single-event effects in STT MRAM	Douglas Martin Naval Surface Warfare Systems
	9:30-9:45 AM	Break	
E4	9:45-10:15 AM	Technology transfers into the defense industry: implications for advanced microelectronics in the future of national security	Mike Burkland Raytheon Technologies
E5	10:15-10:45 AM	Magnetoresistive random access memories for space and radiation-hardened applications	Romney R. Katti Honeywell Aerospace
E6	10:45-11:15 AM	Physical mechanisms affecting performance of perpendicular STT-MRAM cells	Goran Mihajlovic Western Digital
E7	11:15-11:45 AM	STT-MRAM for automotive applications	Kerry Nagel Everspin

Wednesday August 18th, 6:00 pm to 9:15 pm (EDT)

Session F: MAMR			
Session chair: Yasushi Kanai (Niigata Institute of Technology)			

Presentation	Wed AM	Title	Speaker
F1	6:00-6:30 PM	Magnetic recording assisted by spin-transfer-torque-induced magnetization reversal and dynamics	Wenyu Chen Headway Technologies
F2	6:30-7:00 PM	Sub-nanosecond switching of spin-transfer-torque device for energy assisted perpendicular magnetic recording	Yunfei Ding Western Digital
F3	7:00-7:30 PM	Analysis of a spin-torque oscillator using injection locking to an external microwave field	Hirofumi Suto NIMS
	7:30-7:45 PM	Break	
F4	7:45-8:15 PM	Improvement of dual FGL structure for MAS effect dominant MAMR head	Masayuki Takagishi Toshiba Corporation
F5	8:15-8:45 PM	Media optimisation for microwave-assisted magnetic recording	Simon Greaves Tohoku University
F6	8:45-9:15 PM	Spin torque oscillator for microwave assisted magnetic recording	Jian-Gang (Jimmy) Zhu Carnegie Mellon University

TMRC 2021 Contributed Presentations

Thursday August 19th, 6:00 pm to 9:15 pm (EDT)

Session G: HDD / Tape			
Session chairs: Ben Belzer (Washington State University), Simon Greaves (Tohoku University)			

Presentation	Thu PM	Title	Speaker
G1	6:00-6:20 PM	Two serial multi-layer perceptrons for signal detection and modulation code decoding for bit-patterned media recording	Seongkwon Jeong Soongsil University
G2	6:20-6:40 PM	A study of performance evaluation with neural network detector in SMR system	Madoka Nishikawa Ehime University
G3	6:40-7:00 PM	A study of equalization for reproducing a double-layer magnetic recording medium	Yasuaki Nakamura Ehime University
G4	7:00-7:20 PM	Turbo-detection for multilayer magnetic recording using deep neural network-based equalizer and media noise predictor	Amirhossein Sayyafan Washington State University
G5	7:20-7:40 PM	Multi-track detection assisted by multi-task neural network using 2D soft transition information for heat assisted interlaced magnetic recording	Yushu Xu Shanghai Jiao Tong University
	7:40-7:55 PM	Break	
G6	7:55-8:15 PM	Evaluation of sputtered tape media with hard disk drive components	Pierre-Olivier Jubert Western Digital
G7	8:15-8:35 PM	Causes of HAMR transition curvature dependence on bit length	Kun Xue University of Minnesota
G8	8:35-8:55 PM	STO oscillation dependence on in-gap field and main pole magnetization in MAMR	Ryo Itagaki Niigata Institute of Technology
G9	8:55-9:15 PM	Large impact of spin asymmetry at half-metallic Co2Fe0.4Mn0.6Si/CoFe interface on current-perpendicular-to-plane giant magnetoresistance	Yuichi Fujita NIMS

Thursday August 19th, 6:00 pm to 9:15 pm

Session H: MRAM IV			
Session chair: Thomas Boone (Spin Memory)			

Presentation	Thu PM	Title	Speaker
H1	6:00-6:20 PM	The practical material challenges invloved in using the topological insulator BiSb in a spin transfer device	Brian R. York Western Digital
H2	6:20-6:40 PM	Noble metal under layer influence on the temperature dependent Gilbert damping in L10 FePd films with large perpendicular magnetic anisotropy	Dingbin Huang University of Minnesota
H3	6:40-7:00 PM	Switching current density of perpendicular magnetization by spin-orbit torque	Lijun Zhu Cornell University
H4	7:00-7:20 PM	Comparison of two parametric mechanisms reversal in FeCoB nanomagnet. Theory and experiment	Vadym Zayets AIST
	7:20-7:35 PM	Break	
H5	7:35-7:55 PM	Strain-spin coupling induced high-frequency magnetoacoustic resonance in perpendicular magnetic multilayers	Delin Zhang University of Minnesota
H6	7:55-8:15 PM	High spin Hall angle in sputtered BiSb topological insulator (bottom)/ ferromagnet with in-plane magnetization on sapphire substrates	Julian Sasaki Tokyo Institute of Technology
H7	8:15-8:35 PM	LDPC joint decoding scheme for STT MRAM storage	Jinghua Liu Fuzhou University
H8	8:35-8:55 PM	Magneto-optical detection of memory operation in magnetic nanowire device	Mao Takahashi NHK
H9	8:55-9:15 PM	The importance of heat contribution by tunneling: electron spin scattering in magnetic tunnel junction	Shuhan Liu Xi'an Jiaotong University

OPTO-THERMAL SIMULATION OF METALLIC SMEAR'S IMPACT ON HAMR TECHNOLOGY

Robert SMITH, Sukumar RAJAURIA, Richard BROCKIE, Erhard SCHRECK, and Qing DAI

Western Digital Corporation, San Jose, CA, USA

I. INTRODUCTION

Contamination, known as smear, in the head-disk interface poses a significant reliability challenge for heat-assisted magnetic recording (HAMR) technology. While smear in perpendicular magnetic recording (PMR) can induce head-disk spacing instability, light at the HAMR interface produces additional adverse effects on both head reliability and recording quality. Previous studies have demonstrated that optically absorbing smear, such as organic carbonaceous material, is particularly harmful since the heat dissipated at the interface raises the temperature of the near-field transducer (NFT), thereby compromising its reliability [1, 2]. Due to the optical nature of the HAMR interface, the accumulation of metallic smear also presents a significant challenge. Metallic interface materials not only absorb light that is emitted from the NFT, but they can also redirect the path of the propagating plasmon generated at the surface of the NFT. This ability to perturb the near-field coupling to the medium has significant implications for the stability of the HAMR recording process. Thus, both the NFT reliability and recording impact must be investigated to determine the ramifications of metallic smear in HAMR. In this work, we utilize opto-thermal simulation to uncover metallic smear's impact on HAMR reliability and recording performance.

II. MODEL

The opto-thermal model consists of a near-field transducer separated from a HAMR medium by a layer of interface material. We investigated the following interface material configurations: organic smear, organic smear with an embedded metallic particle, and a metallic particle without organic smear. The particle, which is composed of a metal, has a disk-shaped geometry that bridges the gap between the head and the medium and has a diameter corresponding to 20% of the NFT's critical dimension. The metallic particle's down-track position relative to the NFT is also varied in this study. For each of these cases, the NFT temperature and the medium thermal profiles are calculated using the opto-thermal model. The resulting medium thermal profiles are used to calculate the medium thermal gradients as a function of total track width determined using a micromagnetic simulation [3].

III. RESULTS AND DISCUSSION

The simulation reveals that the metallic particle at the interface has a significant effect on the peak NFT temperature and on the medium thermal profiles. The optical absorption contour shown in Fig. 1 illustrates that a metallic particle under the NFT significantly distorts the near-field coupling of light to the medium. This distortion intensely focuses the light onto the medium in the region immediately underneath the particle. The local intensification of the near-field coupling means that the metallic particle acts as a narrow extension of the NFT and has a tremendous impact on the medium thermal gradient. Figure 2 a) shows that the thermal gradient increases by a factor of 2.4 when the metallic particle is underneath the NFT. When the metallic particle is in an air-filled interface free of organic smear, this thermal gradient increase is further amplified due to the high optical impedance of air. The metallic particle's thermal gradient impact is reduced when the particle moves just a couple of nanometers down-track of the NFT. Furthermore, we found that as the particle's lateral diameter exceeds the critical dimension of the NFT, the thermal gradient increase also diminishes. Therefore, to observe the extreme gradient increase, the smear must be metallic, smaller than the critical dimension of the NFT, and immediately underneath the NFT. All of these conditions are necessary for metallic smear to produce an intensification of the near-field coupling. Due to the light absorbed by the metallic smear, the local peak

ROBERT SMITH
E-mail: robert.smith@wdc.com
tel: +1-408-7177931

temperature rise of the NFT is 1.8 times higher than the organic-only smear configuration as shown in Fig. 1 b). As was the case with the thermal gradient increase, this NFT temperature effect is exacerbated when the metallic particle is embedded in an air-filled interface. As the particle moves down-track of the NFT, the spike in NFT temperature attenuates, indicating that the risk to NFT reliability diminishes with increased distance from the NFT.

Due to the high temperature of the HAMR head-disk interface, the formation of smear is highly dynamic, and the combination of organic and metallic smear is more likely than a metallic particle in the air-filled, organic-free interface. As our modeling demonstrates, a mixture of organic and metallic smear still has an extremely significant effect on the NFT temperature and medium thermal gradient. Since HAMR recording quality is dependent on the thermal gradient of the medium, this finding signifies that HAMR technology can be subjected to large recording quality variations solely due to the dynamics of a metallic particle in the interface. The rapid formation of a metallic particle in the smear would produce a sudden and substantial thermal gradient increase, while the abrupt removal of this particle would result in a precipitous decline in thermal gradient. Thus, it is critical to suppress metallic smear in the HAMR head-disk interface.

REFERENCES

1) J. D. Kiely et al., "Write-Induced Head Contamination in Heat-Assisted Magnetic Recording", *IEEE Trans. Magn.,* 53(2) 1-7, (2017).
2) N. Tagawa et al., "Experimental Study on Smear Characteristics Upon Laser Heating in Air and Helium in Heat-Assisted Magnetic Recording," *IEEE Trans. Magn.,* 57(2) 1-5, (2021).
3) E. Roddick et al., "Component Design Considerations for High Areal Density in Heat-Assisted Magnetic Recording," *IEEE Trans. Magn.*, 57 (2) 1-7, (2021).
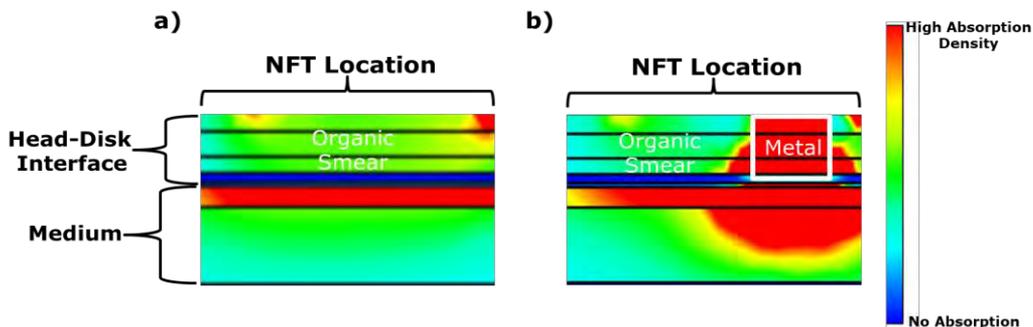
Fig. 1 The optical absorption profile for head-disk interface smear and recording medium underneath the NFT when smear is a) purely organic and b) a metallic particle embedded in organic material.
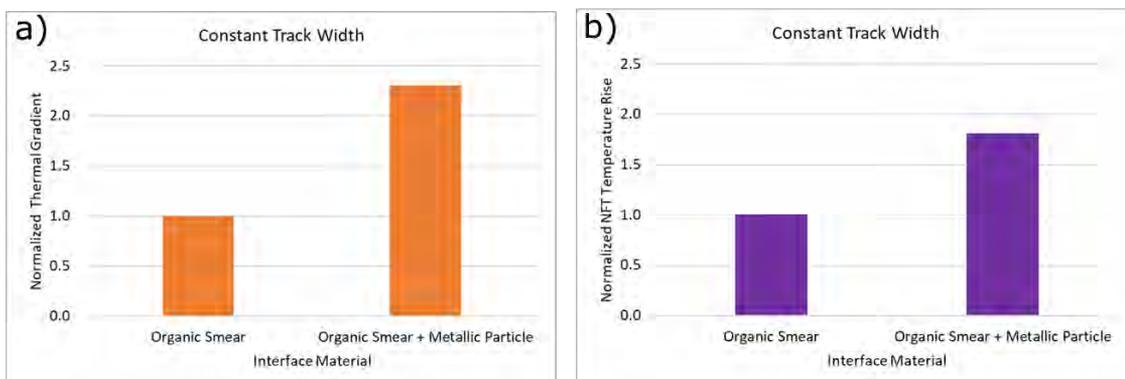
Fig. 2 a) Normalized cross-track thermal gradient in the medium and b) normalized NFT temperature for a head-disk interface with and without the metallic particle.

Simulation of a Thermally Efficient HAMR Ridge Waveguide NFT on an AlN Heat Sink

Wenyi ZHANG, Benjamin A. FRIEDMAN and James A. BAIN

Carnegie Mellon University, Pittsburgh, PA 15213, USA

I.   INTRODUCTION

Heat-assisted magnetic recording (HAMR) promises to increase the areal data density in hard disk drives beyond 1 Tb/in^2 by raising the temperature of the media to its Curie temperature for writing. The metallic optical near-field transducer (NFT) is a key component of the HAMR system. It confines optical energy to a small region below the diffraction limit on the recording media. The challenge with HAMR is that the NFT can reach extreme temperatures due to self-heating. Therefore, thermal reliability of the NFT is of great importance. To help the NFT dissipate heat, AlN is a potential heat sink material with reported thermal conductivity higher than 100 W/m-K [1]. In this work, we proposed a thermally efficient HAMR light delivery system using a ridge waveguide on an AlN heat sink. The relatively large metallic waveguide structure can dissipate heat effectively even in the presence of finite interface thermal conductance while still producing a small thermal spot in the medium. The thermal efficiencies (*TE*), defined as the ratio of peak temperature rise in the media versus in the NFT can be as high as 3.7 in our design.

II.   THERMALLY EFFICIENT NFT DESIGN

A diagram of TiO$_2$-waveguide-excited ridge waveguide NFT is shown in Figure 1 (a). The ridge waveguide uses the fact that under the illumination with light polarized across the gap, the localized surface plasmon polariton (SPP) resonance excited in the cavity can drive charges to the ridge to produce a strong electric field in the gap between the ridge and opposite cavity edge. Maximum transmission efficiency is achieved at resonance when the cavity width is about half of the SPP wavelength [2]. In our simulation, we use 800 nm wavelength light to excite the NFT. The cavity width, cavity height, ridge width and ridge height are 250, 20, 15, and 10 nm respectively in our design. The NFT sits on an AlN heat sink and is covered with SiO$_2$ on the top and side in a plausible geometry. The ridge waveguide cavity is also filled with SiO$_2$. The relatively large metallic ridge waveguide structure offers a large interface between Au and AlN to reduce the thermal interface resistance. In addition, as the field enhancement occurs in the cavity, the thermal interface resistance can be further reduced by adding an interface adhesion layer like Cr without sacrificing the optical properties. The optimal Au width and height depends on the excitation mode and the coupling and thermal efficiency can be optimized by maximizing the mode overlap between the excitation mode and NFT eigenmode. The distances between the cavity edges to the nearby Au/dielectric material interfaces l_{top}, l_{bottom} and l_{side} are set as 100, 100, and 150 nm respectively according to parameter optimization results.
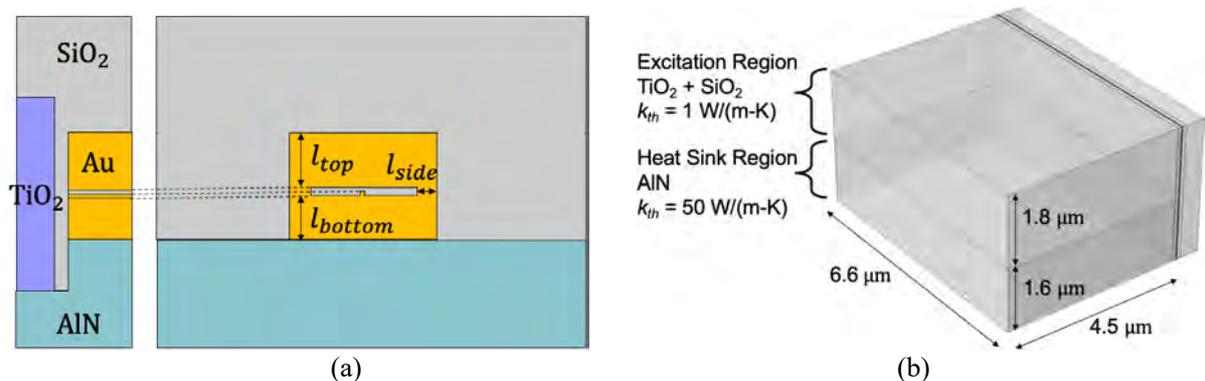

Fig. 1 (a) Diagram of the ridge waveguide NFT with a TiO$_2$ waveguide as the excitation source. (b) The simulation environment for all of the coupling schemes.

The optical and thermal simulation is performed using FEM through COMSOL Multiphysics and the

Wenyi Zhang
E-mail: wenyizha@andrew.cmu.edu
tel: +1-412-251-2045

recording media in the simulation is composed of data layer, interlayer, heat sink layer and substrate with thicknesses of 10, 15, 100, and 500 nm respectively, refractive index of 2.9-2.5j, 1.5, 0.2-5j, and 1.5 respectively, and thermal conductivity of 1.5 (in-plane), 10, 150, and 1 W/m-K respectively. The thermal conductivity of the data layer is anisotropic, having ~4.5x the above value in the direction normal to the film. The simulation geometric configuration is shown in Figure 1 (b). Details of the coupling optics are not shown but the regions above the AlN layer (k_{th} = 50 W/m-K) have low thermal conductivity (SiO$_2$ and TiO$_2$ k_{th} = 1 W/m-K) for all geometries. The Au in the NFT had k_{th} = 100 W/m-k and n = 0.2-5j.

III. METHODS OF NFT EXCITATION

In addition to the NFT geometry, the excitation scheme also has a huge influence on the coupling and thermal efficiency. Four excitation methods were considered and compared in our study: 1) NFT eigenmode excitation; 2) Impinging eigenmode of a dielectric waveguide; 3) Transverse mode of a dielectric waveguide and 4) Transverse mode of a dielectric resonator. For the dielectric waveguide and resonator modes, we choose the modes in which the dominated electric field component is polarized across the gap to maximize the mode overlap between the excitation mode and NFT eigenmode. The excitation schemes are shown schematically in Fig. 2. We define the power absorption ratio, R, as

$$R = P_{NFT}/P_{hotspot}, \tag{1}$$

where P_{NFT} and $P_{hotspot}$ are the power dissipation in the NFT and hotspot respectively. The minimum R is achieved by the NFT eigenmode excitation as other excitation modes always waste some additional energy heating the NFT. This is an infeasible coupling scheme but is an excellent reference case for comparison.

According to our thermal simulations, the thermal resistance of the NFT was around 0.13 K/μW. It should be noted that the presence of the AlN under the NFT was critical to achieving this thermal resistance, as it was 0.52 K/μW when the AlN was changed to SiO$_2$ (a 4x reduction). The effective thermal resistance of the medium hot spot ranged from 1-11 K/μW, depending on spot shape. The resulting TE for the four schemes with AlN (SiO$_2$) underlayers shown in Fig. 2 are 5.0 (1.3), 3.7 (0.9), 0.4 (0.1), and 1.0 (0.3), respectively.

These results show that AlN brings significant thermal benefits and allows at least one feasible design (the impinging dielectric mode, Fig. 2b) to go from unacceptable thermal performance with an SiO$_2$ underlayer *(TE = $\Delta T_{hotspot}/\Delta T_{NFT}$ = 0.9)* to very promising performance with AlN *(TE = $\Delta T_{hotspot}/\Delta T_{NFT}$ = 3.7)*. We would note that the coupled resonators excitation, while potentially desirable from an optical efficiency point of view, have thus far have not yielded a similarly performing design. Improvements in this topology may be possible with different resonator geometries.
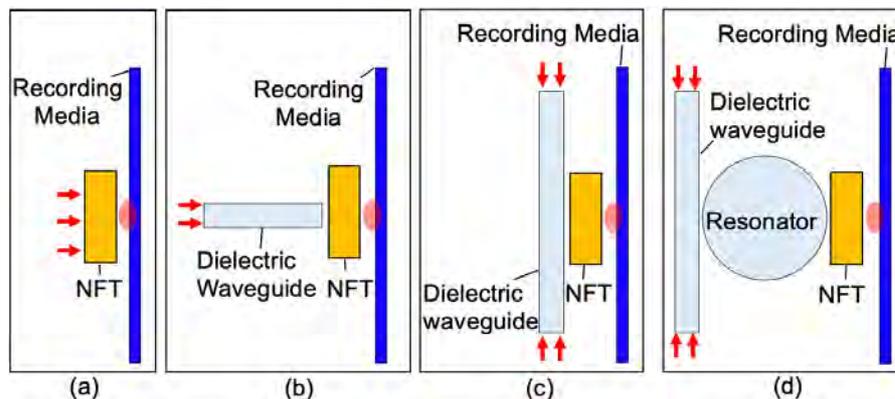

Fig. 2 Coupling schemes: (a) eigenmode excitation (b) impinging dielectric eigenmode excitation (c) transverse mode excitation of a dielectric waveguide and (d) transverse mode of a dielectric resonator.

REFERENCES

[1] R. L. Xu *et al.*, "Thermal conductivity of crystalline AlN and the influence of atomic-scale defects," *J. Appl. Phys.*, vol. 126, no. 18, pp. 1–23, 2019.

[2] T. E. Schlesinger, T. Rausch, A. Itagi, J. Zhu, J. A. Bain, and D. D. Stancil, "An integrated read/write head for hybrid recording," *Japanese J. Appl. Physics, Part 1 Regul. Pap. Short Notes Rev. Pap.*, vol. 41, no. 3 B, pp. 1821–1824, 2002.

QUASI-EQUILIBRIUM STONER-WOHLFARTH VERSUS STRONGLY OUT-OF-EQUILIBRIUM DYNAMICS IN HAMR

A. Truong[1], T. Maletzky[1], M. Dovek[1] and B. Dieny[2]

1) Headway Technologies, Milpitas, California CA, alain.truong@headway.com

2) SPINTEC, Univ. Grenoble Alpes/CEA/CNRS, Grenoble, France, bernard.dieny@cea.fr

I. BACKGROUND

The LLB (Landau-Lifshitz-Bloch) equation is commonly used to simulate the processes involved in HAMR due to its ability to describe magnetization dynamics at elevated temperatures, reaching the ordering temperature (Curie temperature Tc). The stochastic form of the LLB equation is based on the fluctuation-dissipation theorem. It has two fluctuation terms, each of them having different impacts on the magnetization vector depending on the temperature. The longitudinal fluctuations play a dominant role at temperatures close to Tc, while the transverse fluctuations have more impact at lower temperatures [1]. In HAMR writing, two successive stages occur during the cooling of the grain magnetization from above the Curie temperature. When a cooling grain just traverses Tc, its magnetization first grows longitudinally along the effective field which at Tc just consists of the head write field. As in a polarized paramagnet, this longitudinal growth results from a self-averaging of all transverse degrees of freedom within each grain. Then, as the temperature decreases, the grain internal degrees of freedom gradually freeze so that the grain starts behaving as a macrospin. Concomitantly, the effective field becomes more and more vertical due to the rapid growth of the perpendicular anisotropy field. In this regime, the grain magnetization starts precessing around the effective field with a substantially chaotic trajectory due to the thermal fluctuations, until it fully settles along the anisotropy direction at the end of the cooling process. This writing dynamics characteristic of HAMR imposes particular conditions in the optimization of the write field amplitude and angle as a function of thermal gradient and disk velocity. We studied these conditions by LLB numerical simulations.

II. RESULTS

The optimum write field conditions in HAMR result from a tradeoff between two phenomena. On the one hand, it is necessary to maximize the effective write field acting on the grain magnetization to fight against thermal fluctuations especially just below Tc. As in PMR, this argument would favor a tilted orientation of the field, optimally at 45º according to the Stoner-Wohlfarth model. On the other hand, during the cooling of the magnetization from Tc to typically Tc-40ºC, the interval during which the actual writing takes place [2], the effective field acting on the cooling grain magnetization rotates from the writer field direction at Tc to almost vertical at Tc-40ºC. During this phase, it is very important to minimize the ringing of the magnetization, since thermal fluctuations can cause the grain magnetization to switch into the wrong hemisphere, particularly when the head field is tilted away from the vertical. In previous studies, pump-probe experiments on FePt films showed that the magnetization ringing phenomenon can be observed on time scales much longer than 1 ns [2]. To minimize the ringing, a vertical orientation of the writer field when crossing Tc is favored, as it allows the magnetization to directly grow longitudinally along the anisotropy axis yielding almost no ringing. As a result of the tradeoff described above, the LLB simulations clearly shows a gradual transition from a Stoner-Wohlfarth quasi-equilibrium type of switching with an optimum field angle at 45º to a strongly out-of-equilibrium switching with optimum field angle at 90º as a function of temperature gradient and disk velocity (see Fig. 1). At a low disk velocity of 5 m/s, due the heat spreading during the heating phase, the media cools down at a slow rate. It takes ~4 ns for a grain to cool down from Tc to Tc – 40 K. This time scale is sufficiently long to assume that the magnetization reversal occurs in a quasi-equilibrium fashion. As a result, at such low data rates, the optimum field conditions are found to be close to those predicted by the Stoner-Wohlfarth-like switching mechanism (Fig. 1a). In contrast, at high disk velocities, the anisotropy field from the media increases at a much faster rate. It takes ~160 ps for the grain to cool down from Tc to Tc – 40 K. This time scale is significantly shorter than the one over which the ringing is damped. In this case, it is more favorable for the writer field to be vertical to minimize the ringing during this short time period (Fig. 1b and c). The

Alain Truong
E-mail: alain.truong@headway.com
tel: +1-408-9345300

transition of the optimum recording field angle can be seen in Fig. 1 as a function of the disk velocity. The influence of the thermal gradient has also been studied by LLB simulations (Fig. 2). At moderate head field, high thermal gradients lead to a roll-off in SNR due to the superparamagnetic trap effect. This roll-off can be suppressed by using a writer structure capable of generating a higher maximum field. An optimum recording time window was also previously investigated by Zhu et al. [3]
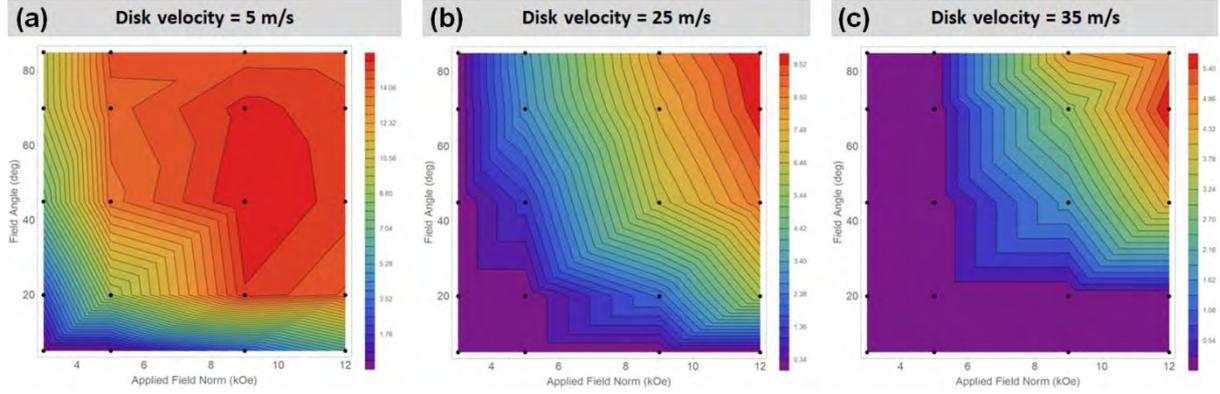

Fig. 1 Simulated contour plot of squeeze SNR as a function of applied field angle and applied field norm, for different values of disk velocity. The optimum recording at low disk velocity is obtained for field angles closer to 45º, while the optimum at high velocities is parallel to the easy axis of the grains (90 º).
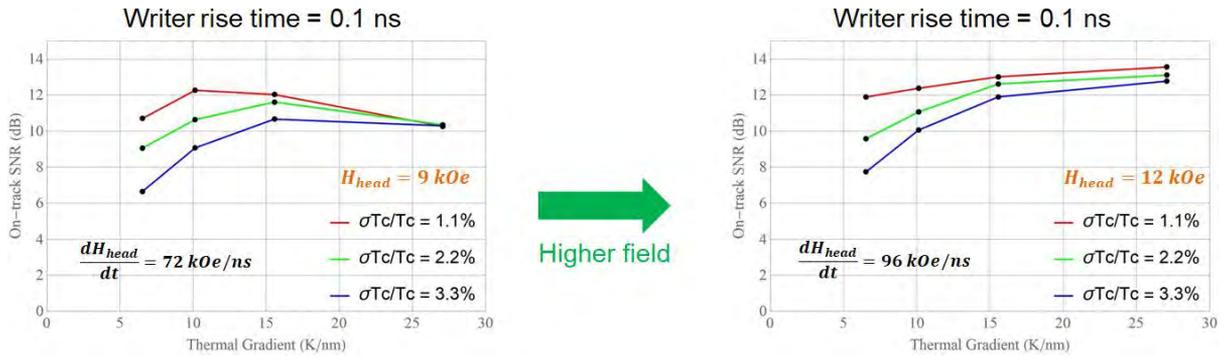
Fig. 2 Influence of thermal gradient on on-track SNR (disk velocity = 25 m/s, field angle = 45º).

Additionally, it was shown that the anisotropy field gradient in the recording layer imposes a constraint on the writer field rise time. In order to obtain high-quality transitions, the rising rate of the writer field should not exceed the rising rate of the anisotropy field; otherwise, the grain magnetization may have to reverse by 180° during the cooling process resulting in very large ringing. Therefore, the following inequality summarizes the necessary condition on the dynamic writer field:

$$dH_k/dx * velocity > dH_{head}/dt \, , \tag{1}$$

where H_k, x, $velocity$, H_{head}, are the grain anisotropy field, down-track dimension, disk velocity and writer field, respectively. While this relationship favors high thermal gradients, too large thermal gradients will also lead to a roll-off in performance (see Fig. 2). Thus, an additional trade-off has limits the gradient.

REFERENCES

1) U. Atxitia et al., "Fundamentals and applications of the Landau-Lifshitz-Bloch equation", *Journal of Physics D : Applied Physics.*, 50, (2017).
2) Z. Chen et al., "Spin waves and small intrinsic damping in and in-plane magnetized FePt film", *Applied Physics Letters,* 101, (2012).
3) J. G. Zhu et al., "Medium optimization for lowering head field and heating requirements in HAMR", IEEE Magnetic Letters., 2427117, (2015).

Interplay of thermal and magnetic fields in HAMR

Niranjan A. NATEKAR, Eric RODDICK, Richard M. BROCKIE

Western Digital Corporation, San Jose, CA 95119, USA

I. INTRODUCTION

The writing process in Heat Assisted Magnetic Recording (HAMR) is an interplay of two effects: thermal and magnetic. While the thermal effects in the HAMR process have been studied in detail, the effect of the head field and the discussion regarding the interplay of these two factors has just begun [1]. These factors together affect the writing contour that defines the transitions. Here, we explore the effect the interplay of these factors has on the writing contour, the transition jitter and the switching nature of the HAMR media.

II. SIMULATION SETUP & RECORDING PARAMETERS

The micromagnetic technique described in detail previously [2, 3] is used to simulate discretized single layer media with granular magnetic grains. Five media (A-E) and three 2d Gaussian profiles stretched in the cross-track (CT) direction with a conical background from [4] are considered. Two kinds of write fields are used in recording simulations: (i) uniform fields of constant magnitude (5, 8, 10, 12.5 & 15kOe) at an angle of 45° in the down-track/vertical plane, (ii) contrived fields with a constant down-track field gradient over a range of distance from the pole, also at 45°. Values for the field at the poles and the downtrack field gradient are from [5]. Thermal gradients during recording are estimated using the technique described in [4]. Additionally, the switching nature of the medium is characterized by *magnetometer-like* simulations where the medium is cooled from a peak temperature down to the ambient temperature in the presence of a uniform external field. At a certain temperature, the field polarity is reversed; a comparison of the initial and final magnetization states determines the switching probability. Repeated simulations for a range of field reversal temperatures enables an estimation of the dynamic field writing temperature (T_{write}) [6, 7]. The cooling rate chosen for the magnetometer simulation is the product of the down-track gradient and the medium velocity (20m/s) in the corresponding recording simulation.

III. MICROMAGNETIC SIMULATION RESULTS & DISCUSSION

The effect of applying different write fields has been explored in a different context in [1]. For the HAMR writing process, as the applied field increases, the temperature required to switch the magnetization decreases. Following an isotherm, the field magnitude from a head field can vary as much as 30% between the track edges and center. In the static field (dc writing) case, the reduction in writing temperature at the center therefore elongates the writing contour in the down-track direction when compared with an isotherm (by a few nm for realistic head fields). For a static uniform field, the writing contour is expected to be an isotherm. Fig. 1(a) shows the static field effect on the writing contour in the presence of uniform head fields. T_{edge} (track edge temperature) is calculated by plotting the isotherm defined by the edges by the written track of width TTW (Total Track Width). As the field magnitude increases, T_{edge} decreases. The minor variation of T_{edge} for different thermal profiles is a consequence of the variation in the cross-track thermal gradient at the track edges.

In HAMR recording, transitions are written due to the reversal of the applied field in the presence of the thermal profile. This fundamentally dynamic process prompts the question of whether the dynamic writing contour has the same shape as the static field (dc writing) case. Fig. 1(b) plots the T_{write} determined using the switching probability analysis of the *magnetometer-like* simulations for the same systems explored in Fig. 1(a). The field strength effect is broadly similar between Figs 1 (a) and (b), but the order in which the thermal profiles are displayed is generally reversed, indicating the presence of dynamic effects.

The presence of dynamic effects can be further demonstrated by analyzing the shape of the written transition created with a uniform field (Fig. 2). The trailing edge of the scaled thermal field (left plot) is analyzed for thermal gradient around the T_{edge} isotherm. This isotherm is plotted at the transition in the average magnetization plot (right). Similar to Fig 1, the isotherm and transition shapes are broadly similar, but there are clear differences, again indicating the presence of dynamic effects. We explore these dynamic effects in detail, as a function of cross-track location and field ramp rate.

Finally, the wide range of simulated components explored enables a broader investigation of the jitter predicted by a proposed analytical formulation with that found from simulation [8]. Our results suggest that the analytical formulation is unable to capture the interplay of the thermal and magnetic fields in its entirety.

REFERENCES

1) J.-G. Zhu and H. Li, doi: 10.1109/TMAG.2016.2614836
2) H. J. Richter and G. J. Parker, https://doi.org/10.1063/1.4984911
3) G. J. Parker and L. Xu, [Online]. Available: https://www.nims.go.jp/mmu/tmrc2017/att/D2.pdf
4) E. Roddick, L. Xu and R. M. Brockie, doi: 10.1109/TMAG.2020.3012941
5) Y. Wang and J.-G. Zhu, https://doi.org/10.1063/1.3540412
6) Z. Liu, P.W. Huang, G. Ju and R.H. Victora, https://doi.org/10.1063/1.4983033
7) N.A. Natekar, W.Tipcharoen and R.H. Victora, https://doi.org/10.1016/j.jmmm.2019.165253
8) N.A. Natekar and R.H. Victora, doi: 10.1109/LMAG.2020.2992221

(a)   (b)
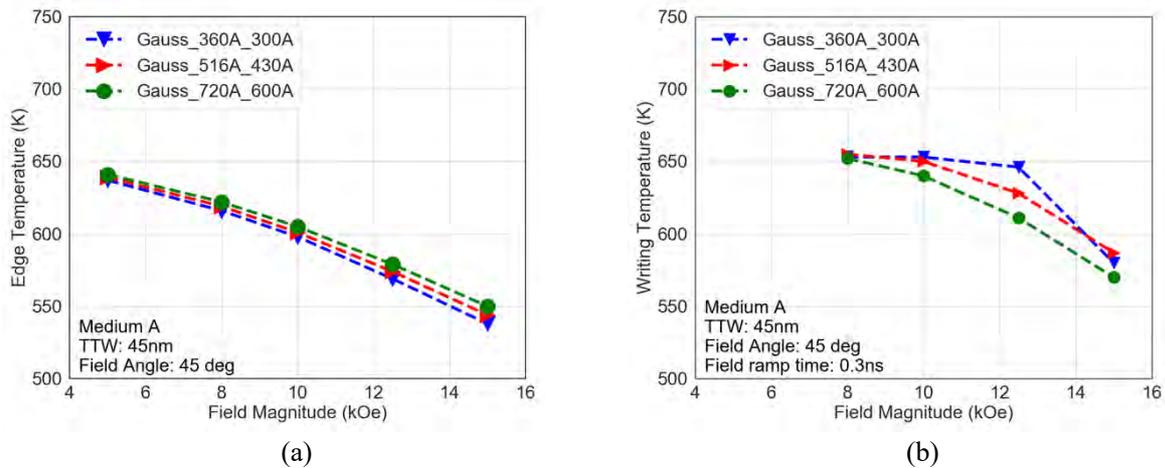
Fig 1. Comparison of static and dynamic field writing temperatures (a) static: T_{edge} and (b) dynamic: T_{write}. Note the reversed order of the thermal profiles in (b) demonstrating the importance of dynamic effects. (Saturated recording does not occur with 5kOe field preventing analysis in the dynamic case.)
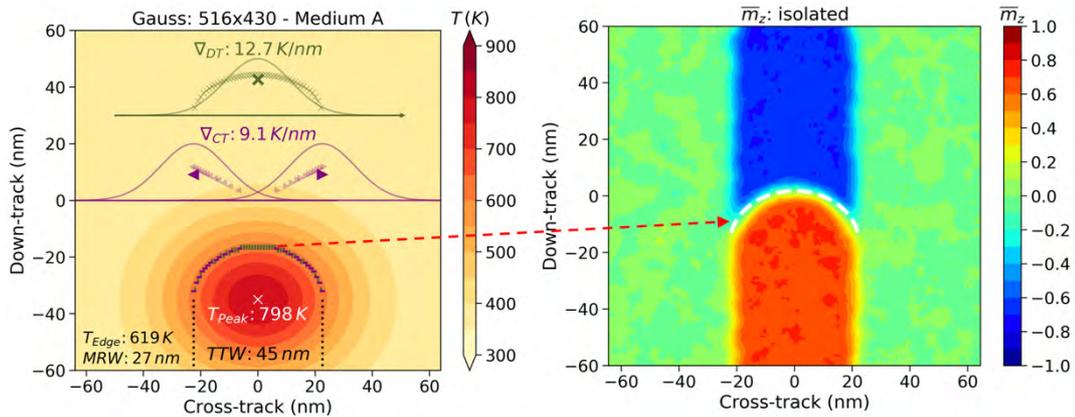
Fig. 2. Comparison of shapes of the scaled thermal profile (left) and the written transition (right) plotted for a uniform field of 8kOe applied at 45° to the vertical. The isotherm from the thermal profile is plotted at the transition location and does not fully match the transition shape.

DIRECT MEASUREMENT OF MAGNETIC TIMING JITTER IN WRITERS

Peter J. CZOSCHKE[1], Chris REA[1], and Zuxuan LIN[1]

1) Recording Head Operations, Seagate Technology, 7801 Computer Avenue South, Bloomington, MN 55435, USA, peter.j.czoschke@seagate.com

I. INTRODUCTION

Non-repeatable positioning of transitions in the media (jitter) is one of the primary limiting factors in achieving higher linear density in magnetic recording. In a typical magnetic recording system, the primary sources of jitter are due to the finite grain size and the switching field distribution of the grains in the media. These contributions to jitter are generally referred to as the "written-in" contributions [1]. However, if the system that delivers the write field to the media itself has jitter, as all real-world systems will, then this "timing jitter" will also contribute to the total written-in jitter.

The most obvious sources of timing jitter are the components that generate the electrical signal delivered to the writer core: the channel and preamp. The jitter of this electrical signal can be readily characterized and is generally specified to a low value (<10 ps) to minimize its overall effect. However, with a magnetic writer there is also the possibility that the complexities of the magnetic reversal process in the writer pole can result in non-repeating switching behavior of the magnetic field when a transition is being written, which will appear as timing jitter. Indeed, if large enough it can even be the dominant source of timing jitter. Since standard tools and techniques measure either the input electrical signal jitter or the final jitter of the written-in pattern, the magnetic timing contribution to the written-in jitter is difficult to measure.

II. EXPERIMENT

Timing jitter of the magnetic field from a magnetic writer is measured directly using a special scanning magnetoresistive microscopy (SMRM) setup that uses a read sensor to detect the write field from a standard magnetic recording head. Such a setup is sensitive enough to detect the write field in real time with picosecond-level precision [2]. A long sequence of transitions is sent to the writer using a data timing generator and drive preamp using a low enough frequency to avoid transmission-line resonances or reflection effects. The write field is measured using a tunneling magnetoresistive sensor, the signal from which is amplified using a wide-band, low-noise amplifier and then captured using a high-bandwidth real-time digital oscilloscope.

The sensor is aligned to the magnetic writer pole tip by using the tool in its imaging mode. The sensor is then positioned at the peak of the signal from the writer while the high-frequency transitions are sent to the writer. A given device is then measured using different write current amplitudes and shapes (overshoot amplitude, duration, and rise time.) The captured waveforms are processed by locating the zero-field crossing point of each transition. Once all transitions are located, their average separation is the recovered clock frequency (which ideally matches the delivered electrical signal frequency), while their standard deviation from the mean is the timing jitter. This method thus directly measures the timing jitter of the magnetic write field delivered to the media, including the magnetic contribution.

III. RESULTS AND CONCLUSIONS

Figure 1 shows an example of a small portion of a timing jitter measurement of a head designed for perpendicular magnetic recording (PMR). The identified zero-field crossing points are shown in red circles. Note that due to AC coupling of the amplifier output (it has a 100 MHz low frequency cutoff), the crossing

PETER J. CZOSCHKE
E-mail: peter.j.czoschke@seagate.com
tel: +1-952-402-8694

points are offset from 0 mV depending on the polarity of the transition. Measurements are performed using a variety of write current preamp settings, read sensors, and writer designs. It is determined that the magnetic contribution to timing jitter is dependent on the write current shape, amplitude, and writer design. Writers designed for PMR have measured timing jitters between 5 and 25 ps. Writers designed for heat assisted magnetic recording (HAMR) are measured to have larger timing jitter of 10 to 50 ps.

REFERENCES

1) J. Hohlfeld, P. Czoschke, P. Asselin, and M. Benakli, "Improving our understanding of measured jitter (in HAMR)", *IEEE Trans. Magn.*, **55**(3) 1-11, (2019).
2) P. Czoschke, S. Kaka, N. J. Gokemeijer, and S. Franzen, "Real-time direct measurement of field rise time and dynamic instability of perpendicular writers", *Appl. Phys. Lett.*, **97**, 242504, (2010).
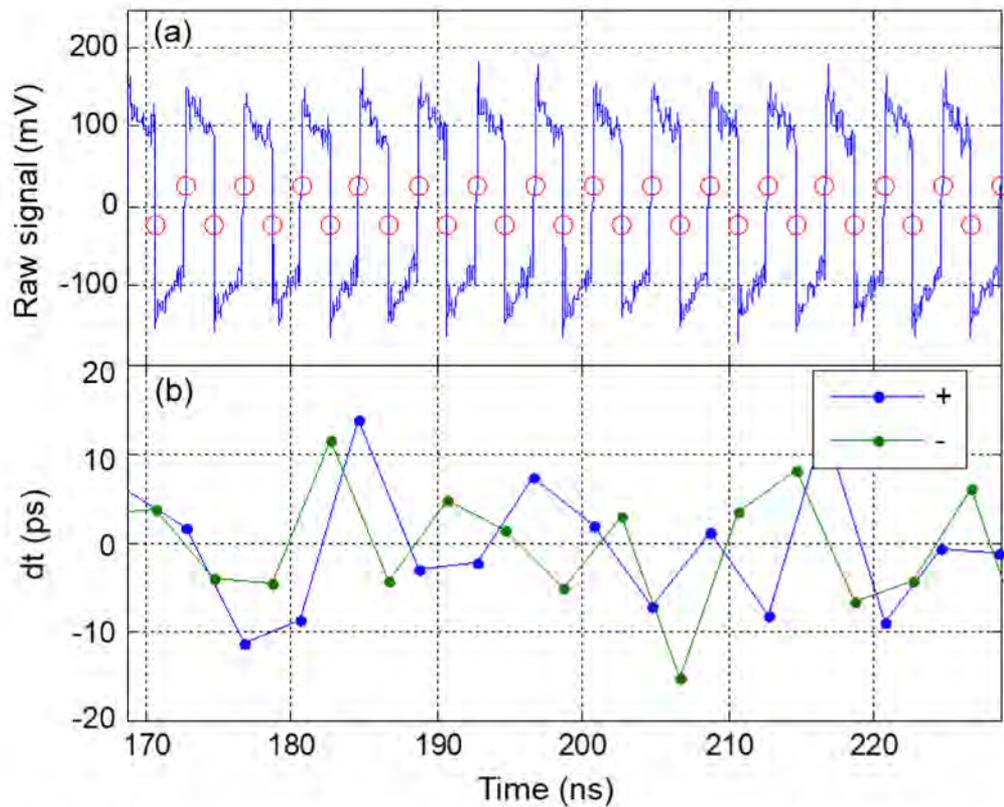
Fig. 1. (a) A subset of a full data capture from a timing jitter measurement showing the identified zero-field crossing points (circles). The crossing points are not at zero signal due to AC coupling of the amplifier output. (b) The deviation of each corresponding transition in (a) from its ideal position, separated out by transition polarity. The distribution of such deviations forms a Gaussian distribution, the width of which is the final jitter value. In this case, the timing jitter was measured to be 6.02 ps.

DEMONSTRATION OF NARROW SWITCHING DISTRIBUTIONS IN STT-MRAM ARRAYS FOR LLC APPLICATIONS AT 1X NM NODE

G. HU, E. R. J. EDWARDS, S. L. BROWN, C. P. D'EMIC, M. G. GOTTWALD, P. HASHEMI, H. JUNG, J. KIM, G. LAUER, J. J. NOWAK, J. Z. SUN, P. L. TROUILLOUD, and D. C. WORLEDGE

IBM T. J. Watson Research Center, Yorktown Heights, USA, hug@us.ibm.com

I. INTRODUCTION

STT-MRAM is a promising candidate for LLC applications in high performance computing systems with improved array density compared to SRAM [1]. Despite the significant progress made in recent years, state-of-the-art STT-MRAM products do not meet the write performance required to provide system-level performance improvement when deployed in last level cache [2-3]. Reliable writing of STT-MRAM devices at sub-5 ns and controlling the write voltage distributions are two of the key challenges. We demonstrated reliable 2 ns writing in standard two-terminal STT-MRAM in our previous work [4]. Here, we further demonstrate array-level write voltage distributions that meet the requirements for 14 nm last level cache applications [5].

II. NARROW SWITCHING VOLTAGE DISTRIBUTIONS WITH 3 NS WRITE PULSES

By materials optimization, we were able to significantly improve the write voltage distributions of STT-MRAM arrays, shown in Fig.1. Fig.2 shows write-error-rate (WER) curves of STT-MRAM arrays with MTJ diameters of 41 nm and 56 nm, written with 3 ns write pulses. Array level WER of 2.4e-10 and 1.05e-11 were demonstrated in the two STT-MRAM arrays respectively. For the 41 nm MTJ array, we demonstrated anomaly-free write performance at 3 ns to the 1e-6 measurement error floor of 3623 electrically healthy bits from a 4 kb array with bit-to-bit write voltage sigma of 3.7% for write 0 and 4.5% for write 1 at the 1e-6 error level. These values meet the write voltage distribution requirements for a 32Mb 14 nm LLC chip design.

By measuring and analyzing WER curves of STT-MRAM arrays with MTJ diameters ranging from 30 nm to 70 nm, we showed that the write voltage distribution is proportional to the Rmin distribution and a significant portion of the write voltage distribution is magnetic in origin. Better materials design is expected to improve the voltage distribution even further.

REFERENCES

1) S. Sakhare et al., "Enablement of STT-MRAM as last level cache for the high performance computing domain at the 5nm node", *IEDM, Tech. Dig.* 420-423 (2018).
2) J. G. Alzate et al., "2 MB Array-Level Demonstration of STT-MRAM Process and Performance Towards L4 Cache Applications", *IEDM Tech. Dig.*, 30-33 (2019).
3) K. Lee, et al., "1Gbit High Density Embedded STT-MRAM in 28nm FDSOI Technology", *IEDM, Tech. Dig.* 22-25 (2019).
4) G. Hu et al., "Spin-transfer torque MRAM with reliable 2 ns writing for last level cache applications", *IEDM Tech. Dig.*, 38-41 (2019).
5) E. R. J. Edwards et al., "Demonstration of narrow switching distributions in STTMRAM arrays for LLC applications at 1x nm node", *IEDM Tech. Dig.*, 509-512 (2020).
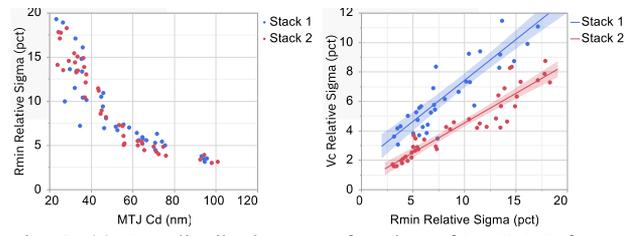
Fig. 1. (a) R_{min} distribution as a function of MTJ CD for two different stacks, showing negligible difference (b) V_{c10ns} distribution as a function of R_{min} distribution for the two stacks, where stack 2 shows significantly better V_c distribution at the same R_{min} distribution
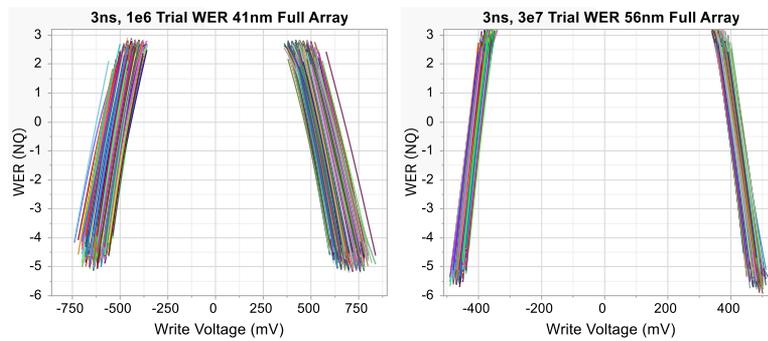

Fig. 2. (a) Full array WER measurement of 1e6 trials at 3 ns write pulse duration for MTJ diameter of 41 nm, demonstrating 2.8e-10 array WER (b) Full array WER measurement of 3e7 trials at 3 ns write pulse duration for MTJ diameter of 56 nm, demonstrating 1.05e-11 array WER

3-Dimensional Integration of Epitaxial Magnetic Tunnel Junctions with New Materials for Future MRAM

Kay YAKUSHIJI[1], Hideki TAKAGI[1], Naoya WATANABE[1], Akio FUKUSHIMA[1], Katsuya KIKUCHI[1], Yuichi KURASHIMA[1], Atsushi SUGIHARA[1], Hitoshi KUBOTA[1] and Shinji YUASA[1,a]

1) National Institute of Advanced Industrial Science and Technology (AIST), Tsukuba, Japan

a) yuasa-s@aist.go.jp

I. INTRODUCTION

(001)-oriented poly-crystal (textured) CoFeB/MgO/CoFeB magnetic tunnel junctions (MTJs) are commonly used in STT-MRAM and read heads of hard disk drives (HDDs) due to their good MTJ performances and high manufacturability [1]. As the MTJ size shrinks, however, the textured MTJs exhibit larger bit-to-bit variations of magnetic and transport properties due to the crystal grains and misorientation, which will limit the scalability of MRAM. Moreover, the very special growth process of textured CoFeB/MgO/CoFeB makes it difficult to replace MgO and/or CoFeB with new materials [1]. Note that the spinel $MgAl_2O_4(001)$ tunnel barrier lattice-matches well with some tetragonal Heusler alloys with very low Gilbert damping, low magnetization and high PMA, which will extend the scaling limit of STT-MRAM [1]. To utilize such new materials, we developed novel 3-dimntional (3D) integration processes (Fig.1) consisting of (a) epitaxial growth of MTJ film on 300 mm Si(001) wafer, (b) surface activation in high vacoom, (c) direct bonding of the epitaxial MTJ wafer and CMOS wafer, (d) removal of backside Si wafer, (e) fabrication of epitaxial MTJ nano-pillars, and (f) fabrication of dielectric and metal interconnects.

II. EPITAXIAL GROWTH OF MTJ FILMS ON SI WAFERS

We deposited epitaxial MTJ films on ϕ300 mm Si(001) wafers by using manufacturing-type PVD system (Canon-Anelva EC-7800). Prior to film deposition, the wafers were wet-etched in 1% diluted hydrofluoric acid to remove the thin native oxide on the surface. We deposited the following MTJ stack: Si-wafer/Ni-Al seed layer(25) / Cr buffer layer(20) / Fe(3)/Co(0.4) free layer / Mg-Al-O tunnel barrier / Co(0.4)/Fe(2.5) reference layer / Ir-Mn(10) / Ta cap layer (unit in nm) [2]. Note that we used spinel $MgAl_2O_4(001)$ tunnel barrier instead of MgO. The high-resolution TEM image in Fig.2 shows almost no dislocations at the barrier/electrode interfaces, indicating ideal lattice matching between Mg-Al-O and Fe-based ferromagnets.

For the direct wafer bonding, the surfaces of both wafers need to be extremely flat. In our previous study with textured CoFeB/MgO/CoFeB MTJ films [3], Ta cap-layer surface with Ra roughness < 0.2 nm was the criterion for high-quality wafer bonding without void formation and degradation of MTJ properties. In the as-grown epitaxial MTJ films, Ra roughness of Ta surface was larger than 0.2 nm. The wafer bonding with such a rough surface resulted in deformation of the MTJ as well as void formation. To obtain atomically flat surface, we performed *in situ* smoothing process [4], which resulted in atomically flat Ta-B surface (Ra ~ 0.15 nm) and excellent wafer bonding without deformation and degradation of MTJ properties.

III. INTEGRATION OF EPITAXIAL MTJS IN STT-MRAM

The 300 mm epitaxial MTJ wafer and 300 mm CMOS wafer for STT-MRAM were bonded in a room-temperature bonding apparatus (Mitsubishi Heavy Industries MWB-12ST) by using the surface activated bonding method [5]. After the bonding, we removed the Si wafer on the backside of the MTJ stack, Ni-Al seed layer and more than half of the Cr buffer layer by using mechanical grinding followed by wet etching with alkali solution. After removing the back-side Si, we fabricated epitaxial MTJ nano-pillars by using standard micro-fabrication processes such as lithography and ion-beam etching. TEM images of the STT-MRAM with epitaxial MTJ nano-pillars are shown in Fig.3. The single-crystal structure of the Mg-Al-O barrier and ferromagnetic layers are confirmed by nano-beam diffraction patterns in Fig.3. We evaluated the bit-to-bit variations of magnetic and transport properties and confirmed that the epitaxial

SHINJI YUASA
E-mail: yuasa-s@aist.go.jp
tel: +81-29-861-5401

MTJs have smaller variations than textured CoFeB/MgO/CoFeB MTJs that we prepared as reference samples.

The epitaxial growth and 3D integration enable to develop novel MTJs with new materials, giving great flexibilities and scalability to future MRAM including voltage-controlled MRAM (VC-MRAM) as well as to read heads for ultrahigh-density HDDs. The technologies will be applicable also to other kinds of tunnel junction devices such as Josephson junctions in superconducting qubit for quantum computing.

IV. ACKNOWLEDGMENTS

REFERENCES

1) S. Yuasa *et al*., *MRS Bulletin*, **43**, 352, (2018).
2) K. Yakushiji *et al*., *Appl. Phys. Lett*., **115**, 202403, (2019).
3) K. Yakushiji *et al*., *Appl. Phys. Express*, **10**, 063002, (2017).
4) A. Sugihara *et al*., *Appl. Phys. Express*, **12**, 023002, (2019).
5) H. Takagi *et al*., *Sensors and Actuators A*, **105**, 98, (2003).
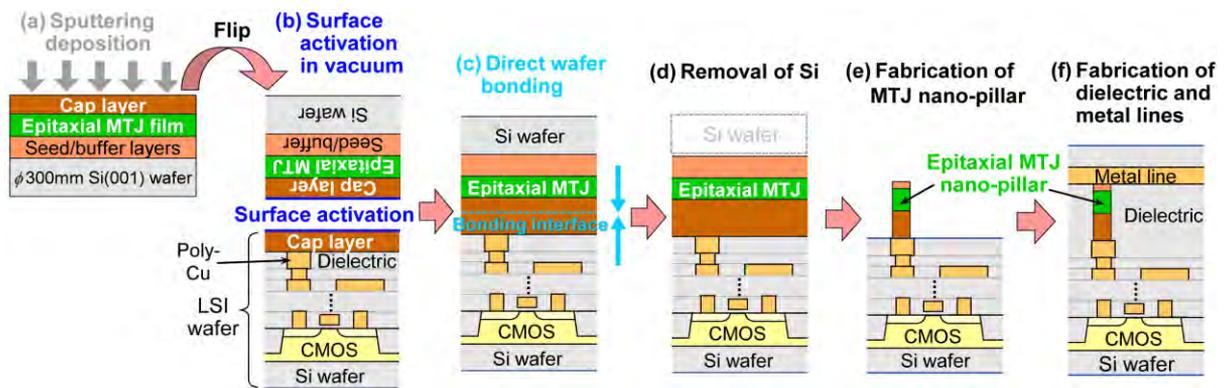
Fig.1 Schematic illustration for 3-dimentional integration of epitaxial MTJs.
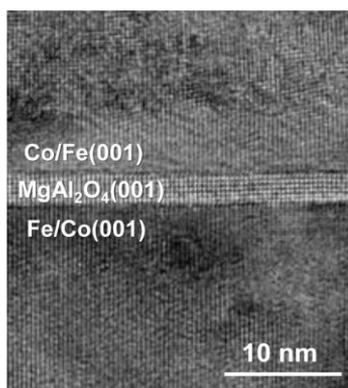
Fig.2 High-resolution TEM images of epitaxial MTJ film with spinel Mg-Al-O(001) tunnel barrier.
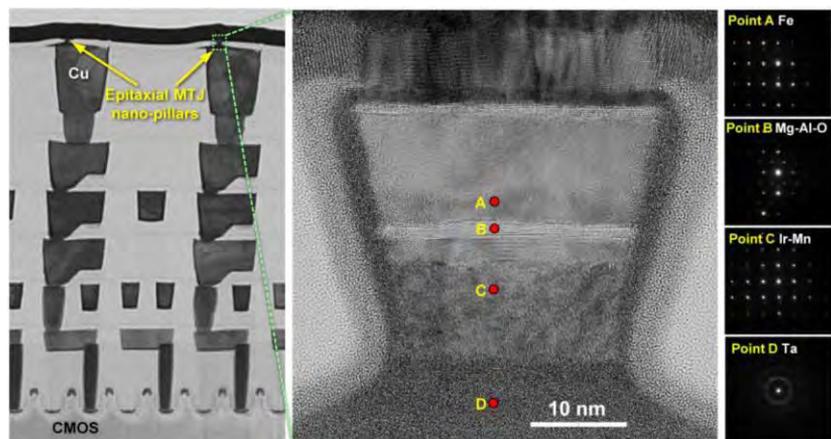
Fig.3 TEM image of epitaxial MTJs integrated in STT-MRAM (left) and high-resolution TEM image of epitaxial MTJ nano-pillar (middle). Nano-beam diffraction patterns (right panels).

Revisiting Fe/MgO/Fe(001):
Giant tunnel magnetoresistance up to ~420% at room temperature

Hiroaki SUKEGAWA, **Thomas SCHEIKE, Qingyi XIANG, Zhenchao WEN, Tadakatsu OHKUBO, Kazuhiro HONO, and Seiji MITANI**

National Institute for Materials Science (NIMS), Tsukuba 305-0047, Japan, sukegawa.hiroaki@nims.go.jp

I. INTRODUCTION

After the demonstration of the giant tunnel magnetoresistance (TMR) ratios at room temperature (RT) using a crystalline MgO barrier based magnetic tunnel junctions (MTJs) in 2004 [1, 2], an application range of spintronic devices, including read-heads of hard disk drives (HDDs) and cells of magnetoresistive random access memories (MRAMs), has been significantly boosted. Use of MgO barriers enabled to obtain large electric output from MTJ structures since a large TMR ratio over 100% can be easily achieved due to the Δ_1 band preferential coherent tunneling mechanism [3]. Fe/MgO/Fe(001) is known as one of the most basic structures exhibiting the giant TMR effect [2]. The structure is very simple, and thus many theoretical calculations have been demonstrated so far [3, 4]. However, experimental TMR ratios (180~220% at RT and 290-370% at low temperature) are much smaller than those of the predictions like >1,000%. In order to create novel MTJ-based applications, such as high-capacity MRAMs, magnetic logics, and brain-morphic devices, further improvement in an experimental TMR ratio is needed. Especially, it should be essential to understand the origin of the TMR gap between experiments and theories. In this study, we revisited the simplest "Fe/MgO/Fe(001)" MTJ to obtain much larger TMR ratios by careful tuning of growth conditions for all the layers, combining sputtering and electron-beam evaporation, and MgO barrier interface modifications [5].

II. EXPERIMENTS

Epitaxial MTJ multilayers with a structure of Cr-buffer/Fe (30 or 50 nm)/Mg (0.5 nm)/MgO (d_{MgO} = 0.5-2.5 nm)/Fe (5 nm)/IrMn (10 nm)/Ru cap (20 nm) were deposited on a single-crystal MgO(001) substrate using a multi-chamber sputtering system as shown in Fig. 1 (a). Magnetron sputtering was used for deposition of the metallic layers, whereas electron-beam evaporation was used for the MgO layer deposition. To tune the MgO interfaces, the MgO layer was post-oxidized using pure-oxygen gas (~5 Pa) for a few min and the Mg layer was inserted to protect the bottom Fe interface from over-oxidation during the process. We also prepare a sample with an ultrathin CoFe insertion at the MgO bottom interface. Each layer was *in-situ* post-annealed in order to improve the crystallinity and flatness. TMR ratios of the prepared wafers were characterized by current-in-plane tunneling (CIPT) measurements. Then, the wafers were patterned into micro-meter scale MTJ pillars using photolithography and Ar-ion etching. The MTJs were evaluated by DC 4-probe measurements at RT (300 K) and 5 K under low bias voltages ~10 mV.

III. RESULTS AND SUMMARY

Figure 1 (b) shows the TMR ratios at RT as a function of d_{MgO} for 3 representative MTJ stacks after modification of the layers. Fe/MgO/Fe MTJs show large TMR ratios exceeding 400% at RT (maximum 417%). The CoFe inserted MTJ (red square) reaches 497% at RT, which is the largest in the exchange spin-valve type MTJs at RT. TMR ratios significantly oscillate with d_{MgO} with a ~0.31 nm period; the peak-to-valley difference of the oscillation is approximately 80%, which is much larger than the previous reported in Fe/MgO/Fe [2]. The very large TMR ratio and oscillation amplitude are well reproduced by CIPT measurements in the wide range of d_{MgO} even in an unpatterned wafer before microfabrication, confirming the large TMR (and TMR oscillation) effect in our fine-tuned MTJs. The origin of the TMR oscillation is still an open question; nevertheless, achievement of such a large oscillation amplitude may be usable to understand the full picture of this behavior in the near future.

Figure 2 shows the TMR ratios as a function of magnetic field (*H*) of an Fe (30 nm)/MgO (2.3 nm)/Fe

Hiroaki SUKEGAWA
E-mail: sukegawa.hiroaki@nims.go.jp
tel: +81-29-860-4642

(5 nm) MTJ measured at 300 K and 5 K. A TMR ratio at 5 K exceeds 900%, which approaches the theoretical prediction values of ~1,000%. This study suggests that there is enough room for enhancing a TMR ratio at RT since significant progress in the TMR ratio was achieved even in the common Fe/MgO/Fe(001). Designing device structures based on the findings may open up the possibility of new applications based on very large TMR ratios at RT.

REFERENCES

1) S.S.P. Parkin, C. Kaiser, A. Panchula, P.M. Rice, B. Hughes, M. Samant, S.-H. Yang, "Giant tunnelling magnetoresistance at room temperature with MgO (100) tunnel barriers", *Nat. Mater.*, 3, 862-867, (2004).
2) S. Yuasa, T. Nagahama, A. Fukushima, Y. Suzuki, K. Ando, "Giant room-temperature magnetoresistance in single-crystal Fe/MgO/Fe magnetic tunnel junctions", *Nat. Mater.*, 3, 868-871, (2004).
3) W. Butler, X.-G. Zhang, T. Schulthess, J. MacLaren, W. Butler, X.-G. Zhang, T. Schulthess, J. MacLaren, "Spin-dependent tunneling conductance of Fe|MgO|Fe sandwiches", *Phys. Rev. B*, 63, 054416, (2001)
4) J. Mathon, A. Umerski, "Theory of tunneling magnetoresistance of an epitaxial Fe/MgO/Fe(001) junction ", *Phys. Rev. B*, 63, 220403(R), (2001).
5) T. Scheike, Q. Xiang, Z. Wen, H. Sukegawa, T. Ohkubo, K. Hono, S. Mitani, "Exceeding 400% tunnel magnetoresistance at room temperature in epitaxial Fe/MgO/Fe(001) spin-valve-type magnetic tunnel junctions", *Appl. Phys. Lett.*, 118, 042411, (2021).
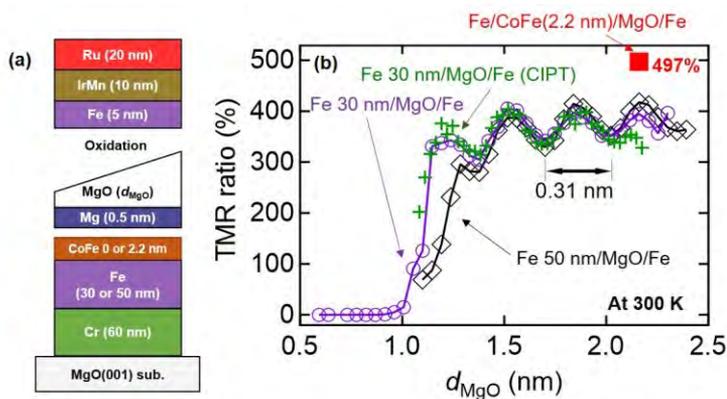
Fig 1. (a) Schematic MTJ stack structure. (b) TMR ratio vs. MgO thickness d_{MgO} of Fe/MgO/Fe(001) and Fe/CoFe/MgO/Fe MTJs at 300 K. + marks indicate the result of CIPT measurements before MTJ patterning.
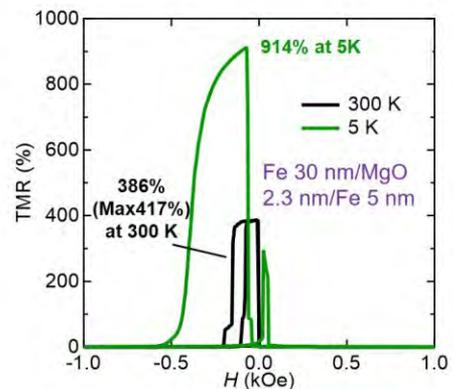
Fig 2. TMR ratio vs. magnetic field H of an Fe/MgO/Fe(001) MTJ at 300 and 5 K.

Recent progresses in STT-MRAMs, SOT-MRAMs for low power AI/IoT Processors

Tetsuo Endoh[1-6]

[1] CIES, Tohoku University Japan, [2] Graduate School of Engineering, Tohoku Univ.,
[3] CSIS, Tohoku Univ., [4] CSRN, Tohoku Univ., [5] RIEC, Tohoku Univ., [6] WPI, Tohoku Univ.

Introduction

STT-MRAM with Double CoFeB/MgO interface perpendicular MTJ has become the de facto standard technology. However, there are still issues for high density memory application and high reliable application. Furthermore, achievement of high speed and high endurance features is still challenging for STT-MRAM, because of its tradeoff relationship among the retention, endurance, and operational speed. Recently, Spin Orbit Torque (SOT) devices have been intensively researched and developed because SOT devices have the potential to achieve high speed and high endurance. To realize the practical use of SOT-MRAM for LSI applications, these issues must be addressed.

This invited paper reviews our recent progresses in STT-MTAM, SOT-MRAM for future AI/IoT processor and its systems that require ultra-low-power and high-performance computing at the same time.

STT-MRAM Technology

We developed novel damage control integration process technologies including new low-damage MgO deposition process, low-damage RIE process, and low temperature cap process. By applying the developed damage control integration process technologies to double interface p-MTJ fabrication, TMR ratio, thermal stability factor, and switching efficiency of Double p-MTJ were successfully improved. Moreover, it was shown that despite the significant increase in thermal stability factor, the endurance of the fabricated Double p-MTJs was over 10^{10}. Finally, with our double-interface p-MTJ technology and novel damage control integration process technologies, fabricated 128Mb STT-MRAMs successfully achieved 14ns/7ns write speed at Vdd of 1.2V/1.8V, respectively.

Next, for further scaling of STT-MRAM, we proposed novel Quad-interface p-MTJ technology which brings forth an increase of thermal stability factor compared with conventional Double-interface p-MTJ technology. We successfully fabricated the quad-interface MTJ using 300mm process based on the damage control integration process. The fabricated Quad p-MTJs achieved an enhancement of switching efficiency in addition to an approximately two times larger thermal stability factor without degradation of TMR ratio. The developed Quad p-MTJ technology will become an essential technology for the scaling of the STT-MRAM beyond 20nm without changing material and process sets from mass-production STT-MRAM. Moreover, the high reliable Quad p-MTJ technology with enough thermal stability factor is suitable for Automobile applications that require high temperature operation such as 150°C.

Field-free SOT-MRAM Technology

To realize practical use of SOT-MRAM for LSI applications, we demonstrated 55 nm-CMOS/SOT-device hybrid MRAM cell with magnetic field free writing for the first time. For field free writing, we developed canted SOT device under 300 mm BEOL process with 400°C thermal tolerance. In addition, we developed its advanced process as follows; PVD process of SOT channel layer for high spin Hall angle under 400°C thermal tolerance, low damage RIE technology for high TMR/thermal stability factor, and ultra-smooth surface metal via process under SOT device to reduce contact resistance. By using the developed technologies, our canted SOT devices achieved fast write speed of 0.35 ns without magnetic field, an enough thermal stability factor of 70 for non-volatile memory (over 10 years retention), and a high TMR ratio of 167%, simultaneously. Moreover, we fabricated a field free canted SOT-MRAM cell with 55 nm CMOS technology and demonstrated its write/read performance. These technologies will open to high speed write non-volatile memory such as 1 level cache application of many kinds of application processors.

REFERENCES

[1] T. Endoh, "Spin Transfer Torque MRAM (SPRAM) and its applications", The International Technology Roadmap for Semiconductors (ITRS)-Emerging Research Material (ERM)/Emerging Research Device

(ERD)-Emerging Research Memory Technologies Workshop, 2010. (Invited)

[2] S. Ikeda, K. Miura, H. Yamamoto, K. Mizunuma, H. D. Gan, M. Endo, S. Kanai, J. Hayakawa, F. Matsukura, and H. Ohno, "A perpendicular-anisotropy CoFeB–MgO magnetic tunnel junction", Nature Mater. 9, 721 (2010).

[3] T. Endoh, T. Ohsawa, H. Koike, T. Hanyu, and H. Ohno, "Restructuring of Memory Hierarchy in Computing System with Spintronics-Based Technologies", Symposia on VLSI Circuits, pp89-90, 2012. (Invited)

[4] T. Endoh, "Spintronics Based NV-Memory/Logic for High Performance & Low Power", 2013 VLSI Technology Short Course of 2013 Symposium on VLSI, 2013.(Invited)

[5] T. Endoh "Nonvolatile Logic and Memory Devices Based on spintronics", 2015 IEEE International Symposium on Circuits and Systems. (Invited)

[6] T. Endoh, H. Koike, S. Ikeda, T. Hanyu, and H. Ohno, "An Overview of Nonvolatile Emerging Memories?Spintronics for Working Memories", IEEE JESCAS, 2016. (Invited)

[7] T. Endoh, "Embedded Nonvolatile Memory with STT-MRAMs and its Application for Nonvolatile Brain-Inspired VLSIs", 2017 International Symposia on VLSI Technology, Systems and Applications. (Invited)

[8] T. Endoh, "STT-MRAM and its Application for Nonvolatile Brain-Inspired VLSIs", SEMICON CHINA, 2017.

[9] T. Endoh, "MRAM (New Memory Technologies Track)", Flash Memory Summit 2018. (Invited)

[10] H. Sato, H. Honjo, T. Watanabe, M. Niwa, H. Koike, S. Miura, T. Saito, H. Inoue, T. Nasuno, T. Tanigawa, Y. Noguchi, T. Yoshiduka, M. Yasuhira, S. Ikeda, S.- Y. Kang, T. Kubo, K. Yamashita, Y. Yagi, R. Tamura, and T. Endoh, "14ns write speed 128Mb density Embedded STT-MRAM with endurance>1010 and 10yrs retention@85°C using novel low damage MTJ integration process", IEDM2018.

[11] H. Honjo, A. Nguyen Thi Van, T. Watanabe, T. Nasuno, C. Zhang, T. Tanigawa, S. Miura, H. Inoue, M. Niwa, T. Yoshizuka, Y. Noguchi, M. Yasuhira, A. Tamakoshi, M. Natsui, Y. Ma, H. Koike, Y. Takahashi, K. Furuya, H. Shen, S. Fukami, H. Sato, S. Ikeda, T. Hanyu, H. Ohno, T. Endoh, "First demonstration of field-free SOT-MRAM with 0.35 ns write speed and 70 thermal stability under 400°C thermal tolerance by canted SOT structure and its advanced patterning/SOT channel technology", IEDM 2019, 28.5.1.

[12] T. Endoh, "Embedded MRAM and NV-Logic for IoT and AI Applications", MRAM Development Day 2019. (Invited)

[13] K. Nishioka, H. Honjo, S. Ikeda, T. Watanabe, S. Miura, H. Inoue, T. Tanigawa, Y. Noguchi, M. Yasuhira, H. Sato, and T. Endoh, "Novel Quad interface MTJ technology and its first demonstration with high thermal stability and switching efficiency for STT-MRAM beyond 2Xnm", 2019 Symposium on VLSI Technology, T120.

[14] K. Nishioka, H. Honjo, S. Ikeda, T. Watanabe, S. Miura, H. Inoue, T. Tanigawa, Y. Noguchi, M. Yasuhira, H. Sato, and T. Endoh, "Novel Quad-Interface MTJ Technology and Its First Demonstration with High Thermal Stability Factor and Switching Efficiency for STT-MRAM Beyond 2X nm", IEEE T-ED 67, 995 (2020).

[15] H.Koike, T.Tanigawa, T.Watanabe, T.Nasuno, Y.Noguchi, M.Yasuhira, T.Yoshiduka, Y.Ma, H.Honjo, K.Nishioka, S.Miura, H.Inoue, S.Ikeda, and T.Endoh,"40-nm 1T-1MTJ 128Mb STT-MRAM with Novel Averaged Reference Voltage Generator Based on Detailed Analysis of Scaled-Down Memory Cell Array Design", IEEE Trans. Mag. DOI: 10.1109/TMAG.2020.3038110

[16] T. Endoh, "Nonvolatile Logic and Smart Nonvolatile Processors with CMOS/MTJ Hybrid Technology for IoT and AI (AIoT) Edge System", 2020 International Solid-State Circuits Conference (ISSCC). (Invited)

[17] M. Natsui, A. Tamakoshi, H. Honjo, T. Watanabe, T. Nasuno, C. Zhang, T. Tanigawa, H. Inoue, M. Niwa, T. Yoshiduka, Y. Noguchi, M. Yasuhira, Y. Ma, H. Shen, S. Fukami, H. Sato, S. Ikeda, H. Ohno, T. Endoh, and T. Hanyu, "Dual-Port Field-Free SOT-MRAM Achieving 90MHz Read and 60MHz Write Operations under 55nm CMOS Technology and 1.2V Supply Voltage", 2020 Symposia on VLSI Technology and Circuits, CM2.2

[18] S. Miura, K. Nishioka, H. Naganuma, T.V.A. Nguyen, H. Honjo, S. Ikeda, T. Watanabe, H. Inoue, M. Niwa, T. Tanigawa, Y. Noguchi, T. Yoshiduka, M. Yasuhira, and T. Endoh, "Scalability of Quad Interface p-MTJ for 1X nm STT-MRAM with 10 ns Low Power Write Operation, 10 years Retention and Endurance > 10^{11}", 2020 Symposia on VLSI Technology and Circuits, TM3.1.

[19] T. Endoh, H. Honjo, K. Nishioka and S. Ikeda, "Recent progresses in STT-MRAM and SOT-MRAM for next generation MRAM", 2020 Symposia on VLSI Technology and Circuits, TMFS.1 (Invited)

[20] H. Naganuma, S. Miura, H. Honjo, K. Nishioka, T. Watanabe, T. Nasuno, H. Inoue,T. V. A. Nguyen, Y. Endo, Y. Noguchi, M. Yasuhira, S. Ikeda, and T. Endoh "Advanced 18 nm Quad-MTJ technology overcomes dilemma of Retention and Endurance under Scaling beyond 2X nm", 2021Symposia on VLSI Technology and Circuits

VOLTAGE CONTROL SPINTRONICS MEMORY (VOCSM) BASED LOW ENERGY CONSUMPTION NONVOLATILE LOGIC-GATES FOR BINARY NEURAL NETWORKS (B.N.N.)

H. YODA[1], K. YAKUSHIJI[2] and A. FUKUSHIMA[2]

1) Spin-Orbitronics Technologies, Inc., Tsukuba, Japan, hi.yoda@sot-i.co.jp

2) Research Center for Emerging Computing Technologies, National Institute of Advanced Industrial Science and Technology, Tsukuba, Japan

Ⅰ. INTRODUCTION

Since data transfer between memories and CPUs or MPUs becomes a bottle-neck for AI applications, in-memory computing becomes one of the hot topics. While, SOT-MRAM and VoCSM were reported to have both low energy consumption and nonvolatility [1]. VoCSM was also reported to work as logic-gates as well as nonvolatile working memories [2]. In this paper, SOT-MRAM and VoCSM and their application to Binary Neural Networks (B.N.N) are reviewed.

II. STRUCTURE OF A UNIT-CELL FOR SOT-MRAM AND VOCSM

Figure 1 shows a structure of a SOT-MRAM-cell (the same as a VoCSM-cell) and the equivalent circuit. The structure is just an in-plane MTJ on a Ta-based electrode, almost the same as a matured conventional in-plane MTJ used for a field-writing MRAM product.

Ⅲ. LOW VOLTAGE WRITING OF A SOT-MRAM-CELL AND

FUNDAMENTAL WRITING PROPERTY OF A VOCSM-CELL

Figure 2 shows the writing performances of SOT-MRAM. The writing voltage, $V_{writing}$, can be as small as 0.1V for WER of 1E-6 or below as shown in Fig.2(a). The switching threshold voltage, V_{SW}, are almost independent of retention energy, ΔE_r as shown in Fig.2(b). The low voltage writing is one of the reasons why SOT-MRAM has a good match with embedded memory applications especially for 7nm node and below.

Figure 3 shows a bias-voltage (V_{bias}) dependence of V_{SW} that is fundamental to VoCSM-cells. The dependence is fitted very well with the equation below.

$$V_{SW}(V_{bias}) = k\,(\alpha_{eff}\,/\,\theta_{SH})\cdot(w_{sl}\,/\,t_{SHE})\cdot\Delta E_{eff\text{-}sw}\,(V_{bias})\cdot R_{SH} \tag{1}$$

Here, α_{eff} and w_{sl} are the effective damping constant and the width of the MTJ, respectively. θ_{SH}, t_{SHE}, and R_{SH} are the spin-Hall angle, the thickness, and the resistance of the spin-Hall electrode, respectively. $\Delta E_{eff\text{-}SW}$ is the effective switching energy of a magnetization in the storage-layer. k is fitting parameter. When bias voltage is applied to the BVT in Fig.1, $\Delta E_{eff\text{-}SW}$ is modulated by voltage-controlled magnetic anisotropy effect (VCMA). As a result, V_{SW} has the dependence on V_{bias}.

Ⅳ. A VOCSM-BASED NONVOLATILE XNOR LOGIC GATES FOR B.N.N.

Figure.4 shows the structure of a VoCSM-based XNOR logic-gate consists of two VoCSM-cells connected by the spin-Hall electrode (SHE) [3], [4]. The logic-gates with relatively large size were proved to work previously [2].　Figure 5 shows an estimation of the execution voltages of the logic-gate with an MTJ size of $50\times90\text{nm}^2$ by the equation(1).The logic-gate works with low voltage as low as 0.5V or the order with reasonable VCMA coefficient of 120fJ/(V·m).

V. SUMMARY

SOT-MRAM has a good match with embedded memories because of the low writing voltage as small as 0.1V. VoCSM works both as nonvolatile memories and as XNOR logic-gates. The execution voltage of VoCSM-based XNOR logic-gates is estimated to be 0.5V. These results promise the applications of VoCSM in-memory computing especially for B.N.N.

HIROAKI YODA
E-mail: hi.yoda@sot-i.co.jp
tel: +81-80-37203456

REFERENCES

1) H. Yoda, *et al.*, "Voltage-Control Spintronics Memory (VoCSM) Having Potentials of Ultra-Low Energy-Consumption and High-Density," *Digests of 62th IEDM*, 27.6 (2016).
2) H. Yoda, *et al.*, *Proceeding of IMW* 2020, https://doi.org/10.1109/IMW48823.2020.9108120.
3) H. Yoda, *et al.*, WO/2021/075343.
4) H. Yoda, *et al.*, PCT/JP2020/047144 (Pending).
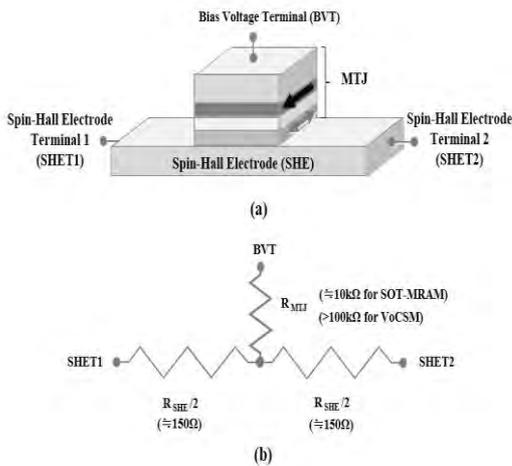
Fig. 1 Structure of a unit cell for SOT-MRAM and VoCSM

Fig. 2 Low voltage writing of SOT-MRAM

Fig. 3 Fundamental writing property of a VoCSM-cell

Fig. 4 Structure and the equivalent circuit of XNOR logic-gate with two VoCSM-cells
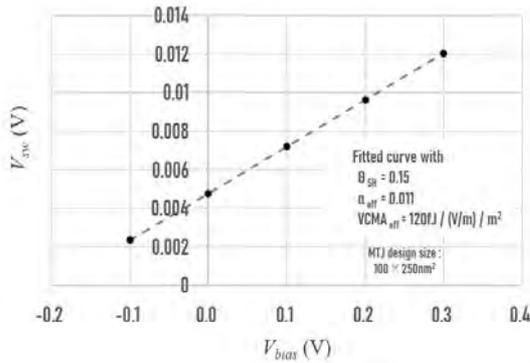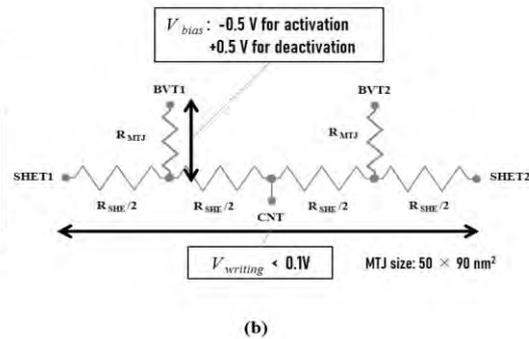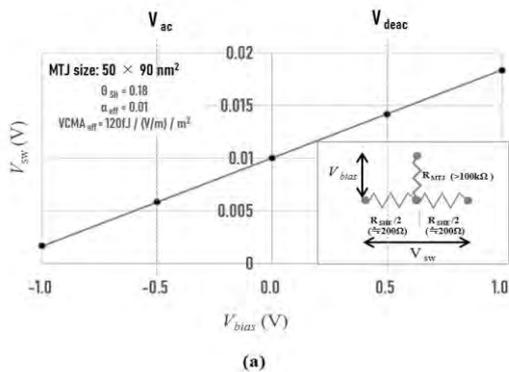
Fig. 5 Estimated execution voltages for nonvolatile XNOR logic-gate

FERROMAGNET-INDUCED SPIN-ORBIT TORQUES

Kyung-Jin Lee[1]

1) Department of Physics, Korea Advanced Institute of Science and Technology (KAIST), Daejeon, Korea, kjlee@kaist.ac.kr

Spin-orbit torque (SOT), which is considered as a write scheme for next-generation MRAMs, arises from the charge-to-spin conversion via spin-orbit coupling (SOC). For commercialization of SOT-MRAMs, it is of crucial importance to enhance the charge-to-spin conversion efficiency, which requires a detailed understanding of various SOC effects. In addition to the widely studied spin Hall effect of non-magnet (NM), recent studies found that SOC of ferromagnet (FM) also contributes to the SOT [1], including (i) interface torque [2-4], (ii) anomalous torque [5-7], and (iii) orbital torque [8-10]. In this talk, we will discuss about these FM-induced SOTs, which provide additional knobs to enhance the net SOT efficiency. The talk will include

(i)   The NM/FM interfaces generate spin currents polarized normal to the film plane [2,3], which allows for field-free SOT switching of perpendicular magnetization at a low current density [4].

(ii)   Transverse spin currents are allowed within bulk FM [5,6], which serve as a source of SOT. Various features of this effect can be described by a recently generalized spin drift-diffusion formalism [7].

(iii)   The spin Hall effect is concomitant with more fundamental orbital Hall effect [8]. As the orbital Hall effect is usually much stronger than the spin Hall effect, a direct injection of orbital currents to FMs can enhance the SOT via SOC of FM [9]. We will show an SOT experiment, necessitating the orbital Hall effect to explain the result [10].

REFERENCES

1) D. Go *et al*., "Theory of current-induced angular momentum transfer dynamics in spin-orbit coupled systems", *Phys. Rev. Research* 2, 033401 (2020).

2) S.-h. C. Baek *et al*., "Spin currents and spin-orbit torques in ferromagnetic trilayers", *Nat. Mater.* 17, 509 (2018).

3) V. P. Amin, J. Zemen, and M. D. Stiles, "Interface-generated spin currents", *Phys. Rev. Lett.* 121, 136805 (2018).

4) D.-K. Lee and K.-J. Lee, "Spin-orbit torque switching of perpendicular magnetization in ferromagnetic trilayers", *Sci. Rep.* 10, 1772 (2020).

5) W. Wang *et al*., "Anomalous spin–orbit torques in magnetic single-layer films", *Nat. Nanotechnol.* 14, 819 (2019).

6) V. P. Amin, Junwen Li, M. D. Stiles, and P. M. Haney, "Intrinsic spin currents in ferromagnets", *Phys. Rev. B* 99, 220405(R) (2019).

7) K.-W. Kim and K.-J. Lee, "Generalized spin drift-diffusion formalism in the presence of spin-orbit interaction of ferromagnets", *Phys. Rev. Lett.* 125, 207205 (2020).

8) H. Kontani *et al*., "Giant orbital Hall effect in transition metals: Origin of large spin and anomalous Hall effects", *Phys. Rev. Lett.* 102, 016601 (2009).

9) D. Go and H.-W. Lee, "Orbital torque: Torque generation by orbital current injection", *Phys. Rev. Research* 2, 013177 (2020).

10) D. Lee *et al*., "Orbital torque in magnetic bilayers", DOI: 10.21203/rs.3.rs-509141/v1.

Kyung-Jin Lee
E-mail: kjlee@kaist.ac.kr
tel: +82-42-350-7923

SPIN-ORBIT TORQUE SWITCHING BASED ON TOPOLOGICAL SPIN TEXTURES AND MAGNONS

Hyunsoo YANG[1]

1) Department of Electrical and Computer Engineering, National University of Singapore, Singapore, eleyang@nus.edu.sg

The most straightforward approach to developing high spin-orbit torque (SOT) devices is by replacing the underlying heavy metal (HM) layer as the source of spin currents. Typically, HMs such as Pt, Ta, W, and Hf are used in these devices which have the effective spin Hall angle (θ_{SH}) in the range of 0.05–0.3. However, there has recently been an interest in exotic and novel materials such as topological insulators (TIs) and Weyl semimetal due to their large charge-to-spin conversion efficiency.

TIs are materials with an insulating bulk and conducting surfaces (topological surface states, TSS). Interestingly, the TSS exhibit spin-momentum locking in which the spin polarization direction of an electron on the TSS is fixed with respect to its momentum. This results in spin accumulation at TSS similar to the spin Hall effect (SHE) and the Rashba effect observed in HMs. TSS dominated spin-orbit torques and magnetization switching at room temperature using Bi_2Se_3 as a spin current source were demonstrated [1]. However, the resistive nature of TIs can cause current shunting issues, leading to a large power consumption.

Advantages of Weyl semimetals over TIs are that Weyl semimetals have a much larger conductivity compared to TIs and they can also generate a strong spin current from their bulk states. The crystal structure of a Weyl semimetal, WTe_2, has only one mirror plane and does not contain a twofold rotational invariance. Therefore, the current-induced spin accumulation response in WTe_2 is anisotropic. As a result, when the current is passed through a low-symmetry axis (*a*-axis), a sizable out-of-plane spin accumulation is detected. This unique property of WTe_2 makes it ideal for use in field-free SOT devices with perpendicular magnetic anisotropy (PMA). We show current-driven magnetization switching in WTe_2/NiFe with a low current density and low power [2]. The in-plane θ_{SH} increases up to 0.8 with increasing the WTe_2 thickness. Interestingly, the required power to switch the magnetization was 19 times smaller in WTe_2/Py than that of Bi_2Se_3/Py and 350 times smaller than that of Pt/Py due to a high efficiency and low resistivity of WTe_2. Furthermore, a threefold reduction in the switching current is demonstrated using dumbbell-shaped magnetic elements in $MoTe_2$/Py heterostructures [3].

While the above mentioned exotic materials have been promising in terms of their charge-to-spin conversion properties, the biggest hindrance toward their practical applications is the difficulty in their fabrication for a large and uniform area as well as their large resistivity leading to a current shunting issue. Single-crystal TIs, semimetals, and other layered materials in a majority of reports have been either exfoliated or fabricated using sophisticate molecular beam epitaxy (MBE). Only very recently sputter-deposited TIs have been shown to produce large SOTs capable of switching an adjacent magnet. While sputter-deposited exotic materials are expected to be more technologically relevant, it is still not clear whether topological features are present and what the role is in the structure with small crystalline clusters and non-stoichiometric inhomogeneous composition. Future research efforts should focus on the fabrication of these novel materials in a fast, efficient, and reliable way.

The current shunting issue can be also overcome if the angular momentum is carried by precessing spins rather than moving electrons (see Fig. 1). Moreover, magnon currents can flow over distances of micrometers even in insulators, and thus, materials are not limited to electrical conductors. Magnon-torque-driven magnetization switching is demonstrated in the Bi_2Se_3/NiO/Py devices at room temperature [4]. By injecting the electric current to an adjacent Bi_2Se_3 layer, spin currents were converted to magnon torques through an antiferromagnetic insulator NiO. While the magnon torque ratio of 0.3 is larger than the electrical spin-torque ratio in typical HMs and is comparable to that of TIs reported recently. Furthermore, the electrical isolation relaxes the requirement for heterogeneous integration with a magnetic

layer, which may address recent technical challenges in vias.

REFERENCES

1) Y. Wang et al., "Room temperature magnetization switching in topological insulator-ferromagnet heterostructures by spin-orbit torques" *Nat. Commun.* 8, 1364 (2017).
2) S. Shi et al., "All-electric magnetization switching and Dzyaloshinskii–Moriya interaction in WTe$_2$/ferromagnet heterostructures" *Nat. Nanotechnol.* 14, 945 (2019).
3) S. Liang et al., "Spin-orbit torque magnetization switching in MoTe$_2$/permalloy heterostructures" *Adv. Mat.* 32, 2002799 (2020)
4) Y. Wang et al., "Magnetization switching by magnon-mediated spin torque through an antiferromagnetic insulator" *Science* 366, 1125 (2019).
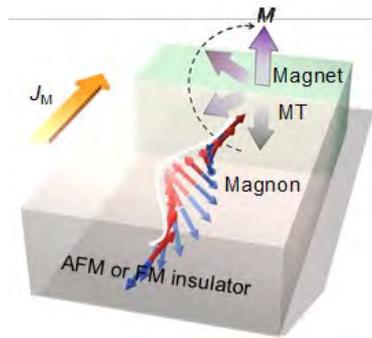
Fig. 1. Schematic of magnon current based magnetization switching.

CHIRAL SPIN TEXTURES AND CHIRAL SPIN-ORBIT TORQUES FOR SPINTRONIC MEMORIES

Stuart S.P. PARKIN[1]

1) Max Planck Institute for Microstructure Physics, Halle (Saale), Germany,
stuart.parkin@mpi-halle.mpg.de

Atomically engineered magnetic heterostructures and their manipulation by current are key to several spintronic memory-storage technologies [1]. One of these is Racetrack Memory in which chiral domain walls can be moved very efficiently with current via spin-orbit torques in synthetic antiferromagnetic (SAF) racetracks [2]. The domain walls act as memory bits and are moved to read and write elements integrated into or adjacent to the racetracks. Using atomically thin "dusting" layers we have recently shown that the critical current density needed to move the domain walls can be reduced several-fold, while increasing the domain wall velocity by more than a factor of five for otherwise the same current density [3]. Racetrack Memory is non-volatile and has the potential, on the one hand, to replace the density memories today, namely hard-disk and solid-state drives and, on the other hand, the fastest, namely SRAM. The latter would be composed of a single domain wall racetrack that can be very fast (~100 ps).

Recently a zoology of complex spin textures stabilized by volume or interface Dzyaloshinskii-Moriya interactions have been discovered including, in our work, anti-skyrmions [4], elliptical Bloch skyrmions [5], two-dimensional Néel skyrmions [6] and fractional antiskyrmions [7]. We discuss our recent observation of Néel skyrmions and conventional magnetic bubbles in two distinct but closely related 2D van der Waal's ferromagnetic compounds. SAF structures are highly promising for spintronics especially since this allows for magnetic structures that have zero net magnetization and, consequently, very small fringing magnetic fields, while, at the same time, these structures have magnetic surfaces that aid the detection of their magnetic state. Antiferromagnetic structures can have nearly zero net magnetization but are much more difficult to detect than SAFs. Highly interesting antiferromagnetic materials are those that are chiral and topological such as the family of Mn3X (X=Ge, Sn, Sb) that have a Kagome structure. We discuss our recent work on the current induced manipulation of the antiferromagnetic order in thin epitaxial films of Mn3Sn. In particular, we introduce the concept of seeded spin orbit torque (SSOT) that allows for the manipulation of the antiferromagnetic order, even in layers that are more than 100 nm thick. The triangular antiferromagnetic structure of Mn3X [8] leads to highly interesting properties including an anomalous Hall effect derived from an intrinsic Berry curvature even though the magnetization is zero. Zero-moment chiral spin textures ranging from domain walls to anti-skyrmions have great promise for highly interesting spintronic technologies for Racetrack Memories and beyond.

REFERENCES

[1] S.-H. Yang, R. Naaman, Y. Paltiel, and S. S. P. Parkin, "Chiral spintronics," *Nat. Rev. Phys.,* vol. 3, pp. 328–343 (2021).

[2] S. S. P. Parkin and S.-H. Yang, "Memory on the Racetrack," *Nat. Nanotechnol.,* vol. 10, pp. 195-198, 2015.

[3] Y. Guan *et al.*, "Increased Efficiency of Current-Induced Motion of Chiral Domain Walls by Interface Engineering," *Adv. Mater.,* vol. 33, p. 2007991, (2021)

[4] A. K. Nayak *et al.*, "Magnetic antiskyrmions above room temperature in tetragonal Heusler materials," *Nature,* Letter vol. 548, no. 7669, pp. 561-566, (2017)

[5] J. Jena *et al.*, "Elliptical Bloch skyrmion chiral twins in an antiskyrmion system," *Nat. Commun.,* vol. 11, p. 1115, (2020).

[6] A. K. Srivastava *et al.*, "Observation of Robust Néel Skyrmions in Metallic PtMnGa," *Adv.*

Stuart S.P. Parkin
E-mail: stuart.parkin@mpi-halle.mpg.de
tel: +49-174-1801802

Mater., vol. 32, p. 1904327, (2020).

[7]   J. Jena *et al.*, "Observation of fractional spin textures and bulk-boundary correspondence," *submitted*, (2021).

[8]   A. K. Nayak *et al.*, "Large anomalous Hall effect driven by non-vanishing Berry curvature in non-collinear antiferromagnet Mn$_3$Ge " *Sci. Adv.,* vol. 2, p. e1501870, (2016).

Interplay of voltage control of magnetic anisotropy, spin transfer torque, and heating on spin-orbit torque switching of MTJs

Viola KRIZAKOVA[1], Eva GRIMALDI[1], Kevin GARELLO[2,3], Giacomo SALA[1], Sebastien COUET[2], Gouri Sankar KAR[2], and Pietro GAMBARDELLA[1]

1) Department of Materials, ETH Zurich, 8093 Zurich, Switzerland

2) imec, Kapledreef 75, 3001 Leuven, Belgium

3) CEA, SPINTEC, F-38000 Grenoble, France

I. INTRODUCTION

Current-induced spin-transfer torque (STT) provides the basic mechanism to manipulate the magnetization state of magnetic tunnel junctions (MTJs) in magnetoresistive random access memories (MRAMs). The main advantages of STT MRAMs are the low power consumption, long retention times, high endurance, scalability, and a limited number of fabrication steps. For these reasons, they are considered universal memories with the capability to replace flash memories, last-level cache, and static RAMs in embedded applications. However, the initial alignment of the quiescent magnetization in the free layer and the spin polarization of the tunneling current results in long incubation delays preceding the reversal. Large current densities can reduce these delays; however, they impose stress on the tunnel barrier and accelerate its degradation. To mitigate this problem, an alternative switching mechanism based on spin-orbit torque (SOT) has been proposed [1]. Writing by SOTs uses an in-plane current that flows separately from the reading path [2], thus lifting the restrictions on switching speed and endurance, and lowering the read disturb errors.

Whereas STT and SOT switching of MTJs have been separately described by many studies, less work has been focused on the combination of STT and SOT. First studies have shown that the combined action of the two torques can allow for field-free switching of MTJs [3], a reduced incubation delay, and very low dispersion of switching events [4,5]. The optimization of the interplay of SOT and STT biasing is thus not only relevant to understand the switching dynamics in MTJs but also for reducing the writing current.

II. DUAL PULSE WRITING

We use three-terminal MTJs fabricated by a CMOS-compatible process [6] employing an embedded in-plane magnet to secure field-free operation [5,7] to study the switching dynamics due to simultaneous SOT and STT voltage pulses [Fig. 1]. We combine real-time and post-pulse detection to unravel the switching characteristics in the time domain for individual reversal events as well as for statistically relevant distributions [8]. We show that simultaneous injection of dual pulses across the SOT track and MTJ pillar allows for reducing the overall writing energy relative to switching by SOT or STT alone while simultaneously preserving the ability to switch the MJT by sub-nanosecond pulses [Fig. 2(a)]. By performing time-resolved measurements and micromagnetic simulations, we discriminate three main effects generated by the MTJ bias – STT, self-heating, and voltage-control of magnetic anisotropy (VCMA) – and separately quantify their impact on the switching times. We find that the incubation delay is minimized by a decrease of the free layer anisotropy by self-heating and VCMA due to the lowering of the energy barrier for domain nucleation. The reversal phase, which proceeds by domain-wall propagation, can be assisted by STT. The relative impact of these effects depends on the strength, polarity, and duration of the bias pulse, as well as on the MTJ size [Fig. 2(b)]. Consequently, certain bias combinations can even lead to a reduction of the switching efficiency compared to SOT [8,9]. Therefore, we provide a compact analytical model that links the effects induced by the MTJ bias to the geometry and material parameters of the device, which allows for their separate tuning and finding the optimal balance between SOT and STT.

III. CONCLUSIONS

The present study unravels the relative impact of SOT, STT, VCMA, and heating on the switching

VIOLA KRIZAKOVA
E-mail: viola.krizakova@mat.ethz.ch

time and efficiency in perpendicular MTJs. The combination of time-resolved electrical measurements, micromagnetic simulations, and analytical modeling provides a detailed quantitative understanding of how these effects concur in the switching process. These findings have general relevance for understanding and optimizing the switching properties of three-terminal MTJ devices, in which multiple current- and voltage-induced effects can be exploited to improve their speed, reliability, and energetic efficiency.

REFERENCES

1) A. Manchon, J. Zelezny, I. M. Miron, *et al*, "Current-induced spin-orbit torques in ferromagnetic and antiferromagnetic systems A.", *Rev. Mod. Phys.* 91, 035004 (2019).

2) I. M. Miron, K. Garello, G. Gaudin, *et al*, "Perpendicular switching of a single ferromagnetic layer induced by in-plane current injection", *Nature* 476, 7359 (2011).

3) M. Wang, W. Cai, D. Zhu, *et al.* "Field-free switching of a perpendicular magnetic tunnel junction through the interplay of spin-orbit and spin-transfer torques" *Nat. Electron*. 1, 582 (2018).

4) E. Grimaldi, V. Krizakova, G. Sala, *et al*, "Single-shot dynamics of spin-orbit torque and spin transfer torque switching in three-terminal magnetic tunnel junctions", *Nat. Nanotech.* 15, 111-117 (2020).

5) V. Krizakova, K. Garello, E. Grimaldi, *et al*, "Field-free switching of magnetic tunnel junctions driven by spin-orbit torques at sub-ns timescales" *Appl. Phys. Lett*. 116, 232406 (2020).

6) K. Garello, F. Yasin, S. Couet, *et al.* "SOT-MRAM 300mm integration for low power and ultrafast embedded memories" *IEEE Symp. VLSI Circ.,* 81-82 (2018).

7) K. Garello, F. Yasin, H. Hody, *et al.* "Manufacturable 300mm platform solution for Field-Free Switching SOT-MRAM" *IEEE Symp. VLSI Technol.,* T194-195 (2019).

8) V. Krizakova, E. Grimaldi, K. Garello, *et al,* "Interplay of Voltage Control of Magnetic Anisotropy, Spin-Transfer Torque, and Heat in the Spin-Orbit-Torque Switching of Three-Terminal Magnetic Tunnel Junctions" *Phys. Rev. Appl.* 15, 054055 (2021).

9) Y. C. Wu, K. Garello, W. Kim, *et al.* "Voltage-Gate Assisted Spin-Orbit Torque Magnetic Random Access Memory for High-Density and Low-Power Embedded Application" *Phys. Rev. Appl.* 15, 064015 (2021).
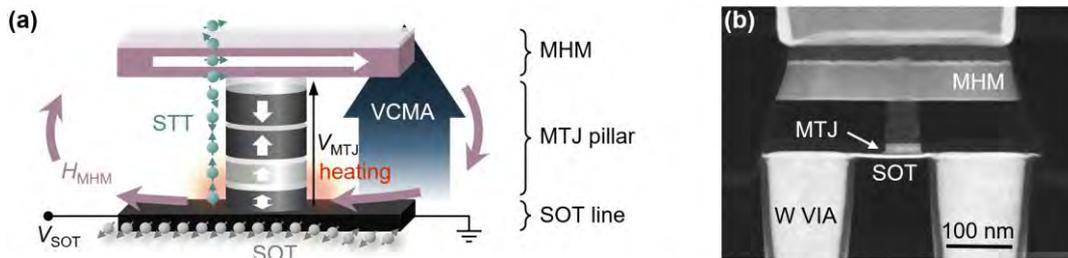
Fig. 1 a) Schematics of the effects induced by voltage bias across the MTJ pillar (V_{MTJ}) and SOT track (V_{SOT}). b) Cross-sectional view of the MTJ device with an embedded magnetic hardmask (MHM).
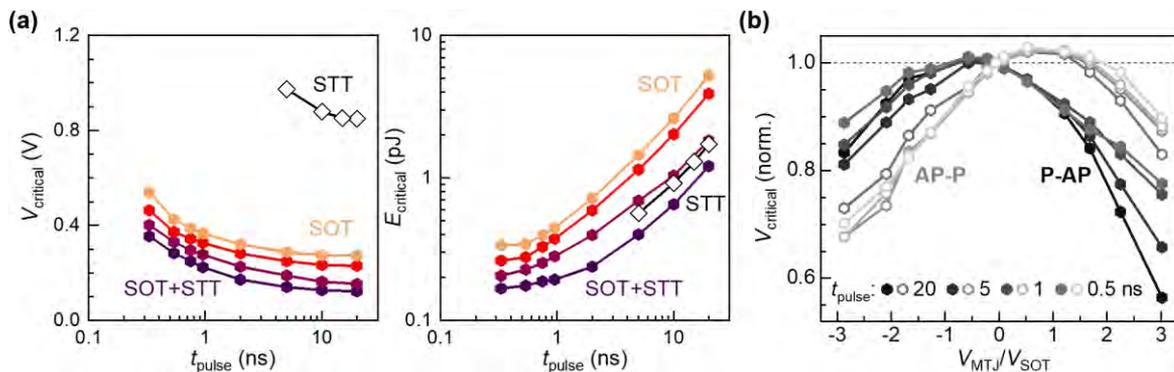

Fig. 2 a) Critical switching voltage and energy for writing by STT (open diamonds), SOT (yellow circles), and combined bias (purple circles). b) Variation of the critical SOT switching voltage with V_{MTJ}.

PMA MECHANISMS AT Fe/MgO INTERFACES: ON ITS VOLTAGE CONTROL AND TEMPERATURE DEPENDENCE

F. IBRAHIM[1], A. HALLAL[1], A. KALITSOV[2], B. DIENY[1], and M. CHSHIEV[1,3]

1) Univ. Grenoble Alpes, CEA, CNRS, SPINTEC, 38000 Grenoble, France,
Fatima.ali.ibrahim@hotmail.com

2) Western Digital Technologies, Inc., 5601 Great Oaks Parkway, San Jose, CA 95119, USA

3) Institut Universitaire de France

I. INTRODUCTION

The perpendicular magnetic anisotropy (PMA) at magnetic transition metal/oxide interfaces (TM/Ox) is a key element in building out-of-plane magnetized magnetic tunnel junctions (p-MTJ) for spin-transfer-torque magnetic random-access memory (STT-MRAM) [1]. The PMA at those interfaces originates from strong hybridizations between the interfacial (Co) Fe-3d and the O-2p orbitals combined with spin-orbit coupling (SOC) [2]. Interestingly, TM/Ox interfaces provide both low switching currents, owing to the relatively weak Gilbert damping, and high thermal stability thanks to their large PMA values. In this context, we theoretically uncover several fundamental aspects of two important phenomena: (1) the voltage control of the magnetic anisotropy (VCMA) where reduction in energy dissipation by a factor of 100 is anticipated, (2) temperature (T) dependence of the PMA which is crucial for understanding the thermal stability of the storage layer magnetization.

II. VOLTAGE CONTROL OF PMA

We employed first-principles calculations to unveil and describe the mechanisms behind the VCMA, namely the charge-mediated [3] and ionic-migration [4] induced VCMA are addressed in Fe/MgO interfaces.

In the charge-mediated VCMA, we elucidate this effect in relation to the intrinsic electric dipole at the Fe/MgO interface, which has been observed and quantified. The increase (decrease) of PMA under an electric field is associated with a decrease (increase) of the interfacial electric dipole field which spontaneously exists even without application of any electrical field. Moreover, our on-site projected PMA analysis reveals that even if the electric field is screened on a very short Thomas-Fermi length (1–2 Å) in the metallic electrode, its influence extends beyond the interfacial Fe layer. In particular, we show that the main contribution to the PMA variation arises from the second Fe layer, a behavior which is understood in view of orbital hybridizations. However, the range of the VCMA efficiency is found to be of the order of tenths fJ/(V.m).

In the ionic-migration mediated VCMA, a characteristic dependence of the effect on oxygen migration at Fe/MgO interfaces was revealed. The VCMA efficiency as a function of the migrated O-atoms concentration exhibits an exponential variation of the form $= \beta_{max} (1-e^{(-P/W)})$, with P, β_{max}, and W respectively being the percentage of migrating oxygen atoms, VCMA efficiency maximum and newly introduced characteristic concentration of migrating ions. Interestingly, depending on the range of variation of the applied voltage, two regimes associated with reversible or irreversible ions displacement are predicted to occur, yielding different VCMA response. In the irreversible case, O-migration mediated VCMA can reach thousands of fJ/(V.m) consistent with the experimental observations.

Based on our findings, one can distinguish from the order of magnitude of the VCMA driving mechanism: an effect of several tens of fJ/(V.m) is likely associated to charge-mediated effect combined with slight reversible oxygen displacements whereas an effect of the order of thousands of fJ/(V.m) is more likely associated with irreversible oxygen ionic migration

FATIMA IBRAHIM
E-mail: fatima.ali.ibrahim@hotmail.com
tel: +33-7-77302479

III. TEMPERATURE DEPENDENCE OF PMA

The correlation between the T-dependent first order anisotropy constant K_1 and magnetization M_s, as described by Callen and Callen [5], follows a power scaling law: $K_1(T)/K_1(T=0) = [M_s(T)/M_s(T=0)]^3$. We analyze the possible mechanisms behind the experimentally-reported deviations from the Callen and Callen scaling power law in Fe/MgO-based structures. First-principles calculations reveal small high-order anisotropy constants compared to first order, thus ruling out an intrinsic microscopic mechanism underlying those deviations. Neglecting higher-order anisotropy terms in the atomisitic spin Hamiltonian, two possible extrinsic macroscopic mechanisms are unveiled namely the influence of the dead layer, always present in the storage layer of STT-MRAM cells, and the spatial inhomogeneities of the interfacial magnetic anisotropy.

Regarding the first mechanism, we show that the presence of a dead layer simultaneously with scaling the anisotropy constant, which is interfacial, by the total magnetization of the sample rather than that of the interface itself lead to low scaling powers. In the second mechanism, increasing the percentage of inhomogeneity in the interfacial perpendicular magnetic anisotropy is revealed to decrease the scaling power. Apart from those different mechanisms, the layer-resolved temperature-dependence of anisotropy is shown to ideally follow the Callen and Callen scaling power law for each individual Fe layer. These results allow to coherently explain the difference in scaling powers relating anisotropy and magnetization thermal variations reported in earlier experiments. This is crucial for the understanding of the thermal stability of the storage layer magnetization in STT-MRAM applications [6].
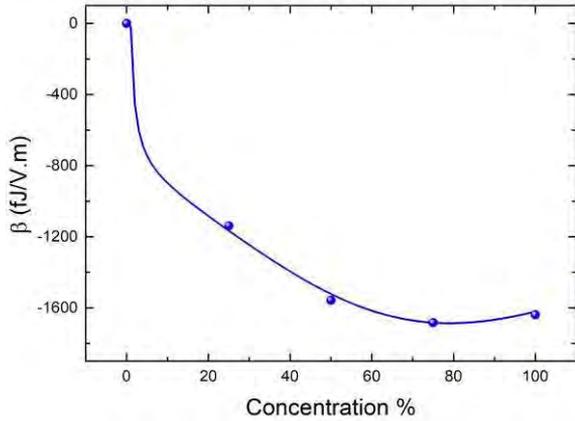
Figure 1: VCMA coefficient β due to oxygen ionic-migration versus the concentration of migrated oxygen at Fe/MgO interface
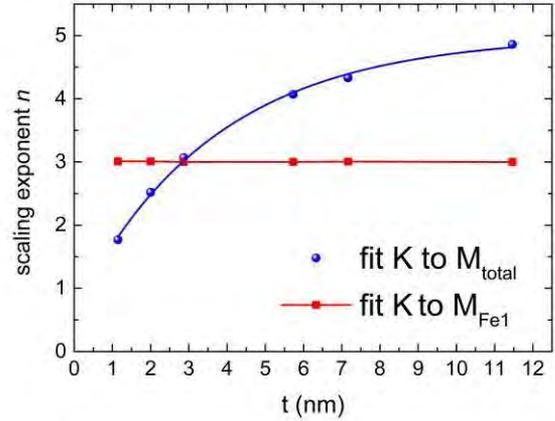
Figure 2: The effect of the magnetic dead layer on the temperature dependence of K is revealed by the variation of the scaling power n as a function of the magnetic layer thickness. The result of fitting K to the interfacial saturation magnetization (total saturation magnetization) M_{Fe1} (M_{total}) is shown by red squares (blue circles), respectively.

.

REFERENCES

1) B. Dieny and M. Chshiev, *Rev. Mod. Phys.* 89 (2), 025008 (2017).
2) H. X. Yang et al., *Phys. Rev. B* 84, 054401 (2011).
3) F. Ibrahim et al., *Phys. Rev. B* 93, 014429 (2016).
4) F. Ibrahim et al., *Phys. Rev. B* 98, 214441 (2018).
5) H. Callen and E. Callen, *J. Phys. Chem. Solids* 27, 1271 (1966).
6) F. Ibrahim et al., arXiv:2011.02220.

SPIN ORBIT TORQUES FROM FERROMAGNETIC LAYERS WITH OUT-OF-PLANE SPIN POLARIZATION

Andrew D. KENT[1], Christopher SAFRANSKI[2], Jun-Wen XU[1], Hoawen REN[1] and Jonathan Z. SUN[2]

1) Center for Quantum Phenomena, Department of Physics, New York University, New York, New York 10003, USA, andy.kent@nyu.edu, junwen.xu@nyu.edu & hr2354@nyu.edu

2) IBM T. J. Watson Research Center, Yorktown Heights, New York 10598, USA, Christopher.Safranski@ibm.com & jonsun@us.ibm.com

3)

Spin currents in present-day MRAM devices are generated by passing an electrical current perpendicular to layers that form a MTJ [1]. However, it is now widely appreciated that current flow in the plane of a layer can generate significant spin currents through spin-orbit coupling, e.g. in Pt, Ta & W. In these cases, however, the spin polarization is confined to the plane of the layers. An important research goal is to create a spin current with a significant out-of-plane spin polarization to enable efficient switching of perpendicularly magnetized elements. In this talk I discuss spin-orbit induced charge-to-spin conversion with magnetic materials. Specifically, I will report our observation of spin torques with a planar Hall effect (PHE) symmetry from CoNi acting on a CoFeB free layer, with a spin polarization in the magnetization direction [2]. Canting the CoNi magnetization out of the film plane thus produces a spin current with an out-of-plane spin polarization that can act on a free layer. The effect is comparable to the SHE in Pt, indicating its promise as a spin current source with a controllable spin polarization direction.

REFERENCES

1) A. D. Kent and D. C. Worledge, "A new spin on magnetic memories." Nature Nanotechnology **10**, 187 (2015)

2) C. Safranski, J.Z. Sun, J-W. Xu and A.D. Kent, "Planar Hall Driven Torque in a Ferromagnet/ Nonmagnet/Ferromagnet System," Physical Review Letters **124**, 197204 (2020)

LARGE PERPENDICULAR MAGNETIC ANISOTROPY AND VOLTAGE CONTROLLED MAGNETIC ANISOTROPY EFFECTS AT CoFe/MgO INTERFACE

Bhagwati PRASAD, Neil SMITH, Lei WAN, Alan KALISTOV, Matt CAREY, Jordan KATINE and Tiffany SANTOS

Western Digital Corporation, San Jose, CA USA; bhagwati.prasad@wdc.com

I. INTRODUCTION

The ongoing thrust in big data mining and artificial intelligence is critically demanding the high-density and fast access data storage, which cannot be fulfilled with current computation architecture due to the slow access speed of memory. Using the nonvolatile memory (NVM) element with high density and high speed can potentially tackle this impasse in the journey of next-generation computing[1]. Among several others, magnetic random-access memory (MRAM) is one of the promising NVM elements [2]. The basic building block of MRAM is a magnetic tunnel junction (MTJ), where the resistance state of the device can be modulated by manipulating the spin state of the magnetic layers via the current or magnetic field. Magnetization manipulation by voltage is an attractive alternative as it reduces the energy consumption by orders of magnitude with faster write/read operation and provides a higher density memory solution compared with current-controlled devices. The common route to use the voltage for this purpose is by exploiting the voltage-controlled magnetic anisotropy (VCMA) effect at the magnetic layer/ MgO interface[3]. Upon the application of voltage, the modification of the electronic occupation states of the d orbitals of the ferromagnetic electrode at the interface modulates the magnetic anisotropy. Additionally, the electric field-induced magnetic dipole moment and the Rashba effect are also proposed mechanisms for the origin of the VCMA effect[4]. In addition to the large VCMA effect for the writing operation, high perpendicular magnetic anisotropy (PMA) is required for thermal stability of data retention in MRAM devices [5]. The enhancement in PMA and VCMA effect in the CoFe/MgO system has resulted from the insertion of a thin metallic dusting layer (e.g. Ir, Mg, Pd, Hf) at the CoFe/MgO interface but at the expense of reducing magnetic moment[6]. In this work, we have demonstrated a large enhancement in PMA, the coercive field of the CoFe layer, and the VCMA effect with the insertion of a thin, novel metallic dusting layer between CoFe and MgO layers without any reduction in magnetic moment. These results demonstrate that the engineering of the ferromagnet/MgO interface with the insertion of a suitable metallic dusting layer can provide a pathway to develop high-density voltage-driven spintronic devices.

II. EXPERIMENTAL

The structure of our VCMA film stacks consists of Ta(10)/Ru(10)/W(3)/CoFeB(d)/X(t)/W(8)/Ta(20)/Ru(50) deposited on Si/SiO_x wafers, where the number in the parentheses is the layer thickness in Å. Five different materials, X (Ir, Pt, Mg-Al, Hf, and HfO_2), were inserted into the CoFeB/MgO interface with varying thicknesses from 0.5 to 5 Å. All metallic layers were grown by DC magnetron sputtering and MgO was grown by RF sputtering at room temperature. Subsequently, the film stacks were annealed at 335 °C for 1 hour. The magnetic properties of the films were measured by a vibrating sample magnetometer. To characterize the VCMA effect, we used the anomalous hall effect (AHE) measurement technique. To fabricate the Hall-bar devices (dimensions of $1X\ 7\ \mu m^2$ to $10 X 70\ \mu m^2$), we first deposited the film stack on pre-patterned wafers comprising the fabricated TiN electrical leads, and subsequently, the film stacks were fabricated by employing photolithography and dry etching. An Al_2O_3 layer was deposited to planarized the patterned stack and later Au leads were fabricated as a top electrode. The schematic of the hall-bar device is shown in Figure 1(a).

III. RESULTS AND DISCUSSION

We investigated the impact of five different insertion layers (Ir, Hf, HfO_2, Mg-Al, and Pt) at the CoFeB/MgO interface on the PMA and VCMA effects. We observed PMA and VCMA enhancement with thin Hf and Ir insertion at the cost of losing magnetic moment up to 30%. PMA enhances nearly 3-fold with Hf and HfO_2 insertions. However, the maximum VCMA effect that we observed with Hf insertion was ~ 60 fJ/V-m.

Interestingly, with the insertion of Mg-Al at the CoFe/MgO interface, PMA enhances dramatically (five times) without any reduction in magnetic moment. The VCMA coefficient with Mg-Al insertion also increased more than three times. Unlike the above-mentioned insertion layers, PMA does not change much with Pt insertion but the VCMA effect significantly improved, yielding VCMA coefficients >100 fJ/V-m.

To estimate the VCMA coefficient, AHE was characterized across the 2 μm X 15 μm hall bar to extract the variation of perpendicular magnetic anisotropy field (H_k) under varying gate voltages by cycling the magnetic field along the hard axis of the CoFeB. The normalized AHE resistance for different gate voltages as a function of in-plane magnetic field for a hall device with 1.5 Å of Mg-Al insertion is shown in figure 1(b). The H_k value for each gate voltage (Vg) was then extracted by using the Stoner-Wohlfarth model (see figure 1c). The VCMA coefficient (ξ) is determined by;

$$\xi = \frac{1}{2}(M_s t)_{FL} t_{MgO}\, \varepsilon$$

Where $(M_s t)_{FL}$ is the saturation magnetization times thickness of the magnetic layer, t_{MgO} thickness of MgO layer, and ε is dH_k/dV_g.

IV. REFERENCES

[1]   H. S. P. Wong and S. Salahuddin, "Memory leads the way to better computing," *Nat. Nanotechnol.*, vol. 10, no. 3, pp. 191–194, 2015.

[2]   B. Dieny *et al.*, "Opportunities and challenges for spintronics in the microelectronics industry," *Nat. Electron.*, vol. 3, no. 8, pp. 446–459, 2020.

[3]   X. Li, A. Lee, S. A. Razavi, H. Wu, and K. L. Wang, "Voltage-controlled magnetoelectric memory and logic devices," *MRS Bull.*, vol. 43, no. 12, pp. 970–977, 2018.

[4]   B. Rana and Y. C. Otani, "Towards magnonic devices based on voltage-controlled magnetic anisotropy," *Commun. Phys.*, vol. 2, no. 1, pp. 1–12, 2019.

[5]   B. Dieny and M. Chshiev, "Perpendicular magnetic anisotropy at transition metal/oxide interfaces and applications," *Rev. Mod. Phys.*, vol. 89, no. 2, 2017.

[6]   M. Tsujikawa *et al.*, "Perpendicular magnetic anisotropy and its electric-field-induced change at metal-dielectric interfaces," *J. Phys. D. Appl. Phys.*, vol. 52, no. 063001, 2019.
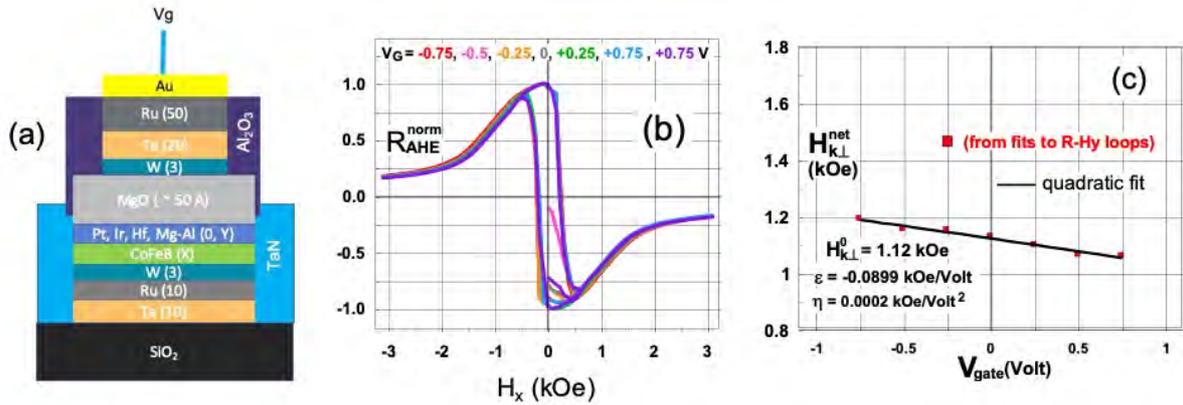
Figure 1: (a) Cross-sectional schematic of a Hall bar device that was used as a test vehicle to estimate the VCMA coefficient with the insertion of metallic dusting layer at CoFeB/MgO interface. (b) Normalized Hall resistance as a function of in-plane magnetic field under varying applied gate voltage for a device with film stack of Ta(10)/Ru(10)/W(3)/CoFeB(11)/Mg-Al(1.5)/W(8)/Ta(20)/Ru(50). (c) Variation of perpendicular magnetic anisotropy field (H_k) with varying gate voltage (V_g).

CRYOGENIC MRAMS FOR SUPERCONDUCTING COMPUTERS

Minh-Hai NGUYEN[1], Graham E. ROWLANDS[2] and Thomas A. OHKI[3]

1) Raytheon BBN Technologies, Cambridge, MA, USA, minh-hai.nguyen@wdc.com

2) Raytheon BBN Technologies, Cambridge, MA, USA, graham.rowlands@raytheon.com

3) Raytheon BBN Technologies, Cambridge, MA, USA, tom.ohki@raytheon.com

The high energy consumption of high-performance computers (HPCs) based on current CMOS technology has become a serious problem when scaling up to exascale performance [1]. Superconducting (SC) computers provide a viable solution for fast and energy-efficient computing: their estimated power consumption is about 2 orders of magnitude lower than CMOS-based supercomputers, even when including the cooling power (see Fig. 1). Furthermore, scalable SC quantum computers will eventually require (classical) cryogenic, and preferably SC, processors and memories for qubit control and fast signal processing. However, the development of SC computers has faced several challenges among which is the lack of fast, power-efficient and scalable cryogenic memories. These memories have to be integrated with SC circuits whose supply power is typically very small.

With the support of IARPA's Cryogenic Computing Complexity (C3) program, a team of more than 7 academic and industrial institutions, led by Raytheon BBN Technologies, over the course of 4 years have studied several potential solutions for cryogenic memories. Most of them are based on spin-torque MRAMs which is a natural choice owing to their high speed, nonvolatility and consistent performance across a wide range of temperatures. Yet, the challenges of scalability and integration with SC circuitry have to be addressed. In particular, these cryogenic MRAMs have to be interfaced with our custom Single-Flux-Quantum (SFQ) control circuits which can supply only 100 µA to a low load of a couple of Ohms. In this talk, we review three potential cryogenic MRAM solutions:

The first one is the in-plane magnetized spinvalve structure with the addition of an orthogonal polarizer [2]. Its impedance is low ~10 Ω and the precessional switching mechanism, enabled by the orthogonal polarizer, enables sub-nanosecond switching time. However, this ultrafast switching at the same time requires precise temporal control of the trigger pulses and, in addition to the low magnetoresistance (MR) typical of spinvalves, makes the write and read operations too difficult for scalable applications.

The second option is the perpendicularly magnetized magnetic-tunnel-junction (pMTJ) structure which has been commercialized for room-temperature applications. We optimized and demonstrated the sub-nanosecond switching of the pMTJ at 4K; and with 4ns pulses, we achieved WER $\leq 5\times10^{-5}$ and switching energy <300 fJ [3]. Similarly low WER at 4K is also achieved with in-plane magnetized spin-orbit-torque MRAM (SOT-MRAM) [4]. The high tunneling MR of 100-200% of these MTJs enables fast readout of large memory arrays. However, their high impedance poses a challenge in interfacing them with SFQ control circuits.

This integration problem can be resolved by the use of a transistor-like SC device called heater-cryotron (hTron) whose operation is based on the creation and dissipation of the local hotspot in the narrow constriction of its gate and channel. Fig. 2 illustrates the cryogenic memory cell consisting of an SOT-MRAM in parallel with an hTron. The cell has input impedance of <1 Ω and can be triggered by a small current pulse of 100 µA which is affordable by SFQ DC circuits. With this basic cell, we demonstrated the reliable performance of a 4×4 memory array at 4K with WER < 10^{-6}. This is the first step towards faster, denser and more power efficient cryogenic memories for superconducting HPCs and quantum computing applications.

REFERENCES

1) Holmes *et al*., "Energy-Efficient Superconducting Computing—Power Budgets and Requirements", *IEEE. Trans. Applied Superconductivity*, 23, 1701610 (2013)

2) Rowlands *et al.*, "A cryogenic spin-torque memory element with precessional magnetization dynamics", *Scientific Reports*, 9, 803 (2019)

3) Rehm *et al*., "Sub-nanosecond spin-torque switching of perpendicular magnetic tunnel junction nanopillars at cryogenic temperatures", *Appl. Phys. Lett*., 115, 182404 (2019)

4) Rowlands *et al*., "Nanosecond Reversal of Three-Terminal Spin-Hall-Effect Memories Sustained at Cryogenic Temperatures", *Phys. Rev. Applied*, 15, L021004 (2021)

5) Nguyen *et al*., "Cryogenic Memory Architecture Integrating Spin Hall Effect based Magnetic Memory and Superconductive Cryotron Devices", *Scientific Reports,* 10, 248 (2020)
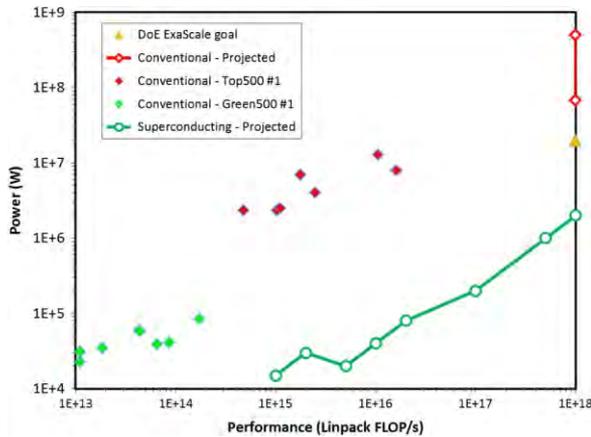
Fig. 1 Power consumption versus performance (LINPACK benchmark) of CMOS-based supercomputers and their projected values at exascale performance. Circles and solid line show the projected power consumption of superconducting computers, including the cooling power, suggesting 2 orders of magnitude lower energy expense than CMOS technology. Courtesy of Ref. [1].
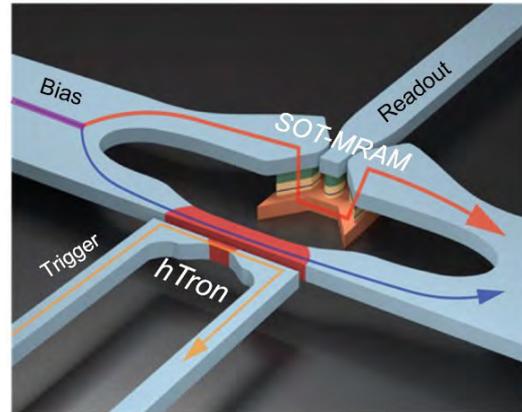
Fig. 2 Illustration of the cryogenic memory cell developed by Nguyen *et al*. [5] The heater-cryotron (hTron) determines the timing and amount of current being diverted from the bias to the SOT-MRAM. Thus, the cell can be triggered by small pulses from a superconducting control circuit. Courtesy of Ref. [5].

USING DOPANTS AND ALLOYING TO OPTIMIZE SPIN HALL MATERIALS FOR MRAM DEVICES

Derek A. STEWART[1], Oliver L. W. MCHUGH[2], Wen Fong GOH[3], and Martin GRADHAND[4,5]

1) Western Digital Technologies, San Jose, USA, derek.stewart@wdc.com

2) University of Bristol, Bristol, United Kingdom, o.mchugh@bristol.ac.uk

3) University of California at Davis, Davis, USA, wfgoh@ucdavis.edu

4) University of Bristol, Bristol, United Kingdom, m.gradhand@bristol.ac.uk

5) Institut für Physik, Johannes-Gutenberg-Universität Mainz, Staudingerweg 7, 55128 Mainz, Germany

I. INTRODUCTION

While commercial spin-transfer-torque MRAM chips are now available, there are still key power and endurance challenges that must be overcome to bring this technology to a broader market. Optimizing materials and interfaces can help in solving these issues. In this talk, we will discuss our recent theoretical work on spin Hall materials for MRAM applications. Using a spin Hall material to flip the spin orientation of a neighboring magnetic layer offers one potential route to low power, high endurance MRAM devices. The spin Hall angle (SHA) is defined as the ratio between the induced transverse spin Hall conductivity due to spin-orbit interactions and the longitudinal electrical conductivity. In this work, we consider two leading spin Hall materials (β-W and Pt alloys) where dopants play a key role. While the metastable β-W (A15) phase of W has one of the largest spin Hall angles measured (~0.3-0.4) [1], the origin of its high spin Hall conductivity (SHC) is still controversial. Since large concentrations (~11%) of dopants (O or N) are required to stabilize β-W, it is unclear if the high SHC is due to intrinsic or extrinsic (skew-scattering) contributions. Platinum possesses a respectable SHA (~0.1) and low resistivity, making it a leading competitor for integration into MRAM applications. Recent studies have shown that alloying can boost the SHA with minimal impact on other device properties. Work is still needed to determine the best binary Pt alloy composition. Using a multi-code approach, we have developed a comprehensive framework to address and optimize all aspects of SHC in complex alloys.

II. SIMULATION APPROACH

Predicting the resistance and spin Hall conductivity as a function of composition can be challenging due to the complex interactions between *extrinsic* (skew scattering from impurities) and *intrinsic* band structure contributions. While several simulation approaches have been developed to address specific SHE mechanisms, very few studies have taken a holistic approach to address all SHC sources. In this study, we used the screened Korringa-Kohn-Rostoker (KKR) method [2] along with the linearized Boltzmann transport equation, Quantum Espresso and PAOFLOW [3] to discover how impurities and alloying (N and O) affect both the intrinsic and extrinsic SHE in α (bcc) and β (A15) phases of W. Alloys are difficult to describe using density functional theory due to the high cost of simulating large supercells. However, the coherent potential approximation (CPA) provides an efficient way to describe the effective alloy structure over the full composition range [4, 5]. With this expanded simulation tool set, we examine different Pt alloys and identify trends in optimal compositions for high spin Hall angles.

III. SPIN HALL CONDUCTIVITY IN β-W

The intrinsic spin Hall conductivity for pristine β-W calculated using both KKR and plane-wave approaches are in good agreement and show a large negative SHC peak for energies near the Fermi energy. The predicted intrinsic SHC is in excellent agreement with experiment. However, when the impact of O or N interstitials on the electronic structure is included, the predicted intrinsic SHC is much lower than the measured values (Fig. 1b). Skew scattering calculations also indicate that extrinsic contributions have a limited effect on the total SHC. To explain these disparate results, we propose that dopants help to

Derek Stewart
E-mail: derek.stewart@wdc.com
tel: +1-408-7175901

stabilize β-W grains during film deposition and afterwards segregate to the grain boundaries [6]. This process results in relatively pristine small β-W grains and grain boundaries with high concentrations of O or N scattering sites. This combination provides high spin Hall conductivity and large electrical resistance, leading to high spin Hall angles. This work demonstrates that engineering grain-boundary properties is an effective way to boost the spin Hall angle.
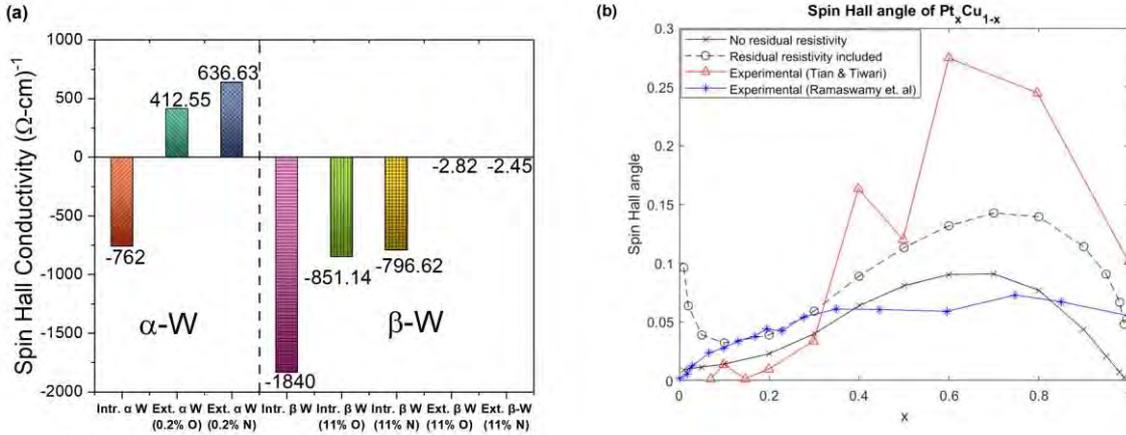

Fig. 1 (a) Predicted intrinsic and extrinsic contributions to SHC of α and β-W. The α-W extrinsic SHC is given for 0.2 at.% O and N doping and predicted electric conductivities match experiment. Intrinsic and extrinsic SHC contributions in β-W for 11 at.% O and N doping are also shown. (b) Spin Hall angle for Pt_xCu_{1-x} using the KKR-CPA approach (with/without residual resistivity) is compared to experiments [7,8].

IV. SPIN HALL CONDUCTIVITY IN PT ALLOYS

The SHA due to alloying was calculated for several binary Pt alloys (see Pt_xCu_{1-x} Fig. 1b). Since the CPA allows for calculations across the whole composition range, the critical concentration where the SHA peaks can be determined. When residual resistivity is accounted for, this has the effect of enhancing and shifting the SHA peak. The Pt_xCu_{1-x} predictions are in reasonable agreement with experiments (Fig 1b).

V. CONCLUSIONS

By combining different *ab-initio* approaches to deliver a holistic view of total SHC, we have provided insight into the key SHC mechanism in β-W and determined the optimal SHC concentration range for Pt alloys. This multi-code approach to disorder shows promise in optimizing SHC in a range of materials.

REFERENCES

1) C. H. Pai et al, "Spin transfer torque devices utilizing the giant spin Hall effect of tungsten", *Appl. Phys. Lett.,* 101 122404, (2012).
2) M. Gradhand et al, "Calculating the Berry curvature of Bloch electrons using the KKR method", *Phys. Rev. B*, 84 075113 (2011)
3) P. D.'Amico et al, "Accurate ab initio tight binding Hamiltonians: Effective tools for electronic transport and optical spectroscopy from first principles", *Phys. Rev. B,* 94 165166 (2016)
4) D. Ködderitzsch et al, "Relativistic formulation of the Korringa-Kohn-Rostoker nonlocal coherent potential approximation", *New J. of Phys.*, 9 81 (2007)
5) P. R. Tulip et al, "Theory of electronic transport in random alloys with short-range order: Korringa-Kohn-Rostoker nonlocal coherent potential approximation", *Phys. Rev. B*, 77 165116 (2008)
6) O. L. W. McHugh, W. F. Goh, M. Gradhand, and D. A. Stewart, "Impact of impurities on the spin Hall conductivity in β-W", *Phys. Rev. Mat.*, 4 094404 (2020)
7) R. Ramaswamy et al., "Extrinsic spin Hall effect in $Cu_{1-x}Pt_x$", *Phys. Rev. Appl.*, 8, 024034 (2017)
8) K. Tian and A. Tiwari, "CuPt alloy thin films for spin thermoelectrics", *Scientific Reports*, 9, 3133 (2019)

DC write head current driven energy assisted magnetic recording

Muhammad Asif Bashir[1], Alexander Goncharov[1], Paul van der Heijden[1], Daniel Bai[1], Suping Song[1], Yaguang Wei[1], Alexander Taratorin[1], Anna Zheng[1], Terence Lam[1], Rick Shi[1] , Lijie Guan[1]

1) Western Digital Corporation, 5601 Great Oaks Parkway, San Jose, CA 95119, USA

I. Introduction

Energy Assisted Magnetic Recording (EAMR) technologies offer a promising future for magnetic hard disk drive based storage devices. The main technologies within EAMR are heat assisted magnetic recording (HAMR) and microwave assisted magnetic recording (MAMR). HAMR utilizes a near field transducer (NFT) based heat source next to the magnetic write pole. Localized heating of the magnetic media reduces the switching field requirement, and a magnetic write pole defines the polarity of the media as 1 and 0 [1]. MAMR technology utilizes a resonance phenomenon. A spin torque based oscillator (STO) embedded between the magnetic write pole and trailing shield provides a magnetic field in the 15-25 GHz frequency range which matches with the media resonance frequency. Once head and media synchronized in frequency, switching field requirement reduces [2]. Both assisted technologies enable an increase in magnetic anisotropy of the media and subsequent grain size reduction while maintaining thermal stability of the media. This offers ADC increase from 1Tbit/inch^2 to 10Tbit/inch^2 on the long run.

We are reporting another phenomena which enables an ADC increase that we discovered while working on MAMR technology. MAMR requires a DC current through the STO. Once we replace the STO embedded in between main pole and trailing side shield with a non-magnetic conducting stack, we are left with a conventional write head for perpendicular magnetic recording (PMR). However, now, we can apply a DC current through magnetic yoke region as the current flows from write pole to trailing side shield and return pole before closing the electrical circuit. The current flow in the magnetic writer generates a local circular magnetic field seen by the magnetic regions of the writer. The effect of this magnetic field is discussed in this paper.

II. Micromagnetic Model

A magnetic write head carrying DC current is studied using micromagnetic simulations. We are using a micromagnetic solver [3] to study dynamic behavior of a magnetic write head used in the current HDD products. The write head geometry is discretized into 8.5 million elements such that we have a fine mesh of 5nm closer to the air bearing surface (ABS) and 40 nm in faraway regions of the main pole volume. We are driving the writer at 2 Gbps. A DC bias current is applied to the writer. Magnetic field generated around the current is show in Figure 1.
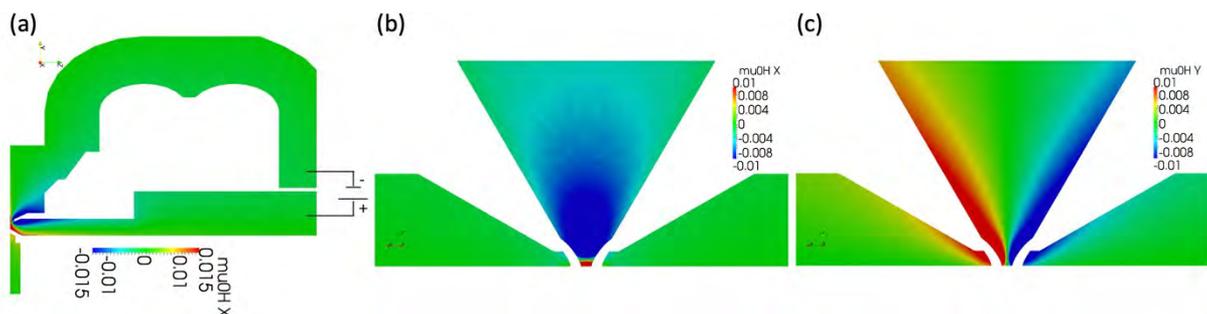
Fig. 1 Micromagnetic model of magnetic writer. Color represents the magnetic field strength in the writer generated by the DC applied current. The circular nature of field generated around bias current is shown in top-down images where Figure 1 (b) shows cross track component and Figure 1 (c) shows down-track component.

III. Results and discussion

The stochastic nature of switching of the magnetic write pole is driven by the nucleation and propagation of magnetic domains inside the write pole once write current polarity changes. The chaotic magnetization switching produces an unpredictable field as seen by the media at every transition and results in lower BPI and ADC. We are proposing a method to tackle this issue by applying a small DC current which generates a magnetic field seen by the writer magnetic volume and ultimately helps us to reduce the stochastic nature of writer switching. Figure 2 (a) shows the magnetization behavior of the main pole tip volume close to the ABS which ideally should flip its magnetization orientation identically each time to write 1 or 0 on the media. The plot show multiple magnetization switching events. A large spread in magnetization switching as a function of time can be seen when no bias current is applied. We can reduce this magnetization jitter by applying a bias current as shown in Figure 2 (b). Figure 2 (c) and (d) present the effective field seen by the media 13nm away from ABS without and with bias.
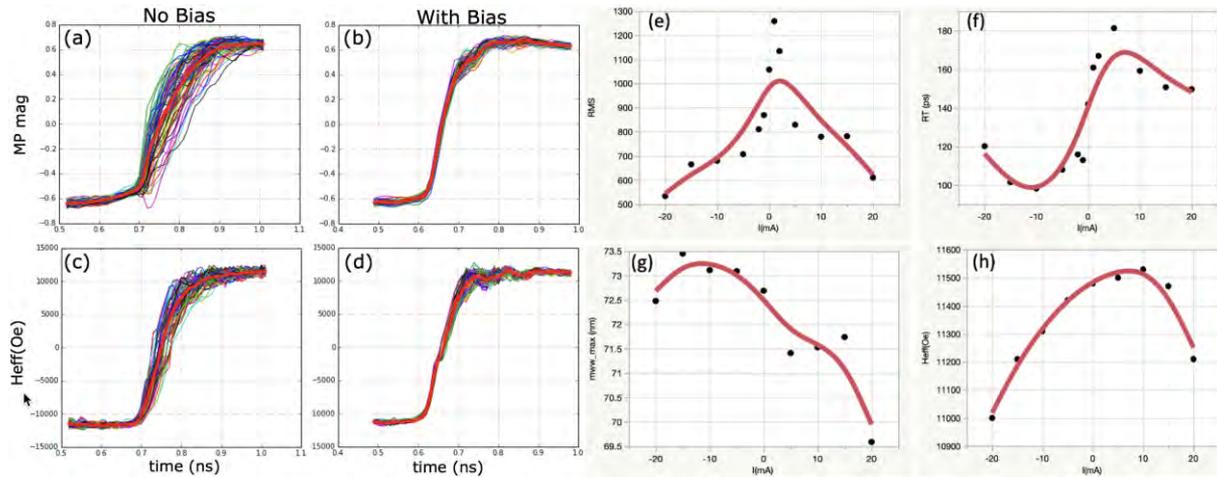
Fig. 2 magnetization behavior without bias (a) and with bias (b) is shown. Effective field seen by the media without bias (c) and with bias ON (d) are shown. Figure (e) has root mean square of effective field noise as a function of bias current strength. Field rise time +/- 80% (f), maximum write width at 8.3KOe (g) and total effective field as a function of bias current are shown in (h).

We can calculate root mean square of the individual to average effective field variations during a complete transition as shown in Figure 2 (e) as a function of bias current strength. It shows a decreasing RMS, write field jitter, with DC bias current. However, as we discussed above, the bias current generates a circular field. Once the bias current is high enough, the cross track field seen by the main pole tip results in a tilt of the main pole magnetization in the cross track direction. This causes a degradation in terms of total field seen by the media as shown in Figure 2 (h). Another phenomena, which we observed with bias current ON is field contours contraction and expansion which results in wider or narrower total magnetic write width as shown in Figure 2 (g). Also, as figure 2 (f) shows, the DC current affects the writer field rise time. We will discuss these effects and present the underlying physics mechanism in our detailed paper.

REFERENCES

1) R. E. Rottmayer, S. Batra, D. Buechel, W. A. Challener, J. Hohlfed, Y. Kubota, L. Li, B. Lu, C. Mihalcea, K. Mountfield, K. Pelhos, C. Peng, T. Rausch, M. A. Seigler, D. Weller, and X. M. Yang, "Heat- assisted magnetic recording", *IEEE Trans. Magn.*, 42(10) 2417–2421, (2006).
2) J. Zhu, X. Zhu, and Y. Tang, "Microwave Assisted Magnetic Recording", *IEEE Trans. Magn.,* 44(1) 125-131, (2008).
3) A. Goncharov "Multi-Level Tensor Grid Acceleration of the Finite Element Micromagnetics.", 12th Joint MMM-Intermag Conference, *CH-03,* 112, (2013).

ROTATED READ HEAD FOR HIGH DENSITY HEAT- ASSISTED SHINGLED MAGNETIC RECORDING

R. H. VICTORA[1] and Wei-Heng HSU[2]

1) University of Minnesota, Minneapolis, MN, USA, victora@umn.edu

2) University of Minnesota, Minneapolis, MN, USA, hsuxx295@umn.edu

I. INTRODUCTION

Recording tracks are written in random order in conventional heat-assisted magnetic recording (HAMR). At high tracks per inch (TPI), two-sided adjacent track erasure (ATE) occurs which can degrade the recording quality [1]. A maximum user density (UD) can be achieved by optimizing the track pitch (TP) before the ATE badly distorts the recorded data [2]. On the other hand, only one-sided ATE occurs in heat-assisted shingled magnetic recording (HSMR) due to the shingled writing nature. Ideally, HSMR yields a higher UD than conventional HAMR at the same TPI. However, two factors limit further improvement in HSMR's UD. First, the remaining track after ATE has significant edge content; the edge's recording quality is worse than that of the track center. Also, the transitions in HSMR are curved and asymmetric relative to the track center [3]. These asymmetrically curved transitions lead to signal loss in readback and limit the recording density. In this study, we show that the UD can be greatly improved by rotating the read head to compensate for asymmetric transitions [4].

II. RESULTS AND DISCUSSION

The read head is rotated to match the transition curvature. Fig. 1 shows the signal-to-noise ratio (SNR), bit error rate (BER), and UD versus the head rotation angle (θ) at various track pitches (TPs) with a 12 nm read head. At small θ, all recording metrics are considerably improved, indicating that the rotated head starts to match the curved transition. If we further rotate the head, the SNR shows a monotonic increase while BER reaches its minimum and UD is at its maximum at a certain θ, which is defined as the optimal θ (θ_{opt}). The θ_{opt} are estimated from the quadratic polynomial fits of the UD curves. It can be seen that a large SNR does not necessarily imply a low BER or high UD. The larger effective shield-to-shield spacing (SSS) resulting from rotation improves the SNR because more low-frequency signals (long-bit) can pass and strengthen the signal, but a larger SSS also leads to a resolution loss in high-frequency signals (short-bit), and thus BER grows and UD drops when θ exceeds θ_{opt}. By comparing the θ_{opt} from the UD curve with the angle based on the head position and the physical shape from the transition, we found that the θ_{opt} of the head generally follows the shape of the transition [Fig. 2(a)]. We found that a wider read head shows a smaller θ_{opt}, because it tends to average out across the transition and thus is less sensitive to the curved transition. By simply rotating the head, the UD demonstrates a significant enhancement compared to conventional (non-rotated) head. It reaches a 5.4 Tb/in^2 maximum from 5.1 Tb/in^2 at TP of 15 nm with a 12 nm head. For a 15 nm head, a 14% improvement can be observed (from 4.4 Tb/in^2 to 5.0 Tb/in^2).

We have considered only the media noise in the discussion so far. However, the head noise should be considered in the readback process, especially the magnetization noise when the magnetoresistive element is small [5]. We consider the head SNR from 17.0 dB to 12.2 dB, where the corresponding head noise power-to-signal power ratio (NSR$_{head}$) is from 2% to 6%. The BER, and the UD versus the NSR$_{head}$ for a 12 nm head at the optimal points are shown in Fig. 2(b). The UD for the rotated head drops from 5.4 to 3.3 Tb/in^2, a 39% reduction when 6% head noise is included.

To further extend the feasibility of the rotated head, we combined it with two-dimensional magnetic recording which is proven to have UD gains. We considered a two-noise-free-reader case, where the final signal is a linear combination of the signals from each head. For the subtractive combination of the signals, we observed a maximum UD of 6.2 Tb/in^2 with a 12 nm read head. This UD is more than 30% greater than a previous projection [2] and more than 50% greater than our prediction for conventional HAMR. It should be noted that the subtractive combination used here only works when the head noise is negligible,

R. H. Victora
E-mail: victora@umn.edu
tel: +1-612-625-1825

otherwise an additive combination is preferred. By combining the rotated read head with TDMR and advanced signal processing techniques, the UD can potentially be extended beyond 6.2 Tb/in^2. This rotated head design is not compatible with HIMR since the transitions are symmetric as found in conventional HAMR, suggesting that HSMR with rotated head may offer higher UD over HIMR with proper optimization. The reduced ATW, and the compatibility with the rotated head make HSMR suitable for very high-density applications.

REFERENCES

[1] N. A. Natekar and R. H. Victora, "Analysis of Adjacent Track Erasure in the HAMR Media," *IEEE Transactions on Magnetics*, vol. 57, no. 3, pp. 1–11, Mar. 2021, doi: 10.1109/TMAG.2020.3038805.

[2] Z. Liu, Y. Jiao, and R. H. Victora, "Composite media for high density heat assisted magnetic recording," *Applied Physics Letters*, vol. 108, no. 23, p. 232402, Jun. 2016, doi: 10.1063/1.4953231.

[3] J.-G. J. Zhu and H. Li, "Correcting Transition Curvature in Heat-Assisted Magnetic Recording," *IEEE Transactions on Magnetics*, vol. 53, no. 2, pp. 1–7, Feb. 2017, doi: 10.1109/TMAG.2016.2614836.

[4] W.-H. Hsu and R. H. Victora, "Rotated read head design for high-density heat-assisted shingled magnetic recording," *Applied Physics Letters*, vol. 118, no. 7, p. 72406, Feb. 2021, doi: 10.1063/5.0044042.

[5] N. Smith and P. Arnett, "White-noise magnetization fluctuations in magnetoresistive heads," *Applied Physics Letters*, vol. 78, no. 10, pp. 1448–1450, Mar. 2001, doi: 10.1063/1.1352694.
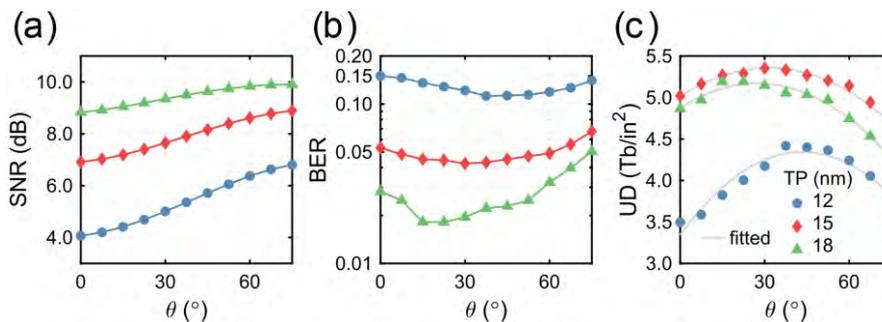
Fig. 1 (a) SNR, (b) BER, and (c) UD in HSMR as a function of θ at varied TPs with a 12 nm read head.
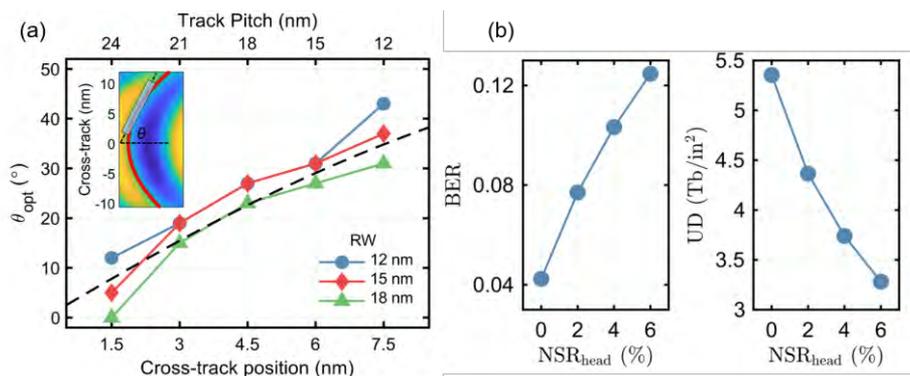
Fig. 2 (a) θ_{opt} versus head position in the cross-track direction with varied reader widths (RWs). The top axis is the corresponding track pitch. The dashed line is the θ derived from the shape of the transition. The inset shows the transition and the fitted line. (b) BER and UD as a function of NSR$_{head}$ at TP = 15 nm for a 12 nm reader.

MICROMAGNETIC STUDIES OF SPIN TORQUE OSCILLATOR READER PHASE NOISE AND SNR

O. HEINONEN[1], V. SAPOZHNIKOV[2], P. KRIVOSIK[3], and M. CONOVER[4]

1) Argonne National Laboratory, Lemont, IL, USA, heinonen@anl.gov

2) Seagate Technology, Bloomington, MN, USA, victor.b.sapozhnikov@seagate.com

3) Seagate Technology, Bloomington, MN, USA, pavol.krivosik@seagate.com

4) Seagate Technology, Bloomington, MN, USA, Michael.j.conover@seagate.com

I.   SPIN TRANSFER TORQUE AND SPIN TORQUE OSCILLATORS

In 1996, Berger and Slonczewski [1,2] predicted that a spin-polarized current incident on a ferromagnetic thin film can exert a torque on the magnetization in the film. The basic physics is that the spin-polarized electrons carry a current of angular momentum, and as the electrons enter the ferromagnetic thin film, they align their magnetic moment with that of the ferromagnet, which exerts a torque on the ferromagnet. The physical realization of this spin transfer torque (STT) is exploited in spin torque random access memories [3], in which current pulses flips the magnetic storage layer in one memory element without causing long-range magnetic stray fields that disturb adjacent memory elements.

In thin film elements, one magnetic layer is usually fixed and acts as a polarizer for the electron current. The torque exerted on the other layer, here called the free layer, is perpendicular to the direction of the magnetization of the polarizer and of the free layer. This can be exploited to engineer the system so that the STT is either parallel or anti-parallel to the intrinsic damping torque. In the former case the STT enhances the damping. In the latter, the STT pumps energy into the free layer magnetization. If the STT is large, that can make the free layer magnetization align with that of the polarizer, but if the energy pumped into the system matches that dissipated by intrinsic damping, the free layer magnetization will oscillate with a very narrow linewidth – this is a spin torque oscillator (STO), which typically has a frequency in the range of a few to some tens of GHz. STOs can be made quite small with diameters down to some tens of nanometers and can readily be integrated with Si-MOS technology. This makes them attractive in applications such as telecommunications.

II. SPIN TORQUE OSCILLATORS AS READERS IN MAGNETIC RECORDING

As hard disk drive (HDD) areal densities increase to 2Tb/in^2 and beyond, it becomes challenging to maintain reader SNR with smaller sensor dimensions. STO readers have been proposed as an alternative to magnetoresistive (MR) sensors [4,5]. Because the STO frequency is modulated by external fields, STO readers respond to media magnetization with frequency rather than amplitude changes. This can potentially offer SNR scaling advantages due to their noise dependence on oscillation phase noise rather than sensor resistance. To study this, we have used micromagnetic STO reader simulations to explore basic STO reader designs as well as noise scaling with temperature. One design challenge is that STT is not imparted only on the free layer – there is also reaction torque (Newton's 3rd law) on the polarizer layer in a standard synthetic antiferromagnetic structure. This makes the reader very noisy, and the reader design has to include means to effectively stiffen the polarizer. Another challenge is that with reduced reader dimensions, the free layer magnetic volume shrinks. As a consequence, thermal noise at normal operating temperature can severely degrade the sensor SNR.

We will here discuss simulation results using finite-temperature micromagnetic simulations that account for dynamics in the synthetic antiferromagnet as well as dynamically adjusted local current density and STT, and strategies for mitigating thermal noise at small reader dimentions. We will also use simulated waveforms to estimate phase noise and SNR for STO reader sensor models. By exploring phase noise scaling with temperature, we estimate reader SNR for ~10 nm STO readers and assess their potential use for high areal density recording.

O. HEINONEN

E-mail: heinonen@anl.gov

tel: +1-630-2524877

REFERENCES

1) L. Berger, "Emission of spin waves by a magnetic multilayer traversed by a current", *Phys. Rev. B* **54**, 9353 (1996)

2) J. C. Slonczewski, "Current-driven excitation of magnetic multilayers", *J. Mag. Mag. Mat.* **159**, L1 (1996).

3) S. Bhatti et al., "Spintronics-based random access memory: a review", *Materials Today*, **20**, 530 (2017).

4) P. M. Braganca, B. A. Gurney, B. A. Wilson, J. A. Katine, S. Maat and J. R. Childress, "Nanoscale magnetic field detection using a spin-torque oscillator," *Nanotechnology*, **21,** 235202, (2010).

5) R. Sato, K. Kudo, T. Nagasawa, H. Suto, and K. Mizushima, "Simulation and experiments toward high-data-transfer-rate readers composed of spin-torque oscillator," *IEEE Trans. Mag.*, **48**, 1758, (2012).

TDMR Performance Gain with Machine Learning Data Detection Channel

Yuwei Qin[1], Pradhan Bellam[2], Rick Galbraith[2], Weldon Hanson[2], Niranjay Ravindran[2], Iouri Oboukhov[2], and Jian-Gang (Jimmy) Zhu[1]

1) Data Storage Center, Carnegie Mellon University, Pittsburgh, PA, 15213

2) Western Digital, 2900 37th Street NW, Rochester, MN, 55901

I. INTRODUCTION

Data recovery with cross-track displaced multiple readers (MR), usually referred to as TDMR, is designed to mitigate the performance degradation impact due to transition curvature, PMR track edge effects and inter-track interference [1]. However, relatively large skew angle variation across disk surface from ID to OD makes physical model based two-dimensional channel equalization very challenging [2]. We have developed a machine-learning (ML) based data detection channel utilizing convolutional neural networks (CNN) for hard disk drives and have expanded it for data recovery with multiple readers [3, 4]. Using sampled waveform directly captured from an actual commercial drive, we have conducted a bit error rate (BER)-based performance comparison between the ML/MR channel and a conventional channel with multiple readers. The study shows that the ML/MR channel can enable significant multi-reader gain.

II. HDD SIGNAL CAPTURES AND CNN DETECTOR

The two-reader setup and the ML-data detector are shown in Fig. 1. Three tracks are written with random data. The center track, which will be referred to as the target track, is written first, then followed by the two side tracks to include the squeezing effects from both sides. Two cross-track and down-track displaced readers are used. The two readers are separated by ~30% track pitch in the cross-track direction. Reader-1 is placed near the target track edge and Reader-2 is at the target track center. The read-back waveforms are digitized by 6-bit ADC as shown in the bottom of Fig. 1.

A convolutional neural network (CNN) is employed as the ML detector. The CNN-detector has 6 hidden layers, each has kernel size (or equivalently the filter tap) of 5 (please note only 2 hidden layers are shown for simplicity of drawing). To accommodate the two-reader setting, CNN is designed with two input channels (or vertical columns of neurons), each channel receiving sampled signals from one reader only. The number of neurons per input channel is 25. The number of filters at each hidden layer is 10, and in total the network has 2700 learnable parameters. Rectified linear unit (ReLU) is used as the non-linear activation function. Supervised learning with stochastic gradient descent algorithm is employed to train the network, and cross-entropy is used as the loss function. The CNN detector is trained to detect the target track data only.

Performance of both the CNN-detector and conventional channel are evaluated at different linear densities for which data rate is changed by writing bits of different physical sizes while maintaining the same disk spinning speed. Consequently, the higher the data rate, the more significant the transition jitter noise is in the signals. At each data rate, 540 4k-Byte sectors are prepared. The first 400 sectors are used to train the network, while the remaining 140 sectors are used to evaluate CNN's detection accuracy. We would like to point out that despite the large training data number, the actual training time only takes a fraction of a second given gigabits/sec hard drive data rates.

III. RESULTS AND DISCUSSION

Fig. 2 plots the detection bit-error rate (BER) as a function of data rate for different detectors using one vs. two readers. The orange/triangle and green/diamond curves represent the single reader detections with CNN. Since there is only reader used in both cases, the networks used only have one input channel, and the rest of the network structure remains the same. The red/circle curve comes from CNN receiving both readers signals, while the black/square curve is from the modeling reference provided by our collaborators at WDC.

With two readers, ML can produce comparable, or even slightly better detection performance to the conventional channel. In addition, the performance gain from ML increases at high data rates. Part of the gain is attributed to the ability of the CNN-detector in dealing with color medium noise such as transition jitter [4].

Now let us look at TDMR gain enabled by ML. Because Reader-2 is closer to the track edge, it produces lower single reader detection accuracy. However, ML can still take advantage of Reader-2 and achieve ~6%

Yuwei Qin

E-mail: yuweiq@andrew.cmu.edu

Tel: (+1) 412-377-0608

linear density gain versus using Reader-1 alone (green/diamond curve). This result shows that under proper training, CNN is able to discover and correlate useful information "hidden" in the raw signals towards more accurate detections, and this can be automatically done through training without any physical modeling.

In the next experiment, we read the same data tracks but under three different reader cross-track positions as Fig. 3 (left) shows. Three reader positions are (1) shifted towards OD, (2) remains at center position, (3) shifted towards ID. Fig. 3 (right) plots the TDMR detection BER from all three head positions at data rate=3330MHz. The black/square curve is from the WDC modeling reference, which is optimized separately for each head position. The blue/diamond curve comes from three CNN detectors: each network is only trained and evaluated at one head position. We obtained the red/circle curve in this way: first we collected signals from all three head positions to form a new dataset. Then we trained one neural network with this aggregated dataset and evaluate the trained CNN at each head position separately.

The blue/diamond curve represents the optimized CNN detection performance at each head position. For the red/circle case, despite only one network is used, CNN can learn and optimize at all three head positions. This observation shows that CNN has the ability to learn very complicated correlations using one set of parameters.

REFERENCES

[1] Wood R, Williams M, Kavcic A, et al. The feasibility of magnetic recording at 10 terabits per square inch on conventional media. IEEE Transactions on Magnetics, 2009, 45(2): 917-923.

[2] Alexander J, Ngo T, Dahandeh S. Exploring two-dimensional magnetic recording gain constraints. IEEE Transactions on Magnetics, 2016, 53(2): 1-4.

[3] Qin Y, Zhu J G. Automatically Resolving Inter-Track Interference with Convolution Neural Network Detection Channel in TDMR. IEEE Transactions on Magnetics, 2020.

[4] Qin Y, Zhu J G. Deep neural network: Data detection channel for hard disk drives by learning. IEEE Transactions on Magnetics, 2020, 56(2): 1-8.
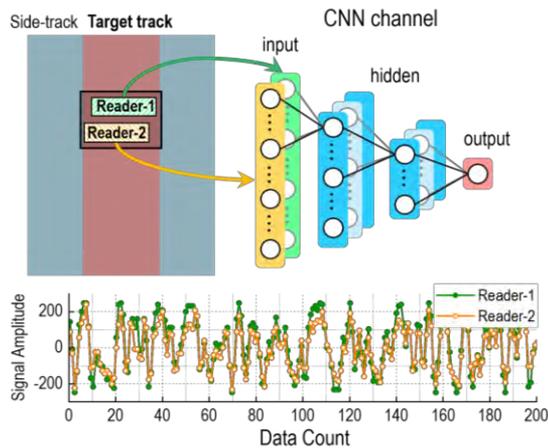
Figure 1. Real HDD signals with two readers. The CNN detector takes both reader signals as input and is trained to detect target track. A short sequence of sampled signals from both readers in the bottom.
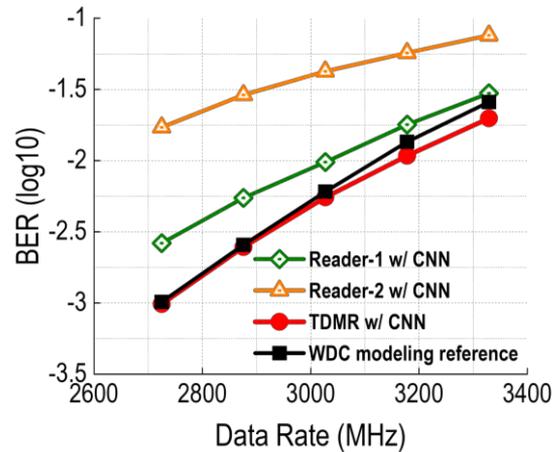
Figure 2. BER vs. data rate. Square: WDC modeling reference with TDMR; Circle: CNN detector with TDMR; Triangle: CNN with Reader-1 only; Diamond: CNN with Reader-2 only.
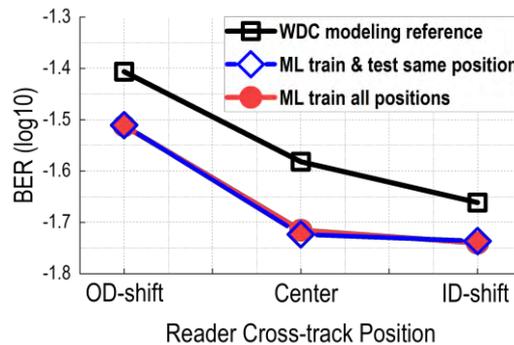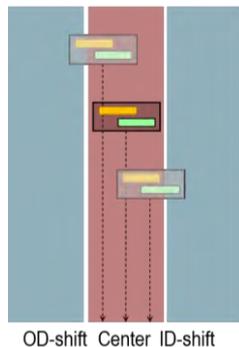
Figure 3. Left: reader position shifts. Right: BER vs. reader position. Square: WDC modeling reference. The channel is optimized at each position; Diamond: CNN optimized at each position; Circle: one CNN trained on all positions.

Asynchronous Partial-Response Equalization to Time-Varying Target for Multitrack Detection of Asynchronous Tracks

Elnaz Banan Sadeghian

Stevens Institute of Technology, Hoboken, USA, ebsadegh@stevens.edu

I. INTRODUCTION

Multitrack detection improves the areal density and throughput in magnetic recording systems. Almost all multitrack detection algorithms assume that the tracks being detected are written synchronously to one another [1],[2]. In practice, however, variations in disk rotational speeds can lead to slightly different bit rates from one track to the next. In conventional single-track detection, synchronization can precede detection without any interaction. In multitrack detection, however, it is impossible to simultaneously synchronize the readback waveforms to more than one track, the fact that prevents the read channel from separating the synchronization and detection functions. For this reason, in a previous work, we proposed the ROTAR algorithm that combines the functions of synchronization and detections into a joint Viterbi algorithm that works on a time-varying target [3]. In this work we complete the read channel by proposing a partial-response equalization scheme, namely an *asynchronous partial-response* equalization to *time-varying* target (APR-TV), that equalizes the unsynchronized ADC outputs to a time-varying target which absorbs the timing asynchrony of the tracks being detected. The proposed equalizer outputs are then fed to the ROTAR detector to help achieve efficient multitrack detection. In essence, the new read channel extends the partial-response maximum-likelihood (PRML) paradigm to the *joint detection* of multiple *asynchronous* tracks. In jointly detecting K tracks from N waveforms, the resulted Viterbi branch metric for the transition from state p to state q at time k is $\gamma_k(p,q) = \|\mathbf{y}_k - \mathbf{o}_k(p,q)\|^2$ where $\mathbf{y}_k$ is the noisy version of the vector collecting the N noiseless equalized outputs at time k given by

$$\mathbf{o}_k(p,q) = \sum_{j=1}^{K}\sum_{\ell=-M_j/2}^{\mu+M_j/2} a_{k-\ell-\nu_k^{(j)}}^{(j)}(p,q)\,\mathbf{h}_j(\ell t - \theta_k^{(j)}), \tag{1}$$

where $\{a_k^{(j)}(p,q)\}$ are the bits of track $j \in \{1, \ldots, K\}$ on the survivor path arriving at the transition from state p at time k to state q at time $k+1$, $\mathbf{h}_j(t) = \left[h_{1,j}(t), h_{2,j}(t), \ldots, h_{N,j}(t)\right]^T$ is the vector-valued time-varying target response (across all N equalized outputs) for track j, $\nu_k^{(j)}$ and $\theta_k^{(j)}$ respectively are the integer and fractional parts of the timing offset of each track j, and where $\mu + M_j$ is the memory of the time-varying target responses for each track j.

II. ASYNCHRONOUS PARTIAL-RESPONSE EQUALIZATION TO TIME-VARYING TARGET

Before equation (1) can be implemented with ROTAR [3], a practically long (possibly time-varying) and unknown channel response should be transformed into a short and known target response. We propose to attain the ideal target responses $\{\mathbf{h}_j(t)\}$ of equation (1) through the APR-TV strategy. Fig. 1 illustrates this strategy where unsynchronized ADC outputs are directly fed into a fixed multiple-input multiple-output (MIMO) equalizer. In effect, we propose to absorb the asynchrony of the ADC outputs into the original bits by applying an appropriate *fractional delay* on the bits of each track in the lower branch (through SYNCH 1, …, SYNCH K blocks) and during the training phase when the user bits are known. The cascade of the time-varying fractional delays with the fixed target forms the desired time-varying target that the ROTAR algorithm is waiting for. We jointly optimize for the equalizer filters, the target responses, and the unknown timing offsets $\{\tau_k^{(j)}\}$, using the recursive least squares (RLS) algorithm combined with a second-order PLL for estimating the unknown timing offsets.

III. SIMULATION RESULTS

We present the performance results of the proposed read channel consisting of the APR-TV equalizer

Elnaz Banan Sadeghian
E-mail: ebsadegh@stevens.edu
Tel: +1-201-2165549

followed by the ROTAR detector on a dataset provided by data storage institute [4]. There are two sets of waveforms provided: in the first set, a write frequency offset of $\tau_k^{(2)} = 2 \times 10^{-4}k$ is injected only to the bits of TRACK 2 while the rest of the tracks have the same bit positions, and the second dataset is generated without any timing offsets. Fig. 3 plots the BER performance of four different detectors for detection of TRACKS 1 and 2. The black curve marked as "OFFSET, APR-TV+ROTAR" is the performance of the proposed read channel, while the blue curve marked as "OFFSET, 2 MISO+2 VITERBI" shows the performance of a conventional 1-D detector that separately detects the two tracks, on the asynchronous dataset. The proposed detector achieves at least a 30% decrease in BER over the conventional 1-D detector. Further, the dashed green curve marked as "NO OFFSET, 2 MISO+2 VITERBI" and the dashed red curve marked with "NO OFFSET, MIMO+JOINT VITERBI", respectively, show the performance of the same conventional 1-D detector and another standard joint detector consisting of a MIMO equalizer followed by a joint Viterbi detector, applied on the synchronous dataset. The proposed detector on the asynchronous dataset performs very close to the standard joint detector on the synchronous dataset.

REFERENCES

1) E. Soljanin and C. N. Georghiades, "Multihead detection for multitrack recording channels," *IEEE Transactions on Information Theory*, vol. 44, no. 7, pp. 2988–2997, Nov. 1998.
2) B. Fan, H. K. Thapar, and P. H. Siegel, "Multihead multitrack detection for next generation magnetic recording, part I: Weighted sum subtract joint detection with ITI estimation," *IEEE Transactions on Communications*, vol. 65, no. 4, pp. 1635–1648, Apr. 2017.
3) E. Banan Sadeghian and J. R. Barry, "The Rotating-Target Algorithm for Jointly Detecting Asynchronous Tracks," *IEEE Journal on Selected Areas in Communications*, vol. 34, no. 9, pp.2463-2469, Sep. 2016.
4) K. S. Chan *et al.*, "Channel models and detectors for two-dimensional magnetic recording," *IEEE Transactions on Magnetics*, vol. 46, no. 3, pp. 804–811, Mar. 2010.
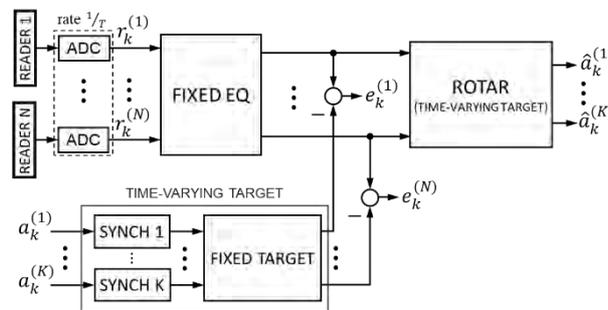
Fig. 1 Asynchronous partial-response equalization to a time-varying target strategy for jointly detecting K tracks from N readback waveforms.
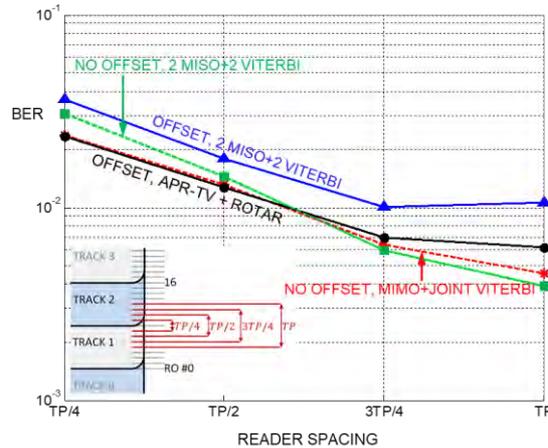
Fig. 3 BER performance of the proposed read channel versus three different detectors.

MITIGATING THE WRITE STOCHASTICITY IN STTMRAMS: SUPPRESSING BACK HOPPING AND MAKING THE WALL MOTION REPRODUCIBLE

Thibaut DEVOLDER[1], Paul BOUQUIN[1], Olivier BULTYNCK[2], Joo-Von KIM[1], Siddharth RAO[2], Gouri S. KAR[2], Sébastien COUET[2].

1) Université Paris-Saclay, CNRS, Centre de Nanosciences et de Nanotechnologies, Palaiseau 91120, France, thibaut.devolder@u-psud.fr

2) IMEC, Kapeldreef 75, Leuven B-3001, Belgium, sebastien.couet@imec.be

I. INTRODUCTION

Magnetization reversal in nanomagnets is often stochastic. This is problematic in information storage, since deterministic switching is sought. We report time-resolved measurements of nanosecond scale switching events in STTMRAM cells. We focus on two major sources of the switching stochasticity: first the "back-hopping" (BH) phenomenon, that is detected as a unexpected bouncing back of the magnetization to its original state after switching ([1] and §II). We then focus on another source of stochasticity, which involves the precessional motion of the domain wall through the cell [2 and §II].

II. WRITE STOCHASTICITY LINKED TO BACK-HOPPING

BH is a counterintuitive phenomenon. We generally expect that the switching probability should always increase with the applied voltage. However the contrary can sometimes occur: in many instances, the MTJ resistance can back-hop to its original state after the apparent successful switching of the FL magnetization, as in the STT loop in Fig. 1 at positive bias. We have analyzed the BH phenomenon in STT induced switching of perpendicularly magnetized tunnel junctions. The back-hopping (Fig. 1) proceeds by two sequential switching events that lead to a final state P' of conductance close to --but distinct from-- that of the conventional parallel state. The P' state does not exist at remanence. It generally relaxes to the conventional antiparallel state if the current is removed. The P' state involves a switching of the sole spin-polarizing part of the fixed layers, i.e. the barrier-facing part of the fixed layers. The analysis of our several material variants indicates that back-hopping occurs only when the spin-polarizing layer is too weakly coupled to the rest of the fixed system. This provides mitigation strategies of back-hopping for next generation STTMRAMs [1].
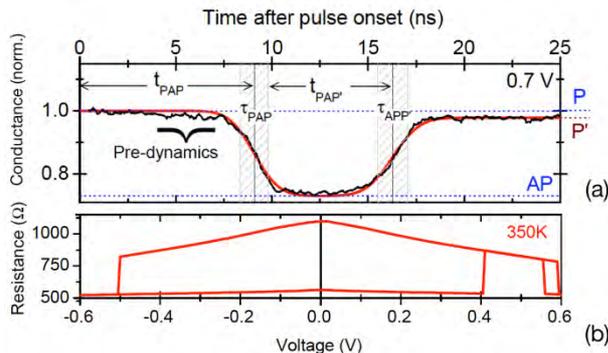
Fig. 1: (a) Representative single shot response with 3 GHz bandwidth with the definition of the P to AP and AP to P' switching times and their transition times. (b) Typical STT loop at high voltage bias and elevated temperatures.

III. WRITE STOCHASTICITY LINKED TO DOMAIN WALL DYNAMICS

We then focus on another source of stochasticity, which involves the precessional motion of the domain wall (DW) through STTMRAM cells. Experiments reveal the oscillatory nature of the conductivity during switching. This arises from the precessional Walker regime of DW propagation with back-and-forth oscillations of the wall. In disc of diameters 70-100 nm, the experiments identify several switching paths that occur stochastically and lead to distinct switching durations (Fig. 2). Micromagnetics incicates that for

Thibaut DEVOLDER
E-mail: thibaut.devolder@u-psud.fr
tel: +33-1 70 27 04 81

discs with 40 nm of diameter, the wall sweeps through the disc in an almost monotonous manner regardless of the initial wall position and of its initial Bloch or Néel character. Conversely at 80-nm diameter, the wall still drifts across the disc but with pronounced superimposed oscillations. The wall can cross the disc center either in a direct manner or with variably marked oscillations before and after the crossing.

To understand the stochasticity of the wall dynamics, we introduce the concept of the retention pond: a region in the configurational space in which centrally-placed walls of tilt close enough to the Néel wall configuration are transiently bound to the disc center. Walls having trajectories approaching close to the pond must circumvent it and therefore suffer longer propagation times. The pond disappears for a specific disc diameter for which wall shall sweep through the disc in a ballistic manner irrespective of the tilt dynamics, which happens for a diameter of ~40 nm. The propagation time is then robust against fluctuations, which is of interest for STTMRAM where reproducible dynamics is desirable.

REFERENCES

1) T. Devolder et al., "Back hopping in spin transfer torque switching of perpendicularly magnetized tunnel junctions", *Phys. Rev. B* 102, 184406 (2020).
2) P. Bouquin et al., "Stochastic Processes in Magnetization Reversal Involving Domain-Wall Motion in Magnetic Memory Elements", *Phys Rev. Applied*, 15, 024037 (2021).
3) P. Bouquin et al., "Spin-torque induced wall motion in perpendicularly magnetized disc", *Phys Rev. B*, 103, 224431 (2021).
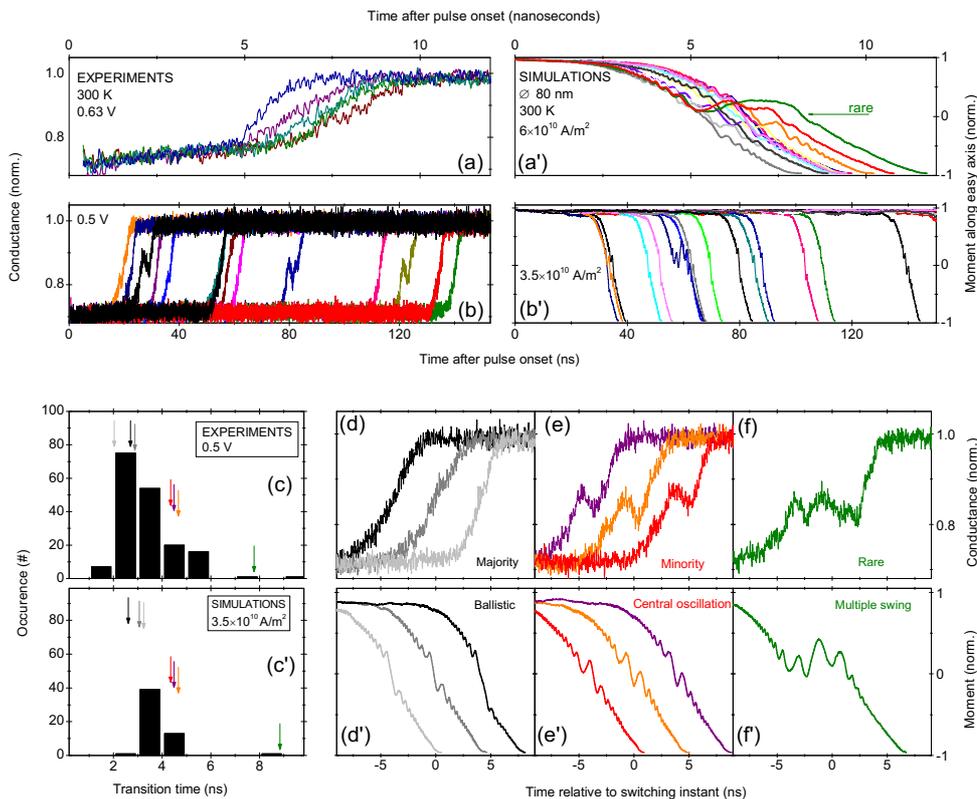
Fig. 2: Experimental and simulated (labeled with primes) signatures of STT-induced switching events. (a) and (a'): for large stimuli. (b) and (b') for lower stimuli near the quasi-static switching threshold. Note the dispersion in incubation delays. (c): statistical repartition of the transition times and (d-f): corresponding representative switching curves as measured (top panels) and as simulated using micromagnetics at 300 K (bottom panels, labelled with primes).

DEMONSTRATION OF NANOSECOND OPERATION IN STOCHASTIC MAGNETIC TUNNEL JUNCTIONS

Christopher Safranski[1], Jan Kaiser[21], Philip Trouiloud[1], Guohan Hu[1], and Jonathan Z. Sun[1]

1) IBM T. J. Watson Research Center, Yorktown Heights, New York 10598, United States

2) School of Electrical and Computer Engineering, Purdue University, Indiana 4790, United States

I. INTRODUCTION

Magnetic tunnel junctions have been a promising candidate for non-volatile memory technologies and have been shown to be compatible with existing CMOS fabrication. In these structures, information is stored in the orientation of a magnetic free layer (FL) that has two stable orientations relative to a reference layer (RL) schematically represented in Fig. 1a. While the development of MTJs has been driven by memory applications, there has been recent interest in their use as a processing bit for probabilistic computing and in the generation of random number bit streams. For this application, MTJ are designed to operate in the superparamagnetic regime, where the energy barrier between states is low enough to where thermal fluctuations allow the bit to stochastically fluctuate between states.

One experimental realization [1] uses MTJs with weak perpendicular anisotropy to perform factorization. These MTJ have a fluctuation timescale on the order milliseconds. In order to increase computational speed, the fluctuation speed of the MTJ need to be increased. The fluctuation timescale is approximately proportional to $1/\alpha\gamma H_k$. For perpendicular MTJ, to make a weak barrier Hk needs to be reduced, which in turn lowers the fluctuation speed. It has been theorized [2] that the fluctuation speed can be increased by switching to in-plane MTJ. In this case, a low energy barrier can be achieved by patterning the MTJ into a circular pattern with the fluctuation speed determined by the demagnetization field. We demonstrate experimentally [3] that the fabrication of such device can achieve nanosecond timescale fluctuations. Further, we investigate the stochasticity of the signal produced in the context of random number generation.

II. EXPERIMANTAL DETAILS

We fabricate in-plane MTJ based on CoFeB/MgO/CoFeB material stacks patterned into circular pillars. The stray field from the RL causes the MTJ to remain in the parallel state with no applied field or current. The application of DC bias can cancel this field through spin transfer torque effect, allowing for control of the fluctuations. In order to observe the MTJ state, an oscilloscope is used to capture real time traces of the junction voltage when a DC bias is applied shown in Fig. 1a.

III. RESULTS

The MTJ signal as a function of time is shown in Fig. 1a. In order to determine the stochasticity of the signal, we compute the autocorrelation of the accumulated time trace. We define the width of the autocorrelation $\Delta\tau_{ac}$ based on the integration of the autocorrelation function shown in Fig. 1b. Measurements performed with different applied bias show in Fig. 1c that the autocorrelation time of the signal is bias dependent and has a correlation time in the nanosecond timescale. To further show the stochasticity, we plot the measured time trace against the same trace delayed by 5 ns. If the MTJ was state was uncorrelated after 5 ns, this plot would be expected to consist of points covering the complete set of possible states for the junction as shown in Fig. 1d.

In order to verify the timescale recorded, we perform a numerical simulation to show such timescales are indeed possible. We model the MTJ using the Landau-Lifshitz-Gilbert equation. We include realistic

Chris Safranski
Christopher.Safranski@ibm.com
tel: +1-914-9453000

material parameters and terms representing interlayer exchange, dipole fields, and thermal fluctuations. Our numerical model qualitatively reproduces the experimental results. Further, this model predicts that the fluctuation timescale is in the nanosecond range. A similar plot of the time trace vs delayed time trace shown in Fig. 1e matches the experimental observation. We conclude from these results, that the experimental timescale on the order of nanoseconds is valid.

REFERENCES

1) Borders, W. A. *et al.* Integer factorization using stochastic magnetic tunnel junctions. *Nature* **573**, 390–393 (2019).
2) Kaiser, J. *et al.* Subnanosecond Fluctuations in Low-Barrier Nanomagnets. *Phys. Rev. Appl.* **12**, 1 (2019).
3) Safranski, C. *et al.* Demonstration of Nanosecond Operation in Stochastic Magnetic Tunnel Junctions. *Nano Lett.* **21**, 2040–2045 (2021).
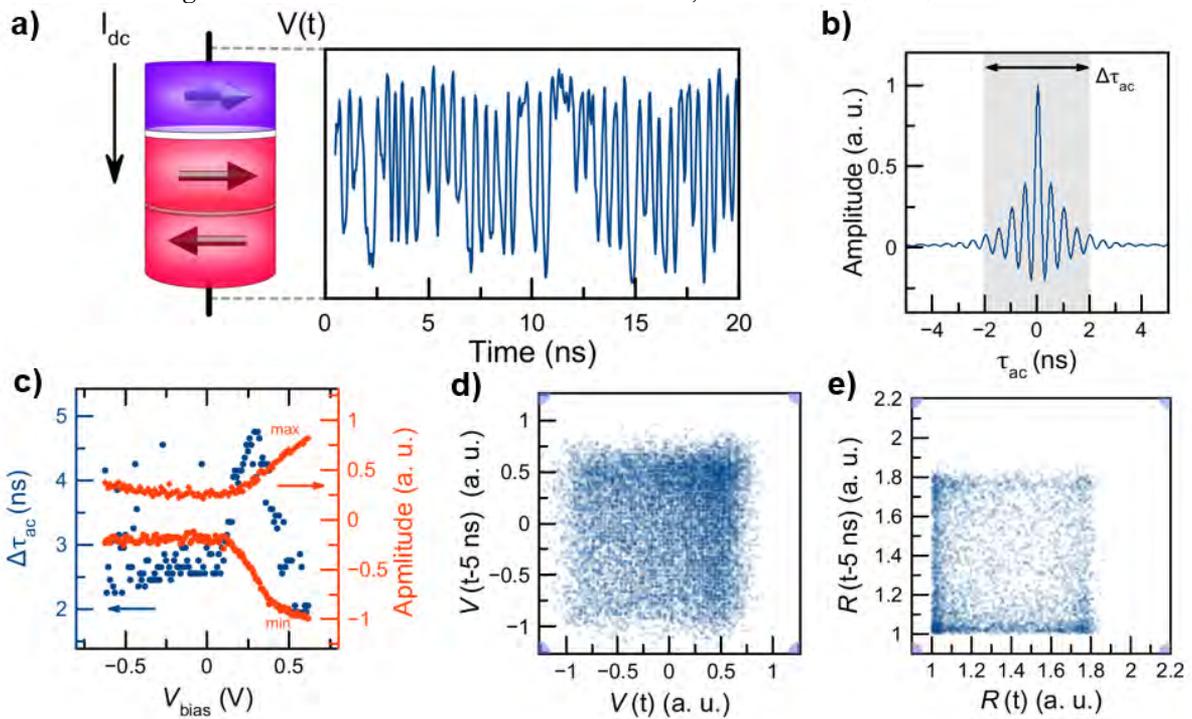
Fig. 1: a) Schematic of MTJ and example time trace of the MTJ fluctuations. b) Example autocorrelation of the MTJ time trace. c) Time trace amplitude and autocorrelation as a function of DC bias. d) Measured MTJ signal plotted against the delayed signal and e) simulated delay plot.

SINGLE-EVENT EFFECTS IN STT MRAM

Douglas Martin[1], K. Deniz Bozdag[2], Mark Savage[3] and John Steele[4]

1), 3) & 4) Naval Surface Warfare Center, Crane, Indiana, USA douglas.martin@navy.mil,
mark.w.savage@navy.mil and john.a.steele@navy.mil

2) Spin Memory, Fremont, California, USA, deniz.bozdag@spinmemory.com

I. INTRODUCTION

STT MRAM's greater memory density and inherent radiation tolerance has made it an attractive non-volatile memory option to the space and radiation effects community. This presentation will discuss two Single-Event Effects (SEE) in STT MRAM. The two Single-Event Effects have a high Linear Energy Threshold (LET > 53 MeV-cm^2/mg) and hence a low error rate probability in space. The two effects are bit-flips and a negative bit resistance shift caused by soft dielectric breakdown [1]. Due to the observation of Single Event Functional Interrupts (SEFIs) for another STT MRAM manufacturer, a simplified method of device irradiation while the device remains unbiased in ESD foam allows decoupling of the Back End of Line (BEOL) transistor circuits from the Front End of Line (FEOL) memory elements. This method allowed recognition of the SEE as a p-MTJ effect. Simulation of SEFIs [2] using a laser to accomplish designer feedback to the manufacturer will be briefly discussed.

II. TEST METHOD

Spin Memory's Gilbert 4 Mb STT-MRAM Array was utilized for characterizing SEE. These devices did not contain Spin Memory's higher retention Precessional Spin Current (PSC) structure within the p-MTJ stack [3]. To decouple STT MRAM effects from underlying CMOS effects, devices were irradiated by placing them in ESD foam with no bias applied. Ten devices were irradiated (two devices per LET). A 3×10^8 ions/cm^2 fluence was used for one device at the lowest LET (53.7 MeV-cm^2/mg) and one device at the highest LET (87.2 MeV-cm^2/mg), otherwise the other 8 devices used a 1×10^8 ions/cm^2 fluence. Bit Resistance (BR) data was used for evaluating Single-Event Effects. The criteria for an event was determined by:

$$\text{Single-Event} \rightarrow [(\text{Post\_BR} - \text{Pre\_BR})/\text{Pre\_BR}] > +/-10\% \qquad (1)$$

III. SINGLE-EVENT EFFECTS

A brief discussion of SEE and how memories are assessed for space applications [4] will be shown in Fig. 1. The analyzed data for one of the two devices which were exposed at an LET of 79.1 MeV-cm^2/mg is shown in Fig. 2. Bit-flips can clearly be observed along with which cluster represents a 0 $\rightarrow$ 1 or a 1 $\rightarrow$ 0 bit-flip. Negative shifted bit resistance due to a soft dielectric breakdown [5] will also be pointed out in Fig. 2. Fig. 3 shows the $\sigma(\text{cm}^2)$ versus LET data for total bit-flips. Since bit-flip SEE is the primary contributor to the overall events observed, the error rate probability was calculated as 6.47E-19 SEE per bit day, or 2.71E-12 SEE per day. The Fig. 3 data was fit to a Weibull curve and input into Creme96 software with a geosynchronous equatorial orbit (GEO), shielding of 100 mils of aluminum with quiet geomagnetic conditions, and at a solar minimum (cosmic ray maximum). It has been reported [6] that the bit-flip is due to a magnetization reversal of ferromagnetic layers induced by a local temperature increase caused by a single strike of heavy ions. However, it has not thoroughly been explained [6]. Fig. 4 shows that the 0 $\rightarrow$ 1 bit-flips are greater than the 1 $\rightarrow$ 0 bit-flips by almost an order of order of magnitude. The negative bit resistance shifted plot is shown in Fig. 5; the plot suggests multiple strikes to cause this shift and may be consistent with percolation chain formation. STT-MRAM manufacturers that hope to use their product in space may encounter SEFIs, which are a latch-up like condition in the FEOL transistor circuits.

Douglas Martin
E-mail: douglas.martin@navy.mil
tel: +1-812-8541526

Laser Assisted Device Alterations (LADA) has been demonstrated as a way to simulate SEFIs and determine the faulty circuit using backside images [2, 7]. These images may serve as feedback to the designer to rectify this condition. An example of LADA is shown in Fig. 6.

IV. REFERENCES

1) R. R. Katti, J. Lintz, L. Sundstrom, T. Marques, S. Scoppettuolo, and D. Martin, "Heavy-Ion and Total Ionizing Dose (TID) Performance of a 1 Mbit Magnetoresistive Random Access Memory (MRAM)", *2009 IEEE Radiation Effects Data Workshop*. pp. 103-105, doi: 10. 1109/REDW.2009.5336307.

2) Martin, Douglas & Gadlage, Matthew & Leung, Wai-Yat & Titus, Jeffrey. (2019). Enhancing Point Defect Isolation by Using Ionizing Radiation. 323-328. 10.31399/asm.cp.istfa2019p0323.

3) G. Wolf, B. Kardasz, J. Vasquez, T. Boone, D. Bozdag, S. Watts, J. Hernandez, P. Manandhar, Y. Chin, M. Pinarbasi, "Perpendicular Magnetized Magnetic Random-Access Memory Cells Utilizing the Precessional Spin-Current Structure: Benefits for Modern Memory Applications." in IEEE Magnetics Letters, vol. 11, pp. 1-4, 2020, Art no. 4503404, doi: 10.1109/LMAG.2020.3001487

4) Titus, J. L. (2018), Discrete Test Tutorial, Unpublished Document, (Created for Radiation Science Branch, GXMR, at NSWC Crane).

5) L. Massengill, et al. "Heavy-ion-induced Soft Breakdown of Thin Gate Oxides," IEEE Trans. Nucl. Sci., vol. 48, no. 6, pp. 1904-1912, Dec. 2001.

6) Daisuke Kobayashi et al 2017 Jpn. J. Appl. Phys. 56 0802B4

7) Martin, D., Beilin, S., Hamilton, B., York, D., Baker, P., & Leung, W. (2013). Application of Advanced Back-Side Optical Techniques in ASICs. Microscopy Today, 21(3), 30-35. doi:10.1017/S1551929513000540

V. ILLUSTRATIONS
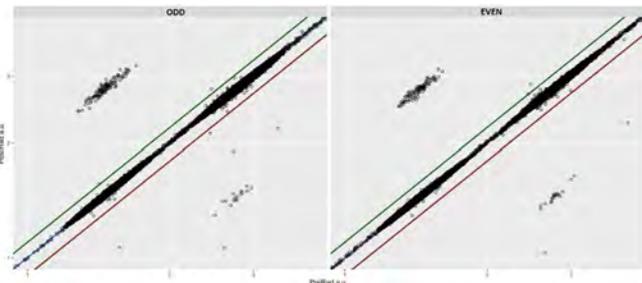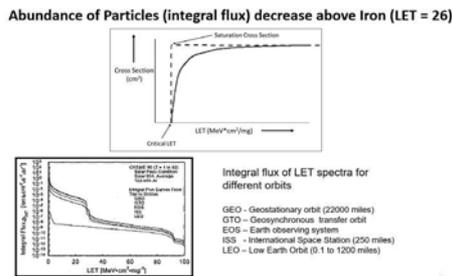
Fig. 1 SEE Information for Space Assessment   Fig. 2 BR in Arbitrary units; x-axis pre_BR, y-axis post_BR
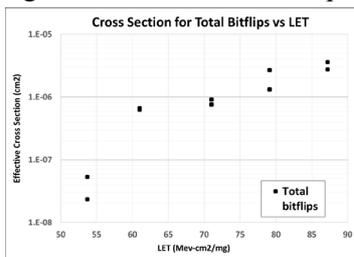
Fig. 3 Total Bit-flip; σ (cm^2) vs LET
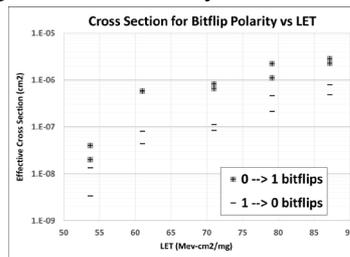
Fig. 4 Bit-flip Polarity; σ (cm^2) vs LET
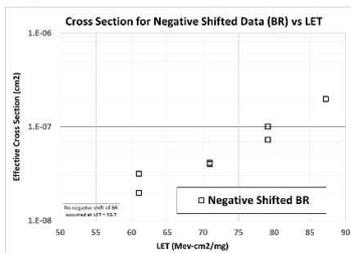
Fig. 5 Negative Shifted Data; σ (cm^2) vs LET   Fig. 6 Using LADA to Simulate SEFIs
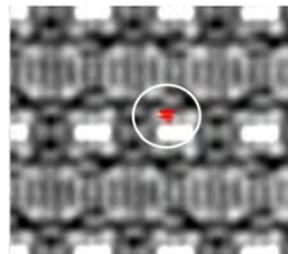
TECHNOLOGY TRANSFERS INTO THE DEFENSE INDUSTRY: IMPLICATIONS FOR SPINTRONICS IN THE FUTURE OF NATIONAL SECURITY

M. BURKLAND, Ph.D

Senior Principal Systems Engineer, Raytheon Missiles & Defense, Tucson, AZ, USA,
mburkland@raytheon.com

There is a long and fascinating history of innovation in technologies driven by critical military need, especially during wartime. Much is known about the Manhattan Project of WWII led by Robert Oppenheimer in the Southwestern US where the first atomic detonation occurred in 1945. At the same time, the development of the Cavity Magnetron was pioneered by I.I. Rabi on the East coast, which was successfully integrated later by Raytheon for Radio Frequency (RF) defense applications. Less known is the development of "Frequency Hopping" during the war by the Hollywood Starlet Hedy Lamarr and co-author George Antheil [1] – an innovation that would later prove to be critical for secure RF communications (Fig. **1**). The process of technology transfer to military use was rapid for the former two cases, but took until the early 1960's for Lamar's innovation to be taken seriously. These three examples, and many others, set the stage for the emergence of the domestic microelectronics industry.

By 1961 President Eisenhower, in his farewell address to the nation, warned "against the unwarranted influence, whether sought or unsought, by the Military-Industrial Complex." The concern of excessive government spending on defense continues to be a contentious issue today. However, coupled with President Kennedy's plan to put a (US) man on the moon, government investment in microelectronics continued through the 1980's helped position the United States as

Fig. 1 Hedy Lamarr, inventor of "Frequency Hopping".

the only super power to emerge from the Cold War – with the defense and aerospace industries driving innovation. Advancements in aeronautics, enabled the emergence of Mach 3+ aircraft propelled by Pratt & Whitney engines, and fighter aircraft with radar cross-sections of a ball bearing [2]. By mid-1990 the tide had shifted with commercial electronics as the market driver of design and applications. In 2014, William Lynn III, the former Deputy of Defense, wrote of "The End of the Military-Industrial Complex," emphasizing the need of the defense industry to work with, and incorporate from, the commercial sector [3].

While the collaboration of the Defense Industrial Base (DIB) with the domestic commercial microelectronics sector has been sufficient to meet the demand, the cost and time of development of advanced microelectronics has dramatically increased while the supply from domestic foundries has become limited with industry consolidation.

A generalized example of the challenges facing the DIB is the thermal effects encountered from computational workloads using conventional von Neumann processing architectures. With demanding Size, Weight & Power constraints limitations to mission capabilities are compounded, Fig. 2.

Additionally, the time delay in adoption of new technologies into defense products can take a decade or more, governed by a prescribed maturation process utilized within

Fig. 2 Increased thermal effects on processing workloads in guidance electronics is detrimental to mission performance

the industry, the Technology Readiness Level (TRL) scale of Fig. 3. The rate limiting processes within the

Michael Burkland
E-mail: mburkland@raytheon.com

TRL lifetime are usually paced by qualification, the degree of disruption to existing systems of adoption, and an establishment of a reliable and affordable supply chain.

The hopeful light at the end of the tunnel may be with the development of low temperature Back-End-Of the Line (BEOL) fabrication of novel memory and logic technologies; specifically vertical CMOS and beyond CMOS devices, with lower fabrication cost. For instance, non von Neumann architectures are being investigated using STT-RAM for high throughput, low energy and latency processing. The MRAM-based Deep In-Memory Architecture (DIMA) is being developed via DARPA [4] utilizing research from the University of Illinois and Princeton which leverages the GLODBALFOUNDRIES 22nm FDX based MRAM, Fig. 4. While spintronics, in general, has narrowed the performance

Fig. 3 The Technology Readiness Level (TRL) – a measure of technology maturation from concept to operational deployment. Traversing the valley of Death (Hedy's problem) is critical to technology adoption since visibility to potential stakeholders is low while cost of development remains high.

gap with CMOS [5], advantages with BEOL customization, density, non-volatility and radiation tolerance are all favorable for defense applications. However, further opportunities emerging from domestic research, such as university research sponsored by the Semiconductor Research Corporation [6], can only be transferable by a robust industrial base supporting successful rapid prototyping and sustained production.

Cognizant of these issues, the United States has recently increased investment in on-shore advanced microelectronics development and manufacturing via the recently passed $52B CHIPS Act. Thus, a pivot by existing commercial microelectronics suppliers, especially those with magnetic-based device fabrication, to support of low volume (compared to commercial) specialized BEOL microelectronics in the near-term would provide for emerging defense needs while laying a foundation for a larger commercial market demand anticipated in the coming five to ten years [6]. As well, opportunities for emerging spintronic-based suppliers could address a market segment of TRL 4-6 range of near-term DIB development needs.

While the economic scale for the DIB microelectronics market will likely not be dominant

Fig. 4 MRAM-based DIMA for low power consumption processing on missile system workloads.

as during the early decades of the 1960's and 70's, government investment in the resurgence of domestic sourced microelectronics affords the commercial industry opportunities critical to meeting the near-term supply for the DIB. The free markets that enable the industrial might of the nation remain "free" and prosperous by virtue of the nation's defense against the threats to undermine and control these markets.

REFERENCES

1) R. Rhodes, "Hedy's Folly", *Vintage,* (2011).
2) B. R. Rich, L. Janos, "Skunk Works", *Little, Brown & Co.,* 63 (1994).
3) W. J. Lynn III, "The End of the Military-Industrial Complex", *Foreign Affairs Magn.,* Nov/Dec (2014).
4) K. Kim et al., "MRAM-based Deep In-memory Architectures", *GOMACTech21,* (2021).
5) Y. C. Liao et al., "Benchmarking and Optimization of Spintronic Memory Arrays", *IEEE J. Exploratory Solid-State Computational Devices and Circuits*, 6(1), 9-17, (2020).
6) J. Neuffrer et al., "Decadal Plan for Semiconductors", *Semiconductor Research Corp.,* (2021).

MAGNETORESISTIVE RANDOM ACCESS MEMORIES FOR SPACE AND RADIATION-HARDENED APPLICATIONS

Romney R. KATTI[1]

1) Honeywell Aerospace, Plymouth, MN, USA, Romney.Katti@honeywell.com

I. INTRODUCTION

Magnetoresistive Random Access Memories (MRAMs) are of interest for space applications and where radiation hardness is required. The solid-state form factor of MRAMs supports modularity, reliability, redundancy, fault tolerance, radiation hardness, and mission assurance with low size, low mass, low power consumption, and non-volatility. MRAMs and MRAM technology provide scaling potential towards and beyond gigabit and gigabyte memories in single-chip packages (SCPs) and multi-chip modules (MCMs); and offer long life, unlimited write endurance, unlimited read endurance, unlimited data retention, non-destructive readback, and low error rates across a broad temperature range. MRAMs also provide higher areal and volumetric bit storage densities with respect to preceding space-qualified non-volatile magnetic solid-state memory technologies, such as magnetic plated wire and magnetic core memories.

MRAMs typically consist of arrays of magnetic devices, such as Magnetic Tunnel Junctions (MTJs) that function as magnetic bits that are radiation hard. To support space and radiation-hardened electronics applications, arrays of MTJs are integrated with circuit designs that use radiation-hardened design practices that are preferably implemented in a radiation-hardened silicon-on-insulator (SOI) CMOS wafer process. Higher memory density, smaller size, and lower power consumption are sought for next-generation MRAM technology and MRAMs for space and radiation-hardened electronics applications while maintaining or improving write and read endurance, data retention, speed, error rate, and reliability. As such, implementing spin-transfer torque (STT) [3] writing in next-generation MRAMs supports scaling beyond that achieved using inductive writing in initial-generation toggle MRAMs.

II. RESULTS AND FINDINGS

Shown in Table 1 are specifications from Honeywell's QML-qualified 16 Megabit (Mb) SCP MRAM [1] and 64Mb MCM MRAMs [2]; with target specifications for Honeywell STT-MRAMs being pursued and developed with nonvolatile memory capacities of ≥64Mb for SCPs and ≥256Mb for MCMs. The intent is to increase memory capacities; and maintain or improve speed, error rate, radiation hardness, size, mass, power consumption, with practically unlimited write and read cycling endurance and data retention times.

Table 1. Honeywell QML 16Mb SCP and 64Mb MCM toggle MRAM product specifications; with target specifications for Honeywell STT-MRAMs for ≥64Mb SCPs and ≥256Mb MCMs.

	16Mb QML MRAM SCP: Specifications [1]	64Mb QML MRAM MCM: Specifications [2]	64Mb+ MRAM SCP & 256Mb+ MRAM MCM: Target Specifications
Supply voltage (V)	3.3	3.3	1.2 to 3.3
Write cycle time (ns)	140	150	<50
Read cycle time (ns)	120	130	<50
Write & read endurance (cycles)	$>10^{15}$	$>10^{15}$	$>10^{15}$
Data retention (years)	>15	>15	>15
Lifetime (years)	>15	>15	>15
Operating Temperature (°C)	-40 to +125	-40 to +125	-40 to +125
Total Ionizing Dose (Mrad(Si))	>1	>1	>1
Error Rate: Geo orbit, solar min, 100mil Al shielding (errors/bit/day)	$<10^{-10}$	$<10^{-10}$	$<10^{-10}$

Figure 1 shows exemplary results [4-5] from radiation-hardened toggle MRAMs, and from 256Mb STT-MRAMs, subject to write/read pattern testing performed before, during, and after heavy-ion irradiation. For the average number of heavy ions per bit graphed as a function of Linear Energy Transfer (LET) level, no hard errors were induced in the MTJ bits for radiation environments for typical applications. As heavy ion fluence and LET are increased, fractional populations of tunnel barriers in MTJ bits show physical damage. As MTJ bit size is reduced via scaling, the average number of ions per MTJ bit is observed to decrease, which suggests that reduced MTJ bit cross-sections in STT-MRAMs will have smaller MTJ bit damage cross-sections and that heavy ion bit-damage performance can be improved via scaling for a given fluence and LET, which is a positive and encouraging result. Since testing to induce hard errors in the STT-MRAMs was not performed, the effect of increasing the number of MTJ bits in higher-capacity STT-MRAMs needs to be evaluated further.
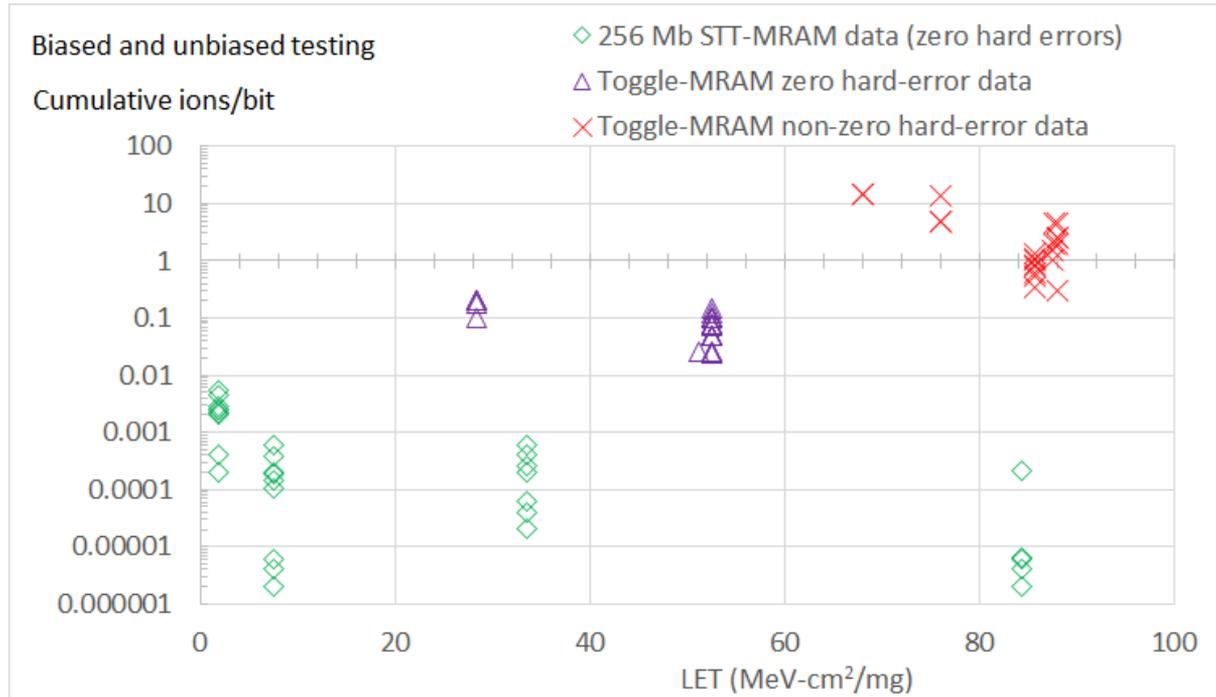
Fig. 1. Cumulative average heavy ions per bit vs. LET for Honeywell QML-qualified toggle MRAMs and for 256 Mb STT-MRAMs. The green diamonds and purple triangles show test results with no heavy-ion induced hard errors. Hard errors induced at elevated fluence and LET are shown in the red x's.

III. ACKNOWLEDGMENTS

REFERENCES

1) SMD 5962-13212, "Microcircuit,Memory,Digital,CMOS/SOI,16Mbit,Radiation-Hardened,NonVolatile Random Access Memory (NVRAM),Monolithic Silicon," https://aerospace.honeywell.com, (2014).
2) SMD 5962-14230, "Microcircuit,Memory,Digital,Radiation-Hardened,CMOS/SOI,64Mbit NonVolatile Random Access Memory (NVRAM),Multichip Module (MCM),"https://aerospace.honeywell.com, (2015).
3) N. Rizzo, et al. "A Fully Functional 64 Mb DDR3 ST-MRAM Built on 90 nm CMOS Technology," *IEEE Trans. Magn*., 49(7) 4441-4446, (2013).
4) R. R. Katti. "Heavy-Ion Device Cross-Section Response in Magnetic Tunnel Junctions for a Radiation Hardened 16Mb Magnetoresistive Random Access Memory (MRAM)," *NSREC REDW*, (2017).
5) R. R. Katti, et al. "Heavy Ion Bit Response and Analysis of 256 Megabit Non-Volatile Spin-Torque-Transfer Magnetoresistive Random Access Memory (STT-MRAM)," *NSREC REDW*, (2018).
6) R. R. Katti. "Heavy-Ion and Radiation Hardness in Magnetoresistive Random Access Memories," *TMRC*, (2019).

Romney R. Katti
Honeywell Aerospace, 12001 State Highway 55, MN14-3C15, Plymouth, MN 55441, USA
E-mail: Romney.Katti@honeywell.com
tel: +1-612-9515115

PHYSICAL MECHANISMS AFFECTING PERFORMANCE OF PERPENDICULAR STT MRAM CELLS

G. MIHAJLOVIĆ[1], N. SMITH[1], T. SANTOS[1], Z. BAI[1], M. TRAN[1], J. LI[1], M. CAREY[1], M. K. GROBIS[1], and J. A. KATINE[1]

1) Western Digital Research Center, Western Digital Corporation, San Jose, CA 95119,
goran.mihajlovic@wdc.com

I. INTRODUCTION

Spin transfer torque magnetoresistive random access memory (STT MRAM) is an alternative to SRAM [1] and Flash [2, 3] in various embedded applications, as it can provide non-volatility concurrently with low power, high speed operation, and high endurance. In order to become a viable option for replacing DRAM as a stand-alone memory at relevant areal densities, further optimization of MRAM performance is needed, as continued technology scaling and advanced computing systems impose challenging specifications on MRAM in terms of its retention (thermal stability), read-out latencies, and write margins [4]. This talk will present our recent experimental, theoretical, and modeling results on understanding physical mechanisms that affect performance of perpendicular STT-MRAM cells under electrical, magnetic and thermal excitations. In particular, we will report experimental and modeling results that extend of our recent work on electrical self-heating in STT-MRAM [5] to smaller device size, describe our work on optimization of FL materials for improving STT efficiency and thermal stability [6], present analytical model for calculating energy barrier for domain-wall-mediated magnetization reversal of the perpendicular FL [7], and show our experimental results which suggest that, contrary to common understanding, fitting the magnetic-field switching probabilities P(H) to a macrospin-reversal model provides approximately correct values of perpendicular magnetic anisotropy field H_k on device level.

II. RESULTS AND DISCUSSION

We previously reported that self-heating can explain RA dependence of critical current density J_{c0} and STT efficiency Δ/I_{c0} obtained by fitting pulse width dependence of V_c to the thermal activation model [5]. In that work we showed that self-heating can be modeled as $T = T_0 + R_{th}A\, V_b^2/RA$ and we determined $R_{th}A \cong 4.0$ Kμm^2/mW for CD $\cong$ 90 nm. Here we extend that work to smaller device size using experimental and modeling studies. We determine the size dependence of thermal resistance-area product $R_{th}A$ experimentally down to CD $\cong$ 25 nm. In the CD range of approximately 25 – 90 nm, the empirical formula $R_{th}A \cong [\ln(0.2651\,CD)]^{1.15784}$ describes the CD dependence well [see Fig. 1(a)]. The functional form of the formula captures a portion of transition from mostly 1D heat flow to more 3D heat flow ($R_{th}A \sim CD$) as CD decreases, while retaining the framework in which the MRAM heat generation is treated in terms of its RA. The consequence of the lower $R_{th}A$ at smaller CDs is that the temperature increase ΔT due to self-heating at a reasonable value of RA = 10 $\Omega\mu$m^2 is estimated to be significantly lower for CD = 20 nm (at $\sim$ 0.6 V, $\Delta T \cong$ 65 K) compared to CD = 50 nm (at $\sim$ 0.6 V, $\Delta T \cong$ 110 K), [see Fig. 1(b)]. We will also show that our experimentally determined RthA values agree well with thermal modeling predictions [see Fig. 1(a)], as well as experimental results of CD dependence of critical STT switching current and time dependent dielectric breakdown voltage and endurance.

Further, we will present our experimental results as a function of the number of W-spacer layers and their respective thickness within the FL and the effect they have on STT efficiency and thermal stability [6]. We will describe an analytical model for calculating the energy barrier for the magnetic field-driven domain wall-mediated magnetization reversal of the free layer (FL) which we then apply to study Δ for various thicknesses of W layers as a function of the cell size and temperature [7]. We find that, by increasing the W thickness, the effective perpendicular magnetic anisotropy (PMA) energy density of the FL film monotonically increases, but at the same time, Δ of the cell mainly decreases [see Fig. 1(c)]. Our analysis

shows that, in addition to saturation magnetization M_s and exchange stiffness constant A_{ex} of the FL film, the parameter that quantifies the Δ value of the cell in this regime is its coercive field H_c, rather than the net PMA field H_k of the FL film comprising the cell. Surprisingly, we also find that H_k values obtained by fitting the P(H) data using uniform macrospin reversal model agree well with those obtained from thermal noise FMR measurements [5] even though the reversal proceeds by domain wall mediation [see Fig. 1(d)]. We conclude that this method could be used for reliably determining device-level H_k values in a simpler way and with more significant statistics than more complicated and slower thermal [5] or spin-torque driven [8] FMR techniques.

III. ILLUSTRATIONS
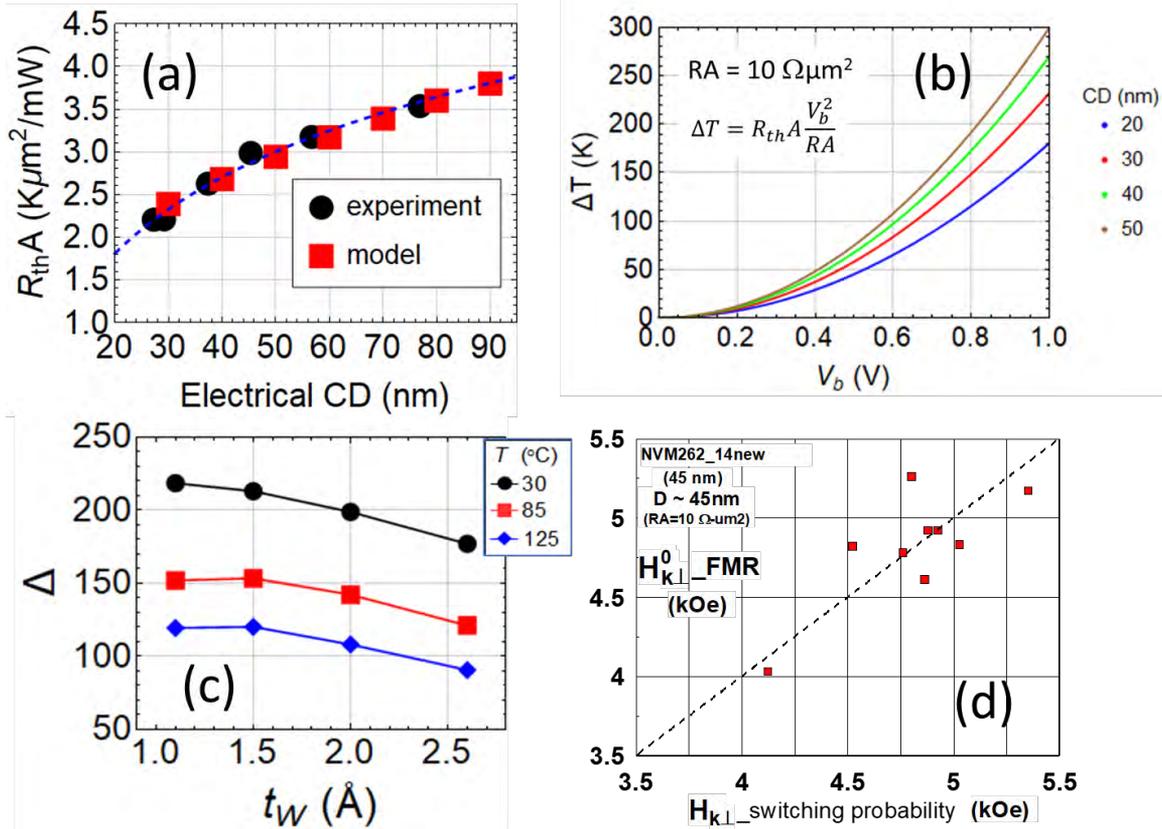
Fig. 1 (a) $R_{th}A$ vs CD determined experimentally and via modeling studies. $R_{th}A \simeq [\ln(0.2651\,CD)]^{1.15784}$ is shown as a dashed blue line. (b) ΔT vs V_b for various CD values calculated using $R_{th}A(CD)$ dependence shown in part (a). (c) Thermal stability factor Δ as a function of thickness of W insertion layers for T= 30, 85, and 125 °C and average device CD = 95 nm. (d) Device level H_k values determined by fitting magnetic field switching probabilities to a macrospin model vs those determined by thermal noise FMR measurements for device CD $\cong$ 45 nm.

REFERENCES

1) S. H. Han et al., IEDM 20-215 (2020).
2) V. B. Naik et al., IEDM 20-219 (2020).
3) Y. -C. Shih et al., IEDM 20-223 (2020).
4) N. Chandrasekaran et al., IEDM 20-203 (2020).
5) G. Mihajlović et al., Phys. Rev. Appl. 13, 024004 (2020).
6) T. Santos et al., J. App. Phys. 128, 113904 (2020).
7) G. Mihajlović et al., App. Phys. Lett. 117, 242404 (2020).
8) L. Thomas et al., IEDM 17-848 (2017).

STT-MRAM for Automotive Applications

K. NAGEL[1], S. AGGARWAL[2], G. SHIMON[3], S. IKEGAWA[3], F. MANCOFF[4], and J. SUN[5]
1) Everspin Technologies, Chandler, United States, kerry.nagel@everspin.com
2) Everspin Technologies, Chandler, United States, sanjeev.aggarwal@everspin.com
3) Everspin Technologies, Chandler, United States, shimon.shimon@everspin.com
4) Everspin Technologies, Chandler, United States, sumio.ikegawa@everspin.com
5) Everspin Technologies, Chandler, United States, jijun.sun@everspin.com

I. INTRODUCTION

There is a growing need for fast, endurant, non-volatile solutions for automotive that can meet the harsh requirements of automotive conditions. Automotive applications place severe demands memory devices. In the case of data retention, Automotive Grade 0 requires survival of $T_{ambient}$ 150 °C for 20 years with no loss in data integrity. In order to meet the higher temperature grades, an increase in data retention temperature capability is required. However, simply increasing the data retention can have a negative impact on write voltage, and, consequently, on endurance. Therefore, a similar methodology to improve write distribution as has been used on our 1 Gb memory array for datacenter applications is beneficial when applied to these products.

II. OPTIMIZATION OF WRITE DISTRIBUTION

In order to produce manufacturable automotive arrays, it was important to optimize write distribution. The write distribution includes elimination of any extrinsic tail. Reducing the tail distribution helps relative to the switching current available at small cell size, as well as increases the margin with respect to the endurance limit. Figure 1(a) shows an example of improvement in STT distribution for a full memory array with ECC off.

The Vc is defined as the voltage at which 50% of the bits in an array switch. The Vop (operating voltage) can be further defined as voltage at which all of the bits switch, as measured to a specified bit error rate. The optimized process reduced the level of Vop and the sigma in Vop to achieve the design objectives, as shown in Figure 1(b). Referring to Figure 1(a), the reduction in Vop is partially related to a reduction in Vc, but primarily related to an improvement in distribution at low bit error rate.

Further, the improvement in sigma at a specified pulse width also improves the Vop as pulse width is reduced. The combination of a shorter pulse width while controlling the increase in Vop at short pulse width is a large benefit to overall power consumed.

III. INCREASE IN DATA RETENTION

Data retention can always be increased at the expense of an increase in write voltage. The disadvantage of a higher write voltage is higher power consumption and the possibility of a decrease in endurance. The process optimization for improved switching distribution allows increasing the data retention without increasing the write voltage by an excessive amount. Consequently, higher data retention without degraded endurance is enabled.

Data retention is validated by testing with a series of times and temperatures. From this accelerated data, it is possible to extrapolate to the data retention time specification as a function of temperature, as shown in Figure 3. The dashed line is equivalent to 20 years of data retention. The new process can survive with data integrity for that length of time, to the specified bit error rate, at temperatures up to 150 °C.

KERRY NAGEL
E-mail: kerry.nagel@everspin.com
tel: +1-480-3471094

E7

REFERENCES

1) S. Ikegawa, F. B. Mancoff, J. Janesky, and S. Aggarwal, "Magnetoresistive random access memory: present and future," IEEE Trans. Electron Devices, vol. 67, no. 4, pp. 1407-1419, April 2020.

2) N. D. Rizzo et al., "A fully functional 64Mb DDR3 ST-MRAM built on 90 nm CMOS technology," IEEE Trans. Magn., vol. 49, pp. 4441–4446, July 2013.

3) J. M. Slaughter et al., "Technology for reliable spin-torque MRAM products," IEDM Tech. Dig., pp. 21.5.1-21.5.4, 2016.

4) S. Aggarwal et al., "Demonstration of reliable 1Gb. standalone spin-transfer torque MRAM for industrial applications," IEDM Tech. Dig., pp 2.1.1-2.1.4, 2019-12.

ILLUSTRATIONS
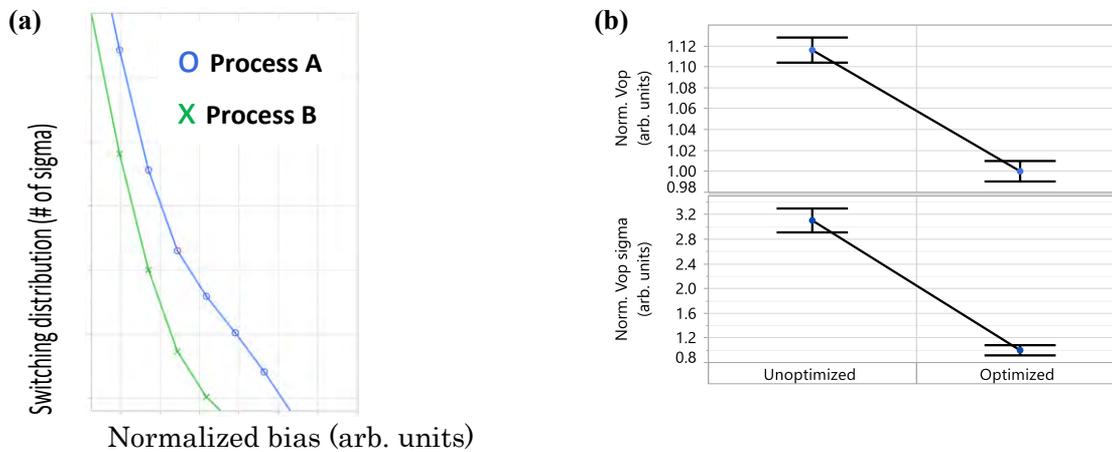
Fig. 1 (a) Switching distribution comparison of an entire 1 Gb die with optimized and un-optimized processes and ECC off. (b) Reduction in Vop (operating voltage) and sigma of Vop with process optimization.
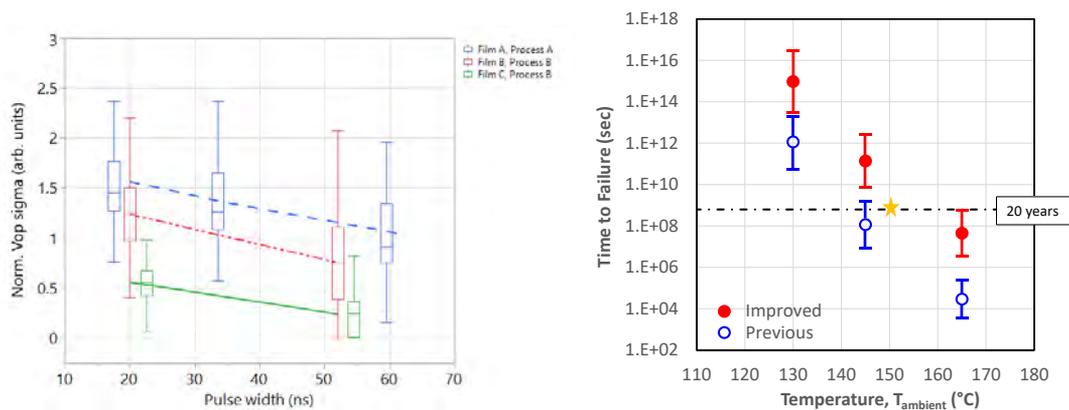
Fig. 2 Reduction in normalized Vop sigma with process is a further improvement at lower pulse width.

Fig. 3 Improved process demonstrating data retention performance in excess of 150 °C for 20 years.

KERRY NAGEL
E-mail: kerry.nagel@everspin.com
tel: +1-480-3471094

Magnetic Recording Assisted by Spin-Transfer-Torque-Induced Magnetization Reversal and Dynamics

Wenyu CHEN[1*], Zhenyao TANG[2], Akimasa KAIZU[2], Shohei KAWASAKI[1], and Tetsuya ROPPONGI[1]

1) Headway Technologies Inc., Milpitas, CA USA

2) Advanced Products Development Center, TDK Corporation, Japan

* Corresponding author, email: wenyu.chen@headway.com

I. INTRODUCTION

With the requirement of increasing data areal density in hard disk drive (HDD) recording, one of the main applied approaches that effectively reduce recording bit size is to incorporate a spin transfer torque (STT) device in the magnetic writer, either to reverse a magnetic layer in the device in order to guide the magnetic flux of the writer pole more concentrated towards the into and out-of air bearing surface (ABS) directions[1], or to drive a magnetic layer into large angle oscillations for a sufficiently large radiofrequency (rf) field in the media to realize the assist[2]. Micromagnetic simulations of the magnetic device inside the write gap (WG) between the main writer pole and its magnetic shield with an alternating write gap field, were conducted incorporating STT interactions between the magnetic layers. Modeling results for understanding assist performance optimized by STT device design from these two main approaches will be discussed in this talk.

II. RECORDING ASSISTED BY STT INDUCED MAGNETIC LAYER REVERSAL

In the design of the spin transfer torque induced magnetization reversal that assists the write field, the key device located in the WG is typically composed of a magnetic flux control layer (FCL) and a spin polarizer (SP) magnetically coupled to the writer shield, as shown in Fig. 1(a). When the electrons flow from the FCL to the SP, the STT tends to flip the FCL against the gap field, and its final stable state depends on the competition between the strength of the damping torque of the FCL and that of the STT. The total effective FCL moment flipped against the WG field under the biasing current density allowable for device reliability is the top consideration. The model assumes a normal FCL damping constant of 0.02 and a spin polarization of 0.4, and the results are shown in Fig. 2(a). An FCL with a low moment per area (Mst), such as 4 nmT in Fig, 2(a), can be easily flipped by the spin torque under low current density well below 3×10^8 A/cm². However, its maximal possible flipped moment to assist the write field is limited by its low total moment. An FCL with a higher Mst, such as 8 nmT, has a better potential for flipped moment, but >80% flipping only occurs at current density higher than 6×10^8 A/cm². Furthermore, under an alternating write current that typically reaches >1 GHz frequency in our current HDD recording, the trend of the amount of flipped magnetic moment vs current density is also different compared to that under a lower write frequency. The optimal design consideration of magnetization reversal by real-time micromagnetic simulations under different write frequencies will be presented.

III. RECORDING ASSISTED BY STT INDUCED MAGNETIC LAYER DYNAMICS

When multiple magnetic layers are applied in the write gap such as the one shown in Fig. 1(b), the effects of rf field generated by the STT device to the media may become more dominant compared to reducing or reversing magnetic moment in the WG. Typically the

Corresponding Author: Wenyu Chen

E-mail: wenyu.chen@headway.com

Tel: 408-934-5351

main magnetic layer is now sandwiched between two spin polarizers: SP1 that is coupled to the write shield and SP2 that is free to rotate. The simulation results are shown in Fig. 2(b) and (c): the total moment along the gap field is close to zero under J>4x10^8 A/cm^2 [Fig. 2(b)], whereas the total moment in the film plane starts to dominate [Fig. 2(c)], so that the main magnetic layer is now named the rf field generation layer (FGL). Device design that is used to enhance the rf field for optimal assist in writer applications will also be discussed.

REFERENCES

[1] Extended concept of MAMR and its performance and reliability, *TMRC Conference 2020*, Paper ID C1, by A. Takeo et al,

[2] Microwave Assisted Magnetic Recording*, IEEE Trans. Magn.*, vol. 44, pp.125-131 (2008) by J.-G. Zhu, et al
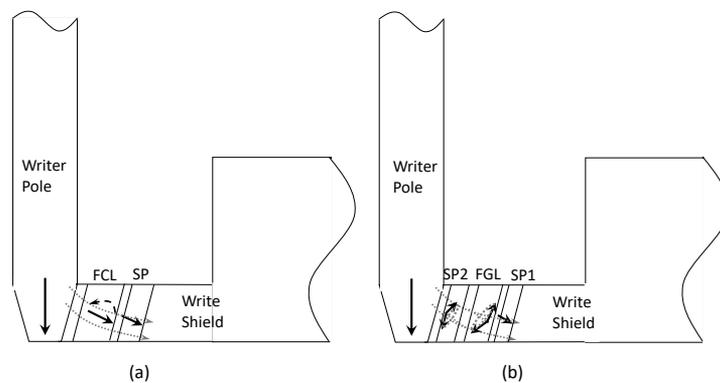
Figure 1: Schematic of one design each for writer assisted by STT induced magnetic layer reversal [in (a)], and by STT induced magnetic layer dynamics [in (b)].
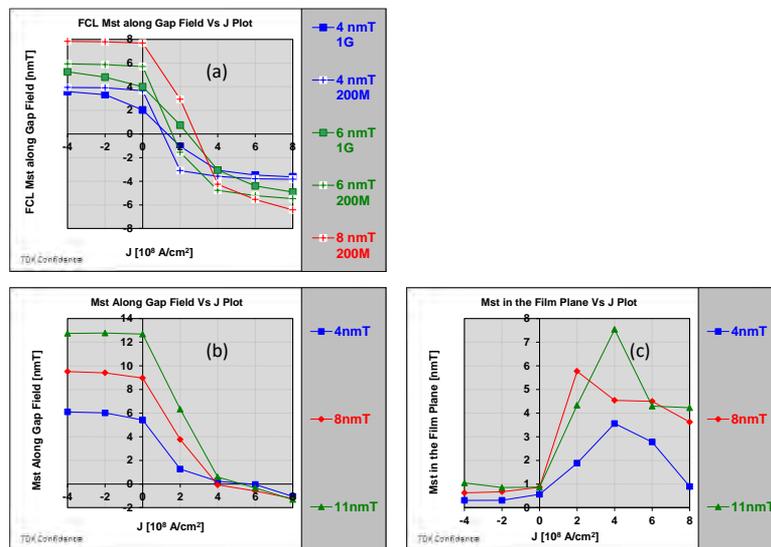
Figure 2 (a): Simulation results of STT induced magnetic layer reversal as a function applied current density, described in part II, with a variety of FCL Mst and writer frequencies. (b) (c): Simulation results of the magnetic layer dynamics described in part III with the total Mst along the gap field shown in (b) and dynamics in the film plane shown in (c).

Sub-nanosecond switching of spin-transfer-torque device for energy-assisted perpendicular magnetic recording

Yunfei DING[1], Hui ZHAO[2], Alexander GONCHAROV[3]

1) Western Digital Corp, San Jose, U.S., yunfei.ding@wdc.com
2) Formerly Western Digital Corp, San Jose, U.S., zhaohui.5@gmail.com
3) Western Digital Corp, San Jose, U.S., alexander.goncharov@wdc.com

I. INTRODUCTION

One of the key challenges for perpendicular magnetic recording (PMR) heads in hard disk drives (HDD) is to generate high enough magnetic field to switch the magnetization of the recording media grains with high magnetic anisotropy. In a start-of-art writer design a trailing shield (TS) separated from the main magnetic pole (MP) by a narrow non-magnetic top gap (TG) is used to produce a high down-track field gradient, the narrow TG however causes flux leakage between MP and TS and reduces the maximum field amplitude seen by media. To mitigate this trade-off a new magnetic write head structure was proposed to have an additional spin-transfer torque (STT) device, with a current-perpendicular-to-plane (CPP) giant magnetoresistance (GMR) structure, inside this narrow TG, as shown in Fig 1(a)[1]. During write operation, a bias current is applied and electrons flow from the soft magnetic spin torque layer (STL) to TS. The electron flow generates a large enough torque to the magnetization of the STL and makes it overcome the large gap field and switch its direction to be antiparallel to the gap field and TS magnetization. The antiparallel STL magnetization reduces the flux leakage, improves both field amplitude and gradient seen by the media. This mechanism of STL magnetization switching direction is similar with the switching of the free layer magnetization to antiparallel state in spin-transfer-torque magnetic random-access memory (STT-MRAM), except that here the STL magnetization switching has to overcome a very large magnetic field, and that it has to switch very quickly when writing high frequency data patterns. The write time of STT-MRAM is typically a few nanoseconds, the STL switching time however needs to be in less than about 500 picoseconds, or the shortest bit length in magnetic recording. In this study we measured the switching time of the STL and found it can be 300 picoseconds or below, as predicted by micromagnetic simulation.

II. EXPERIMENTS

Fully integrated recording heads with STT devices are used to characterize the switching of STL. When a constant bias current is applied to writer coil and STL, in equilibrium state the STL magnetization is aligned antiparallel to TS magnetization, and the magnetoresistance (MR) stays at high resistance state. When the coil current suddenly switches polarity the MP and TS magnetizations will go through a switching process, which lasts for ~200ps before they fully switch direction. Subsequently, the STL will also go through a switching process, driven by the spin torque that varies with time as a function of the relative angle between STL and TS, and under the influence of the also time varying gap field, before eventually settling down and becoming antiparallel to TS magnetization again. During this complex switching process the STL and TS are no longer antiparallel, as a result the device will momentarily show a smaller MR. We studied the switching behavior of the device by monitoring the MR signal in real time.

The schematic of the experimental setup is shown in Fig 1(b). In this setup a high-speed function generator is used to generate square waves to the writer coil of the head, a Keithley2400 source meter provides a direct current (DC) bias to the STL and measures the MR value, a real time oscilloscope with 12GHz bandwidth is used to monitor the voltage on the STL/TS GMR structure. We typically make two such measurements, one with and one without bias to the STL. The subtraction between the two minimizes the large background crosstalk signal between coil and STL circuit and allows observation of the relatively small MR signal. We also did quasi-static MR measurement while sweeping the DC bias to measure MR curve and determine the critical switching current of the STL.

Yunfei Ding
E-mail: yunfei.ding@wdc.com
tel: +1-408-717-5568

III. MAIN RESULTS

A typical quasi-static MR curve is shown in Fig 2(a), and the time domain MR signal during the switching process of the same head is shown in Fig 2(b). At -65mV bias the spin torque is large enough to switch the STL to become antiparallel to the TS, leading to a resistance jump in the MR curve. The time domain MR signal in Fig 2(b) shows a dip with FWHM of ~500ps, corresponding to the total switching time of the STL. It is noted that this time also includes the switching of TS, since the MR signal is a function of relative angle between the STL and TS. We found that the switching time is a strong function of STL volume, the bias current, especially when the bias is close to the critical switching bias, and the switching speed of the writer itself. With a fast writer and high enough bias current on the STL, the switching time can reach ~ 300ps. The measurement results and the comparison to micromagnetic simulation will be discussed in detail.

IV. ILLUSTRATIONS
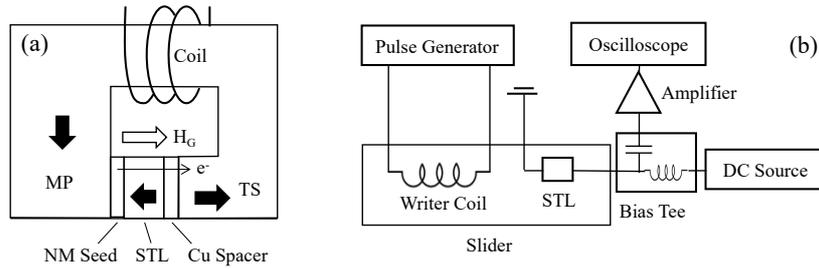
Fig 1. (a) Schematic of the writer with STT device inside the TG. Thick arrows denote magnetization orientations of MP, TS and STL. Electrons flow from STL to TS, inducing a spin torque that aligns STL magnetization antiparallel to TS magnetization and gap field H_G; (b) Schematic of the measurement setup.
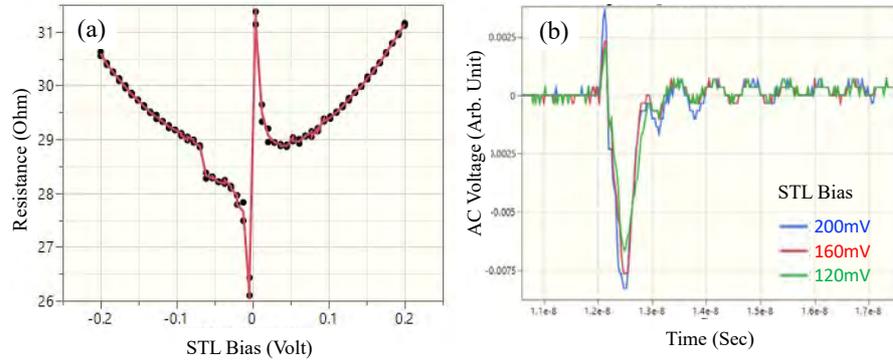
Fig 2. The quasi-static MR curve (a) measured with sweeping STL bias voltage, and the time domain waveform (b) of the MR signal captured during the switching of the coil current. During MR curve measurement the writer is saturated with a high constant coil current. The large spikes at +/- zero volt of the MR curve are due to a small constant error of the measured voltage of the source meter, this small offset doesn't affect the measurement in the bias voltage range of interest. In the time domain waveform the writer switches at ~ 12ns, the three colors in the time domain waveforms denote three different STL bias levels. The decaying oscillation after the main peak is the residual crosstalk coupled in from the writer coil circuit and its ringing due to imperfect impedance matching of the circuit.

REFERENCES

1) J. T. Olson, H. Hoshiya, A. Goncharov, M. Shiimoto, M. Sugiyama , "Magnetic write head for providing spin-torque-assisted write field enhancement", *US Patent No. 10366714B1*, (2019).

ANALYSIS OF A SPIN-TORQUE OSCILLATOR USING INJECTION LOCKING TO AN EXTERNAL MICROWAVE FIELD

H. Suto[1], N. Asam[1], S. Tamaru[2], H. Sepehri-Amin[1], A. Bolyachkin[1],
W. Zhou[1], T. Nakatani[1], H. Kubota[2], and Y. Sakuraba[1]

1) National Institute for Materials Science (NIMS), Tsukuba, Japan, SUTO.Hirofumi@nims.go.jp

2) National Institute of Advanced Industrial Science and Technology (AIST), Tsukuba, Japan

I. INTRODUCTION

A spin-torque oscillator (STO) is a key device in microwave-assisted magnetic recording (MAMR). Conventionally, the magnetization dynamics of STOs has been analyzed using the high-frequency electrical signal from the STO (STO signal). However, the STO signal is sometimes undetectable because of the highly symmetric magnetization trajectory or contains several frequency components that do not correspond to the frequency of the actual magnetization oscillation [1]. Furthermore, when the STO is integrated into the write head, the STO signal is expected to attenuate heavily in the write head, making it difficult to extract the STO signal. These facts prevent identifying the oscillation frequency from the STO signal, and a new analysis method of the STO that does not rely on the STO signal is required.

In this study, we demonstrate a new technique to characterize the actual frequency of the magnetization oscillation of an STO using injection locking to an external microwave magnetic field [2,3]. When the frequency of the microwave field is in the locking range around the intrinsic oscillation frequency of the STO, the STO magnetization synchronizes with the microwave field. This injection locking modifies the magnetization trajectory of the STO and, consequenctly, changes the dc resistance of the STO. By detecting the STO resistance change, the oscillation frequency can be identified without measuring the STO signal.

II. MICROMAGNETIC SIMULATION

First, we performed a micromagnetic simulation to show the principle of the new method. The simulation model was an all-in-plane (AIP) STO, which consisted of two in-plane magnetic layers: a field generation layer (FGL) and a spin injection layer (SIL). AIP-STOs have been proposed as a promising STO design for MAMR application. The FGL and SIL magnetization oscillated at a frequency of $10\ \mathrm{GHz}$ and $34\ \mathrm{GHz}$, respectively, as shown in Fig. 1(a). In the resistance change, which represents the STO signal, a peak appeared only at 24 GHz (difference between the SIL and FGL oscillation frequencies). This result indicates that the actual oscillation frequency cannot be identified from the STO signal. Next, a microwave magnetic field (H_{MW}) was introduced in the simulations. Figure 1(b) shows the oscillation cone angle of FGL (θ_{FGL}) and that of SIL (θ_{SIL}) as a function of a microwave field frequency (f_{MW}). When the f_{MW} is close to the intrinsic oscillation frequency, θ_{FGL} changes to make the oscillation frequency match f_{MW}. The change of θ_{FGL} also varies the spin-transfer torque from FGL to SIL, changing θ_{SIL}. Figure 1(c) shows the change in the product of dc resistance R and the device area A (ΔRA) of the STO as a function of f_{MW}. The f_{MW} dependence of the ΔRA also exhibited the peak-and-valley feature, which can act as an indicator of the intrinsic STO oscillation frequency.
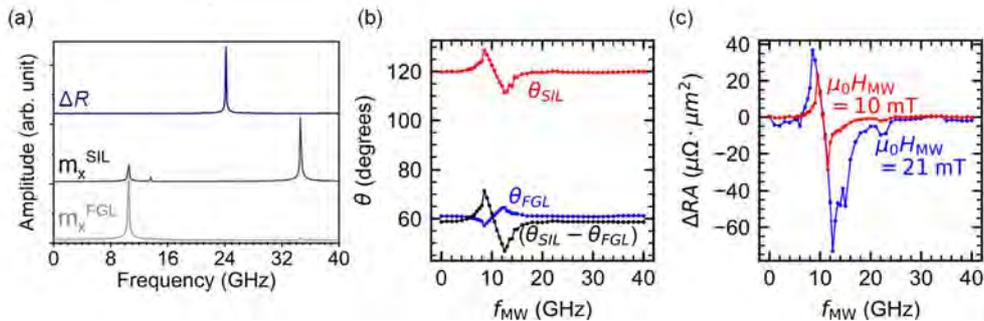

FIG. 1. (a) Spectra of resistance change of the STO, the SIL magnetization, and FGL magnetization, respectively. A current density of $3 \times 10^8\ \mathrm{A/cm^2}$ and a perpendicular magnetic field of $\mu_0 H_z = 900\ \mathrm{mT}$ were applied. (b) Cone angles of STO oscillation. (c) Change in the resistance-area product (ΔRA) of the STO.

Hirofumi SUTO
E-mail: Suto.hirofumi@nims.go.jp
tel: +81-29-859-2324

III EXPERIMENTAL METHOD AND RESULTS

Figure 2 shows the measurement setup. We prepared an AIP-STO with an antenna to generate a microwave magnetic field. Two bias-tees with a different cut-off frequency were used to separate low frequency (LF), intermediate frequency (IF), and high frequency (HF) components. A dc bias voltage (V_{dc}) was applied through the LF component. In the conventional method, the HF component containing the STO signal was monitored by a spectrum analyzer. In the new method, a pulse-modulated microwave field with a pulse frequency of 1 MHz was applied to the STO, and the change in the STO resistance caused by injection locking to H_{MW} was measured by a lock-in amplifier through the IF component. Note that 1 MHz is much lower than the frequency of the STT-induced magnetization oscillation of the STO; thus, this measurement detects the dc resistance.

Figure 3(a) shows the STO signal spectra obtained by the conventional method. A peak appeared at around 32 GHz. Note that, only this information, we cannot determine whether this peak originates from the oscillation of FGL or SIL or from the difference frequency between them. Figures 3(b) shows ΔR as a function of f_{MW} obtained by sweeping f_{MW} from 100 MHz to 40 GHz. A characteristic peak-and-valley feature appeared also at around 32 GHz. The peak-and-valley feature became more pronounced when the microwave field amplitude increased by increasing the microwave power. This result qualitatively agrees with the results of the micromagnetic simulation and demonstrates that the oscillation frequency can be identified by combining the injection locking and detection of the ΔR without measuring the STO signal. Since injection locking occurs only for the actual magnetization oscillation, the peak was attributed to the actual magnetization oscillation and not to the difference frequency.
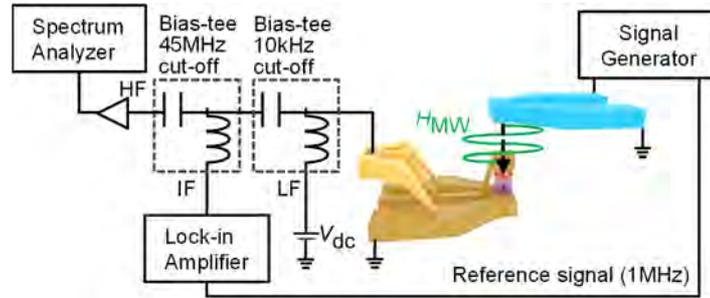
FIG. 2. Experimental setup.
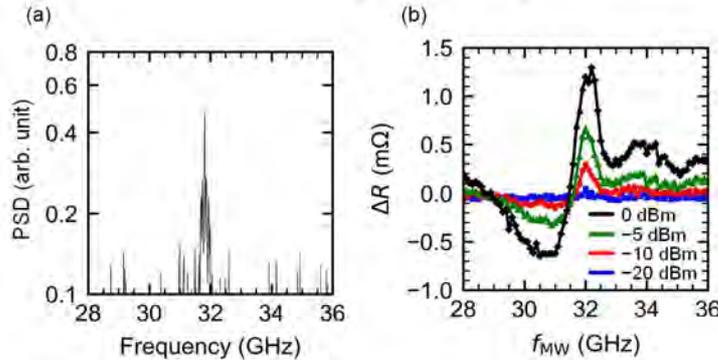
FIG. 3. (a) Spectrum of the STO signal obtained by applying V_{dc} = 50 mV and $\mu_0 H_{ext}$ = 1200 mT tilted by $\theta_H = 20°$ from the perpendicular direction. (b)ΔR signal versus f_{MW} for different microwave power values under the same conditions as (a).

REFERENCES
1)   W. Zhou, et al., Appl. Phys. Lett. **114**, 172403 (2019).
2)   H. Suto, et al., Appl. Phys. Express **14**, 053001 (2021).
3)   N. Asam, et al., Appl. Phys. Lett. (submitted)

Improvement of Dual FGL structure for MAS Effect Dominant MAMR Head

Masayuki Takagishi[1], Naoyuki Narita[1], Yuji Nakagawa[1], Tomoyuki Maeda[1], Akihiko Takeo[2],

1) Corporate Research and Development Center, Toshiba Corporation, Kawasaki Japan
2) Toshiba Electronic Devices & Storage Corporation, Yokohama Japan

I. INTRODUCTION

Microwave Assisted Magnetic Recording (MAMR) is one of the most promising candidates for the next generation hard disk drive (HDD) [1]. While MAMR dominated by well-known magnetic assisted switching (MAS) effect is expected a large potential to high areal density, it also requires various techniques to achieve the practical use, such as frequency matching, interaction reduction between spin torque oscillators (STO) and write pole and so on. We have indicated that dual field generation layer (FGL) structure [2] can be satisfied with some of these key factors. On the other hand, this structure also has a disadvantage due to its large magnetic thickness of FGL. In this talk, this negative point of dual FGL and how to improve it will be discussed on a simulation basis

II. NEGATIVE FC EFFECT

When an oscillation cone angle (refer to the Fig. 1a) of the FGL magnetization is larger than 90 degrees, large flux control (FC) effect [3][4] is expected. It also means that a cone angle smaller than 90 degrees will much degrade the magnetic recording quality. In this talk it will be called "negative FC effect". As the dual FGL structure has two FGLs, the magnetic thickness, which means the product of film thickness and saturation magnetization of the film, is much larger than a single FGL structure. This large magnetic thickness can cause a large negative FC effect in the dual FGL structure.

III. HOW TO IMPROVE THE NEGATIVE FC EFFECT

In order to estimate the negative FC effect of dual FGL, the relation between a cone angle and SNR was studied as Fig. 1c. For the simulation, Landau-Lifshitz-Gilbert (LLG) equation with spin torque term including both write head and STO was solved. FGL spacing in Fig. 1c is defined in Fig. 1b. The FGL spacing in the original design of dual FGL [2] is 2nm or less because dual FGL structure requires a strong magnetic coupling between the FGLs. The blue line in Fig. 1c indicates the signal to noise ratio of 2T frequency (2T-SNR) of the original dual FGL. The original dual FGL's performance deteriorates sharply as the cone angle decreases. The simulation was calculated under a middle diameter condition of 3.5" HDD at 2600kFCI. The higher Hk media than that in normal HDDs was employed in this calculation.

The other lines in the Fig. 1c indicate 2T-SNRs of dual FGL with larger FGL spacing. The large FGL spacing improve the 2T- SNR degradation. The cause of this improvement could be that the large FGL spacing decreases the negative FC effect under the write gap center and increases STO rotational field.

Fig. 2 indicates the Areal Density (AD) gain or loss due to both MAS effect and negative FC effect. Zero-gain of this y-axis means AD by using conventional perpendicular magnetic recording (PMR). When the FGL with 2nm FGL spacing rotates at a cone angle of 50degs, negative FC effect loss is comparable to MAS effect gain and total AD gain reaches below zero. On the other hand, when using FGL spacing of 8nm or 10nm, AD loss due to negative FC effect is less than 2% and we can get the AD gain due to MAS effect with smaller cone angle. The large FGL spacing can much improve the AD loss due to the negative FC effect. As these gains have not been optimized, we will discuss more optimal gain in our presentation.

As the large FGL spacing should cause the other problems such as STO vertical field effect [5], there should be an optimum value of FGL spacing. The large FGL spacing requires other measures against weak magnetic coupling between FGLs. We will discuss these points and will introduce some experimental data

Masayuki Takagishi
E-mail: masayuki.takagishi@toshiba.co.jp
Tel: +81-44-549-2391

of dual FGLs in our presentation.

REFERENCES

[1] J.-G. Zhu et al., IEEE Trans. Magn., **44**(1), 125–131 (2008)
[2] M. Takagishi et al., IEEE Trans. Magn., **57**(3), Art. no. 3300106 (2021).
[3] A. Takeo et al., Digest of TMRC 2020, **B1**, (2020).
[4] N. Narita et al., IEEE Trans. Magn., **57**(3), Art. no. 3300205 (2021).
[5] T. Olson et al., IEEE Trans. Magn., **51**(11), Art. no. 3001004 (2015).
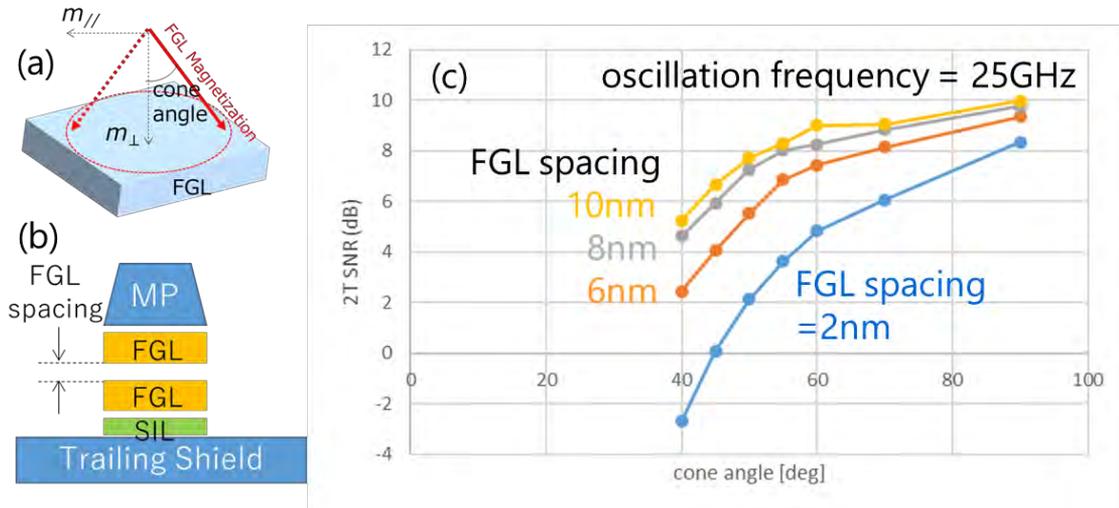
Fig. 1 (a) the definition of cone angle (b) the definition of FGL spacing (c) the relation between cone angle and 2T-SNR of dual FGL structure.
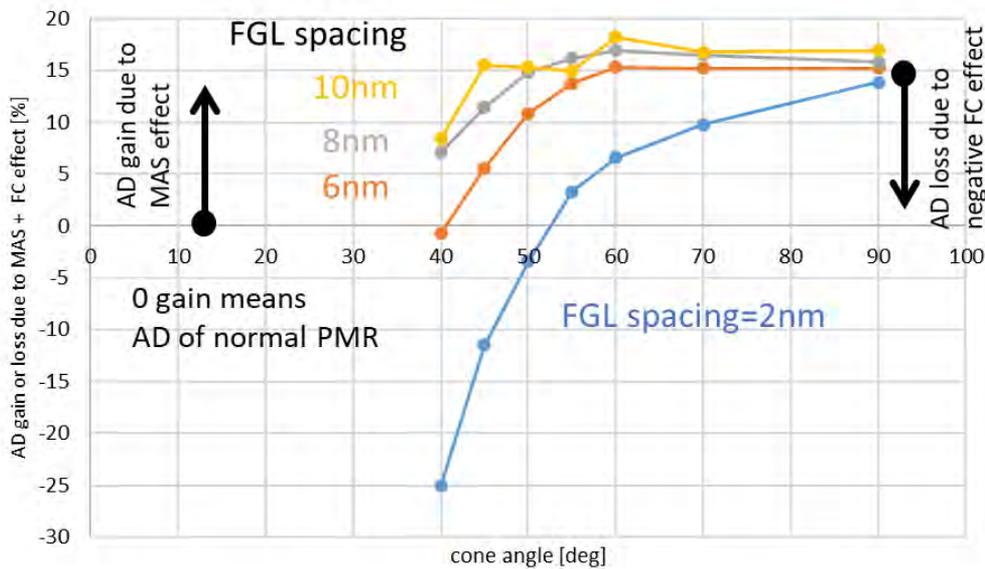
Fig. 2 The relation between cone angle and AD gain or loss of dual FGL structure

MEDIA OPTIMISATION FOR MICROWAVE-ASSISTED MAGNETIC RECORDING

Simon GREAVES[1]**, Ryo ITAGAKI**[2] **and Yasushi KANAI**[2]

1) RIEC, Tohoku University, Sendai, Japan, simon@riec.tohoku.ac.jp

2) IEE, Niigata Institute of Technology, Kashiwazaki, Japan, kanai@iee.niit.ac.jp

I. INTRODUCTION

Microwave-assisted magnetic recording (MAMR) makes use of a high frequency (HF) magnetic field generated by a spin torque oscillator (STO) to assist the switching of grains in the recording medium. The efficacy of MAMR is strongly linked to the strength of the HF field and is therefore highly dependent on the head-medium spacing.

The structure of the recording medium also has a significant effect on its response to the HF field. In this work we attempt to determine optimum recording medium structures for head-medium spacings of 4.5 nm, 9.5 nm and 14.5 nm.

II. THE MODEL

Recording media were 12 nm thick, consisting of a 4 nm hard layer capped by a 8 nm soft layer. Recording media were categorised into three types based on the variation of the uniaxial anisotropy (K_u) through the depth of the soft layer. Media in which the soft layer K_u was constant are termed ECC media. Media in which the soft layer K_u decreased towards the surface are called Graded media, and media in which the soft layer K_u increased towards the surface are denoted as Notched media. The soft layer was divided into four, 2 nm thick segments for the purpose of varying K_u.

A write head with a 40 nm wide main pole and 20 nm gap between the main pole and the trailing shield was simulated in a finite element model. The gap between the air bearing surface (ABS) of the main pole and the soft magnetic underlayer (SUL) was varied from 20 nm to 30 nm. Fig. 1 shows the vertical head fields in the recording layer for head-medium spacings of 4.5 nm, 9.5 nm and 14.5 nm.

Fig. 2 shows the maximum values of the HF fields from a 20 nm $\times$ 8 nm $\times$ 20 nm field generating layer (FGL) as a function of distance from the ABS. The rectangles show the fields applied to the recording media for each of the three head-medium spacings. When the head-medium spacing reached 14.5 nm the maximum in-plane HF field was about 300 Oe at the top of the recording medium.

Two hundred sequences of four bits with a 1/0/1/0 pattern were written on small portions of recording media. The average magnetisation of the second and third bits was used as a measure of the "signal" and the variation of the signal among the 200 tracks was the "noise". The "bit SNR" was calculated using these signal and noise values. This approach allowed the recording performance of the media to be evaluated much faster than by writing longer tracks in larger media instances.

III. RESULTS

Fig. 3 shows the bit SNR as a function of the soft layer K_u for a 9.5 nm head-medium spacing. The SNR was calculated for tracks written with and without a STO; the SNR gain from using MAMR depended on K_u soft, but was at least 2 dB. With or without the STO the SNR peaked when K_u soft was 15% - 17.5% of K_u hard.

Next, the average value of K_u soft was fixed and the soft layer K_u gradient was varied. Positive K_u gradients represent notched media (K_u increasing towards the surface) and negative K_u gradients are graded

Simon Greaves
RIEC, Tohoku University,
Katahira 2-1-1, Aoba ku,
Sendai, 980-8577
E-mail: simon@riec.tohoku.ac.jp
Tel: +81-22-217-5458

media. Fig. 4 shows the bit SNR as a function of soft layer K_u gradient for four average values of K_u soft. When K_u soft was 15% of K_u hard the SNR increased with the soft layer K_u gradient and the highest SNR was found for notched media.

As the average value of K_u soft increased, the optimum soft layer K_u gradient decreased. When K_u soft was 22.5% of K_u hard, ECC media had the highest SNR. When K_u soft reached 27.5% of K_u hard, graded anisotropy media were the best.

Based on the SNR values in fig. 4 it appears that notched media would give the highest SNR overall. However, the written track width should also be considered. In general, as the soft layer K_u gradient increased, the written track width also increased, meaning the track width was wider in notched media than graded media. A figure of merit (SNR / Track width) was used to compare the different media. Under this analysis notched media were still the best performers when the average soft layer K_u was sufficiently small, although the optimum point shifted to lower K_u gradients, i.e. closer to the ECC media.

Results for the other head-medium spacings will be presented in the talk. The conclusions are broadly the same, with the SNR gain due to MAMR showing a strong dependence on the head-medium spacing, as expected.
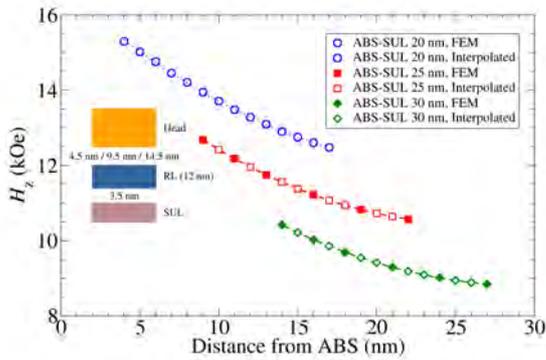
Fig. 1 Vertical component of head field underneath the trailing edge of the main pole for three head-medium spacings.
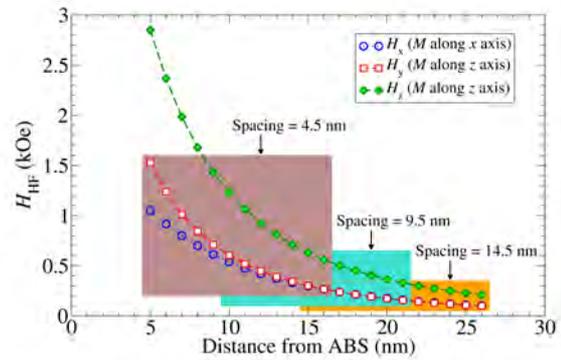
Fig. 2 Fields from FGL in recording media for three head-medium spacings. x = cross-track, y = down-track, z = vertical.
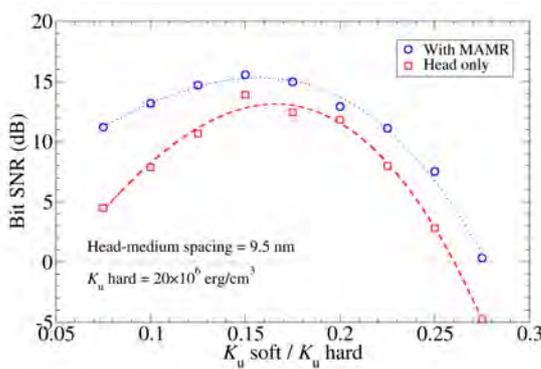
Fig. 3 Bit SNR vs. soft layer K_u for recording with / without a STO. Head-medium spacing = 9.5 nm, hard layer $K_u = 20 \times 10^6$ erg/cm^3.
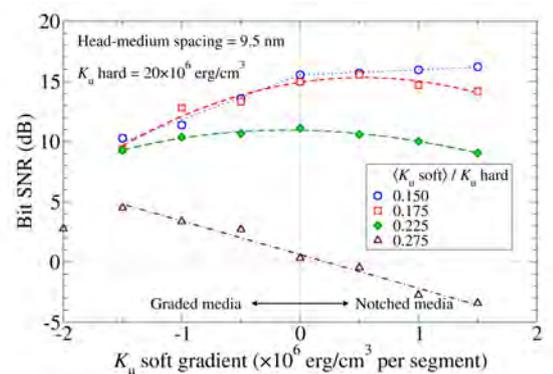
Fig. 4 Bit SNR vs. soft layer K_u gradient for various values of $\langle K_u$ soft$\rangle$. Head-medium spacing = 9.5 nm, hard layer $K_u = 20 \times 10^6$ erg/cm^3.

Spin Torque Oscillator for Microwave Assisted Magnetic Recording

Jian-Gang (Jimmy) Zhu

Data Storage Systems Center, Dept. of Electrical and Computer Engineering
Carnegie Mellon University, Pittsburgh, PA, USA

As microwave assisted magnetic recording (MAMR) and its precursor are starting to be employed into hard disk drive products [1-3], viable techniques enable efficient implementation of the technology becomes critically important. In this paper, we discuss a modeling study of a spin torque oscillator with a synthetic antiferromagnet trilayer as spin polarization layer.

In MAMR, the frequency of the assisting AC field is important for achieving recording performance enhancement [4]. Higher AC field strength also requires higher ac field frequency for reaching optimal area density gain. Such high frequency AC field is generated by a spin torque oscillator (STO), with a DC current injection, embedded inside the trailing shield gap of a write head [1]. The injected current becomes spin polarized by the spin polarization layer (SPL) in the STO. The transfer from the angular momentum of the spin polarized electrons generates an effective anti-damping torque in the field generating layer (FGL). The torque causes the magnetic moment of the FGL to orient away from the direction of the total magnetic field in the write gap, yielding magnetic moment rotation at roughly the ferromagnetic resonance frequency. It is important to note that the calculation results presented in this paper also considers the spin transfer torque in the SPL layer with the spin polarization resulted from FGL.

Figure 1 shows the design of the STO with SPL being a synthetic antiferromagnet of a Co/Ru/Co trilayer. The each of the two Co layers is assumed to have a thickness of 1 nm and the antiparallel coupling energy density is assumed to be $\sigma = -1.2$ erg/cm^2. The write head field inside the trailing shield gap is assumed to be $H=1.6$T and is assumed to be normal to the film plane of the STO. The head field switches its direction according to the binary write data at 1Gbps data rate with an assumed rise time of $\tau_r = 0.1$ns. The current injected to the STO a constant DC current. Figure 2 shows the FGL oscillating frequency as a function of injecting current density for different area moment density values, $M_s\delta$, of the FGL. In this case, the saturation magnetization of the FGL is kept at Ms=2.0Tesla while its thickness is varied. For the case with the highest $M_s\delta$ value, a 30GHz oscillation frequency can be reached. For the case of $M_s\delta =12.1$ nm*T, the peak frequency is $f_{peak} = 36$GHz. The chirality of the FGL magnetic moment rotation reverses its direction whenever the head field switches its polarity. The upper plot in Fig. 3 shows the time-domain waveform of in-plane FGL magnetization component perpendicular to air bearing surface. The lower plot shows the dynamic frequency plot over more expanded time region and the opposite sign indicates the opposite rotation chirality. Frequency and chirality switching are very sharp. Slight reductions of both amplitude and frequency right after the switching can be observed over a very small fraction of a nanosecond. After that, a steady oscillation is reached with the magnetization component over 90% in the film plane averaged over the entire FGL.

[1] J.-G. Zhu, et al, "Microwave Assisted Magnetic Recording," IEEE Trans. Magn., vol. 44, no. 1, 125-131, 2008.

[2] A. Takeo, et al. "Extended Concept of MAMR and Its Performance and Reliability," Paper C1, The Magnetic Recording Conference, 2020.

[3] N. Narita, et al, "Design and Numerical Study of Flux Control Effect Dominant MAMR Head: FC Writer," Paper C2, The magnetic Recording Conference, 2020.

[4]. J.-G. Zhu, "Impact of Spin Torque Oscillator Frequency in Microwave Assisted Magnetic Recording," IEEE Trans. Magn., vol. 55, No. 12, 6700808, 2019.
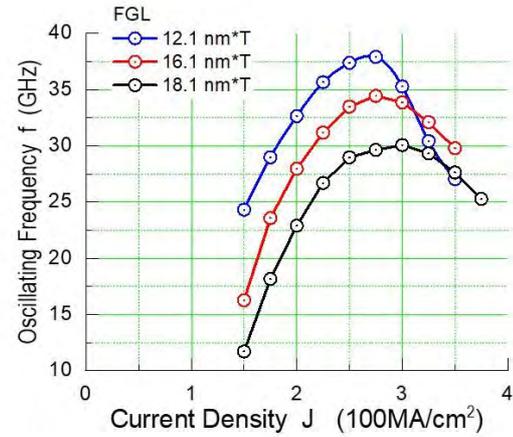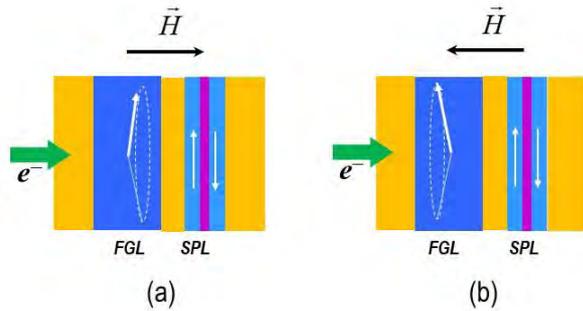
Fig. 1 Spin torque oscillator design with a synthetic antiferromagnet as the spin polarization layer. The write head field in the trailing shield gap are indicated in the figure and they are assumed to be normal to the film plane.

Fig. 2 The FGL oscillation frequency as function of the injected current density for three FGL thickness. The saturation magnetization is fixed at Ms=2.0Tesla.
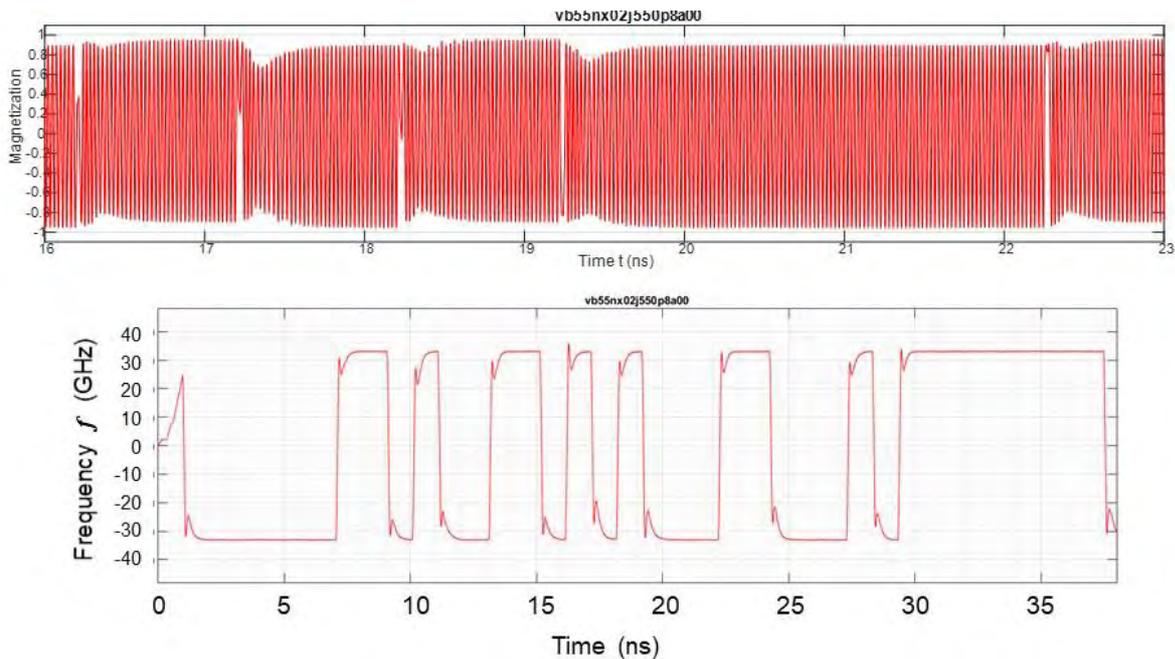
Fig. 3. *Upper:* Time domain profile of FGL in-plane magnetization component of the STO oscillation with write head field switching at 1Gbps with random binary data. *Lower:* Corresponding dynamic frequency of the FGL oscillation for an expanded time regime. Not the negative frequency indicates the opposite chirality.

TWO SERIAL MULTI-LAYER PERCEPTRONS FOR SIGNAL DETECTION AND MODULATION CODE DECODING FOR BIT-PATTERNED MEDIA RECORDING

Seongkwon JEONG[1] and Jaejin LEE[2]

1) Soongsil Univ., Seoul, South Korea, skwon917@gmail.com
2) Soongsil Univ., Seoul, South Korea, zlee@ssu.ac.kr

I. INTRODUCTION

Since conventional data storage systems are faced with difficult problems such as superparamagnetic limit and thermal effect, bit-patterned media recording (BPMR) which resolves these problems receives attention as a promising next generation magnetic data storage system. The advantages of BPMR are reduced track edge noise and nonlinear bit shift and easily simplified tracking. However, the reduced spacing between islands to increase areal density causes severe intersymbol interference (ISI) and intertrack interference (ITI) which degrade BPMR system performance. To prevent error patterns that bring more ITI, modulation coding schemes was proposed [1]. Also, to improve system performance, neural networks have been applied to detection and decoding in data storage system [2]. In this paper, we propose two serial multi-layer perceptrons (MLPs) which are used for signal detection and modulation decoding, respectively, for BPMR.

II. PROPOSED SCHEME USING TWO MLPS

Fig. 1 shows a block diagram of the proposed system. One-to-one mapping is used to encode user data a_k to encoded data $c_{j,k}$ before the $c_{j,k}$ passes through the BPMR channel. In the proposed scheme, two MLPs are used. In a first MLP as signal detector shown in Fig. 2(a), the readback signal $\mathbf{r}_{j,k}$ sequence from BPMR channel is an input value and the data $c_{j,k}$ of modulation encoder output before passing through the channel is a target value for MLP training. The MLP consists of an input layer, two hidden layers, and an output layer. A rectified linear unit (ReLU) and identity function are used as the activation function in all hidden layers and output layer, respectively. Each hidden layer has 64 neurons and the output layer has one neuron. A binary cross entropy is used as a loss function.

In a second MLP as modulation decoder illustrated in Fig. 2(b), the $\hat{\mathbf{c}}_{j,k}$ sequence from the output of the MLP as signal detector is input data. And we use one-hot encoding labels of $\mathbf{c}_{j,k}$ as target value. The MLP structure as MLP decoder is composed of an input layer, two hidden layers, and an output layer. The ReLU function as the activation function is used in all hidden layers. Since modulation decoder has to selects the one of best possible codeword among the codewords, softmax function is used as the activation function in the output layer for multiclass classification. Each hidden layer has 64 neurons and the neurons of output layer is the number of codeword. A categorical cross entropy is used as a loss function. The label with the largest probability value which is selected by the second MLP is determined as the transmitted codeword. The label is decoded by one-to-one demapping.

III. SIMULATION AND RESULTS

For performance evaluation, we simulate the proposed scheme at BPMR channel and use a 4/6 modulation code. To compare the BER performance, we use a partial response maximum likelihood (PRML) detector without the modulation at 2 Tb/in^2, which consists of 2D MMSE equalized with 1D GPR target and 1D SOVA, MLP modulation decoder with PRML at 3 Tb/in^2 [1], and the proposed scheme at 3 Tb/in^2. When the BER is 10^{-6}, the performance of proposed scheme is approximately 1.7 dB and 1.2 dB better than the PRML detector at 2 Tb/in^2 and MLP modulation decoder with PRML at 3 Tb/in^2, respectively.

Jaejin Lee
E-mail: zlee@ssu.ac.kr
tel: +82-2-8200901

IV. CONCLUSION

In this paper, we propose two serial MLPs which are used for signal detection and modulation decoding, respectively, for BPMR. Since each MLP is exploited as a signal detector and a modulation decoder, respectively, the proposed scheme shows better performance compared to the PRML detector and MLP modulation decoder with PRML.

REFERENCES

1) S. Jeong and J. Lee, "Modulation code and multilayer perceptron decoding for bit-patterned media recording", *IEEE Magn. Lett.,* 11 6502705, (2020).
2) S. Han, G. Kong, and S. Choi S, "A detection scheme with TMR estimation based on multi-layer perceptrons for bit patterned media recording", *IEEE Trans.Magn.*, 55(7) 3100704, (2019).
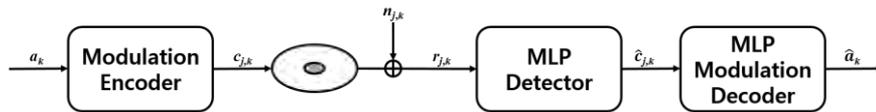
Fig. 1 Block diagram of the proposed scheme.
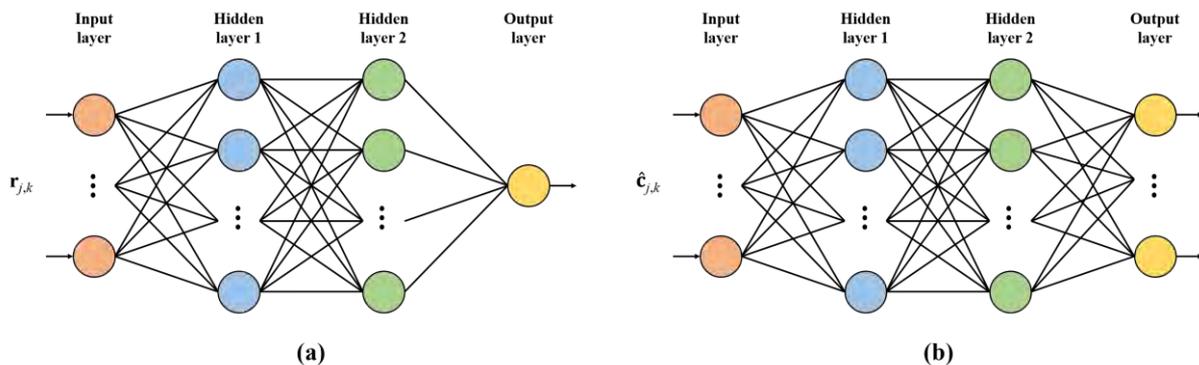
Fig. 2 Structures of the two MLPs as (a) signal detector and (b) modulation decoder.
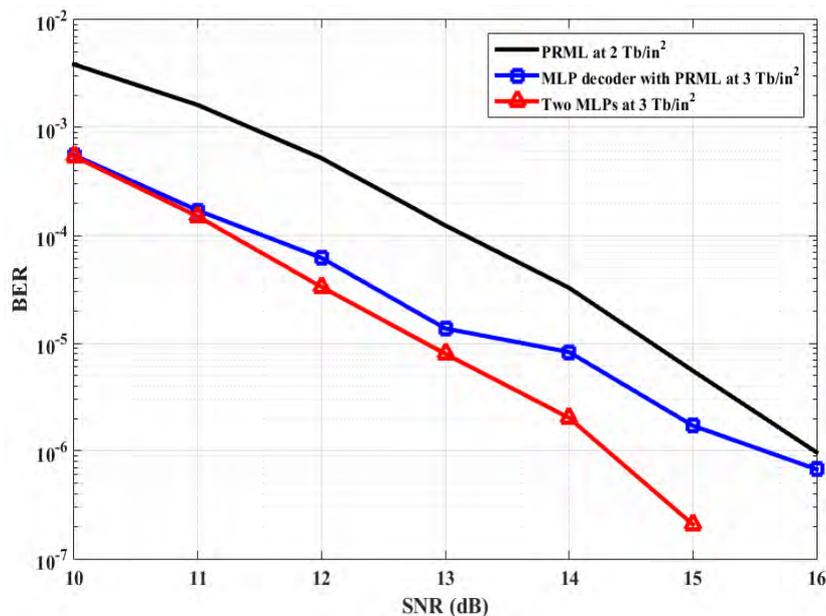
Fig. 3 BER performance of the proposed scheme according to SNR.

A STUDY OF PERFORMANCE EVALUATION WITH NEURAL NETWORK DETECTOR IN SMR SYSTEM

M. NISHIKAWA[1], Y. NAKAMURA[1], Y. KANAI[2], and Y. OKAMOTO[1]

1) Graduate School of Science and Engineering, Ehime University, Matsuyama, Japan,
{ nishikawa, nakamura, okamoto }@rec.ee.ehime-u.ac.jp

2) Department of Engineering, Niigata Institute of Technology,
Kashiwazaki, Japan, kanai@iee.niit.ac.jp

I. INTRODUCTION

We previously applied a neural network detector (NND) [1] to the low-density parity-check (LDPC) [2] coding and iterative decoding system in shingled magnetic recording (SMR) system [3]. In this study, we evaluate the performance of iterative decoding using a new NND by computer simulation. Furthermore, we clarify that the NND brings the almost same effect as the a posteriori probability (APP) decoder in the iterative decoding system.

II. READ/WRITE CHANNEL

Figure 1 shows the read/write system with the NND. The input sequence is encoded by a 128/130(0, 16/8) run-length-limited (RLL) encoder and a (30, 3)-regular LDPC encoder [2]. The recording sequence is recorded on a granular medium model [4] under the specification of 4 Tbit/inch^2. In the reading process, the decoding target track and the adjacent tracks are read composed by the array head with three readers at the same time [5], [6], and the additive white Gaussian noise (AWGN) is added to each waveform as the system noise. The signal-to-noise ratio (SNR) for the system noise at the reading point is defined as $\text{SNR}_S = 20\log_{10}(A/\sigma_S)$ [dB], where A is the positive saturation level of the waveform reproduced from an isolated magnetic transition and σ_S is the root-mean-square (RMS) value of the system noise in the bandwidth of the channel bit rate f_c. A channel bit response including read/write (R/W) process on the decoding target track is equalized to the partial response class-I (PR1) target [7] by the equalizer composed of three low-pass filters (LPFs) having cut-off frequency x_h normalized by the f_c and the two-dimensional finite impulse response (TD-FIR) filter with N_t taps. Therefore, the total number of taps for a reader is $3 \times N_t$. We assume that these parameters are set to $x_h = 0.4$ and $N_t = 15$. The output waveform from the PR1 channel is iteratively decoded by the turbo equalization performed between an NND and a sum-product (SP) decoder [8]. Here, i_{sp} and i_{global} stand for the maximum number of iterations in the SP decoder and the turbo equalization, respectively. After given iterations in the turbo equalization for the decoding target track, the output sequence is obtained through a hard decision unit and the RLL decoder. Finally, a bit error rate (BER) is provided by comparing the input sequence and the output sequences.

III. NEURAL NETWORK DETECTOR

Figure 2 shows the configuration of NND. The NND consists of the 3-layer neural network and the log-likelihood ratio (LLR) calculator. In the figure, D is the delay operator for a bit interval, $N_m(m = 1 \sim 3)$ is the number of elements in the mth layer, and $y_i^{(m)}$ is the output of the mth layer and i^{th} ($i = 1 \sim N_i$) element. We set $N_1 = 30$, $N_2 = 30$, $N_3 = 8$. At $i_{global} = 0$, the neural network calculates the factors to determine LLR_{NND} using only TD-FIR filter outputs, but in $i_{global} \geq 1$, it uses SP decoder inputs and outputs at $(i_{global} - 1)$ in addition to the TD-FIR filter outputs. In the training process, we set to the training signals for the 3 consecutive recording bits in the down-track direction. Thus, the elements in the 3$^{\text{rd}}$ layer output (1,0,…,0) for "000", (0,1,0,…,0) for "001", (0,…,0,1,0) for "101" for (0,…,0,1) for "100" as the training signals for the 3 consecutive recording bits "*0*" in the down-track direction, as well, (0,0,1,0,…,0) for "011", (0,0,0,1,0,…,0) for "010", (0,…,0,1,0,0,0) for "110" or (0,…,0,1,0,0) for "111" as the teacher signals for "*1*". Also, we use the soft-max function in the 3$^{\text{rd}}$ layer. Furthermore, LLR calculator provides LLR_{NND}

Madoka NISHIKAWA
E-mail: nishikawa@rec.ee.ehime-u.ac.jp
tel: +81-89-927-9776

defined as $\text{LLR}_{NND} = \ln\left((y_3^{(3)} + y_4^{(3)} + y_5^{(3)} + y_6^{(3)})/(y_1^{(3)} + y_2^{(3)} + y_7^{(3)} + y_8^{(3)})\right)$.

Figure 3 shows the BER performances for SNR_S. The symbols of the magenta circle, the blue triangle show the cases of the new NND at $i_{sp} = 1$ and $i_{global} = 24$ and the conventional NND [1] at $i_{sp} = 10$ and $i_{global} = 15$, respectively. Also, the symbol of the black square shows the case of the APP decoder at $i_{sp}= 10$ and $i_{global} = 10$. As can be seen from the figure, the system with the new NND improves about 1.0 dB in required SNR_S to achieve no-errors compared to the case with the conventional NND, and shows the almost same performance as the case with the APP decoder.

REFERENCES

1) M. Nishikawa, Y. Nakamura, H. Osawa, Y. Kanai, and Y. Okamoto, *Intermag 2021*, IP-07, (2021).
2) R. G. Gallager, *IRE Trans. Inform. Theory*, Vol.IT-8, 21-28 (1962).
3) R. Wood, M. Williams, A. Kavcic, and J. Miles, *IEEE Trans. Magn.*, 45(2) 917−923, (2009).
4) M. Yamashita, Y. Okamoto, Y. Nakamura, H. Osawa, S. J. Greaves, H. Muraoka, *IEICE Trans. Electron.*, E96-C(12), 1504−1507, (2013).
5) R. Suzuto, Y. Nakamura, H. Osawa, Y. Okamoto, Y. Kanai, and H. Muraoka, *IEEE Trans. Magn.,* 52(7) 3001604, (2016).
6) Y. Nakamura, R. Suzuto, H. Osawa, Y. Okamoto, Y. Kanai, and H. Muraoka, *AIP Advances*, 7(5) 056509-1−056509-5, (2017).
7) E. R. Kretzmer, *IEEE Trans. Magn.*, 14(1) 67−68, (1966).
8) P. Robertson, E. Villebrun, and P. Hoeher, *Proc. IEEE Int. Conf. Commun.*, 1009–1013, (1995).
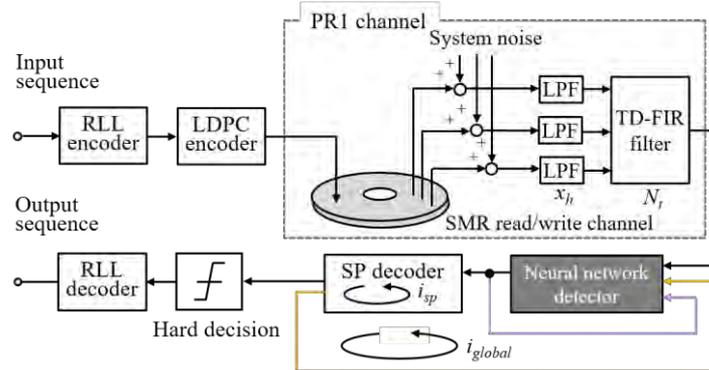
Fig. 1   Read/write system.
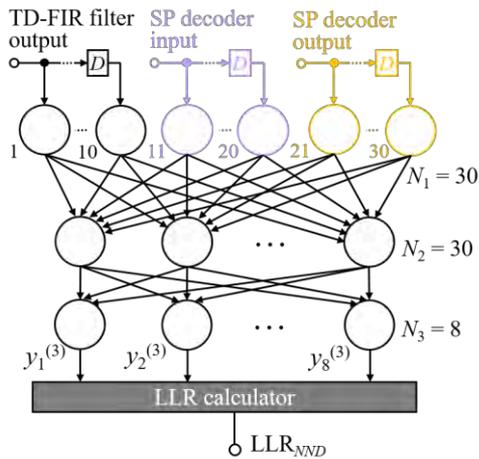

Fig. 2   Configuration of NND.
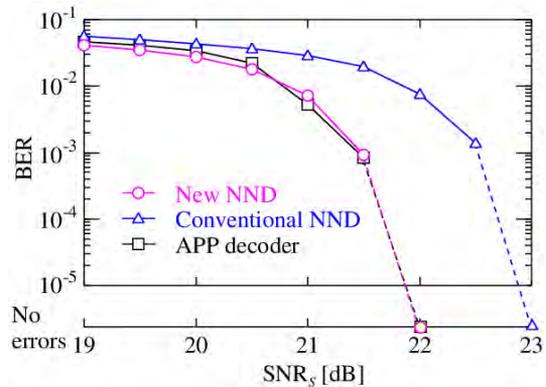
Fig. 3   BER performance for SNR_S.

A STUDY OF EQUALIZATION FOR REPRODUCING A DOUBLE-LAYER MAGNETIC RECORDING MEDIUM

Yasuaki NAKAMURA[1], Madoka NISHIKAWA[1], Yasushi KANAI[2], and Yoshihiro OKAMOTO[1]

1) Ehime University, Matsuyama, Japan, {nakamura, nishikawa, okamoto}@rec.ee.ehime-u.ac.jp
2) Niigata Institute of Technology, Kashiwazaki, Japan, kanai@iee.niit.ac.jp

I. INTRODUCTION

To increase the recording density of hard disk drives (HDD), the three-dimensional magnetic recording using microwave-assisted magnetic recording (MAMR) [1] with multiple recording layers is attracting much attention as a next-generation recording method. Developing a signal processing method for 3D magnetic recording using the multiple conventional recording layers and an MR head reading system [2] is desired. In this study, we evaluate two-dimensional partial response maximum likelihood (PRML) channels by the bit error rate (BER) performance, where the transfer function of the PR channel is determined by the response of the in-phase or differential-phase bits between layers in a double-layer magnetic recording medium [3].

II. DOUBLE-LAYER MAGNETIC RECORDING MEDIUM AND EVALUATION SYSTEM

Figure 1 shows the cross-section of head-medium geometry with the double recording layers. In this study, we assume that the writing process is a simple rectangular recording without the jitter, phase error, grain size fluctuation, and so on. We also assume that each stray field does not influence another layer. In this paper, the channel bit length l_c = 7.3 nm and the track pitch l_{tp} = 22.1 nm [4] are assumed. Thus each areal recording density is 4 Tbits/inch^2, and the gross areal recording density is 8 Tbits/inch^2. We define the magnetic spacing between the bottom of a reader and the top of each recording layer as Δ_1 and Δ_2. And we also define a magnetic spacing with a single recording layer as Δ.

Figure 2 shows the block diagram of the evaluation system with the double recording layers and an MR head reading. Here, the black thin and red thick arrowed lines show the discrete and mixed signals, respectability. In the writing process, the input data sequence #1 is recorded on the 1st layer, and the input data sequence #2 for the 2nd recording layer. In the reading process, the information written on each recording layer is read out in a lump as a reproducing waveform mixed by one MR sensor. The additive white Gaussian noise (AWGN) is assumed as system noise and is superimposed on the reproducing waveform. The signal-to-noise ratio (SNR$_S$) of the system noise for isolated waveform from magnetic transition at the reading point is defined as SNR$_S$ = $20\log_{10}(A_{4nm}/\sigma_S)$ [dB], where A_{4nm} is the positive saturation level of the waveform reproduced from an isolated magnetic transition at Δ = 4.0 nm and σ_S is the root-mean-square (RMS) value of the system noise in the bandwidth of the channel bit rate f_c = $1/T_c$. Then, the reproducing mixed-signal waveform is equalized to be the GPR characteristic by a low-pass filter (LPF) with a cut-off frequency x_h = 0.4 normalized by f_c and the finite impulse response (FIR) filter with 15 taps, where the tap-coefficients of the FIR filter are obtained by the mean squared error (MSE) algorithm. After that, the equalized mixed reproducing waveform is fed to the Viterbi detector which decodes the information written in the dual recording layers all at once separately outputs the reproduced data sequences of #1 and #2.

Figure 3 shows the channel time-domain responses without the system noise. The open green and purple circles show the responses for the layers with Δ = 2.0 nm and 5.0 nm, respectively. And the filled blue and red circles show the responses of in-phase and differential-phase bits between layers determined from the transfer functions of each recording layer. We determine the two-dimensional PR channels based on these in-phase and differential-phase responses.

Yasuaki NAKAMURA
E-mail: nakamura@rec.ee.ehime-u.ac.jp
tel: +81-89-927-9784

IV. SIMULATION RESULTS AND DISCASSION

Figure 4 shows the bit error rate (BER) performances of PRML channels for system noise. The filled blue and red circles show the BER's of PRML channels for in-phase and differential-phase responses, respectively. As can be seen from the figure, a BER of 10^{-4} can be achieved by the PRML channel for the differential-phase response with the SNR_S for system noise greater than 26.0 dB.

ACKNOWLEDGMENT

REFERENCES

1) J. Zhu, X. Zhu, and Y. Tang, "Microwave assisted magnetic recording," *IEEE Trans. Magn.*, 44(1) 125-131, (2008).
2) S. Greaves, Y. Kanai, and H. Muraoka, "Multiple layer microwave-assisted magnetic recording," *IEEE Trans. Magn.*, 53(2) 3000510, (2017).
3) Y. Nakamura, M. Nishikawa, Y. Kanai, and Y. Okamoto, "A study of multi-dimensional magnetic recording system with double recording layers", *Digest of INTERMAG 2021*, IP-08, (2021).
4) Y. Nakamura, H. Osawa, Y. Okamoto, Y, Kanai, and H. Muraoka, "Bit error rate performance for head skew angle in shingled magnetic recording using dual reader heads," *J. Appl. Phys.*, 117(17) 17A901-1-17A901-4, (2015).
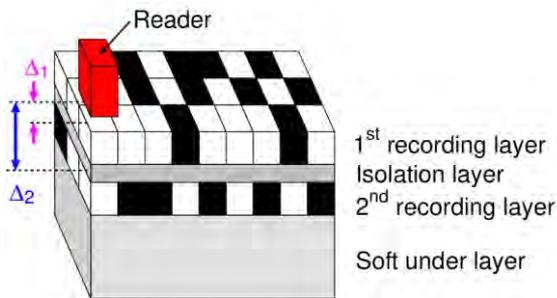
Fig. 1 Cross-section of head-media geometry for double recording layer medium and MR sensor.
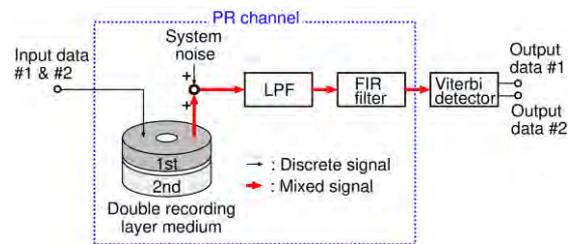
Fig. 2 Block diagram of the evaluation system with the double recording layers.
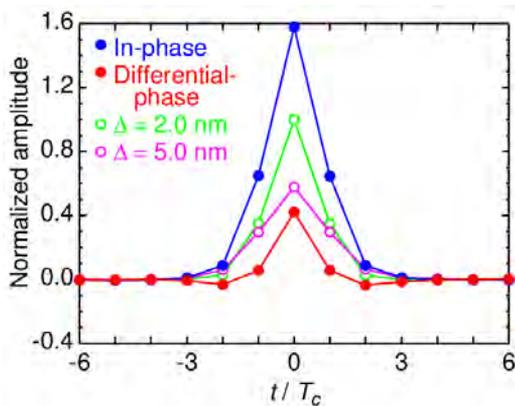

Fig. 3 Channel responses.
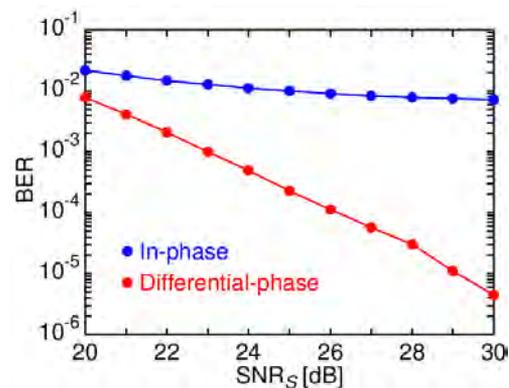
Fig. 4 BER performance for system noise.

Turbo-detection for Multilayer Magnetic Recording Using Deep Neural Network-based Equalizer and Media Noise Predictor

Amirhossein SAYYAFAN[1], Ahmed ABOUTALEB[1], Benjamin J. BELZER[1], Krishnamoorthy SIVAKUMAR[1], Simon GREAVES[2]

1) Washington State University, Pullman, WA, USA, (a.sayyafan, ahmed.aboutaleb, belzer, siva)@wsu.edu
2) RIEC, Tohoku University, Sendai 980-8577, Japan, simon@riec.tohoku.ac.jp

I. SYSTEM MODEL

In the hard disk drive (HDD) industry, new technologies are being developed to increase density such as two-dimensional magnetic recording (TDMR). TDMR utilizes 2D signal processing without changes to existing magnetic media to get remarkable density gains [1]. In multilayer magnetic recording (MLMR), an additional magnetic media layer is vertically stacked to a TDMR system to achieve additional density gains [2], [3]. We study deep neural network (DNN) based methods for equalization and detection for MLMR, using a realistic grain switching probability (GSP) model [4] for generating waveforms.

Fig. 1 shows a cross-track view of the MLMR system. There are six tracks written at track pitch (TP) 24 nm and bit length (BL) 10 nm on the upper layer. The three tracks are written at TP 48 nm and BL 20 nm on the lower layer. Thus, the system stores four bits on the upper layer for every one bit on the lower layer. To be consistent with [3], we denote the bit sequences written on the upper left and right tracks by $a_{2,L}$ and $a_{2,R}$ respectively, and the bit sequence on the lower track by a_1 for the tracks of interest. There are two boundary tracks $a_{b,L}$ and $a_{b,R}$ on the left and right sides of $a_{2,L}$ and $a_{2,R}$, respectively. Readings are obtained at track positions (relative to r_0, which is centered on track $a_{b,L}$) of 0, 24, 36, 48, and 72nm, from left to right, and denoted by r_0 to r_5, respectively.
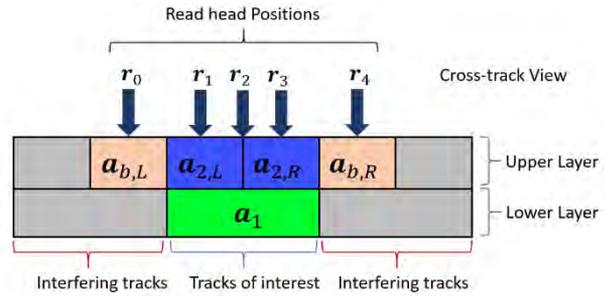

Fig. 1 Cross-track view of the MLMR System

The effective channel model has a media noise term which models signal dependent noise due to, e.g., magnetic grains intersected by bit boundaries. Trellis based detection with pattern dependent noise prediction (PDNP) [5] is standard practice in HDDs. The trellis detector sends soft coded bit estimates to a channel decoder, which outputs user information bit estimates. PDNP uses a relatively simple autoregressive noise model and linear prediction; this model is somewhat restrictive and may not accurately represent the media noise, especially at high storage densities. To address these problems, we design and train DNN based equalizer-separators and media noise predictors. The proposed turbo-detector assumes a channel model for the kth equalizer-separator output $\hat{\mathbf{s}}_k$:

$$\hat{\mathbf{s}}_k = (\mathbf{h}_k * \mathbf{u})(k) + n_m(k) + n_e(k), \tag{1}$$

where $\mathbf{h}_k$ is the partial response (PR) target, $\mathbf{u}$ are the coded bits on the track, $*$ indicates 1D/2D convolution, $n_m(k)$ is media noise, and $n_e(k)$ is reader electronic noise modeled as additive white Gaussian noise (AWGN).

In [3] we proposed a CNN equalizer-separator for MLMR followed by 1D soft output Viterbi Algorithm (SOVA) detectors for all three tracks a_1, $a_{2,L}$ and $a_{2,R}$. We proposed BCJR-LDPC-CNN turbo detectors for 1D magnetic recording (1DMR) and TDMR in [6]. This paper combines the equalizer-separator of [3] with a modified version of [6] designed for MLMR.

Fig. 2 Architecture of the CNN Equalizer-Separator

II. CNN EQUALIZER-SEPARATOR

We investigate a method for equalization of bit sequences a_1, $a_{2,L}$ and $a_{2,R}$ from readings r_0 to r_5 [3]. Fig. 2 illustrates a convolutional neural network (CNN) equalizer-separator. For the upper layer, the inputs include a sliding window of readings with the size of 5×17. For the lower layer, a rate converter multiplexes the additional readings across-track to have 10×17 input examples, since each reader collects two samples per lower

Benjamin J. BELZER
E-mail: belzer@wsu.edu
tel: +1-509-335-4970

layer bit, and to maintain a 17-bit down-track footprint. The CNN equalizer iterates with a constrained mean squared error (MSE) solver to adjust the PR target during the training. The lower layer CNN is provided with the reading samples $\mathbf{r}$ for the five sequences to generate the equalized waveforms $\hat{\mathbf{s}}_1$ for the lower track. The upper layer CNN produces the equalized waveform $\hat{\mathbf{s}}_2$ for the four upper tracks.

III. BCJR-LDPC-CNN TURBO-DETECTOR

Fig. 3 shows the MLMR BCJR-LDPC-CNN turbo-detector. BCJR-LDPC-CNN turbo-detectors for 1DMR and TDMR are employed for the lower and upper layers, respectively. For each layer's turbo-detector, the separate BCJR trellis-based ISI/ITI detector and CNN-based media-noise predictor exchange log-likelihood-ratio (LLR) and media noise estimates to iteratively reduce the BER until convergence. The upper layer's 2D-BCJR detector generates LLR estimates of $\boldsymbol{a}_{2,L}$ and $\boldsymbol{a}_{2,R}$ by performing ISI/ITI equalization on input $\hat{\mathbf{s}}_2$. Since the PR target $\mathbf{h}_2$ is 3×3, the 2D-BCJR state-input window is 2×3, and its trellis has 16 states. The CNN media noise predictor uses the 2D-BCJR LLRs $\mathbf{LLR}_{b_0}$ and $\hat{\mathbf{s}}_2$ to estimate the media noise $\hat{\mathbf{n}}_{m_2}$. The noise $\hat{\mathbf{n}}_{m_2}$ is fed back to the 2D-BCJR to obtain a lower BER. Next, the 2D-BCJR passes LLRs $\mathbf{LLR}_b$ to a low-density parity check (LDPC) decoder. At the end of each turbo-iteration, the decoder generates the final LLRs $\mathbf{LLR}_l$. The lower layer employs a 1D-BCJR with a three-tap PR target $\mathbf{h}_1$ to estimate $\boldsymbol{a}_1$, so its trellis has four states. Areal density (AD) is determined by increasing the LDPC code rate until the decoded BER is $\leq 10^{-5}$. Dotted lines in Fig. 3 indicate optional inner iterations between the BCJR layer detectors.

Fig. 3 BCJR-LDPC-CNN turbo-detector for MLMR system

IV. RESULTS AND DISCUSSION

Table I presents simulation results for the proposed turbo-detectors for MLMR on the GSP model [4]. Each block contains 82,412 bits per track on the upper layer and 41,206 bits per track on the lower layer. For the CNN equalizer-separator and BCJR-LDPC-CNN detector, we use 59, 1, and 20 blocks as the training, validation and test datasets respectivly. The average BERs before the LDPC decoder are shown in Table I. As a reference, we evaluate a one-layer TDMR system (without lower layer interference) with TP 24 nm and BL 10 nm using the upper layer's BCJR-LDPC-CNN architecture. The maximum code rate achieved by the reference system is 0.8222. In comparison, for the MLMR system, the maximum code rates are 0.7306 and 0.8195 on the upper and lower layers, respectively. Since there are four bits on the upper layer per one bit on the lower layer, the total rate of the MLMR system is 0.7306 + 0.8195/4 = 0.9354. *Thus, the areal density gain of the MLMR system over the TDMR system is (0.9354 – 0.08222)/ 0.8222 = 13.77%.* The conventional baseline comparison involving a linear equalizer followed by 1D-PDNP will be reported in an expanded version of this paper.

Table I Simulation results for MLMR

Method/ Layer	Detector BER	AD (Tb/in^2)	Code Rate
Reference	0.0146	2.2102	0.8222
Upper	0.0485	1.9640	0.7306
Lower	0.0274	0.5507	0.8195

REFERENCES

[1] K. S. Chan, R. Radhakrishnan, K. Eason, M. R. Elidrissi, J. J. Miles, B. Vasic, and A. R. Krishnan, "Channel models and detectors for two-dimensional magnetic recording," *IEEE Trans. Mag.*, vol. 46, no. 3, pp. 804–811, March 2010.

[2] K. S. Chan, A. Aboutaleb, K. Sivakumar, B. Belzer, R. Wood and S. Rahardja, "Data Recovery for Multilayer Magnetic Recording," *IEEE Trans. Mag.*, vol. 55, no. 12, pp. 1-16, Dec. 2019.

[3] A. Aboutaleb, A. Sayyafan, K. Sivakumar, B. J. Belzer, S. Greaves, K. S. Chan, and R. Wood, "Deep Neural Network-based Detection and Partial Response Equalization for Multilayer Magnetic Recording," *IEEE Trans. Mag.*, vol. 57, no. 3, pp. 1-12, March 2021.

[4] S. Greaves, K. S. Chan, and Y. Kanai "Areal Density Capability of Dual-Structure Media for Microwave-Assisted Magnetic Recording," *IEEE Trans. Mag.*, vol. 55, no. 12, pp. 1-9, Dec. 2019.

[5] J. Moon and J. Park, "Pattern-dependent noise prediction in signal dependent noise," *IEEE Jour. Sel. Areas Commun.*, vol. 19, no. 4, pp. 730–743, Apr 2001.

[6] A. Sayyafan, A. Aboutaleb, B. J. Belzer, K. Sivakumar, A. Aguilar, C. A. Pinkham, K. S. Chan, and A. James, "Deep Neural Network Media Noise Predictor Turbo-detection System for 1-D and 2-D Dimensional High-Density Magnetic Recording," *IEEE Trans. Mag.*, vol. 57, no. 3, pp. 1-13, March 2021.

MULTI-TRACK DETECTION ASSISTED BY MULTI-TASK NEURAL NETWORK USING 2D SOFT TRANSITION INFORMATION FOR HEAT ASSISTED INTERLACED MAGNETIC RECORDING

Yushu XU and Yao WANG

School of Electronic Information and Electrical Engineering, Shanghai Jiao Tong University, Shanghai 200240, China.

I. INTRODUCTION

The recently proposed heat assisted interlaced magnetic recording (HIMR) [1] can improve the areal density significantly compared to conventional heat assisted magnetic recording (HAMR). However, the circular thermal profile of top low temperature written tracks in HIMR system causes severe transition curvatures, which bring nonlinear distortions to readback signals. Moreover, the two-dimensional inter-symbol interference (ISI) and thermal jitters also become more severe with the increasing areal density, which degrade the bit error rate (BER) performance. Therefore, we proposed a novel multi-track detection algorithm based on the 2D soft transition information assisted multi-task neural network and modified BCJR detector (2DST-MTNN-MB), which can effectively mitigate the nonlinear distortion, 2D ISI and thermal jitters compared to the conventional 2D neural network and linear equalizers followed by 1D BCJR detector.

II. CHANNEL MODELING AND SIGNAL PROCESSING

By utilizing a simplified micromagnetic write model, the pseudo random bit sequence (PRBS) is written on the Voronoi grains with average size of 6nm in HIMR system. The medium is assumed as FePt with mean T_C of 775 K (σT_C=2% and σH_K=5%) and the writing temperatures for bottom tracks and top tracks are 1007 K and 792 K, respectively. The corresponding track width and bit length are 23nm and 9nm, respectively, which corresponds to the channel bit density of 3.12 Tb/in^2. Then the recorded bits are readback by using a read head array (RHA) with free layer length of 40 nm and magnetic fly height of 7 nm. In order to mitigate the nonlinear distortion of readback signals and obtain the estimated sidetracks during the multi-track detection, we proposed a multi-task neural network (MTNN) with joint loss function to minimize the equalization errors and the erroneous soft estimation of three tracks jointly. Here the readback signals of high temperature written sidetracks (HT1 and HT3) and low temperature written middle track (LT2) are fed into MTNN to obtain equalized signals [y_1, y_2, y_3] and soft estimation [$\tilde{a}_1, \tilde{a}_2, \tilde{a}_3$] of three tracks simultaneously (Fig.1(a)). Accordingly, the following 1D BCJR detector is modified by designing the branch metrics to include both the downtrack ISI and estimated inter-track interference (ITI) from sidetracks, shown as Eq. (1). Here the branch metric γ_2 of low temperature written track LT2 is taken as an example.

$$\gamma_2 = exp\left\{\frac{-[\vec{y}_2 - \boldsymbol{G_{2D}}*\boldsymbol{a} - (\overrightarrow{g_1}*\tilde{a}_1 + \overrightarrow{g_3}*\tilde{a}_3)]^2}{2\sigma^2}\right\} \tag{1}$$

where $\vec{y}_2$ refers to the equalized signal of LT2, $\boldsymbol{G_{2D}}$ refers to the 2D target, $\tilde{a}_1$ and $\tilde{a}_3$ are estimated sidetracks HT1 and HT3, $\overrightarrow{g_i}$ is the ith row of $\boldsymbol{G_{2D}}$, $\boldsymbol{a}$ is the recorded PRBS of HT1, LT2, HT3 and σ is the standard deviation of white Gaussian noise. This proposed algorithm is named as multi-task neural network and modified BCJR detector (MTNN-MB), which can mitigate the nonlinear distortion and estimate the ITI simultaneously. Additionally it is found that distinct transition patterns will cause constructive or destructive effect on the readback signal due to different erasures after write and 2D ISI effects. Here the transition patterns only consider the recorded bits prior to the current bit; hence the number of 2D transition patterns is 4 considering the symmetry of pattern, as shown in Fig. 1(b). The hard transition (HT) information is denoted as T=1 when the magnetization polarities of two adjacent bits are opposite and T=0 when the polarities are the same. Then the probability distribution functions (PDF) of readback signals' amplitude corresponding to different transition patterns are shown in Fig. 1(c). It is found that the averaged signal amplitude decreases with the increased transitions, and the polarity of readback signal even flips when the number of transition reaches 3. This is because increased transitions will cause more severe erasure after write effect and also deteriorate the readback signal due to the 2D ISI. Correspondingly the proposed multi-task neural network is further improved by using additional transition information to characterize the complex nonlinear relationship between transition patterns and readback signals. To mitigate the possible error propagation caused by the hard transition information, the soft transition (ST) information is defined by the probability of transition (Eq. (2)).

$$SPT(a, b) = P(a = 1) \cdot P(b = -1) + P(a = -1) \cdot P(b = 1) \tag{2}$$

where a and b are two adjacent bits, $P(\cdot)$ denotes the probability, $P(a = 1) = exp(L^{LDPC})/(1 +$

Yao Wang
E-mail: yaowang898@sjtu.edu.cn
tel: +86-13677620870

$exp(L^{LDPC})$) and $P(a = -1) = 1/(1 + exp(L^{LDPC}))$. L^{LDPC} refers to the log-likelihood ratio (LLR) outputted by LDPC decoder. The proposed 2DST-MTNN-MB algorithm is shown in Fig.1(a). During the first iteration, the readback signals of three tracks are fed into multi-task neural network (MTNN) to mitigate the nonlinear distortion of readback signal and obtain the soft estimations of three tracks simultaneously. Then the equalized signal and estimated sidetracks are embedded into the branch metrics of modified BCJR detector (Eq.(1)), and the following LDPC decoder outputs the decoded LLR, which is transformed into the soft 2D transition information (Eq.(2)). Here 2D transition information contains both transition information along the cross track and down track for HT1, LT2 and HT3, while the 1D transition information only considers the down track transition. Then during the second iteration, additional 2D soft transition information besides readback signals are sent to MTNN in order to assist both the equalization of signals and estimation of bits, which are then fed to the modified BCJR detector and LDPC decoder again. Similar equalization and detection process is implemented iteratively until the BER performances are not further improved.

III. RESULTS AND DISCUSSIONS

With numerical simulation, it is found in Fig.2 (a) that the conventional 2D neural network equalizer and 1D BCJR detector (2D-NNE-B) can provide 0.9 dB SNR gains compared to the 2D linear equalizer and 1D BCJR detector (2D-LE-B) for the low temperature written track (LT) since the former can mitigate the nonlinear distortion of readback signals caused by the thermal curvature effectively. More interestingly the proposed multi-task neural network and modified BCJR detector (MTNN-MB) can further provide 3.2 dB SNR gains compared to the conventional 2D-NNE-B algorithm since the neural network simultaneously outputs the soft estimation and equalized signals of three tracks, which can improve the multi-track detection since the estimated sidetracks' information provides more reliable ITI estimation compared to 2D-NNE-B algorithm. By using the additional 2D soft transition information in the multi-task neural network (MTNN), the 2DST-MTNN-MB algorithm (Fig.2 (a)) can obtain 2.0 dB SNR gains compared to MTNN-MB algorithm because the 2D soft transition information can facilitate the neural network to implement the equalization and estimation of three tracks more accurately. Additionally, compared to the MTNN using 2D hard transition information (2DHT-MTNN-MB) and 1D hard transition information (1DHT-MTNN-MB), the proposed 2DST-MTNN-MB algorithm can provide 0.8 dB and 1.0 dB SNR gains, respectively, since the soft estimated transition information can reduce the error propagation caused by the hard transition information. The proposed multi-track detection algorithm can also provide significant SNR gains compared to the conventional 2D-NNE-B and 2D-LE-B algorithms for the high temperature written tracks (HT), shown as Fig.2 (b).

REFERENCES

1) S. Granz, W. Zhu and E. Seng et al., "Heat-assisted interlaced magnetic recording", *IEEE Trans. Magn.*, 54(2)1-4, (2018).
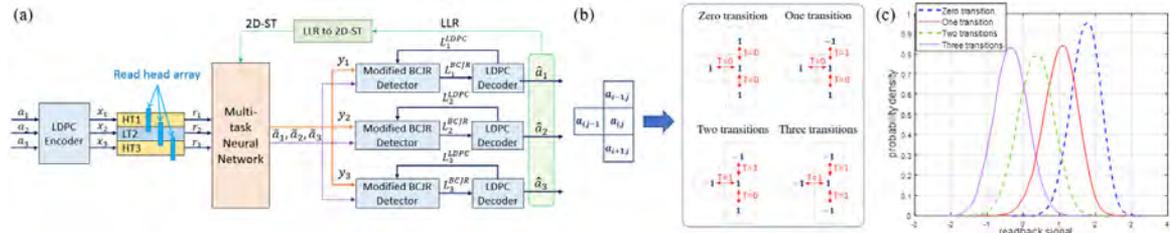
Fig. 1 (a) The proposed multi-track detection algorithm based on the 2D soft transition information assisted multi-task neural network and modified BCJR detector (2DST-MTNN-MB). (b) Various transition patterns ($a_{i,j}$ is the jth bit of ith track). (c) PDF of readback signal's amplitude for different transition patterns at SNR = 13dB.
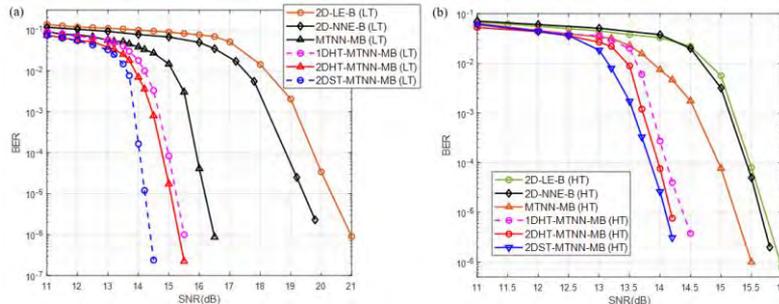

Fig.2 Decoded BER of (a) LT and (b) HT for the proposed 2DST-MTNN-MB algorithm.

EVALUATION OF SPUTTERED TAPE MEDIA WITH HARD DISK DRIVE COMPONENTS

Pierre-Olivier JUBERT[1], Yuri OBUKHOV[2], Cristian PAPUSOI[3] and Paul DORSEY[4]

1) Western Digital, San Jose, California, USA, Pierre-Olivier.Jubert@wdc.com

2) Western Digital, Rochester, Minnesota, USA, Iouri.Oboukhov@wdc.com

3) Western Digital, San Jose, California, USA, Cristian.Papusoi @wdc.com

4) Western Digital, San Jose, California, USA, Paul.Dorsey @wdc.com

Magnetic tape is used for deep archival storage as a means of storing large amount of infrequently accessed data. Current magnetic tape media consists of a random assembly of small Ba-Ferrite particles encapsulated in a polymeric film coated on a 5 micron-thick plastic substrate. The areal density in current tape products is about 11 Gb/in^2. Latest particulate media recording demonstrations have achieved 123 Gb/in^2 with 1600nm^3 BaFe particles and 317 Gb/in^2 with 950nm^3 strontium ferrite particles [1,2]. Hard-disk drives (HDD) have been using thin-film magnetic media for more than 40 years and current perpendicular magnetic recording technology in HDD products has achieved recording densities up to 1 Tb/in^2. As a result, there has been a strong interest to use sputtered thin-film media technology for tape recording. Recent developments in sputtered perpendicular magnetic recording thin film on tape have demonstrated recording densities up to 201 Gb/in^2 [3-5].

In this work, we evaluate the magnetic properties and the recording capability of sputtered tape media using hard-disk-drive components. The sputtered tape media, provided by Sony Storage Media Solutions Corporation, consists of a CoPtCr-SiO$_2$ granular magnetic layer capped with a thin CoPtCrB cap layer. We find that the magnetic cap improves the properties of the sputtered tape significantly. The recording performance is also much improved compared to samples without cap. We demonstrate that such sputtered tape could achieve an areal density of 400 Gb/in^2 under shingled magnetic recording (SMR) conditions. Comparison to a perpendicular magnetic recording disk having a similar magnetic stack and developed for HDD products in 2009 is also provided, showing potential for further improvements of the tape medium.

The microstructure of the sputtered media is measured using transmission electron microscopy. For all media, the stack includes TiCr/NiW seed layers, two Ru seed layers, a CoPtCr-SiO2 granular magnetic layer, a CoPtCrB magnetic cap of varying thicknesses, and a thin carbon overcoat. The structures and grain sizes of the magnetic layers are very similar for the tape media and the HDD medium. The magnetic properties are measured by polar Kerr (PK) and vibrating sample magnetometry. The cap layer is found to improve the medium switching field distributions, increase the grains lateral exchange and improve the media thermal stability. KV/k_BT varies from 69 without cap to 93 with 7-nm-thick cap. For comparison, KV/k_BT is 120 for the HDD medium.

The recording capability evaluation is performed using a piezo scanning write/read tester. Although different from the conditions of a reel-to-reel tester, for which the head/tape velocity is close to several meters per second, this approach allows us to compare the sputtered tapes and the HDD disk under the same recording settings. In addition, HDD head gimbal assemblies with state-of-the-art writer and reader components can be used for the evaluation of these thin-film media. Here, the HDD head uses a PMR single pole writer having a write width close to 100 nm and a TMR reader with a magnetic reader width of 30 nm. For areal density evaluation, 511-bit pseudo-random patterns are recorded on the media as isolated tracks and as shingled tracks with varying track offsets. This allows to test the media recording capability under SMR conditions and at different track densities. The recording linear density is also varied systematically in the range of 850kfci to 2540kfci. For each medium and each linear density, 20 such images are recorded and the readback waveforms are processed with a state-of-the-art HDD software channel model to extract, in particular, soft-output Viterbi algorithm bit-error-rate (SOVA-BER) as a function of linear density and SMR track density.

Fig. 1 shows the evolution of SOVA-BER as a function of the SMR track pitch for two sputtered tape media without cap and with a 7-nm-thick cap. The recorded linear density is 1270 kfci. It clearly illustrates

Pierre-Olivier JUBERT
Pierre-Olivier.Jubert@wdc.com
tel: +1-408-717-6071

the gain in recording performance provided by the addition of a magnetic cap with an optimized thickness.

The recording capability of the sputtered tape media with the optimized magnetic cap thickness is also evaluated at different linear densities. For each linear density, the SMR track pitch that gives a target SOVA-BER of 1e-(1.5) is determined. Fig. 2 shows different linear density and track density conditions that satisfy this BER target. The linear density is calculated with a code rate of 0.815, that include the LDPC code rate and track ECC and Reed-Solomon erasure protection. We find that the sputtered tape medium can satisfy the BER target at a linear density of 1035 kbpi and a SMR track pitch of 66 nm or track density of 386 ktpi. This corresponds to an areal density of 400 Gb/in^2.

Fig. 2 also shows the linear and SMR track density conditions that give a 1e-(1.5) SOVA-BER for the HDD perpendicular medium described above. The same head and recording conditions are used. As expected from the comparison of the media structures and magnetic properties, the HDD medium achieves a better recording performance, close to 600 Gb/in^2. This illustrates that the areal density of the sputtered tape medium with a single recording layer and a magnetic cap could be further improved.

REFERENCES

1) S. Furrer, "317 Gb/in2 Recording Areal Density on Strontium Ferrite Tape", *IEEE Trans Magn*. (2021).
2) M. A. Lantz, "123 Gbit/in2 Recording Areal Density on Barium Ferrite Tape", *IEEE Trans Magn*., 51(11) 3101304, (2015).
3) S. Furrer, "201 Gb/in2 Recording Areal Density on Sputtered Magnetic Tape", *IEEE Trans Magn*., 54(2) 3100308, (2018).
4) J. Tachibana, "Exploratory Experiments in Recording on Sputtered Magnetic Tape at an Areal Density of 148 Gb/in2", *IEEE Trans Magn*., 50(11) 3202806, (2014).
5) N. Sekiguchi., "The Development of Perpendicular Magnetic Recording Tape By Roll-to-Roll In-Line Sputtering", *IEEE Trans Magn*., 50(11) 3202904, (2014).
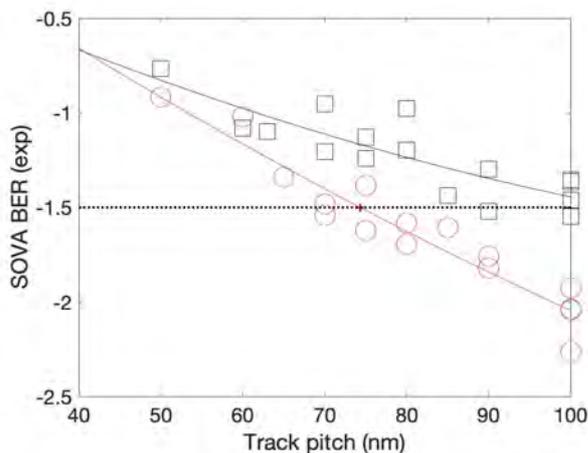
Fig. 1: *SOVA-BER vs. shingled track pitch for the sputtered tape media without cap (black square) and with a 7 nm cap (red circle).*
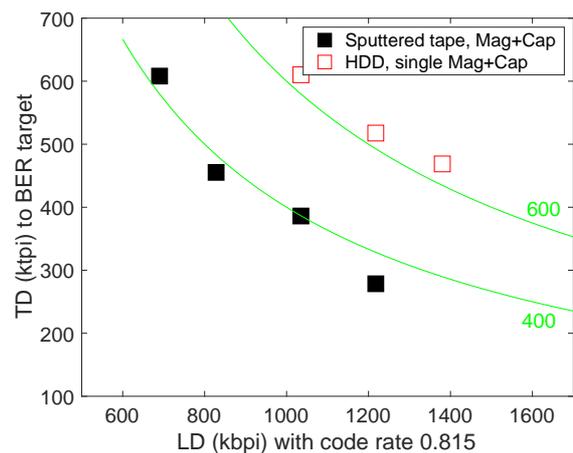

Fig. 2: *Recorded linear density and track density conditions that satisfy a SOVA-BER of 1e-(1.5).*

Causes of HAMR Transition Curvature Dependence on Bit Length

Kun XUE[1] and R. H. VICTORA[1]

1) University of Minnesota, Minneapolis, MN, USA, xue00050@umn.edu

I. INTRODUCTION

Heat Assisted Magnetic Recording (HAMR) technology has reached an areal density of over 2Tb/in^2, but the Signal to Noise Ratio (SNR) as well as the overall recording quality clearly decreases with the recording bit length (BL). In HAMR, recording patterns typically have a crescent shape due to the moving heat spot. The curvature of this crescent shape is of great significance as it is a source of transition broadening of the readback signal [1][2]. Various methods have been applied to determine and modify this curvature for better recording performance [3][4][5]. Thus, investigating how this curvature varies with different bit lengths and studying the change of this curvature during the HAMR writing process may help improve HAMR performance at the highest linear densities. Here, a detailed study of the dependence of curvature in HAMR transitions on bit length is presented.

II. NUMERICAL METHODS

With the help of micromagnetic simulations, HAMR transition patterns for three different bit lengths, 10.5nm, 15nm and 21nm, were obtained and analyzed. For each bit length, 256 bits were written on multiple media and overlapped. Curvatures were then calculated using these averaged patterns. AC-erased thermal Exchange Coupling Composite (ECC) media were used, where a superparamagnetic layer with high Curie temperature forms the writing layer and a doped FePt layer with relatively low Curie temperature serves as the storage layer [6]. The change in curvature during the cooling process was also tracked for pure FePt media. Transition slopes were investigated as well to make sure that no transition broadening happens. Curvatures of DC-erased thermal ECC media were tested as well for comparison. Introduction of intergranular exchange was also implemented to find potential optimizations of HAMR system designs.

Micromagnetic simulations in this study are guided by the Landau-Lifshitz-Gilbert equation. Renormalization group theory is applied to enable inclusion of atomic level phenomena [7]. Media dimension is 384nm x 48nm x 9nm. The averaged pattern on DC-erased media with BL 15nm is shown in Fig. 1. The left edge of the -1 bit (blue-colored) is chosen for curvature calculation. This curve is fitted to a parabolic curve and its second order coefficient multiplied by two is taken as its curvature.

III. RESULTS AND DISCUSSION

In HAMR, the cooling process could potentially modify the written bits as magnetic properties of the media materials, such as saturation magnetization and magneto-crystalline anisotropy, change greatly with temperature [6][7]. Curvatures before and after the cooling process for both AC-erased thermal ECC media and pure FePt media with BL10.5nm, 15nm and 21nm can be found in [8].

Basically, for both thermal ECC media and pure FePt media, curvatures experience a bigger drop during the cooling process for smaller bit lengths. The reason lies in the distance between the bit edge and the heat spot. When a -1 bit is just written, the left edge of this bit is about twice the bit length away from the heat spot. For BL10.5nm case, this distance is 21nm, which is much smaller than that for BL15nm and BL21nm cases. This implies that for BL10.5nm case, this bit edge is under a much higher temperature and spins here have a greater chance to be switched due to their reduced anisotropy fields. When the magnetic field switches as the head moves on, some spins at the edge area of this left bit edge would flip, which will flatten the curve and thus cause the curvature to decrease. This leads to the interesting conclusion that this enhanced erase-after-write effect is actually beneficial owing to the resulting reduction in curvature.

In order to further study the transition broadening issue, transition slope is also investigated. Fig. 2 shows the transition slopes (at middle of track) before and after cooling of thermal ECC media with BL15nm. The blue curve shows the magnetization slope before cooling, and its right half is a plateau since it's under high temperature and nothing has been written there yet. Once this bit is written as the heat spot

Kun Xue
E-mail: xue00050@umn.edu
tel: +1-215-9643077

moves rightwards, the slope of this part will go up and match that in the red curve (after cooling case). The transition slopes are found to remain the same during HAMR cooling process for both media, indicating that no transition broadening happens.

Curvatures for DC-erased thermal ECC media are found to be larger than those for AC-erased media in all three BL cases. This is because the +1 background of DC-erased media provides stronger dipole interaction than the averaged 0 background of AC-erased media. Spins have a higher switching probability, especially in the middle of the track. For AC-erased thermal ECC media, when intergranular exchange was introduced, a decrease in curvature was seen in all the three BL cases. This results from the weaker intergranular exchange effect received by the two transition corner areas than by the central areas due to the averaged 0 background. The two corners are then removed and the curvature is reduced.

REFERENCES

1) Liu, Z., Gilbert, I., Hernandez, S., Rea, C., Granz, S., Zhou, H., … Rausch, T. (2019). Curvature and Skew in Heat-Assisted Magnetic Recording. IEEE Transactions on Magnetics, 55(3).
2) Tseng, C. Y., Hurben, M. J., Sandler, G. M., Saunders, D. A., & Fernandez-De-Castro, J. J. (2011). Transition curvature and transition broadening analysis using the spin-stand imaging technique. IEEE Transactions on Magnetics, 47(10), 2974–2976.
3) Hashimoto, M., Salo, M., Ikeda, Y., Moser, A., Wood, R., & Muraoka, H. (2006). Analysis of written transition curvature in perpendicular magnetic recording for spin-stand testing. INTERMAG 2006 - IEEE International Magnetics Conference, 43(7), 448.
4) Zhu, J. G. J., & Li, H. (2017). Correcting Transition Curvature in Heat-Assisted Magnetic Recording. IEEE Transactions on Magnetics, 53(2).
5) Scholz, W., & Batra, S. (2005). Micromagnetic simulation of head-field and write bubble dynamics in perpendicular recording. IEEE Transactions on Magnetics, 41(10), 2839–2844.
6) Liu, Z., Jiao, Y., & Victora, R. H. (2016). Composite media for high density heat assisted magnetic recording. Applied Physics Letters, 108(23).
7) Victora, R. H., & Huang, P. W. (2013). Simulation of heat-assisted magnetic recording using renormalized media cells. IEEE Transactions on Magnetics, 49(2), 751–757.
8) Xue, K., & Victora, R. H. (2021). Dependence of HAMR transition curvature on bit length. IEEE Transactions on Magnetics. (under review)
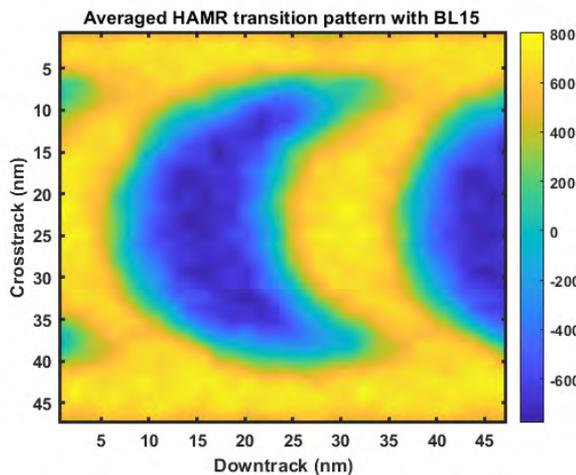
Fig. 1 Averaged HAMR transition patterns on DC-erased media with BL 15nm.
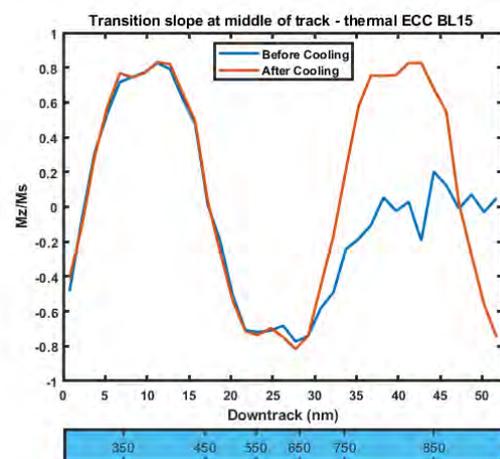

Fig. 2 Transition slope at middle of track before and after cooling of thermal ECC media with BL15nm. The blue bar shows the temperature values along the downtrack direction for the blue curve (before cooling).

STO OSCILLATION DEPENDENCE ON IN-GAP FIELD AND MAIN POLE MAGNETIZATION IN MAMR

Ryo ITAGAKI[1], Yasushi KANAI[1] and Simon J. GREAVES[2]

1) Niigata Institute of Technology, Kashiwazaki, Japan, {r_itagaki@cc, kanai@iee}.niit.ac.jp

2) Tohoku University, Sendai, Japan, simon@riec.tohoku.ac.jp

I. INTRODUCTION

Previously, we carried out micromagnetic simulations of write heads for microwave-assisted magnetic recording (MAMR) [1] and showed that a spin torque oscillator (STO) inserted into a write head gap did not oscillate as stably as a standalone STO due to magnetostatic interactions between the write head and STO [2] . In this paper, we investigated the effect of the magnetization rotation in the main pole and the in-gap fields on the STO oscillation. It was found that the write head gap structure affected the magnetization oscillation in the main pole (MP), which in turn affected the in-gap field, which then influenced the STO oscillation.

II. MODELS

Fig. 1 shows the write gap vicinity of the model used for the calculations, where θ represents the angle of the head gap and the STO. We assumed θ to be either 0° (we call this model "perpendicular" as the STO is perpendicular to the recording medium) or 15°. The gap length = 20 nm. As shown in Fig. 2, the size of the STO inserted into the write head gap was 20 nm × 20 nm × thickness. The thickness of each layer was: field generation layer (FGL) = 10 nm, spin injection layer (SIL) = 2 nm, and the non-magnetic layer between the FGL and SIL = 2 nm. The STO materials were: for FGL, saturation magnetization, $4\pi M_s$ = 18 kG, anisotropy field, H_k = 31.4 Oe, exchange, $A = 2.5 \times 10^{-6}$ erg/cm, and Gilbert damping factor, $\alpha = 0.01$; for SIL, $4\pi M_s$ = 9 kG, H_k = 31.4 Oe, exchange, $A = 1.25 \times 10^{-6}$ erg/cm, $\alpha = 0.05$. We assumed a STO using transmission spin torque. The overall dimensions of the write head were 2500 nm × 2500 nm × 2500 nm. Prior to the STO simulations, we carefully performed degaussing of the write head for 100 ns (80 ns with decaying coil current, then 20 ns without coil current). To solve the LLG equation with a spin-torque term, we used the FastMag Micromagnetic Simulator (Numerics and Design, Inc.).

III. RESULTS

Figs. 3 and 4 respectively show the results for $\theta = 0°$ and 15° (a) the magnetization oscillation, perpendicular to the STO, in the main pole at p_3 (Fig. 1), (b) the perpendicular component of the in-gap field applied to the STO at points p_1 and p_2 (Fig. 2), and (c) the y-component of the FGL rotation at points p_1 and p_2. The $\theta = 15°$ model had the following characteristics compared with $\theta = 0°$ model. 1) The MP magnetization in the main pole started to switch with a larger delay with respect to the coil current, while the switching duration was comparable. The perpendicular component of magnetization was larger and the oscillation due to the STO rotation was smaller. 2) The in-gap field was larger (35.8 kOe$_{pp}$ at p_1 and 42.6 kOe$_{pp}$ at p_2 compared with 30.5 kOe$_{pp}$ and 36.8 kOe$_{pp}$) and the delay was larger. 3) The FGL switching was faster with respect to the coil current despite the slower switching of the in-gap field, which is quite interesting. The switching duration was shorter, the oscillation was stabler and the oscillation frequency was higher (46.8 GHz vs. 32.0 GHz). Moreover, the FGL oscillation was more consistent between points p_1 and p_2. The stable oscillation of the $\theta = 15°$ model is considered to originate from weaker magnetostatic interactions. The higher frequency of FGL magnetization oscillation was due to the larger in-gap field. The large in-gap field and the weak magnetostatic interactions are considered to be the due to the tilted write gap structure.

REFERENCES

1) J.-G. Zhu, X. Zhu, and Y. Tang, *IEEE Trans. on Magn.*, 44(1), 125 (2008).
2) T. Katayama, et al., *Journal of App. Phys.*, 117, 17C503 (2015).

Ryo Itagaki
E-mail: r_itagaki@cc.niit.ac.jp
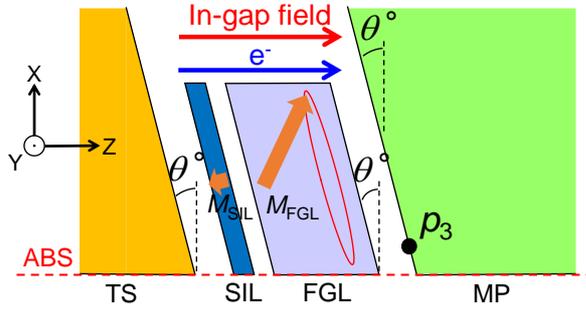
Fig. 1 Write head gap vicinity and arrangement of STO. p_3 shows the point where the MP magnetization was observed.
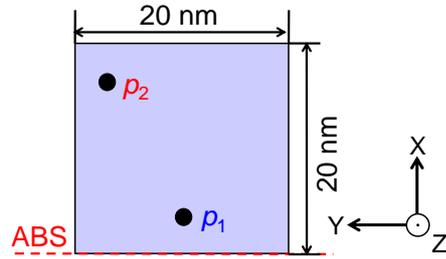
Fig. 2 Locations p_1 and p_2 where the in-gap field and magnetization were observed.
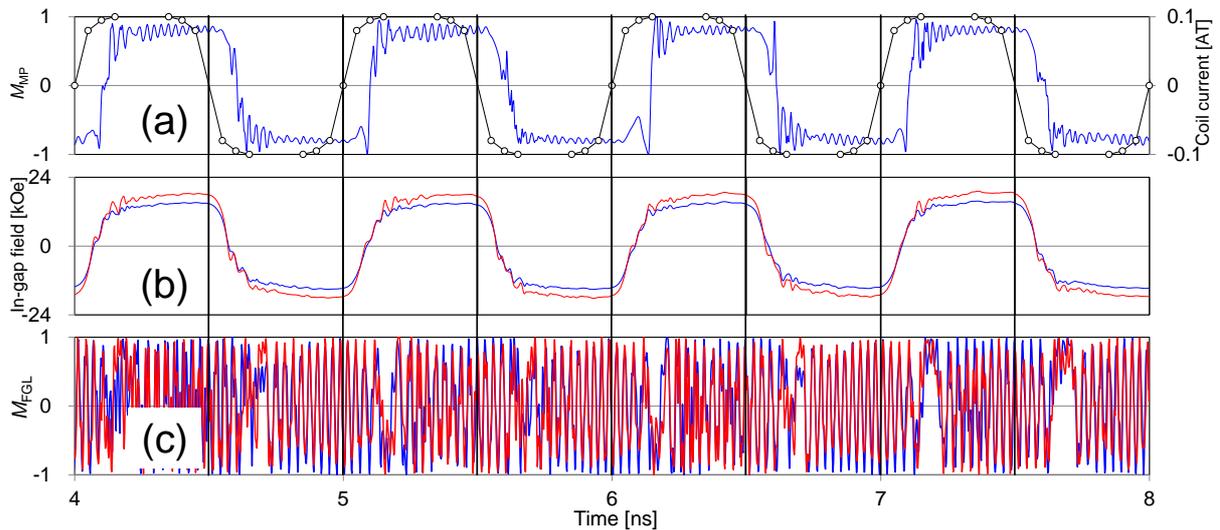
Fig. 3 (a) 1 GHz coil current and magnetization rotation, perpendicular to the STO, in the main pole at p_3, (b) perpendicular component of in-gap field applied to the STO at points p_1 (blue) and p_2 (red), and (c) in-plane component of FGL rotation at points p_1 (blue) and p_2 (red). $\theta = 0°$ model.
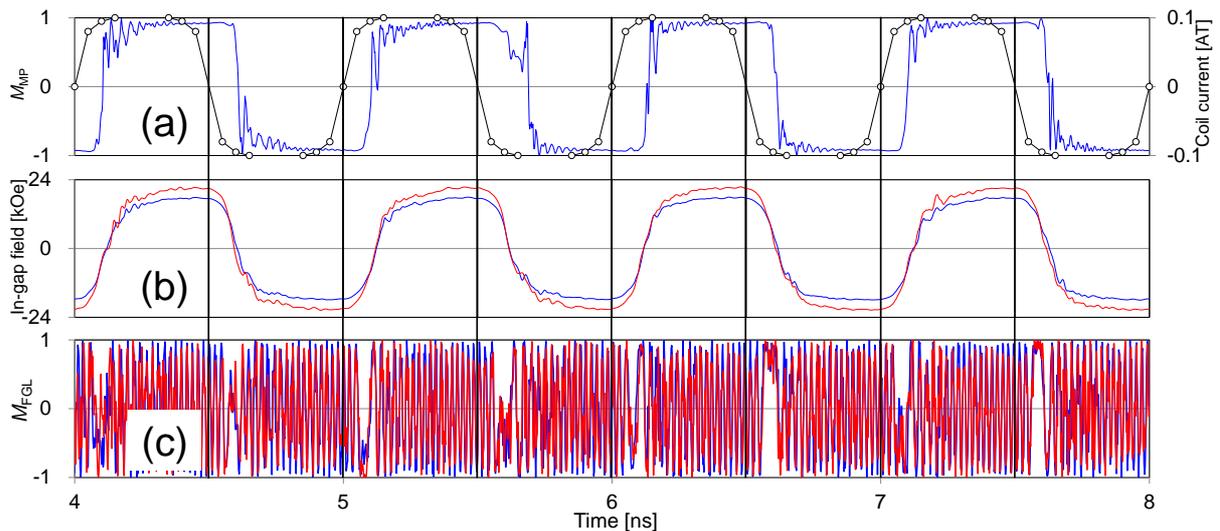
Fig. 4 (a) 1 GHz coil current and magnetization rotation, perpendicular to the STO, in the main pole at p_3, (b) perpendicular component of in-gap field applied to the STO at points p_1 (blue) and p_2 (red), and (c) in-plane component of FGL rotation at points p_1 (blue) and p_2 (red). $\theta = 15°$ model.

Large impact of spin asymmetry at half-metallic $Co_2Fe_{0.4}Mn_{0.6}Si$/CoFe interface on current-perpendicular-to-plane giant magnetoresistance

Y. Fujita[1], Y. Miura[1], T. Sasaki[1], T. Nakatani[1], K. Hono[1], and Y. Sakuraba[1]

1) National Institute for Materials Science, 1-2-1 Sengen, Tsukuba, Ibaraki 305-0047, Japan.

I. INTRODUCTION

Current-perpendicular-to-plane giant magnetoresistance (CPP-GMR) devices are promising for next-generation magnetic read-head sensors [1]. The resistance change-area product (ΔRA) in the CPP-GMR devices is largely influenced by the interface spin asymmetry (γ) at ferromagnet (FM)/nonmagnet (NM) interfaces [2]. Although previous investigations pay attention to γ at only FM/NM interfaces, spin-dependent scattering occurs even at FM/FM interfaces [3]. Actually, γ at the Co/Ni interface was estimated to be quite large, 0.94 at 4.2 K. Thus, the addition of FM/FM interfaces to FM/NM/FM CPP-GMR may result in the enhancement of ΔRA if large γ is obtained at FM/FM interfaces at RT.

Half-metallic FM (HMF)/FM interface is expected to generate quite large γ at RT because HMFs have a semiconducting gap only in one spin band. The half-metallic Co-based Heusler alloys, e.g., $Co_2Fe_xMn_{1-x}Si$ ($x = 0$ and 0.4), have widely been utilized in the CPP-GMR devices and large γ at the Co-based Heusler alloy/NM has successfully been verified by experiments and theoretical calculations [4,5]. Here, we show the presence of γ at half-metallic $Co_2Fe_{0.4}Mn_{0.6}Si$ (CFMS)/CoFe ($\gamma_{CFMS/CoFe}$) and its large impact on ΔRA at RT by first-principles ballistic transport calculations for (001)-CoFe/CFMS/CoFe and magnetoresistance (MR) measurements in fully epitaxial CPP-GMR devices with CoFe/CFMS layers.

II. FIRST PRINCIPLES BALLISTIC TRANSPORT CALCULATIONS

First-principles ballistic transport calculations were performed based on Landauer formula for (001)-CoFe/CFMS/CoFe. Conducting electrons are scattered due to the interfacial potential in the ballistic transport junctions. The open quantum system was consisting of a tetragonal supercell containing 13 atomic layers of CFMS and 7 atomic layers of CoFe. Figure 1(a) shows the in-plane wave vector ($\boldsymbol{k}_\parallel$) dependence of majority-spin and minority-spin conductance at the Fermi energy normalized by e^2/h averaged over the two-dimensional (2D) Brillouin zone (BZ) for CoFe/CFMS/CoFe with the FeMnSi-terminated CFMS layer and the Co-terminated CoFe layer. For the majority spin, highly conductive channels are distributed in almost whole region of $\boldsymbol{k}_\parallel = (k_x, k_y)$ in 2D BZ, while the minority-spin path has conductive channels with quite small conductivity only around $\boldsymbol{k}_\parallel = (\pm 0.5, \pm 0.5)$. Further, we obtained qualitatively the same result for CoFe/CFMS/CoFe with the Co-terminated CFMS layer and the Fe-terminated CoFe layer. Thus, it is indicated that larger resistance-area product (RA) for the minority-spin channel than that for the majority-spin channel and suggests large $\gamma_{CFMS/CoFe}$.

III. MEASUREMENT AND SIMULATION OF CPP-GMR DEVICES

We fabricated fully epitaxial CPP-GMR pseudo-spin valves (PSVs) with the entire structure of MgO(001) substrate/Cr(20 nm)/Ag(80 nm)/$Co_{50}Fe_{50}$ ($7 - t$ nm)/CFMS(t nm)/Ag(5 nm)/CFMS(t nm)/$Co_{50}Fe_{50}$ ($7 - t$ nm)/Ag(5 nm)/Ru(8 nm) with various t ($t = 0$, 0.75, 1.5, 3, 4, 5, and 7 nm) by processes with dc and rf sputtering at RT and *in-situ* post-deposition annealing in an ultrahigh vacuum sputtering system. We confirmed (001)-oriented fully epitaxial growth of PSVs by X-ray diffraction, the $L2_1$ ordered phase in the CFMS layers by nanobeam electron diffraction, and no atomic interdiffusion in the PSV by the energy dispersive X-ray spectroscopy (not shown here). We can confirm that the CoFe/CFMS/Ag/CFMS/CoFe PSV structure has flat and smooth interfaces from the cross-sectional high-angle annular dark-field scanning transmission electron microscope (HAADF-STEM) image in Fig. 1(b). Conventional processes were used to fabricate pillar-type CPP-GMR devices. MR effect was measured by a dc four-probe method at RT. Figure 1(c) shows MR curves observed in the devices with $t = 4$ nm (red) and $t = 7$ nm (blue). ΔRA for $t = 4$ nm (15.7 m$\Omega\mu m^2$) are clearly larger than for $t = 7$ nm (10.0 m$\Omega\mu m^2$), suggesting that the CFMS/CoFe structure can enhance ΔRA. ΔRA clearly has a peak at $t = 4$ nm in its t dependence as shown in Fig. 1(d). The ΔRA values for $t = 0$ nm (CoFe/Ag/CoFe), $t = 4$ nm (CoFe/CFMS/Ag/CFMS/CoFe), and $t = 7$ nm (CFMS/Ag/CFMS) were 4.05 m$\Omega\mu m^2$, 19.1 m$\Omega\mu m^2$, and 9.25

Yuichi Fujita
E-mail: FUJITA.Yuichi@nims.go.jp
tel: +81-29-851-3354(6819)

mΩμm², respectively. The larger ΔRA for $t = 7$ nm compared to that for $t = 0$ nm is attributed to the enhancement of bulk spin asymmetry of FM and γ at FM/NM interface by changing FM from CoFe to CFMS. To explain the origin of the entire t-dependence of ΔRA in Fig. 1(d), we additionally consider the presence of $\gamma_{CFMS/CoFe}$. The t dependence of ΔRA with a peak was qualitatively reproduced by the simulation based on the generalized 2CSR model [6] with considering $\gamma_{CFMS/CoFe}$ as shown in Fig. 1(e). Thus, the t-dependent behavior of ΔRA in Fig. 1(d) is the direct evidence for the large impact of $\gamma_{CFMS/CoFe}$ on the GMR effect at RT.

IV. CONCLUSION

We presented the existence of $\gamma_{CFMS/CoFe}$ and its large impact on GMR effect. The first-principles ballistic transport calculations for (001)-CoFe/CFMS/CoFe exhibited strongly spin-dependent conductance at the CFMS/CoFe interface, suggesting large $\gamma_{CFMS/CoFe}$. ΔRA observed in the fully epitaxial CPP-GMR PSVs with top and bottom CFMS(t nm)/CoFe($7 - t$ nm) ($0 \le t \le 7$) layers showed t dependence with a clear peak, which was reproduced qualitatively by the simulation based on the generalized 2CSR model by considering $\gamma_{CFMS/CoFe}$. Since the effect of γ at HMF/FM interface on the enhancement of ΔRA is expected to be obtained even in polycrystalline CPP-GMR devices, introducing additional γ at HMF/FM interface by forming HMF/FM/NM /FM/HMF structure in CPP-GMR devices will lead to the improvement of sensitivity of CPP-GMR read-head sensors [1]. This work was partly supported by KAKENHI (Nos. 17H06152, 20H02190, and 20K22487) from JSPS.

REFERENCES

1) T. Nakatani *et al*., "Advanced CPP-GMR spin-valve sensors for narrow reader applications", *IEEE Trans. Magn.* **54**(2), 1-11 (2018).
2) J. Bass, "CPP magnetoresistance of magnetic multilayers: A critical review", *J. Magn. Magn. Mater.* **408**, 244 (2016).
3) H. Y. T. Nguyen *et al*., "Conduction electron scattering and spin flipping at sputtered Co/Ni interfaces", *Phys. Rev. B* **82**, 220401(R) (2010).
4) Y. Sakuraba *et al*., "Mechanism of large magnetoresistance in Co₂MnSi/Ag/Co₂MnSi devices with current perpendicular to the plane", *Phys. Rev. B* **82**, 094444 (2010).
5) Y. Miura *et al*., "First-principles study of ballistic transport properties in Co₂MnSi/X/Co₂MnSi (001) ($X =$ Ag, Au, Al, V, Cr) trilayers", *Phys. Rev. B* **84**, 134432 (2011).
6) N. Strelkov *et al*., "Extension of the semiclassical theory of current-perpendicular-to-plane giant magnetoresistance including spin flip to any multilayered magnetic structures", *J. Appl. Phys.* **94**, 3278 (2003).
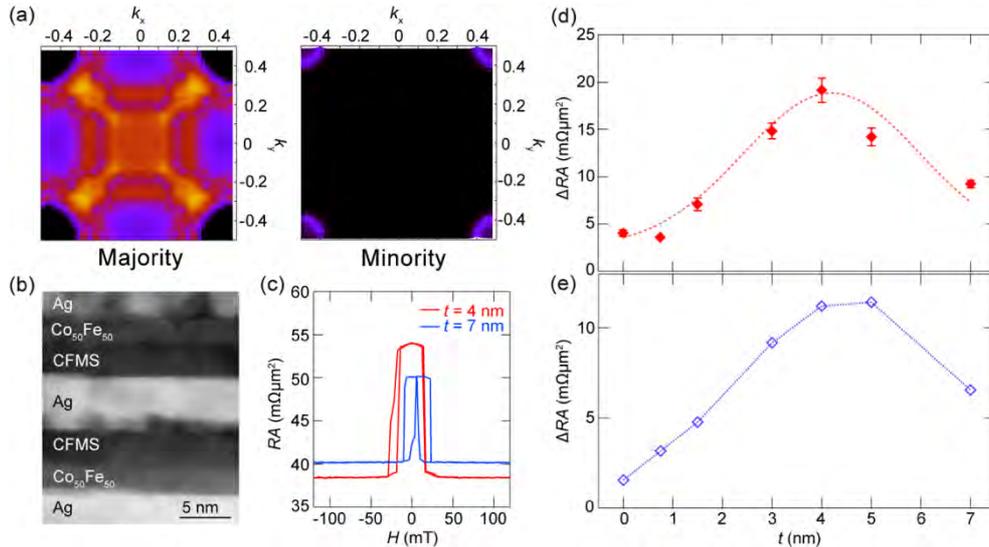
Fig. 1 (a) $k_\parallel$ dependence of majority-spin (left) and minority-spin (right) conductance at Fermi energy for (001)-CoFe/CFMS/CoFe. (b) Cross-sectional HAADF-STEM image of the fabricated PSV. (c) MR curves for $t = 4$ nm (red) and $t = 7$ nm (blue). (d) Observed and (e) simulated ΔRA as functions of t.

The Practical Material Challenges Involved in using the Topological Insulator BiSb in a Spin Transfer Device

B. York[1*], P. Hai, Q. Le[1], C. Hwang[1], K. Nguyen[1], H. Ho[2], J. Sasaki[2], X. Liu[1], S. Le[1], M. Ho[1], H. Takano[1]

1) Western Digital Corporation, San Jose CA, USA

2) Tokyo Institute of Technology, Tokyo Japan

*Email: brian.york@wdc.com

Introduction

The Topological Insulator (TI) BiSb, grown with a (012) film texture using molecular beam epitaxy, and coupled with a FM layer has been shown to have a very high Spin Hall Angle (SHA) > 2 and high electrical conductivity ($>10^5$ Ohm^{-1}m^{-1}) in thin film stacks[1]. This makes the TI material ideally suited for spin transfer devices requiring several orders of magnitude less power consumption to operate than other traditional devices[2]. However, the practical implementation of this TI material into devices using PVD requires you overcome many severe material challenges. The BiSb material is very soft, easily damaged in ion milling or by subsequent depositions, it has a very low melting point ~ 280C, and hence possesses a very large in-plane grain size as deposited at room temperature, ~6X the targeted thickness in devices. Thermal Migration of Sb out of the TI material is also a severe problem, which is exacerbated by film roughness and large grain sizes, and all of this must be solved while growing and maintaining a non-prismatic (012) texture of BiSb with low roughness, good interfacial TI properties, at reasonable operating temperatures > 180C in actual device stacks, non-epitaxially on SiOx or ceramic substrates. We discuss here how we addressed these challenges through appropriate selection of epitaxial and non-epitaxial materials for buffer layer(s) (bottom interface), and (top interface) interlayer(s), and by using a non-uniform thickness doping of the BiSb(X) material to stabilize and grow a BiSbX(012) textured layer with low roughness, good TI properties, at elevated temperatures in FM thin film stacks.

Results and Discussion

Early on it was shown that BiSb could be grown with a (001) orientation on surfaces with a 3-fold symmetry, by MBE on GaAs(111) substrates[1], and with a (012) orientation on surfaces with a 4-fold symmetry, on MBE grown MnGa(001) thin films on GaAs(100) substrates[2]. More recently[3] it has been shown that pure Bi(012) oriented films could be grown in ultra-thin films < 40A thick on 3-fold symmetry Si(111) substrates, and with slightly modified lattice parameters of Bi1-xSbx alloys in the range of 9at.% to 26 at% Sb, much thicker (012) oriented BiSb alloy films, ~ 500A could be grown, on 3 fold (111)Si substrates. We have shown that higher Sb concentrations larger than 26 at.% Sb, are outside the matching condition and revert back to a more stable (001) orientation. It is much more difficult to grow the non-prismatic (012) orientation in polycrystalline BiSb films in the useful TI range of 8 at% to 22 at.% Sb, then the prismatic (001) orientation, without special buffer layers. Figure 1 shows the use of thin (111) oriented polycrystalline buffer layer A (~18A thick) with the correct lattice matching range can be used to grow a strong BiSb(012) oriented polycrystalline film on a thermal oxide Si wafer (SiOx), while buffer layer B (~12A) outside this matching range, grows a strong (001) oriented BiSb polycrystalline films. Because of the low melting point (~ 280C), low modulus, and high atom mobility, polycrystalline thin films of BiSb are easily grown with large grain size, and roughness at RT. Rough films generally promote significant Sb migration out of the bulk of the BiSb layer at RT. Significant reduction of the Sb migration can be accomplished by reducing the roughness of the BiSb layer and/or through buffer or interlayer confinement layers which also promote and control (012) growth. Dopants can be added to BiSb to reduce the as-deposited grain size by about a factor of 2X while still maintaining good TI surface properties with lower roughness, and

improved (012) oriented growth. Dopants are selected to have limited interaction with Sb and Bi (many potential dopant elements will interact with Sb at temperature then with Bi), but still maintain interfacial TI properties. In general, there is an optimum dopant level range (nominally between 3-12 at. %) were as-deposited film roughness, in the 50-200A thickness range, remains low and increases above and below this range but still retains good TI properties. However, dopants with increased reactivity with either Sb or Bi at temperature will likely show poorer surface conduction (TI) properties on anneal. It is possible to find dopants with low reactivity to Sb (Bi) which not only reduce roughness, maintain or control (012) orientation during growth, but also maintain good TI surface conduction properties at elevated temperatures. Using such dopants in combination with buffer and interlayers which control and maintain (012) oriented growth serve as Sb confinement layers keeping the Sb within the BiSb layer at higher processing temperatures.

Figure 1 (a) Conductivity vs. film thickness of BiSb film with dopant levels for X,Y given, (b) Resistance change of 100A thick BiSbX, BiSbZ films vs. temperature, (c) Grain size and roughness of BiSbX vs X, (d) as deposited and 280C 3hr. post annealed BiSbX – XRD in-plane patterns (taken at RT).
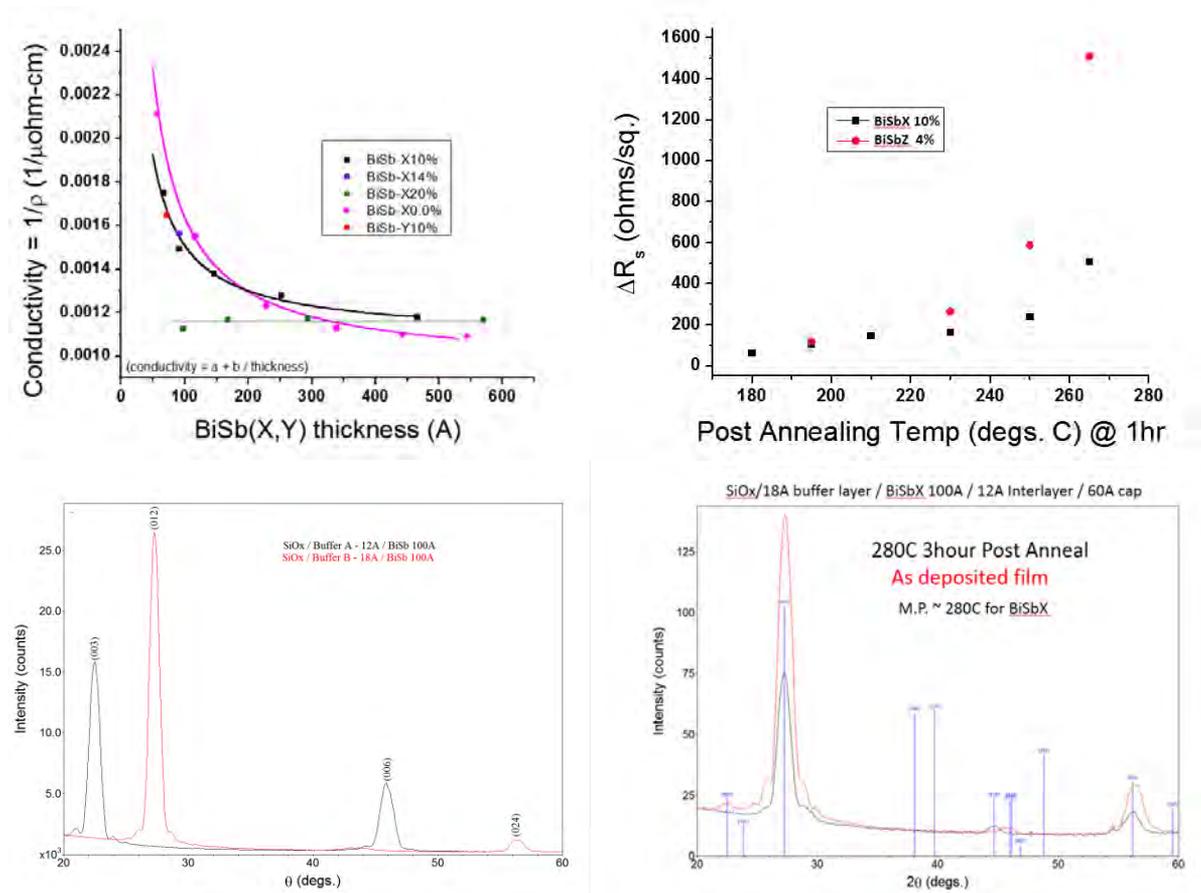
References

1. Y. Ueda, et.al., APL, 2017

2. N.H.D. Khang, et.al., Nat. Mater. 17, 808-813 2018

3. E. Walker et.al., Phys Rev Mater., 3, 064201 2019

Noble metal underlayer influence on the temperature-dependent Gilbert damping in L1$_0$ FePd films with large perpendicular magnetic anisotropy

Dingbin HUANG[1], Delin Zhang[2], Jian-Ping WANG[3], Daniel B. GOPMAN[4], and Xiaojia WANG[5]

1) Univ. of Minnesota, Twin Cities, Minneapolis, MN, USA, huan1746@umn.edu

2) Univ. of Minnesota, Twin Cities, Minneapolis, MN, USA, dlzhang@umn.edu

3) Univ. of Minnesota, Twin Cities, Minneapolis, MN, USA, jpwang@umn.edu

4) National Institute of Standards and Technology, Gaithersburg, MD, USA, daniel.gopman@nist.gov

5) Univ. of Minnesota, Twin Cities, Minneapolis, MN, USA, wang4940@umn.edu

I. INTRODUCTION

The moderate bulk perpendicular magnetic anisotropy (PMA, $K_u \approx 1$ MJ/m^3) and low Gilbert damping ($\alpha < 0.01$) make L1$_0$-FePd a strong candidate for energy efficient, dense spintronic devices with non-volatility down to 10 nm pitch or even lower. Existing applications subject spintronic devices to a wide temperature operating range from –55°C to 150°C [1]. In order to better address the technological viability of FePd based devices, it is of utmost importance to evaluate the anisotropy strength and Gilbert damping of L1$_0$-FePd at elevated temperatures.

We have previously demonstrated the robust thermal stability of Ru-seeded L1$_0$-FePd which can sustain a low Gilbert damping (ranging from 0.006 to 0.012) as the testing temperature varies from room temperature (RT, 25°C) to 150°C [2]. This study suggests the great potential of Ru-seeded FePd in magnetic tunnel junctions (MTJs) for device operation at elevated temperatures. Following this, we have systematically explored the engineering of buffer/seed layers (*e.g.*, Cr/Pt, Cr/Ru, Cr/Ir, Cr/Rh, Mo/Ir, and Ir) to simultaneously optimize the K_u and α of L1$_0$-FePd at RT [3]. It was found that the L1$_0$-FePd film buffered with Cr/Pt has the highest PMA ($K_u \approx 0.9$ MJ/m^3) while the one buffered with Cr/Ru has the lowest damping ($\alpha \approx 0.008$) at RT. Motivated by our prior studies, we will further examine the impacts of buffer layers on the Gilbert damping and PMA of FePd at elevated temperatures (up to 150 °C) using the ultrafast, laser-based time-resolved magneto-optical Kerr effect (TR-MOKE) metrology.

II. SAMPLE INFORMATION AND METHODOLOGY

The sample stack consists of MgO(001, sub.)/[buffer layer]/FePd(8)/Ru(2)/Ta(3) (numbers in parentheses are in nanometers). The buffer layers are Cr(15)/Ru(4) and Cr(15)/Pt(4). For comparison, an 8-nm FePd film on MgO substrate without any buffer layer was also prepared. All films were deposited at 350°C by ultrahigh vacuum dc magnetron sputtering and post-annealed *in situ* at 500°C for 30 min, leading to a moderate degree of L1$_0$ order greater than 0.6. Details about the sample preparation, structural and magnetostatic properties can be found in Ref. [3]. The α and effective anisotropy field ($H_{k,eff}$) of these L1$_0$-FePd films were measured with TR-MOKE, which uses ultrafast pump and probe pulses to initialize and detect magnetization precession of magnetic films. The testing temperatures (T_{test}) range from RT to 150°C, as controlled by a sample environmental heater [2].

III. RESULTS AND DISCUSSION

Figure 1(a) depicts a schematic of TR-MOKE configuration and the sample stack structure. Figure 1(b) shows several representative TR-MOKE signals under increasing external magnetic fields. The precession frequencies and relaxation time are extracted from the time-resolved scans for estimation of α and $H_{k,eff}$ at a given T_{test}. Figure 1(c) shows $H_{k,eff}$ of samples with different buffer layers as a function of T_{test}. A general trend of $H_{k,eff}$ decreasing with T_{test} is observed for all samples. However, the decrease in $H_{k,eff}$ is the fastest for MgO/FePd (56% of its RT $H_{k,eff}$ at 150°C), followed by Cr/Ru/FePd and Cr/Pt/FePd (62% and 75%, respectively). The change in $H_{k,eff}$ is correlated with the L1$_0$ ordering parameter (S) of FePd (S: MgO/FePd < Cr/Ru/FePd < Cr/Pt/FePd). A more nuanced temperature dependence arises across the α vs T plots in

Xiaojia Wang

E-mail: wang4940@umn.edu

Tel: +1-612-625-1583

Fig. 1(d). When T_{test} varies from RT to 150°C, α stays constant within our experimental uncertainty for MgO/FePd. For the samples with noble metal underlayers, we observe a slight increase (from 0.011±0.002 to 0.013±0.003) for Cr/Pt/FePd, but a more significant relative increase in Cr/Ru/FePd, where α increases from 0.005±0.003 to 0.009±0.002. Although the FePd layers are nominally identical, increasing T_{test} above RT increases the buffer layer resistivity, which can in turn reduce the spin diffusion length (λ). The interplay between the shorter λ of Pt (<2 nm) and Ru (4 nm) at RT compared with the buffer layer thickness (4 nm) [4,5] can determine the extent to which spin-pumping induced α enhancement takes place at elevated temperature.

In conclusion, we have demonstrated the buffer/seed layers play a significant role in determining the temperature-dependent α of FePd. Our initial data suggest Cr/Ru/FePd has a weaker spin-pumping contribution to α at RT. However, the Gilbert damping increases faster with temperature compared with that of Cr/Pt/FePd. The buffer/seed layers also affect the reduction of $H_{k,eff}$ at elevated temperatures, which is correlated with the L1$_0$ ordering of the FePd layers.
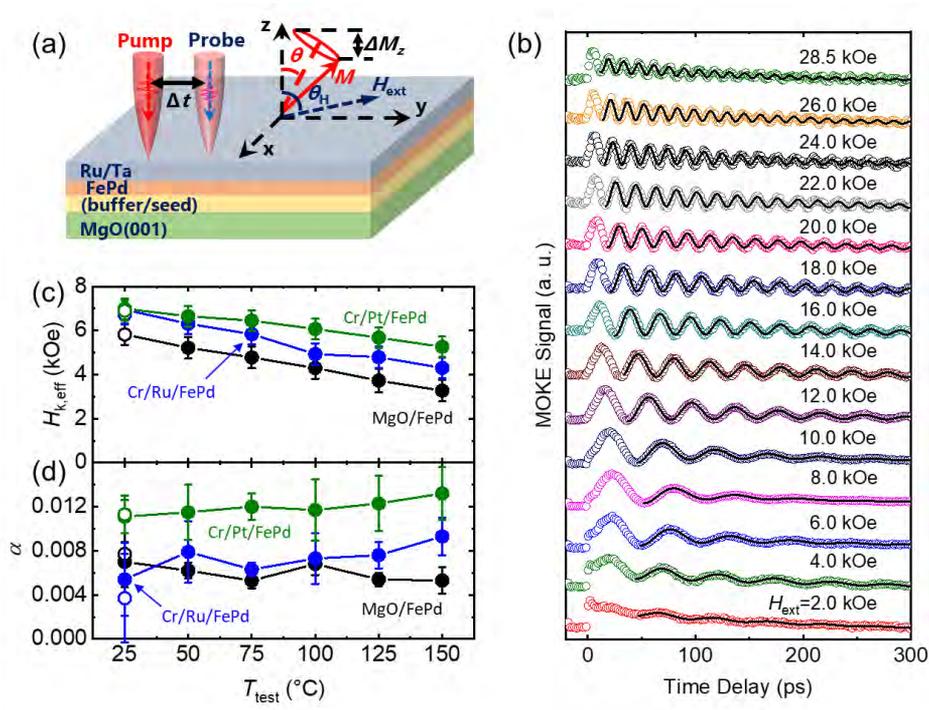

Fig. 1 (a) Schematic of the TR-MOKE measurements and sample stack. (b) TR-MOKE signals for the Cr/Pt/FePd sample at RT. (c) Temperature-dependent Gilbert damping, α, and (d) temperature-dependent effective anisotropy field, $H_{k,eff}$, for FePd samples with different buffer layers.

REFERENCES

1) J. M. Iwata-Harms, *et al.,* "High-temperature thermal stability driven by magnetization dilution in CoFeB free layers for spin-transfer-torque magnetic random access memory", *Sci. Rep.,* 8, 14409 (2018).
2) D. Zhang, *et al.,* "Low Gilbert damping and high thermal stability of Ru-seeded L1$_0$-phase FePd perpendicular magnetic thin films at elevated temperatures", *Appl. Phys. Lett.,* 117, 082405 (2020).
3) X. Wang, *et al.,* "Buffer layer engineering of L1$_0$ FePd thin film with large perpendicular magnetic anisotropy", *AIP Adv.* **11**, 025106 (2021).
4) K. Roy, "Estimating the spin diffusion length and the spin Hall angle from spin pumping induced inverse spin Hall voltages", *Phys. Rev. B* **96**, 174432 (2017).
5) S. Yakata, *et al.*, "Temperature dependences of spin-diffusion lengths of Cu and Ru layers", *Jpn. J. Appl. Phys*, **45**, 5A (2006).

SWITCHING CURRENT DENSITY OF PERPENDICULAR MAGNETIZATION BY SPIN-ORBIT TORQUE

Lijun ZHU[1,2]**, D. C. RALPH**[1]**, R. A. BUHRMAN**[1]

1) Cornell University, Ithaca, New York 14850, USA
2) Institute of Semiconductors, Chinese Academy of Sciences, Beijing 100083, China

I. INTRODUCTION

Strong dampinglike spin-orbit torque (SOT) can efficiently switch the magnetic free layers of magnetic tunnel junctions (MTJs) at the nanosecond timescale [1]. Enormous efforts have been made on developing energy-efficient, high-endurance, integration-friendly spin current generators (SCGs)[2,3] that can provide high dampinglike SOT efficiency (ξ_{DL}^{j}). This is mainly motivated by the fact that ξ_{DL}^{j} of a SCG/ferromagnet (FM) heterostructure directly connects to the density of the critical switching current inside the SCG layer (j_c) and thus the *total* switching current (I_c, the sum of the currents in the SCG and the FM layers) that will define the energy efficiency ($\propto I_c^2$), the scalability (the transistor dimension $\propto I_c$), and the endurance (electro-immigration $\propto I_c^2$) of SOT-MTJs.

In simplified models, ξ_{DL}^{j} of a heterostructure with perpendicular magnetic anisotropy inversely correlates to j_c via Eq. [1] in the macrospin limit and via Eq. [2] in the domain wall depinning regime,

$$j_c = e\mu_0 M_s t_{FM} (H_k - \sqrt{2}|H_x|)/\hbar\xi_{DL}^{j}, \qquad (1)$$

$$j_c = (4e/\pi\hbar) \, \mu_0 M_s t_{FM} H_c/\xi_{DL}^{j}, \qquad (2)$$

where e is the elementary charge, $\hbar$ is the reduced Planck constant, μ_0 is the permeability of vacuum, H_x is the applied field along the current direction, and t_{FM}, M_s, H_k, and H_c are the thickness, the saturation magnetization, the effective perpendicular anisotropy field, and the coercivity of the FM, respectively.

II. RESULTS

Here, we demonstrate by a variety of examples that there is no simple correlation between the critical switching current density j_c and ξ_{DL}^{j} of a micrometer-sized perpendicular SCG/FM bilayer [4]. As a consequence, the magnitudes of j_c by themselves do not provide reliable guidance about the relative strengths of ξ_{DL}^{j} or the relative potential of different spin-current-generation materials for technological applications. We find that ξ_{DL}^{j} can be overestimated by up to thousands of times if j_c is assumed to represent the critical switching current density of a rigid macrospin. When j_c is assumed as the critical current for depinning chiral domain walls, ξ_{DL}^{j} can be either under-estimated or overestimated by up to tens of times.

REFERENCES

1) Lijun Zhu, Lujun Zhu, Shengjie Shi, D. C. Ralph, R. A. Buhrman, "Energy-efficient ultrafast SOT-MRAMs based on low-resistivity spin Hall metal Au$_{0.25}$Pt$_{0.75}$", *Adv. Electron. Mater*. **6**, 1901131 (2020).
2) Lijun Zhu, R. A. Buhrman, "Maximizing spin-orbit torque efficiency of Pt/Ti multilayers: Tradeoff between the intrinsic spin Hall conductivity and carrier lifetime", *Phys. Rev. Appl*. **12**, 051002 (2019).
3) Lijun Zhu, Lujun Zhu, R. A. Buhrman, "Fully Spin-Transparent Magnetic Interfaces Enabled by the Insertion of a Thin Paramagnetic NiO Layer", *Phys. Rev. Lett*. 126, 107204 (2021).
4) Lijun Zhu, D.C. Ralph, R.A. Buhrman, "Lack of Simple Correlation between Switching Current Density and Spin-Orbit-Torque Efficiency of Perpendicularly Magnetized Spin-Current-Generator–Ferromagnet Heterostructures", *Phys. Rev. Appl*. 15, 024059 (2021).

Lijun Zhu
E-mail: lz442@cornell.edu
Tel: +1-607-2557500

COMPARISON OF TWO PARAMETRIC MECHANISMS OF MAGNETIZATION REVERSAL IN FeCoB NANOMAGNET. THEORY AND EXPERIMENT.

Vadym ZAYETS

Platform Photonics Research Center, AIST, Japan, v.zayets@gmail.com

I. PARAMETRIC MECHANISM OF MAGNETIZATION REVERSAL

The reduction of energy consumption is one of major challenges of the present MRAM development. The recording mechanisms of the Spin Torque (ST) MRAM and the Spin-Orbit Torque (SOT) MRAM are based on the spin injection between the "pin" to "free" layer of a MRAM cell. A possible reduction of the MRAM recording power is limited by a minimum amount of the injected spin- polarized electrons, which is necessary to create a sufficient ST or SOT torque in order to reverse the magnetization of the "free" layer. This fundamental limitation is difficult to avoid. The reduction of the volume of the "free" layer is only a feasible method for the reduction of the MRAM recorded power.

Recently, a new mechanism of recording for a MRAM cell, which is based on a parametric resonance, was proposed. [1]. This mechanism requires a substantially smaller spin torque for the magnetization reversal due to the resonance nature of this recording mechanism and, therefore, it can be a solution for further reduction of the recording energy for the MRAM operation.

Depending on a magnetic parameter, which is modulated in a resonance with magnetization precession, there are several possible mechanisms of the parametric magnetization reversal. In this presentation, we experimentally study and compare efficiency of two parametric mechanisms. The first mechanism is due to a modulation of the magnetic field of the Spin- Orbit Torque. The second mechanism is due to modulation of the anisotropy field.

II. MECHANISM 1: PARAMETRIC RESONANCE DUE TO CURRENT-INDUCED MAGNETIC FIELD OF SPIN-ORBIT TORQUE

An electrical current flowing through a nanomagnet can create an accumulation of spin- polarized electrons at nanomagnet boundaries. The magnetic field $H^{(CI)}$, which is originated by the accumulated spins, causes a torque, which may reverse the magnetization direction of the nanomagnet. This torque is called the spin-orbit torque [2].

A conventional measurement method of $H^{(CI)}$ is the method of the second harmonic [2]. Recently, a new method high-precession measurement of $H^{(CI)}$ was proposed [2]. Figure 1 shows $H^{(CI)}$ measured in a FeCoB nanomagnet by this method as a function of a current density and a external perpendicular magnetic field H_z. $H^{(CI)}$ is linearly proportional to the current density. The dependence of the magnitude
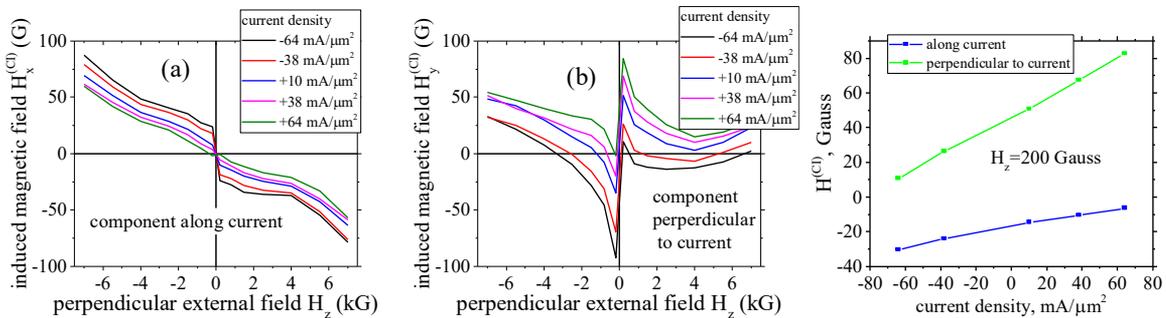

Fig.1 Parametric mechanism 1. Measured in-plane magnetic field $H^{(CI)}$ induced by the spin accumulation as a function of a perpendicular-to- plane magnetic field H_z and current density in a FeCoB nanomagnet. Measured components of $H^{(CI)}$ (a) along current (b) perpendicular to current as a function of an external magnetic field H_z. (c) $H^{(CI)}$ vs. current density at H_z =200 Gauss.

Vadym Zayets
E-mail: v.zayets@gmail.com
tel: +81-29-861-5426

and direction of $H^{(CI)}$ on H_z is substantial and complex. Since $H^{(CI)}$ is relatively small ~60 Gauss,, a static external magnetic field of the same magnitude is unable to reverse the magnetization, because the nanomagnet magnetization is kept along its easy magnetic axis by a substantially stronger internal magnetic field, which is measured to be about 4 kGauss. However, when the electrical current, which flows through the nanomagnet, and, therefore, $H^{(CI)}$ are modulated at a frequency close to the Larmor frequency ω_L of the magnetization precession, even the small magnetic field $H^{(CI)}$ is able to enhance the magnetization precession and to reverse the magnetization direction [1].

A unique feature of the parametric pumping is the ability to induce the magnetization precession and the magnetization reversal by a DC electrical current when there is no external parameter modulated at the precession frequency. This effect occurs only in a magneto-resistant structure when the electrical current is modulated by the magnetization precession and the modulated current creates the magnetic field $H^{(CI)}$,which parametrically enhances the same precession. There is a positive feedback loop, which is able to enhance the precession of a tiny thermal oscillation until a magnetization reversal occurs [1].

III. MECHANISM 2: PARAMETRIC RESONANCE DUE TO MODULATION OF ANISOTROPY FIELD BY ELECTRICAL CURRENT

The parameter, which characterized the strength of the Perpendicular magnetic anisotropy (PMA) is the anisotropy field. The anisotropy field H_{ani} is the magnetic field, at which the nanomagnet magnetization is fully turned in-plane under an external in-plane magnetic field. A spin accumulation at a nanomagnet boundary affects PMA and, as a result, modulates H_{ani}. Figure 2 shows H_{ani} measured in a FeCoB nanomagnet [4] as a function of a current density and an external perpendicular magnetic field H_z. The dependence of H_{ani} on current density is substantial and non-linear. The dependence of H_{ani} on H_z is weak.

In contrast to Mechanism 1, the parametric enhancement of magnetization precession by this mechanism can occur only when an external in-plane magnetic field is applied. In this case, the nanomagnet magnetization turns out from its equilibrium perpendicular- to- plane direction and the modulation of H_{ani} changes the magnetization angle. When the modulation is in resonance with the precession, the parametric enhancement occurs.

REFERENCES

1) V. Zayets, "Mechanism of parametric pumping of magnetization precession in a nanomagnet. Parametric mechanism of current-induced magnetization reversal.", *arXiv:2104.13008 (2021)*.
2) K. Garello, I. M. Miron, C. O. Avci, F. Freimuth, Y. Mokrousov, S. Blügel, S. Auffret, O. Boulle, G. Gaudin, and P. Gambardella, "Symmetry and magnitude of spin-orbit torques in ferromagnetic heterostructures," *Nat. Nanotechnol. 8, 587–593 (2013)*.
3) V. Zayets, "High-precision measurement method of magnetic field induced by spin- accumulated electrons in FeCoB nanomagnet" *Intermag CB-04, (2021)*.
4) V. Zayets, " Measurement of anisotropy field under external perpendicular magnetic field in FeCoB and FeB nanomagnets. Study of PMA features in a nanomagnet" *MMM N4-03 (2020)*.
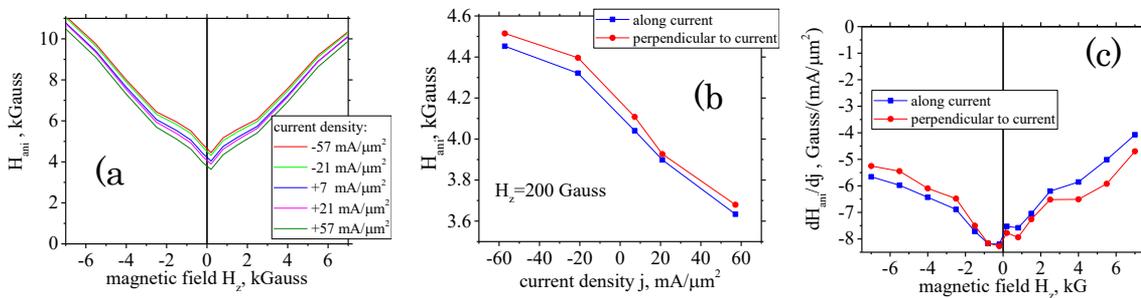
Fig.2 Parametric mechanism 2. Measured dependence of the anisotropy field H_{ani} in a FeCoB nanomagnet on perpendicular-to- plane magnetic field and current density. (a) H_{ani}vs.H_z. A line of different color correspond to a different current density j. (b) (a) H_{ani}vs. current density measured along and perpendicularly to the current direction. (c) the slope dH_{ani}/dj vs. H_z measured along and perpendicularly to the current direction.

Strain-spin coupling induced high-frequency magnetoacoustic resonance in perpendicular magnetic multilayers

D. ZHANG[1*], J. Zhu[2], T. Qu[3], D. M Lattery[2], RH Victora[1,3], X. Wang[1,2], J.-P. Wang[1,3]

1) Department of Electrical and Computer Engineering; 2) Department of Mechanical Engineering; 3) School of Physics and Astronomy, University of Minnesota, Minneapolis, MN 55455, USA.

INTRODUCTION

Among the abundant physical phenomena from the magnon-phonon coupling, the strain-assisted magnetoacoustic resonance in ferromagnetic materials provides an energetically efficient path for rapid switching of spin state, which is required for applications in spintronic devices. In this talk, we will present the observation of the coupling of magnons and phonons in both time and frequency domains upon femtosecond laser excitation. This strain-spin coupling leads to a magnetoacoustic resonance in perpendicular magnetic $[Co/Pd]_n$ multilayers, reaching frequencies in the extremely high frequency band, e.g., 60 GHz. The results of this work offer a potential pathway to manipulating both the magnitude and timing of extremely high frequency and strongly coupled magnon-phonon excitations (1).

II. EXPERIMENTAL DETAILS

All samples with the stack of $[Co(x)/Pd(y)]_n/Co(x)/Ta(3)$ (x = 0.30 to 0.70 nm; y = 0.70 to 1.80 nm) are deposited on Si/SiO_2 (300 nm) substrate at room temperature using a six-target Shamrock magnetron sputtering system with the ultrahigh vacuum (base pressure < 5.0×10^{-8} torr). Both TDTR and TR-MOKE methods are used to investigate the magnetic dynamic and spin-strain coupling. A mode-locked Ti:Sapphire laser with a pulse duration of ~100 fs and a center wavelength of 783 nm at a repetition rate of 80 MHz are used for TDTR and TR-MOKE measurements.

III. RESULTS AND DISCUSSION

Figure 1a illustrates the time-resolved magneto-optical Kerr effect (TR-MOKE) and time-domain thermoreflectance (TDTR) ultrafast measurement configuration, together with a schematic of the sample stack. We select the $[Co(0.8 nm)/Pd(1.5 nm)]_{11}$ multilayered structure with a larger thickness as a model system. It has a perpendicular anisotropy with an effective field of $H_{k,eff}$ ~ 6.5 kOe and magnetic anisotropy of K_u ~ 4.4 Merg/cc, as shown in Fig. 1b. The TR-MOKE results of $[Co(0.8 nm)/Pd(1.5 nm)]_{11}$ with the range of H_{ext} from 10 kOe to 29 kOe are plotted in Fig. 1c. Interestingly, we find that for 18 kOe < H_{ext} < 24 kOe, TR-MOKE signals show the amplitude of precessional oscillations of M_z increases instead of the usual decrease in the first 60 ps following the pump excitation. From Fig. 1d of TDTR data, we can find that the acoustic strains prevail in the first 60 ps. For the range of 18 kOe < H_{ext} < 24 kOe, the injected energy by the strain overcomes the magnetically dissipated energy, leading to the enhanced amplitude of spin precession roughly within this first 60 ps, in contrast to the monotonic decaying trend of a typical damped feature of spin precession at other fields.

To accurately describe the time-domain behavior and compare directly with TR-MOKE signals, we employ micromagnetic simulation based on the Landau-Lifthitz-Gilbert (LLG) equation, including the magnetostriction effect and the damping. Comparing with the experimental data from TR-MOKE as shown in Fig. 2a, we can see that the theoretical model we propose can capture all the key features in this ultrafast magnon-phonon coupling behavior, as plotted in Fig. 2b (simulated result). From the energy perspective, the phonon initially pumps enough energy into the magnon system to overwhelm the energy dissipation. Figure 2c plots the frequencies of spin precession of the $[Co(0.8 nm)/Pd(1.5 nm)]_{11}$ multilayer, which are fitted from the TR-MOKE signal as a function of H_{ext}. There are 2 modes, the low frequency mode being labeled Mode 1 (open black circles), and the high frequency mode being labeled Mode 2 (open red diamonds). These two modes are weakly coupled. The amplitudes of both modes increase in the hybridization regime, as shown in Fig. 2d. The original phonon-driven mode is now highly visible owing to the admixed magnon, where its amplitude changes from a negligible value to a notable value. The original magnon-driven mode is enhanced owing to the pumping from phonon, where its amplitude enhancement is caused by the strain amplitude, which also results in magnon-phonon hybridization. In addition, this hybridization appears as a magneto-acoustic resonance at the resonance field (the strongest effect) and nearby, as verified by the enhanced wave envelope in the TR-MOKE signals in Fig. 1c. We can conclude the magnon-phonon coupling substantially influences the spin dynamics and induces a resonant

state.

REFERENCES

1). D. L. Zhang, et al., "High-frequency magnetoacoustic resonance through strain-spin coupling in perpendicular magnetic multilayers", Sci. Adv. 6, eabb4607 (2020).
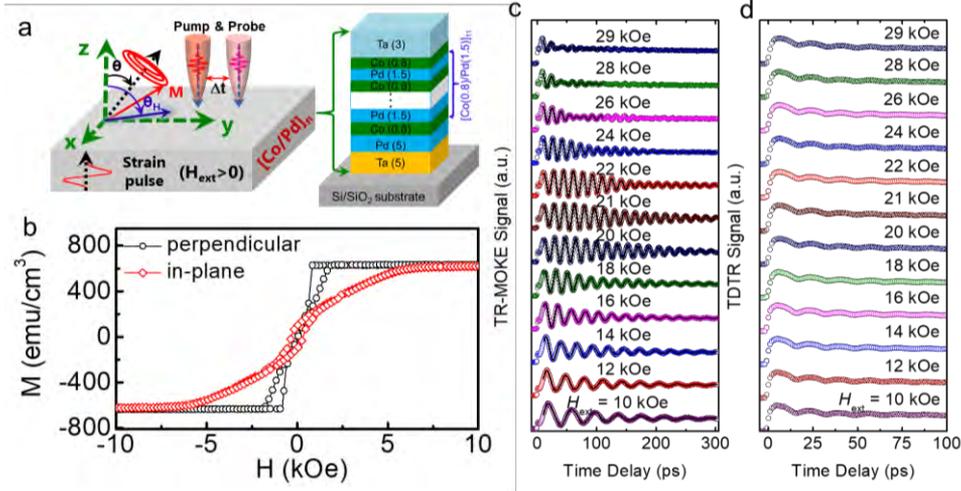
Fig. 1 (a) Illustration of the ultrafast TR-MOKE measurements on the [Co/Pd]n multilayer with numbers in parentheses denoting layer thicknesses in nanometers. (b) The magnetic hysteresis loops of the [Co(0.8 nm)/Pd(1.5 nm)]$_{11}$ multilayer with a magnetic anisotropy field H$_{k,eff}$ of ~6.5 kOe. (c) The experimental and fitted TR-MOKE signals and (d) the experimental TDTR signals as a function of H$_{ext}$ (10 to 29 kOe). Magnetization precession presents a resonance phenomenon while for 18 kOe < H$_{ext}$ < 24 kOe.
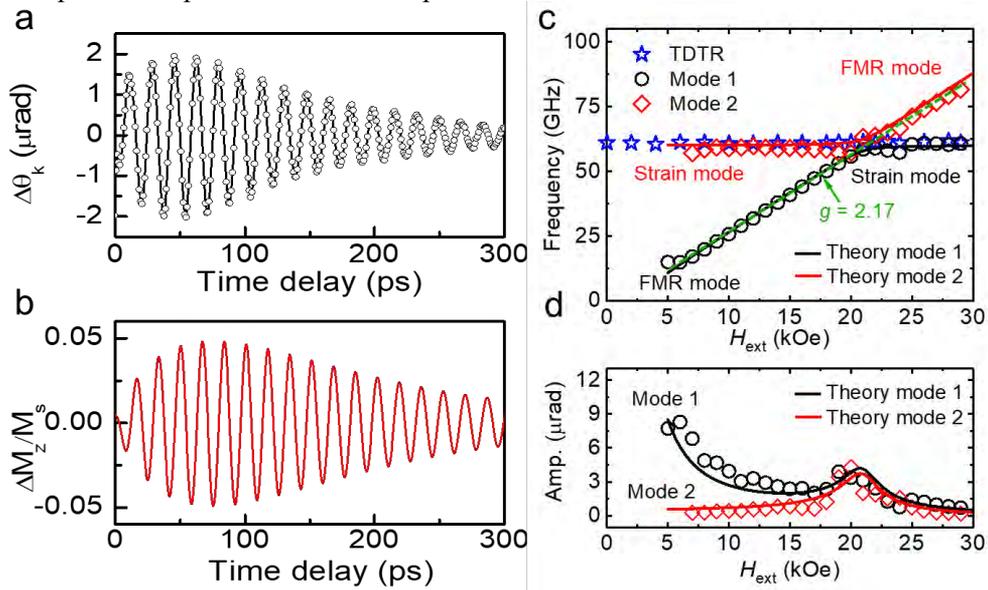

Fig. 2 (a, b) The experimental and simulated TR-MOKE signal of the [Co(0.8 nm)/Pd(1.5 nm)]$_{11}$ multilayer with H$_{ext}$ = 21 kOe, respectively. The strain used to produce the simulated signal is 0.5%. (c) The frequency of the [Co(0.8 nm)/Pd(1.5 nm)]$_{11}$ multilayer as a function of H$_{ext}$. The anti-crossing point of mode 1 and mode 2 occurs at the resonance field (H$_{ext}$ ≈ 21 kOe), where the frequencies of modes 1 and 2 split and open a gap Δf. (d) The individual M$_z$ amplitudes of modes 1 and 2 from both the experiment and the theory as a function of H$_{ext}$ for the [Co(0.8 nm)/Pd(1.5 nm)]$_{11}$ multilayer. There exists an apparent amplification of both modes due to the coupling between these two modes near the anti-crossing point.

Delin Zhang
E-mail: dlzhang@umn.edu
tel: +1-612-402-0710

High spin Hall angle in sputtered BiSb topological insulator (bottom)/ ferromagnet with in-plane magnetization on sapphire substrates

J. Sasaki[1*], H.H. Huy[1], N.H.D. Khang[1], P.N. Hai[1],

Q. Le[2], B. York[2], X. Liu[2], S. Le[2], C. Hwang[2], M. Ho[2], H. Takano[2]

1) Tokyo Institute of Technology, Tokyo, Japan

2) Western Digital Inc, CA, USA

* Email: sasaki.j.ab@m.titech.ac.jp

I. INTRODUCTION

Topological isolators (TIs) are room-temperature quantum materials that have semiconducting bulk states and conductive surface states. The large spin Hall effect in TIs makes them promising materials for various spin-orbit torque (SOT) applications. Among TIs, BiSb is particularly promising as it shows large spin Hall angle and high electrical conductivity ($\theta_{SH} \sim 52$, $\sigma \sim 2.5 \times 10^5$ $\Omega^{-1}m^{-1}$) in epitaxial BiSb (top) /MnGa [1] and sputtered polycrystalline BiSb (top)/(Pt/Co)$_n$ ($\theta_{SH} \sim 12.4$, $\sigma \sim 1.5 \times 10^5$ $\Omega^{-1}m^{-1}$) [2], where the magnetic layers show perpendicular magnetic anisotropy.

In SOT applications, however, BiSb (bottom) / ferromagnet (FM) structure is more preferred for simple device implementation. This structure also has the benefit of causing less damage to the magnetic layers by the heavy Bi/Sb atoms during deposition.

In this work, we report on large spin Hall effect in BiSb (bottom)/ FM with in-plane magnetization deposited by magnetron sputtering on sapphire substrates. Here the FM has in-plane magnetization and includes interfacial layer (Pt, Ru, Ti 0 – 1 nm) / Co (0.4 – 1 nm) / Pt 1 nm. We achieved a high effective spin Hall angle of 3 in BiSb (bottom)/Pt 1 nm/ Co 1 nm/ Pt 1 nm structure.

II. METHODOLOGY

We deposited multilayers of $Bi_{0.85}Sb_{0.15}$ 10 nm (bottom) / interfacial layer (Pt, Ru, Ti) 0 –1 nm / Co 0.4 – 1 nm/ Pt 1 nm on c-plane sapphire substrates by magnetron sputtering. The 10 nm-thick BiSb layer on sapphire has (001) orientation and sheet resistance of 750 Ω. Samples were patterned into 25 μm-wide Hall bars by optical lithography and lift-off technique.

Spin Hall effect was estimated by measuring DC anomalous Hall effect (R_{AHE}) and high field AC second harmonic Hall effect ($R_H^{2\omega}$). At a given bias current, the antidampinglike field H_{AD} is obtained by fitting the high field $R_H^{2\omega}$- magnetic field H_x data using the following formula

$$R_H^{2\omega} = \frac{R_{AHE}}{2} \frac{H_{AD}}{(H_x + H_k)} + C_{ONE}H_x + C_{ANE}$$

Here, H_k is the anisotropic magnetic field, C_{ONE} represents the ordinary Nernst effect, and C_{ANE} represents the anomalous Nernst effect. The contribution of the fieldlike term is neglectable. The effective spin Hall angle θ_{SH}^{eff} is then calculated from the $H_{AD} - I_{BiSb}$ relationships.

III. RESULTS AND DISCUSSION

Figure 1 shows the spin Hall angle measured in a series of samples of BiSb 10 nm (bottom)/ Pt 0 – 1 nm / Co 0.4 nm / Pt 1 nm as function of the interfacial Pt layer thickness. Due to the surface roughness (~ 8 Angstrom) of BiSb in this series, the Co 0.4 nm does not form a continuous film without the Pt interfacial layer and no spin Hall effect was observed. However, with increasing the interfacial Pt thickness, the effective spin Hall angle is significantly improved and reaches θ_{SH}^{eff} = 1.6 at the Pt thickness of 1 nm. Figures 2 and 3 show the change of R_{ANE} and the anisotropic magnetic field H_k of the Co layer as a function of the interfacial Pt layer thickness. With increasing the interfacial Pt layer thickness, R_{ANE} increases and H_k decreases, indicating improved Co morphology and enhanced Pt/Co interfacial perpendicular magnetic anisotropy. Our results indicate that smoothing the BiSb/FM interface is important to achieve a high spin Hall angle. However, θ_{SH}^{eff} drastically decreases when Pt thickness is 1.5 nm, probably due to spin loss in the thick Pt layer.

Next, we measured the spin Hall effect in a series of samples of BiSb 10 nm (bottom) / Pt,Ru,Ti 1 nm / Co 1 nm / Pt 1 nm. The surface roughness of BiSb in this series is reduced to about 5.6 Angstrom. A large $\theta_{SH}^{eff} = 3.0$ is obtained for the interfacial Pt 1 nm, followed by $\theta_{SH}^{eff} = 1.5$ for Ru 1 nm and $\theta_{SH}^{eff} = 0.5$ for Ti (see Table I).

Our results show that it is possible to achieve a high spin Hall angle in BiSb (bottom) / FM with in-plane magnetization by optimizing the interfacial layer for SOT applications.

REFERENCES

1) N. H. D Khang, Y. Ueda, P. N. Hai. "A conductive topological insulator with large spin Hall effect for ultralow power spin–orbit torque switching." *Nat. Mater.* 17, 808–813 (2018).

2) T. Fan, N. H. D. Khang, S. Nakano, P. N. Hai. "Ultrahigh efficient spin-orbit torque magnetization switching in all-sputtered topological insulator - ferromagnet multilayers", arXiv:2007.02264.
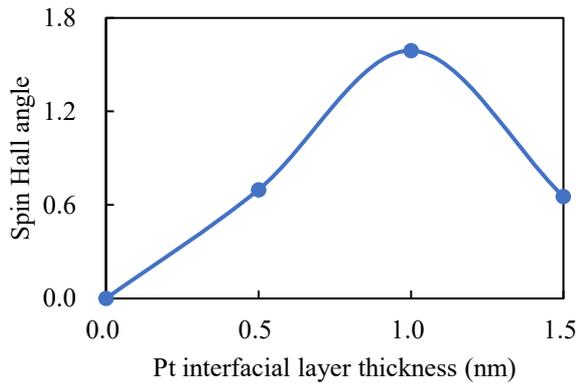
Fig. 1 Spin Hall angle as a function of the Pt interfacial layer thickness in BiSb 10 nm (bottom) / Pt 0 − 1 nm / Co 0.4 nm / Pt 1 nm.

Table I. Effective spin Hall angle with various interfacial layer material in BiSb 10 nm (bottom) / Pt,Ru,Ti 1 nm / Co 1 nm / Pt 1 nm.

| Interfacial layer material (1nm)	θ_{SH}^{eff}
Pt	3.0
Ru	1.5
Ti	0.5
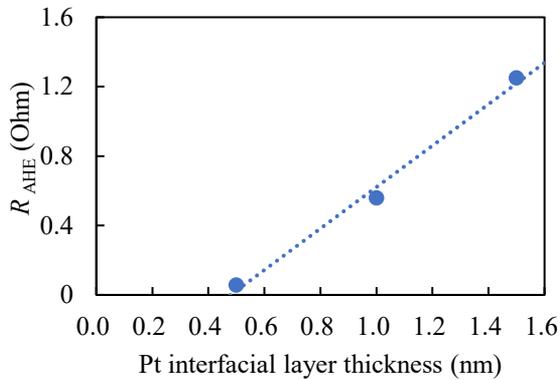
Fig. 2 Anomalous Hall resistance as a function of the Pt interfacial layer thickness in BiSb 10 nm (bottom) / Pt 0 − 1 nm / Co 0.4 nm / Pt 1 nm.
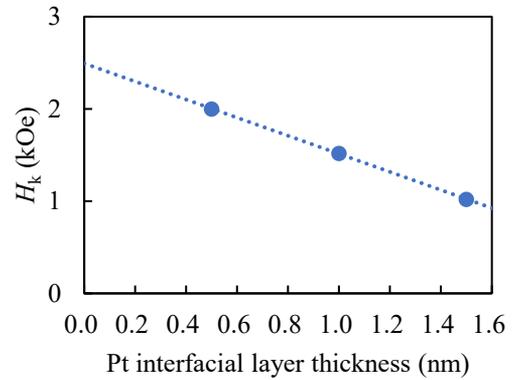

Fig. 3 Anisotropic magnetic field as a function of the Pt interfacial layer thickness in BiSb 10 nm (bottom) / Pt 0 − 1 nm / Co 0.4 nm / Pt 1 nm.

Jinghua Liu[1], Pingping Chen[2]

1）Fuzhou Univ., Fuzhou, China, jhl_fzu@163.com

2）Fuzhou Univ., Fuzhou, China, ppchen.xm@gmail.com

I.Abstract

Thanks to its superior feature of non-volatility, fast read/write speed, high endurance, and low power consumption, spin-torque transfer magnetic random access memory(STT-MRAM) has become a promising non-volatile memory (NVMs) technology that is suitable for many application. An STT-MRAM cell consists of magnetic tunneling junction(MTJ) as the data storage element and an nMOS transistor as the access control device. But, due to the physical characteristics of MTJ, the smallest storage unit of STT-MRAM, the write error transition probabilities differ by several orders of magnitude. Due to the asymmetric channel of write errors, the maximum error transition probability is of the order of 10^{-4}. Therefore, to flip these small data bits correctly, dynamic slient-variable-node-free scheduling (D-SVNFS) is used to correct these variable nodes quickly. However, due to the greedy nature of D-SVNFS, D-SVNFS may flip the corrected data bits again. To solve the increase of decoding error rate caused by the greedy nature of D-SVNFS, D-SVNFS and RBI-MSD (reliablity-based iterative min-sum decoding) decoding algorithms are combined by a joint method. After D-SVNFS corrects the error data bits, switch to RBI-MSD to further correct and verify the codes. Simulation results show that joint decoding has better error correction ability than RBI-MSD for LDPC code error caused by unexpected bit reversal in the STT-MRAM channel.

II.Implementation

SVNFS scheme strives to correct the potentially erroneous variable nodes on a priority basis by allowing unsatisfied check nodes to forward new message updates. In this process, given a selected variable node v_p, only its unsatisfied (if any) neighbor check nodes are short-listed for the next C2V message propagation based on the largest C2V residual[1]. This step expedites the decoding convergence speed as the unreliable variable nodes (connected with unsatisfied check nodes) will receive new message updates more often.

To better implement LDPC decoding on hardware, the decoding method uses the RBI-MSD algorithm. RBI-MSD algorithm utilizes integer reliability information and requires only binary logical and integer operation which results in low computational complexity[2].

Through simulation, when the resistance distribution of STT-MRAM memory cells overlap less ($\sigma0/\mu0$ is smaller), the simulation result of D-SVNFS is the worst, the simulation effect of RBI-MSD is in the

Jinghua Liu

E-mail: jhl_fzu@163.com

tel: +0086-17805973487

derived from paper [3]. In the simulation, 4 bits uniform quantization method is directly used to quantify the read voltage. In simulations, D-SVNFS is used to participate in the joint decoding and iterated twice, and then RBI-MSD decoding is performed. Through simulation, the performance of joint scheme is better than RBI-MSD when the resistance distribution is good. The code type used in Figure 1 is from paper [4] with a code rate of 0.83.
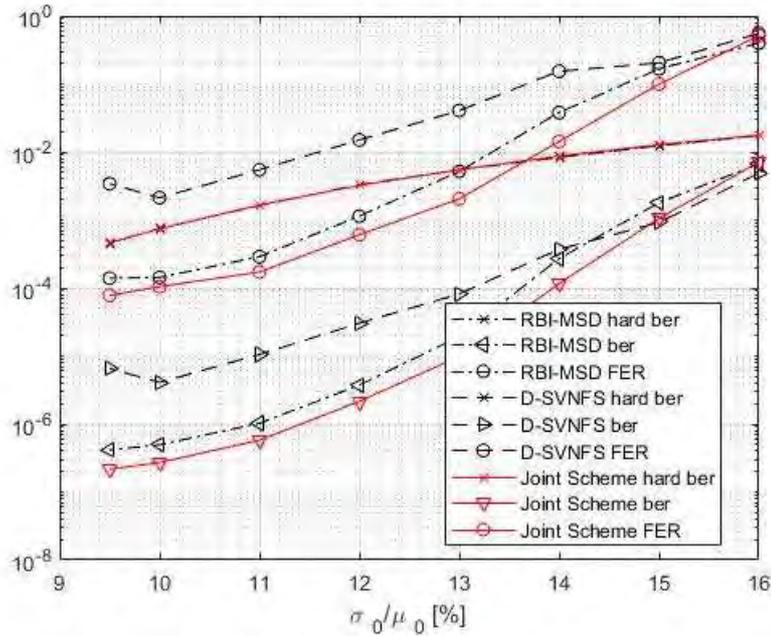

Fig. 1 Simulation result

III.Summary

It can be concluded that the joint decoding takes advantage of the fast convergence of D-SVNFS decoding, and combines with RBI-MSD decoding to control the greediness's negative effects of D-SVNFS decoding. Based on RBI-MSD, the joint decoding further improves the accuracy of decoding by increasing the computational complexity.

REFERENCES

1)Aslam,C.A.,et al. "Low-Complexity Belief-Propagation Decoding via Dynamic Silent-Variable-Node e-Free Scheduling." IEEE Communications Letters (2017).

2)Chen, H. , et al. "Comparisons Between Reliability-Based Iterative Min-Sum and Majority-Logic Decoding Algorithms for LDPC Codes." IEEE Transactions on Communications 59.7(2011):1766-1771.

3)Cai, K. , and K. Immink . "Cascaded Channel Model, Analysis, and Hybrid Decoding for Spin-Torque Transfer Magnetic Random Access Memory." IEEE Transactions on Magnetics 53.11(2017):1-1.

4)Zhong, X. , et al. "Design of Rate-Compatible Protograph LDPC Codes for Spin-Torque Transfer Magnetic Random Access Memory (STT-MRAM)." IEEE Access 7.99(2019):182425-182432.

MAGNETO-OPTICAL DETECTION OF MEMORY OPERATION IN MAGNETIC NANOWIRE DEVICE

Mao TAKAHASHI, Naoki NAKATANI, Kei OGURA, Norihiko ISHII
and Yasuyoshi MIYAMOTO
Science & Technology Research Laboratories, *NHK* (Japan Broadcasting Corporation),
Tokyo, JAPAN, takahashi.m-ob@nhk.or.jp

I. INTRODUCTION

With the advancement of television technology, required transfer-rate for storage has been increasing. For example, future spatial image reproduction 3D-TV storage requires ultra-high transfer-rate of at least 100 Gbps and ultra-large capacity. However, there is no existing storage that satisfies these requirements. It has been reported that fast current-driven domain wall motion [1] opens up the possibility leading to ultra-fast transfer-rate. Therefore, we have been studying a magnetic nanowire memory [2,3] on the basis of the domain wall motion, such as a famous racetrack memory [4]. Figure 1 shows a schematic illustration of the proposed nanowire memory consisted of parallel-aligned multiple magnetic nanowires as recording media. The binary information is stored as the direction of the magnetic moment in magnetic domains. A nanowire memory works as follows: 1. Write (magnetic field is generated by a current applied to a writer, which forms magnetic domains in nanowires.), 2. Drive (The written domains are shifted along the nanowires by a current applied to nanowires.) By repetition of write and drive, sequential binary data is stored into the nanowire media. Unlike conventional magnetic recording devices, it all works electrically, and we aim to achieve ultra-high transfer-rate by synchronizing parallel-aligned magnetic nanowires.

II. CALCULATION & EXPERIMENTAL RESULTS

First of all, we investigated the configuration of the writer by simulation, using the Landau–Lifshitz–Gilbert (LLG) equation. We simulated the magnetization reversal of magnetic nanowires in two writer cases, (a) a single metal wire and (b) a U-shaped metal wire, and compared their behaviors as shown in Figure 2. When a write current was applied to (a) the single-wire writer to generate a magnetic field, a magnetic domain was formed in the magnetic nanowires. However, the far end of the formed magnetic domains became distorted and unstable on each elapsed time. On the other hand, the magnetic domain formed with (b) the U-shaped writer was stable because the synthetic field was confined in the narrow gap between the two wires.

Thus, we fabricated a magnetic nanowire device using four parallel nanowires and a U-shaped writer. Figure 3 shows a microscopy image of the device and the configuration of the evaluation system. The U-shaped writer was stacked normal to and above the four magnetic nanowires consisted of $Pt(3)/[Co(0.3)/Tb(0.6)]_3$ (units in nm, layers from top to bottom) separated by a $SiO_2(20)/Si_3N_4(5)$ insulating layer. The write and drive processes were observed with a magneto-optical Kerr effect (MOKE) microscopy. Before the measurement, the magnetization direction of all the nanowires was initialized by an external field. After a write pulse current applied to the U-shaped writer, the formed magnetic domains in the gap are shifted to the right by drive pulse currents applied to four nanowires independently. Figure 4 shows MOKE images after write and drive, where dark regions (surrounded red lines) are written magnetic domins. Thus we succeeded in demonstrating fundamental memory operation in the device. In addition, instead of attaching an HDD-like write head to each magnetic nanowire, one U-shaped writer was able to write all the parallel-aligned nanowires simultaneously, which reduced the total amount of write current. Going forward, we will consider arranging notches regularly in magnetic nanowires to controll the dispersion of magnetic domain size and shift length because of Joule heating and unintended pinning sites.

Mao TAKAHASHI
Science & Technology Research Laboratories,
NHK (Japan Broadcasting Corporation),
E-mail: takahashi.m-ob@nhk.or.jp
Tel/Fax: +81-3-5494-3234
1-10-11 Kinuta, Setagaya, Tokyo 157-8510, Japan
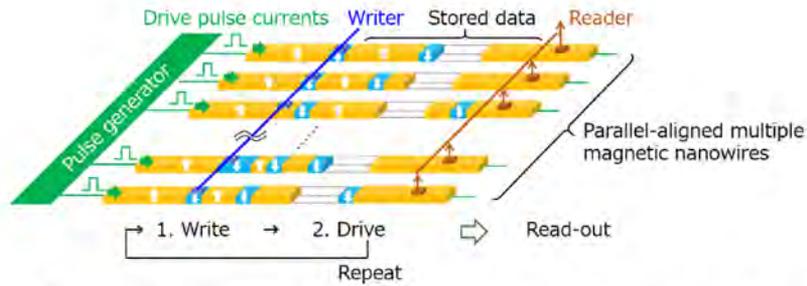
Fig. 1 Schematic illustration of proposed magnetic nanowire memory.
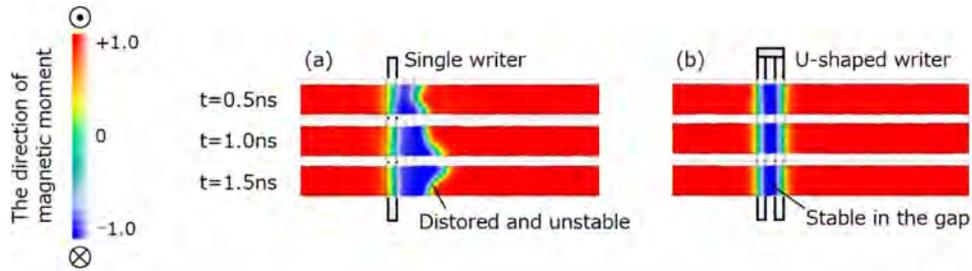

Fig. 2 LLG simulation results of magnetic domain formation on each elapsed time in magnetic nanowire with (a) single and (b) U-shaped writer.
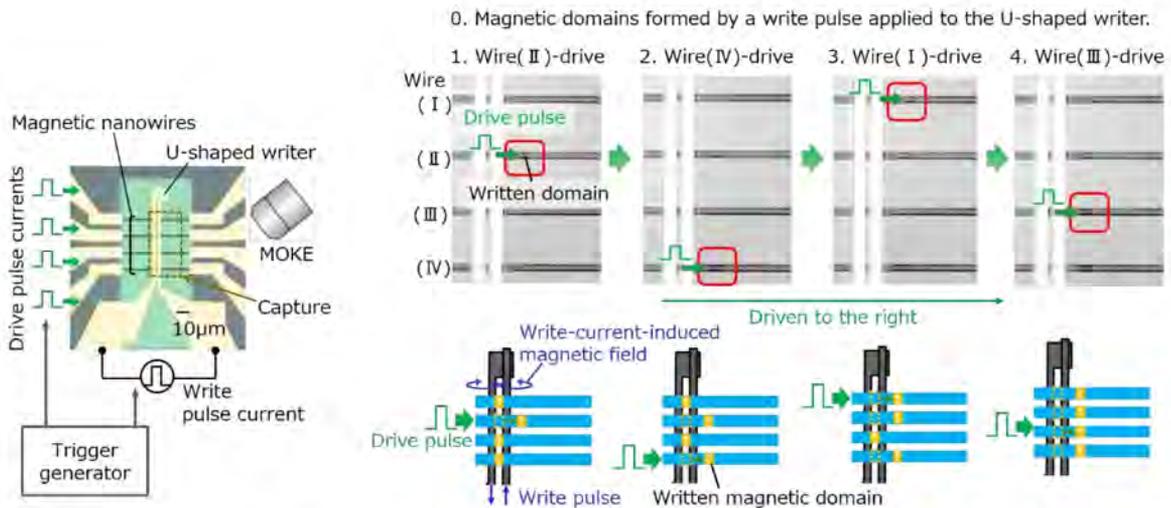

Fig. 3 Microscopy image of magnetic nanowire device and the configuration of measured system.

Fig. 4 MOKE images and illustrations of written and current-driven magnetic domains in four nanowires.

REFERENCES

[1] P. Van Thach et al., Joint MMM-Intermag 2019, CF-13 (2019)
[2] M. Okuda et al, IEEE Trans. Magn., **52**(7) 3401204, (2016)
[3] Y. Miyamoto et al, Joint MMM-Intermag 2019, GN-01 (2019)
[4] S. S. P. Parkin et al., Science, **320**, 190 (2008)

THE IMPORTANT HEAT CONTRIBUTION BY TUNNELING ELECTRON SPIN SCATTERING IN MAGNETIC TUNNEL JUNCTION

S. LIU[1], S. HU[1]

1) Xi'an Jiaotong University, Xi'an, China, lsh309@stu.xjtu.edu.cn

1) Xi'an Jiaotong University, Xi'an, China, shaojiehu@xjtu.edu.cn

I. INTRODUCTION

MRAM, as a new type of nonvolatile memory device, has attracted much attention due to its unlimited endurance, high speed, and low power consumption. However, it's a great challenge to reduce the critical switching current density with higher thermal stability [1]. To overcome this issue, a series of assisted data writing processes such as microwave-assisted switching (MAS) and thermal-assisted switching (TAS) have been developed[2,3]. Since discovering the spin caloric effects, converting heat current and spin current, a new promising method to reverse the magnetic momentum has emerged by thermal spin-transfer torques. [4] Both the TAS scheme and the spin-caloric effects are related to the heating process in the magnetic tunneling junction (MTJ). Therefore, it is vital to explore the production and transport of heat flow in MTJs. The impacts of Joule heating, which is the main contributor to heat in general cognition, have already been reported a lot [5]. Meanwhile, the tunneling spin scattering heating is another critical heating source caused by the inelastic scattering to excite magnons and phonons at the arrival FMs. [6] Sousa et al. once used a heat equation in 1D structure to simulate the heat process with the tunneling electron heating [7]. However, the tunneling spin scattering can induce different temperature profiles in the ferromagnetic layers with different magnetic states. Here, we systematically studied the temperature and temperature gradient induced by the tunneling spin scattering in MTJ by using 3D numerical simulations.

II. METHODS

The tunneling spin scattering is related to the two ferromagnetic states in MTJ. So the generated heat by tunneling spin scattering heat can be expressed as follows[7]:

$$q_{P(AP)} = \frac{jV_{P(AP)}}{l} e^{\left(-\frac{x}{l}\right)} \qquad (1)$$

Where j is the current density, V_P and V_{AP} refer to the voltage drop through the tunneling barrier at P and AP states of the MTJ. l is inelastic scattering mean free path, and x is the stack position of the barrier. In the simulation, we applied one constant bias current density 7.8×10^{10}A/m². The electrical conductivity of the barrier is about 64.3 S/m and 127.4 S/m for parallel and antiparallel states, respectively [8].

III. RESULTS AND DISCUSSION

Figure 1(a) shows the significant difference in the voltage drop in MTJ for the two states. The splitting voltage indicates a quite different tunneling spin scattering in the fixed layer. Fig. 1 (b) displays the temperature distribution of the nanopillar in P and AP states with and without tunneling spin scattering heat. The temperature profile clearly shows over 50 K enhancement with considering tunneling spin scattering. For AP state, the temperature reaches a 25 K enhancement at the junction. The extra temperature rise will lead to reduced thermal stability. Fig. 1(c) shows the temperature gradient profile. The enhanced temperature gradient by tunneling spin scattering heat at the interface could contribute additional thermal spin-transfer torque. The reduced thermal stability and enhanced temperature gradient in a fixed ferromagnetic layer should be the main reason for the asymmetry of the critical switching current density from P to AP and AP to P.

IV. SUMMARY

To summarize, we investigated the tunneling spin scattering heat in parallel (P) and antiparallel (AP) states using finite element simulation in magnetic tunneling junction. It showed a significantly different temperature contribution by the heating from tunneling electron spin scattering for the two states. The total temperature is increased to 25K for the P state to the AP state, resulting in reduced thermal stability. The significant temperature gradient enhancement in the fixed magnetic layer was also confirmed, contributing to the additional thermal spin-transfer torque to the free layer. Our demonstration may offer a new idea for MTJ design for thermal assistant magnetic switching by using tunneling spin scattering heat.

S. HU

E-mail: shaojiehu@xjtu.edu.cn

tel: +86-29-82667748

REFERENCES

1) S. Ikeda et al., "Magnetic tunnel junctions for spintronic memories and beyond," IEEE Trans. Electron Devices 54 (5) 991-1002, (2007).

2) C. Thirion et al., "Switching of magnetization by nonlinear resonance studied in single nanoparticles," Nat. Mater. 2 524-527, (2003).

3) I. L. Prejbeanu et al., "Thermally assisted MRAM," J. Phys.: Condens. Matter. 19 165218, (2007).

4) O Gomonay et al., "Spin caloric effects in antiferromagnets assisted by an external spin current," J. Phys. D: Appl. Phys. 51 264004, (2018).

5) D. H. Lee et al., "Increase of temperature due to Joule heating during current-induced magnetization switching of a MgO-based magnetic tunnel junction," Appl. Phys. Lett., 92(23) 233502, (2008).

6) S. Zhang et al., "Quenching of Magnetoresistance by Hot Electrons in Magnetic Tunnel Junctions," Appl. Phys. Lett., 79 (19) 3744-3747, (1997).

7) R. C. Sousa et al., "Tunneling hot spots and heating in magnetic tunnel junctions," J. Appl. Phys., 95(11) 6783-6785, (2004).

8) J. Hayakawa et al., "Current-induced magnetization switching in MgO barrier based magnetic tunnel junctions with CoFeB/Ru/CoFeB synthetic ferrimagnetic free layer," Jpn. J. Appl. Phys., 45(40) L1057-L1060, (2006).
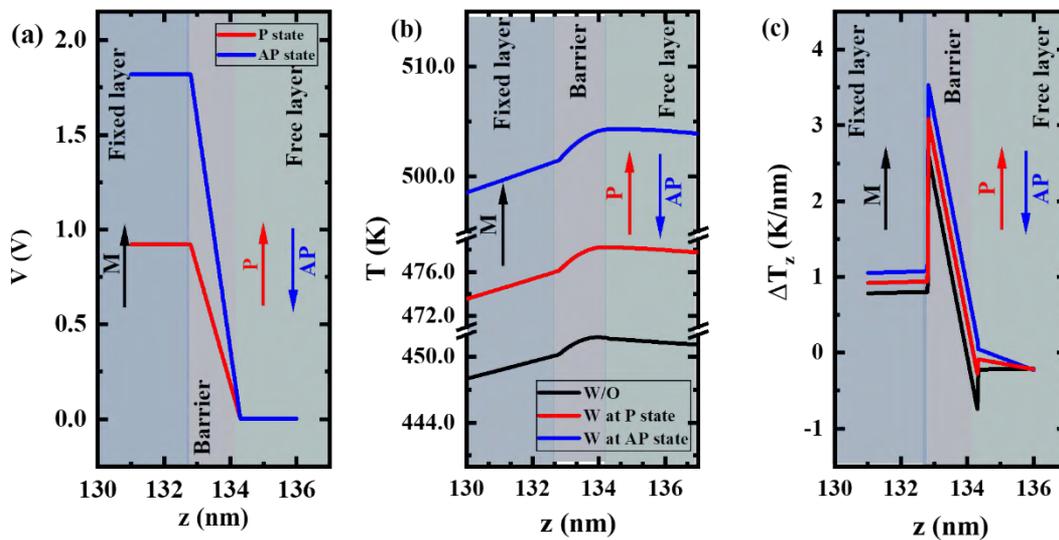
Fig. 1 (a)The voltage drop in MTJ in barrier at P and AP. The temperature (b) and temperature gradient (c) distribution with the bias current density 7.8×10^{10} A/m² in the MTJ.